


Heat and Mass Transfer

Series Editors: D. Mewes and F. Mayinger

**Springer-Verlag
Berlin Heidelberg
GmbH**

Engineering  **ONLINE LIBRARY**

<http://www.springer.de/engine/>

Martin Sommerfeld (Ed.)

Bubbly Flows

Analysis, Modelling and Calculation

With 194 Figures



Springer

Series Editors

Prof. Dr.-Ing. Dieter Mewes
Universität Hannover
Institut für Verfahrenstechnik
Callinstr. 36
30167 Hannover, Germany

Prof. em. Dr.-Ing. E.h. Franz Mayinger
Technische Universität München
Lehrstuhl für Thermodynamik
Boltzmannstr. 15
85748 Garching, Germany

Editor

Prof. Dr.-Ing. Martin Sommerfeld
Universität Halle-Wittenberg
Fachbereich Ingenieurwissenschaften
Institut für Verfahrenstechnik
06099 Halle (Saale), Germany

Library of Congress Cataloging-in-Publication-Data

Bubbly flows : analysis, modelling, and calculation / Martin Sommerfeld (ed.).

p. cm. -- (Heat and mass transfer)

Includes bibliographical references.

ISBN 978-3-642-62150-5

1. Multiphase flow. 2. Bubbles. I. Sommerfeld, Martin. II. Series.

TP156.F6B83 2004

660'.2832--dc22

ISBN 978-3-642-62150-5 ISBN 978-3-642-18540-3 (eBook)

DOI 10.1007/978-3-642-18540-3

This work is subject to copyright. All rights are reserved, whether the whole or part of the material is concerned, specifically the rights of translation, reprinting, reuse of illustrations, recitations, broadcasting, reproduction on microfilm or in any other way, and storage in data banks. Duplication of this publication or parts thereof is permitted only under the provisions of the German copyright Law of September 9, 1965, in its current version, and permission for use must always be obtained from Springer-Verlag. Violations are liable for prosecution under the German Copyright Law.

<http://www.springer.de>

© Springer-Verlag Berlin Heidelberg 2004

Originally published by Springer-Verlag Berlin Heidelberg New York in 2004

Softcover reprint of the hardcover 1st edition 2004

The use of general descriptive names, registered names trademarks, etc. in this publication does not imply, even in the absence of a specific statement, that such names are exempt from the relevant protective laws and regulations and therefore free for general use.

Typesetting: Digital data supplied by editor

Cover design: deblik Berlin

Printed on acid free paper 62/3020/M - 5 4 3 2 1 0

Preface

The priority research „Analysis, Modelling and Numerical Calculations of Multiphase Flows“ was running for 6 years (from 1996 to 2002) and financially supported by the Deutsche Forschungsgemeinschaft (DFG). The main objective of the research programme was to provide a better understanding of the physical basis for multiphase gas-liquid flows as they are found in numerous chemical and biochemical reactors. The research comprised steady and unsteady multiphase flows in three frequently found reactor configurations, namely bubble columns without internals, loop reactors, and aerated stirred vessels. For this purpose, new and improved measurement techniques should be developed. From the resulting knowledge and data, new and refined models for describing the underlying physical processes should result, which can be used for the establishment and improvement of analytic as well as numerical methods for predicting multiphase reactors. Thereby, the development, lay-out and scale-up of such processes should be possible on a more reliable basis.

For achieving this objective three research areas were defined:

- development and improvement of experimental techniques which allow accurate measurements in steady and unsteady multiphase flows
- elaboration of new modelling approaches in order to describe the basic transport processes for mass, momentum, and heat in bubbly flows
- development of analytical and numerical methods supplemented by the new modelling strategies in order to support optimisation and lay-out of technical multiphase processes.

In order to enhance cooperation within the priority research five working groups were established:

- bubble driven flows as for example in bubble columns and loop reactors
- three-phase flows (i.e. gas-liquid-solid flows)
- aerated stirred vessels
- experimental techniques
- modelling and numerical calculations

More details about the individual projects and their achievements can be found at www-mvt.iw.uni-halle.de. This homepage will be maintained for some period.

Within the priority research in total 22 projects were supported with durations between 2 and 6 years. This corresponds in total to about 105 man-years of scientists. The entire financial support through the DFG was about 6.9 million Euro. The scientific outcome of the research programme was published in about 60 journal papers and 100 conference contributions.

The final colloquium of the priority research was held in Freyburg (Unstrut) from 23. – 25. September 2002. During the colloquium most of the participants presented the main achievements of their research effort. In addition other research groups working in similar fields were invited to present recent research.

The financial support of the final colloquium by BASF Ludwigshafen is gratefully acknowledged.

Prof. Dr.-Ing. M. Sommerfeld
Dr.-Ing. B. Giernoth

Table of Contents

Bubble driven flows

O. Borchers and G. Eigenberger Detailed experimental studies on gas-liquid bubble flow in bubble columns with and without recycle	1
G. Brenn, V. Kolobarić and F. Durst Basic experimental investigations on the hydrodynamics of bubble columns	11
D. Bröder and M. Sommerfeld Examination of bubble collisions and coalescence in bubbly flows	21
Ch. Brücker and W. Schröder PIV-Study on bubble interaction and wakes in multiphase flows.....	37
S. Godo, K. Junghans, A. Lapin and A. Lübbert Dynamics of the flow in bubble column reactors	53
S. Scheid, S. John, O. Bork, H. Parchmann, M. Schlüter, N. Räßiger Improved model for the calculation of homogeneous gas-liquid flows	67
O. Gnotke, R. Jeschke and R. Loth Experimental and theoretical investigation of bubble break-up and coalescence in bubbly flows	85
D. Lucas, E. Krepper and H.-M. Prasser Experimental investigation and modeling of air/water flows in vertical pipes.....	101
D. Schmitz and D. Mewes Experimental and theoretical investigation of instationary bubble flow and mass transfer in a bubble column	117
A. Seeger, U. Kertzscher, K. Affeld, L. Goubergrits and E. Wellnhofer X-ray based particle tracking velocimetry for bubble columns with high void fraction	129

Modelling and numerical calculations

M. van Sint Annaland, N.G. Deen and J.A.M. Kuipers Multi-level modelling of dispersed gas-liquid two-phase flows	139
D. Bothe, M. Koebe, K. Wielage, J. Prüss and H.-J. Warnecke Direct numerical simulation of mass transfer between rising gas bubbles and water.....	159
M. F. Göz and M. Sommerfeld Analysis of bubble interactions in bidisperse bubble swarms by direct numerical simulation.....	175
D. Kuzmin and S. Turek Finite element discretization tools for gas-liquid flows	191

F. Lehr and D. Mewes	
A transport equation for the interfacial area in bubble columns using a population balance approach.....	203
D. Wiemann, F. Lehr and D. Mewes	
Flow fields in bubble columns with mass transfer	217
Three-phase flows	
M. Behling and D. Mewes	
X-ray computational tomography measurement of 3-phase flow in bubble columns	233
E. Bourloutski and M. Sommerfeld	
Euler/Lagrange calculations of gas-liquid-solid-flows in bubble columns with phase interaction	243
J. H. Enß, J. Schallenberg, V. Michele, H. Dziallas, D. C. Hempel	
Local parameters of three-phase flow in column reactors with high disperse phase hold-up	261
S. John, S. Scheid, H. Parchmann, O. Bork, M. Schlüter and N. Rübiger	
Model fundamentals for the design of three-phase loop reactors.....	275
U. Kertzscher, A. Seeger, K. Affeld and E. Wellnhofer	
Simultaneous measurement of the local liquid and the local solid velocities	287
Stirred vessels	
E. Gharabai and W. Polifke	
A numerical model of dispersed two phase flow in aerated stirred vessels based on presumed shape number density functions.....	295
V. Ilchenko, R. Maurus and T. Sattelmayer	
Influence of the operating conditions on the bubble characteristics in an aerated stirred vessel.....	307
F. Mayinger and O. Feldmann	
Bubble dispersion in aerated stirred vessels.....	319
A. F. Nassar, G. Zivkovic, B. Genenger and F. Durst	
PDA measurements and numerical simulation of turbulent two-phase flow in stirred vessels.....	337

Errata

Due to format incompatibility the following figures have not been correctly printed within the book:

Page 105

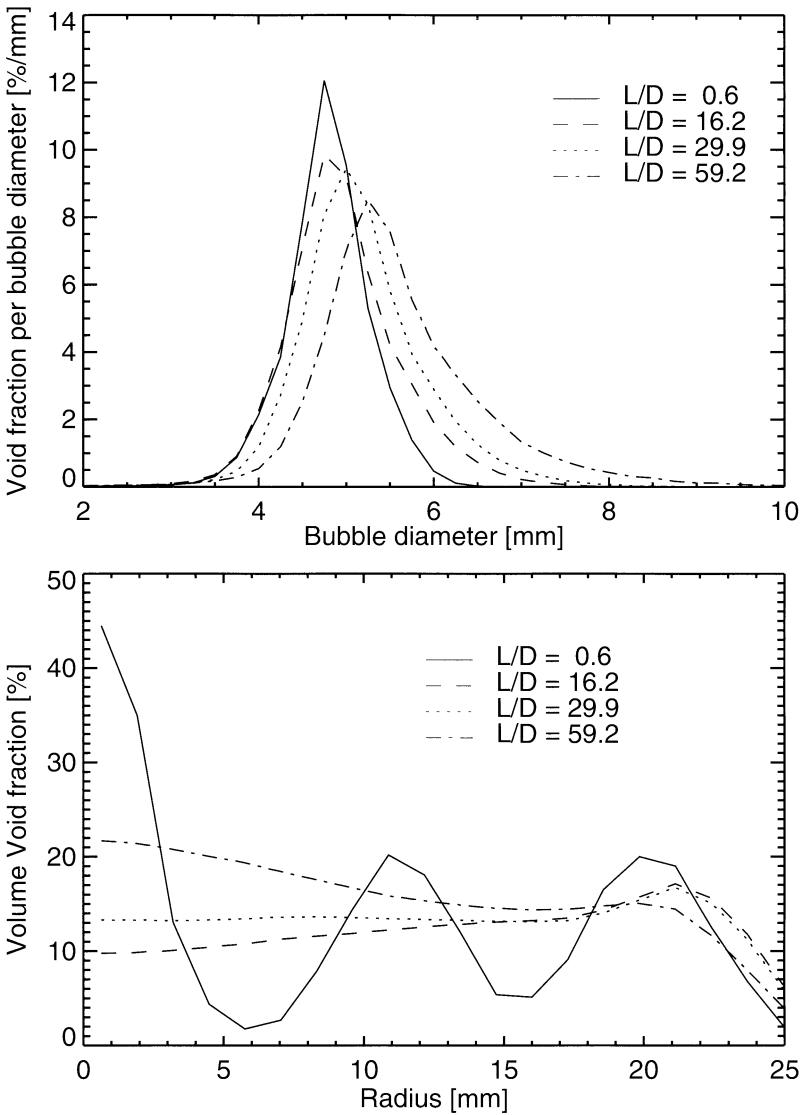


Fig. 2. Bubble size distributions (upper picture) and radial gas volume fraction profiles (lower picture) for different distances from the gas inlet. Superficial velocities: $j_l = 1.0$ m/s, $j_g = 0.14$ m/s.

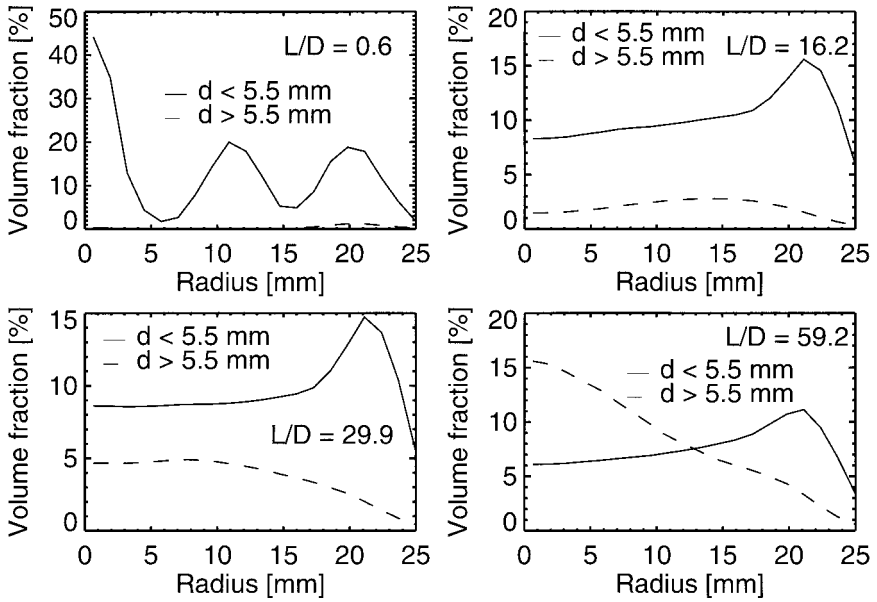


Fig. 3. Radial volume fraction profiles decomposed for different bubbles sizes at four different distances from the gas inlet. Superficial velocities: $j_l = 1.0$ m/s, $j_g = 0.14$ m/s.

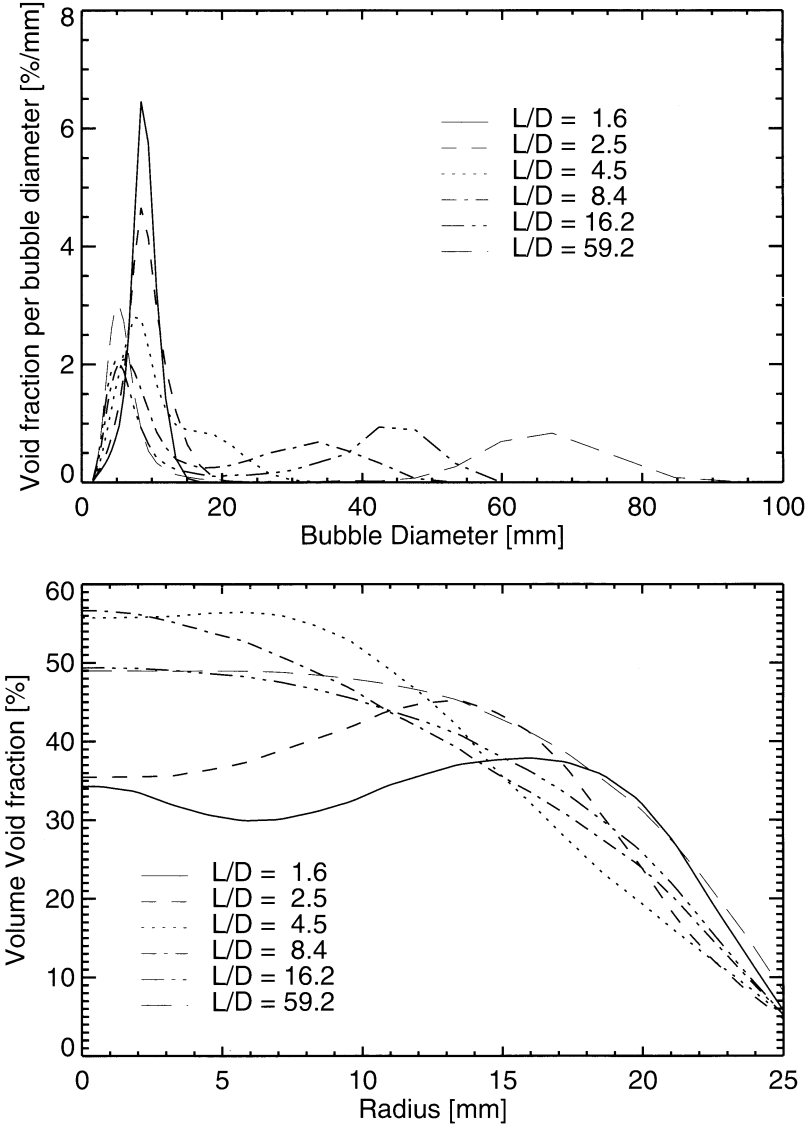


Fig. 4. Bubble size distributions (upper picture) and radial gas volume fraction profiles (lower picture) for different distances from the gas inlet. Superficial velocities: $j_l = 0.4$ m/s, $j_g = 0.34$ m/s.

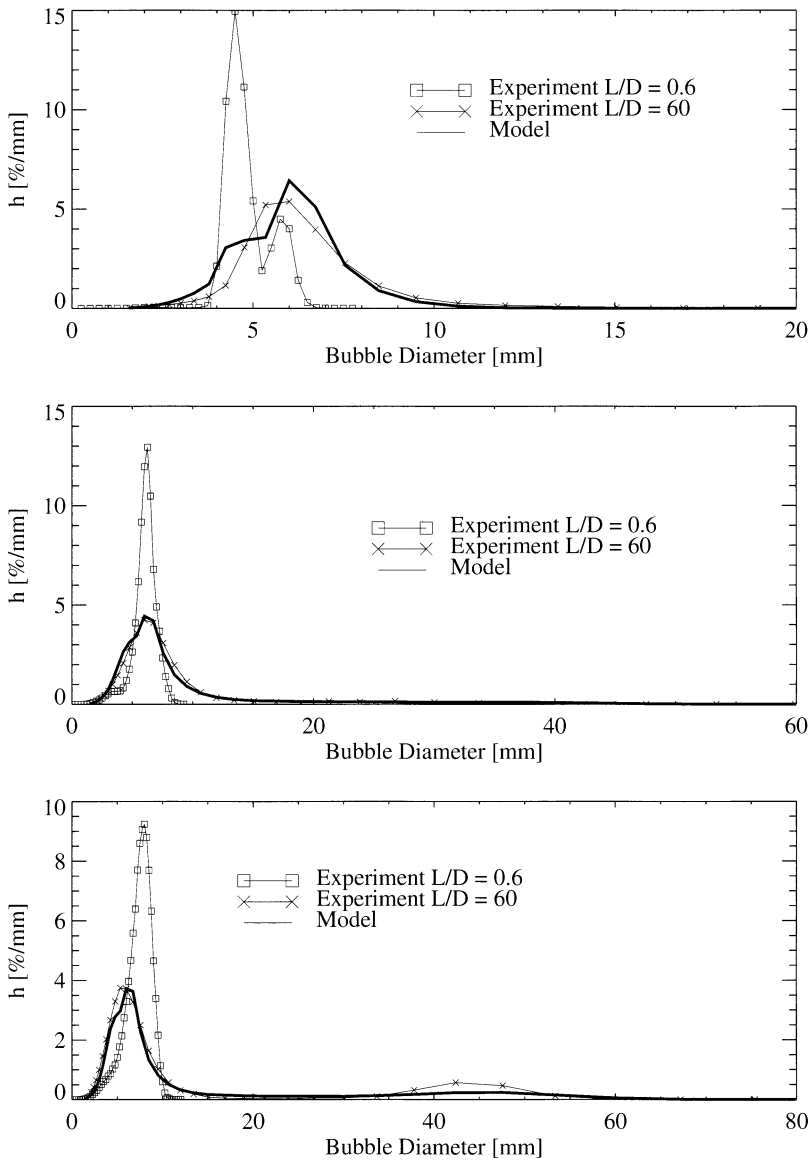


Fig. 6. Experimental bubble size distribution at the gas inlet and experimental and calculated bubble size distributions at the upper end of the test section. Superficial velocity of the liquid: $j_l = 0.4$ m/s.

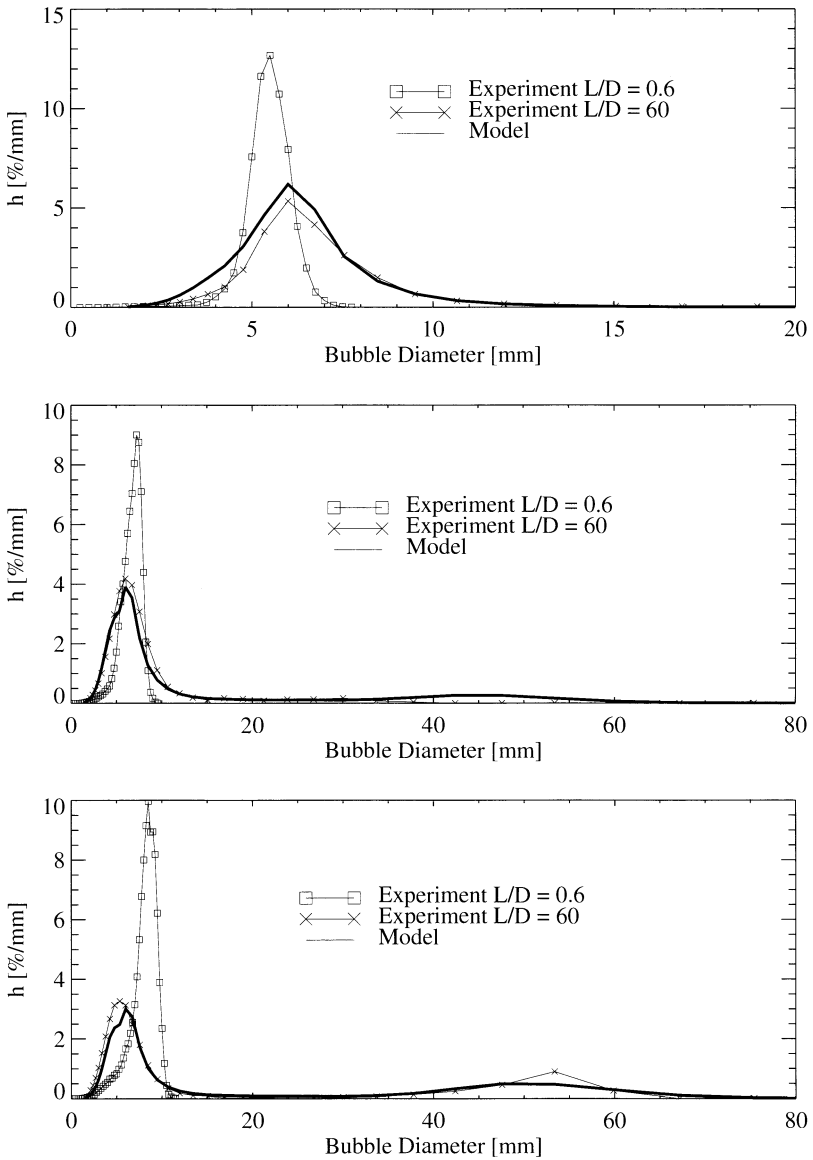


Fig. 7. Experimental bubble size distribution at the gas inlet and experimental and calculated bubble size distributions at the upper end of the test section. Superficial velocity of the liquid: $j_l = 0.64$ m/s.

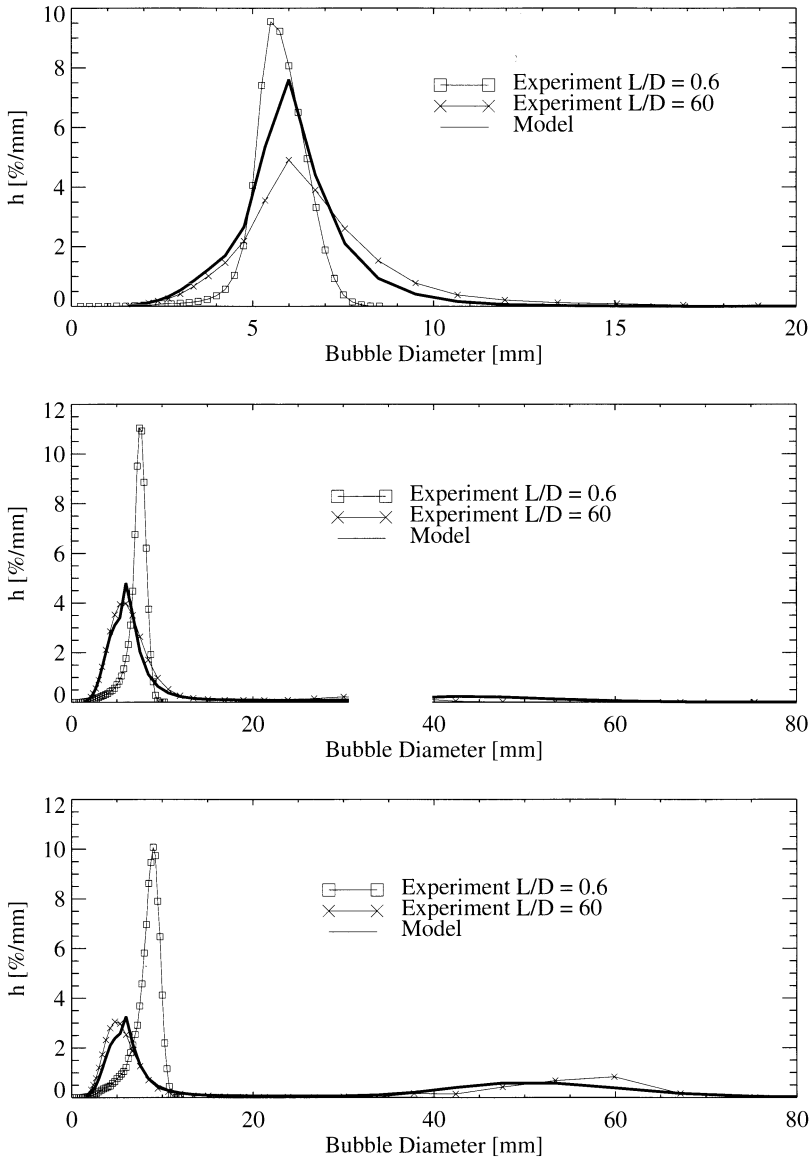


Fig. 8. Experimental bubble size distribution at the gas inlet and experimental and calculated bubble size distributions at the upper end of the test section. Superficial velocity of the liquid: $j_l = 1.0$ m/s.

Detailed experimental studies on gas-liquid bubble flow in bubble columns with and without recycle

Oliver Borchers, Gerhart Eigenberger

Institut für Chemische Verfahrenstechnik, Böblinger Straße 72, D-70199 Stuttgart,
email: egb@icvt.uni-stuttgart.de

Abstract:

Various flow configurations in a flat bubble column reactor were investigated with optical measurement techniques such as Laser Doppler Anemometry (LDA) and a newly developed image processing method based on Particle Tracking Velocimetry (PTV). Using the new two-phase PTV, bubble and liquid phase velocity with high resolution in time (up to 2,000 Hz data rate) and space (video imager resolution down to 4 μm per pixel) were examined simultaneously at a local gas hold-up up to 12%. The detailed experimental data was used for validation of numerical modeling and simulations of the hydrodynamics in two-phase flow as described in the contribution of Sokolichin and Eigenberger. Good agreement could be stated for bubble flow with local gas volume fractions up to 5% regarding both time averaged velocities as well as turbulence data.

Keywords:

Bubble column, two-phase bubble flow, particle tracking velocimetry, laser Doppler anemometry

1 Introduction

Numerical modeling and simulations of bubble column reactors require the combined calculation of flow structures, mass transfer and reaction. The main difficulty lies in the proper modeling of the complex hydrodynamics of gas-liquid bubble flow. Therefore, many contributions have focused on this topic, e. g. Delnoij et al. [1], Lain et al. [2], Sokolichin and Eigenberger [3].

Any improvement of hydrodynamics modeling and simulation requires a detailed comparison and validation with experimental results. Recently, good agreement could be stated for several bubble flow configurations (Borchers et al. [4]), but many important questions remain unsolved. They comprise the question of bubble swarm velocity and its relation to single bubble velocities (Schlüter and Rübiger [5]), the question of bubble-bubble interactions via coalescence and redispersion and two-phase and bubble-induced turbulence. Mathematical models

for the bubble-induced turbulence are often derived in analogy to the single-phase k - ε -model with additional bubble-induced source terms for the turbulent kinetic energy k and the turbulent energy dissipation ε (e. g. Kataoka and Serizawa [6]). While established measurement techniques such as LDA and PIV allow for a direct determination of the turbulent kinetic energy k , the turbulent energy dissipation ε is subject of estimation.

Examination of single-phase turbulence and slip velocity requires experimental methods, which record the velocity of both phases simultaneously and with high resolution in time and space. Measuring the turbulent kinetic energy and the dispersion coefficient allows for validation of the parameters chosen for modeling bubble-induced turbulence. For this purpose, non-intrusive measurement techniques like Laser Doppler Anemometry and digital image processing methods are discussed. A new versatile method based upon Particle Tracking Velocimetry has been developed and will be presented in this contribution.

Experiments with the new measurement technique were carried out in two flat bubble columns with rectangular cross-section. This type of apparatus has several advantages in comparison to the more common cylindrical reactors. The depths of 4 and 8 cm, respectively, enables measurements in bubbly flow at high gas volume fractions up to 12 %. Furthermore, no refraction correction at the walls is necessary as in cylindrical columns. The flat columns can be modeled more easily with a rectangular space grid and boundary conditions are easier to implement.

2 Experimental

2.1 Gas-liquid reactor facility

The experimental studies were performed in flat bubble column reactors with rectangular cross-sections, see Fig. 1. For measurements of the hydrodynamics, the columns were filled with water and aerated with air by frit spargers and hole plate spargers leading to bubble diameters in the range of 3 to 5 mm. Glass and plexi-glass plates on the front and back side allow for use of optical, non-intrusive techniques such as LDA and image processing. Due to the rectangular cross-section, no correction to the refraction index is needed. Mounting fixed internals in the 2 meter column allowed for a loop reactor configuration with forced circulation flow. By variation of water level, gas flow rate, sparger type and position, various flow configurations were realized.

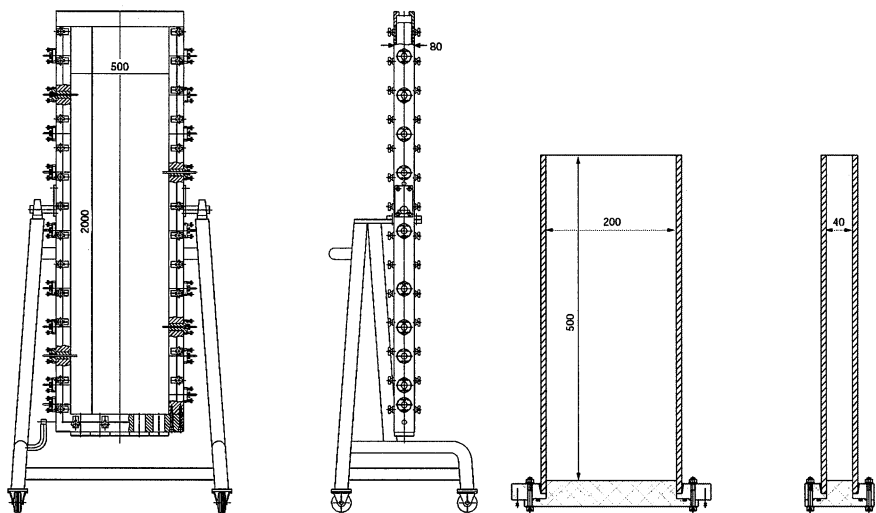


Fig. 1. Flat bubble column reactors with rectangular cross-section, dimensions in mm

2.2 Laser Doppler Anemometer

LDA measurements of the liquid velocity were performed with a DANTEC two-component system which operated in backward scattering mode. Laser light was provided by a 300 mW argon ion laser. Two laser wavelengths of 514.5 nm and 488 nm were used in order to measure two velocity components simultaneously. For detection of the liquid phase, hollow glass sphere particles with 10 μ m diameter having almost no slip and the same density as water were added to the flow. In both columns, measurements were taken in the mid plane between the front and the back plate at regular grid points 10 or 20 mm apart.

Bubble velocity measurements with LDA by use of special electronics or in combination with Phase Doppler Anemometry (PDA) was topic of several studies (e. g. Martin et al. [7], Brankowic et al. [8]). However, these were focused on single bubble experiments or bubbles with diameters less than 1 mm. Recent contributions have shown that LDA velocity measurements of the gaseous phase are not reliable in realistic bubbly flow (Groen et al. [9]). Hence, LDA was used for liquid velocity measurements only. Tracer particles were added in high concentrations so that few incidences of bubble signals could be neglected in relation to tracer signals as reported by Borchers et al. [4].

LDA provides time dependent data at single points, from which information on high and low-frequency flow fluctuations can be obtained. Hence, flow maps and velocity profiles for quantitative validation of numerical simulations are reliable only with long time averaged data while dynamic flow behavior was analyzed at single points. Calculating time weighted averages, the biasing error was minimized.

2.3 Image processing: two-phase PTV

The image processing procedure consisted of three major steps. Firstly, image sequences were recorded using a Weinberger high-speed video camera. Images with 512 x 512 pixels resolution were captured at up to 1000 Hz frame rate and at 2000 Hz with half of the maximum resolution. After storing the sequences on CD ROM, they were processed with image processing C-algorithms which are described in detail by Borchers [10].

In the gray scale images, bubbles and tracer particles were detected and stored in binary images as objects with label 1 (white in Fig. 2) while the background was set to 0 (black). After this time consuming segmentation step, bubbles and tracer particles were discriminated by their different sizes. The third step consisted of tracking the detected objects over successive images. Velocities were calculated from the displacement of corresponding bubbles and particles.



Fig. 2. Gray scale image of bubbly flow with added tracer particles (left), detected objects in the binary image (middle) and instantaneous velocity vectors (right).

3 Flow configurations

Various flow structures were established by changing the aeration and/or the internals of the bubble column reactor sketched in Fig. 1 (left). Fig. 3a shows the influence of water level for local aeration in central position and a gas flow rate of 1 l/min. In case the ratio of height to width (H/W) equals 1, the flow has an essentially stationary character in which one circulation cell spreads over the full width of the bubble column. As H/W increases slightly over 1.5, an unsteady flow structure develops with two staggered rows of vortices moving downwards in a periodic way. The bubble swarm distribution is shown for aspect ratios of 2, 3 and 3.8 at different times. Increasing gas flow rate, the periodic flow structure becomes more and more irregular until the fluctuations are completely chaotic. The time dependent behavior of the oscillating bubble swarm with liquid vortices moving downwards is depicted in Fig. 4 for a H/W ratio of 2.

Using two frit spargers for aeration, two separated bubble swarms oscillate irregularly but correlated to each other as shown in Fig. 3b. This flow configuration is extremely susceptible to changes of the experimental conditions.

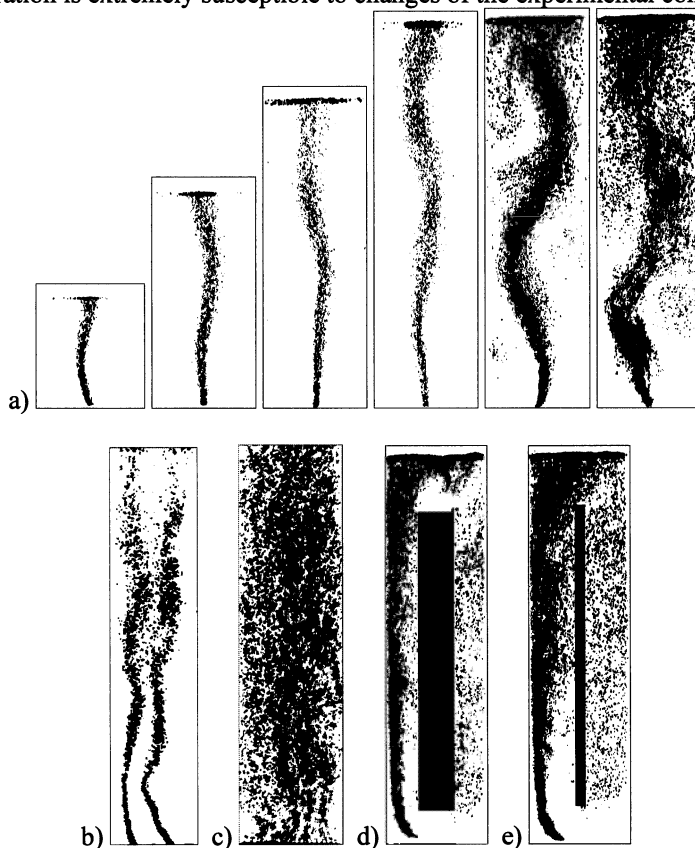


Fig. 3. Bubble column configurations with different water level and gas flow rate (a), with two correlated bubble swarms, with homogeneous aeration (c) and loop reactor configurations with flexible reactor internals (d and e)

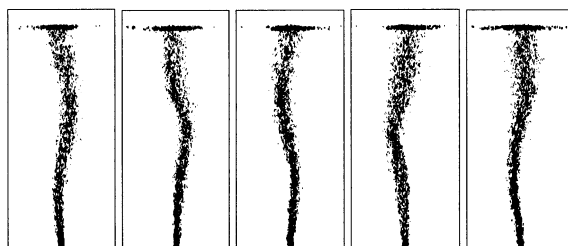


Fig. 4. Bubble column configuration with oscillating bubble swarm

A plate sparger with one single line of 0.3 mm holes generated a homogeneously aerated bubble column configuration (Fig. 3 c). Mounting of different internals in combination with local aeration forced clock-wise circulation of the liquid flow leading to loop reactor configurations (Fig. 3 d and e).

4 Results and discussion

4.1 Reproducibility and accuracy of flow investigations

Although the mean flow structure in a bubble column is described to be either steady-state or periodic, it is still turbulent and has therefore an essentially chaotic character on a smaller scale. Hence, the measuring time interval for mean values must be chosen long enough in order to get reproducible results. Fig. 5 shows the cumulated time averaged liquid velocity as function of the length of the averaging time for two different experiments at the same position and with identical conditions. The measuring time has to be chosen long enough so that periodic and high frequency fluctuations do not influence the mean value. However, it can be clearly seen that the flow has a substantially transient character even on the long time scale.

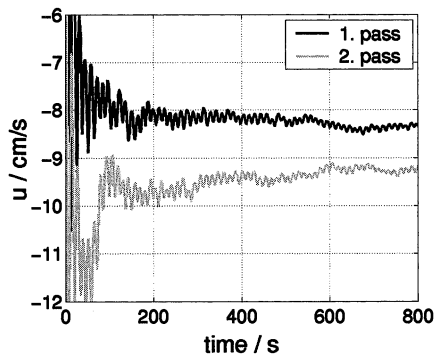


Fig. 5. Long time LDA measurements in a periodic flow under identical conditions: accumulated average of the liquid velocity

4.2 Validation with LDA: example

LDA measurements and validation of the corresponding simulations were performed for the flow configurations of Fig. 3 under various conditions. Here, the

configuration sketched in Fig. 3a with an aspect ratio of 2 shall be presented exemplarily.

Quantitative comparison of LDA measured and calculated liquid velocity data is shown in Fig. 6. Since dynamic measurements with LDA are restricted to single points, only the time-averaged velocity patterns can be compared with respective simulation results. Due to this long time averaging the oscillations caused by moving vortices result in a symmetrical flow structure. The long-time averaged liquid velocity flow map shows two liquid vortices on both sides of the bubble swarm. A similar flow structure was obtained in the simulations. Also one-dimensional velocity profiles at different heights show good agreement of experiments and simulations. Differences occur only in the region directly above the aeration where the flow has a very turbulent, chaotic structure.

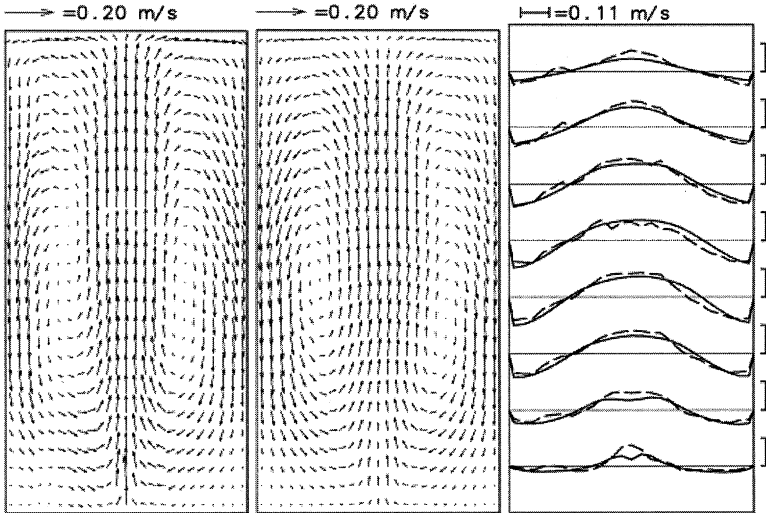


Fig. 6. Long time averaged liquid velocity profiles for the flat bubble column reactor with 100 cm water level and 1 l/min gas flow rate as in Fig. 4 – LDA measurements (left) and simulations (middle). Comparison of measured (---) and calculated (—) vertical velocity component.

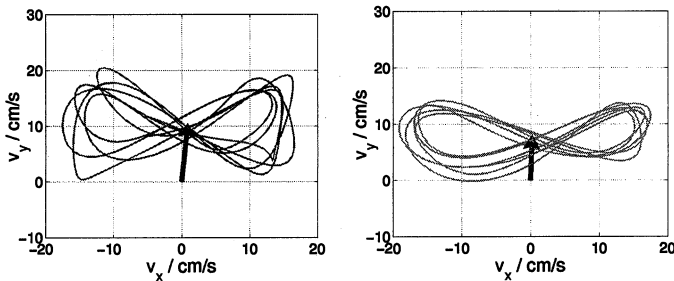


Fig. 7. Trajectories of FFT-filtered liquid velocities: experimental data (left) and simulations (right) in the column center.

The presented quantitative results are based on time averaged velocity data. This analysis neglects the dynamics of the strongly transient flow which is the main reason for lateral mixing. The flow dynamics consist of a low-frequency part due to the bubble swarm's periodic motion and a superimposed turbulent high-frequency part. In the following, dynamics concerning the low-frequency periodic liquid motion are analyzed.

The LDA system provides time-dependent, two-dimensional liquid velocities at single measurement points. In Fig. 7 a comparison of measurements and simulations will be presented for the central point of the regarded flow configuration.

Phase trajectories enable the simultaneous visualization of the two-dimensional change in velocity with the time. To get such a phase trajectory, the time dependent trace of the velocity vector is plotted. In case of periodic motion, the phase trajectories remain close together following a common curve. In case of chaotic motion the trace will randomly cover a larger area of the velocity plane.

Experimental and simulation data were low-pass filtered to get the low-frequency motion, the trajectories of which are drawn in Fig. 7 for a time of 200 sec. The center of mass of subsequent curves equals the time averaged velocity at the measuring point, indicated by the black arrow. In the column center, liquid vortices pass on both sides so that the trajectory resembles a horizontal 8.

4.3 Validation of two-phase PTV

For validation of the newly developed two-phase PTV technique, the bubble column configuration shown in Fig. 3b was measured with LDA and PTV. The measured time averaged, two-dimensional vertical velocities and standard deviations of both phases are shown for the whole width at 121 cm height in central depth position. Liquid velocities are measured with PTV and LDA, bubble velocities with PTV only (Fig. 8).

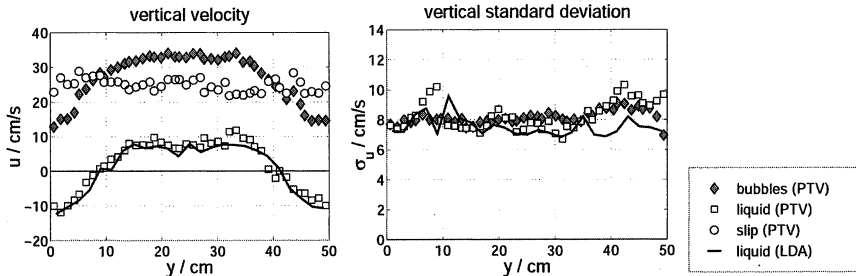


Fig. 8. Vertical liquid velocity and standard deviation in bubble column configuration (3b) at 121 cm height

The transient liquid flow structure averages to a circulation flow consisting of two macro-scale eddies with up-stream flow in the center and downstream flow near the column walls. Hence, the vertical liquid velocities are positive in the central position and negative at the sides. For bubbles, the curve is similar but shifted to higher values. Therefore, the slip between bubble and liquid velocity is nearly constant across the column width. The standard deviation is identical for both phases and nearly constant across the column width. The good agreement between LDA and PTV results was a general finding for a large number of similar measurements.

4.4 Two-phase PTV at high local gas hold-up

Optical measurement techniques are always restricted to lower gas hold-up in bubble flow due to multiple refraction and reflection of light beams. PTV measurements were performed in the homogeneously aerated bubble column configuration of Fig. 3c. In Fig. 9, the PTV measured, time averaged slip velocity is compared with corresponding predictions calculated by Ishii and Zuber and Mudde and Simonin [11] for local gas volume fractions up to 13%.

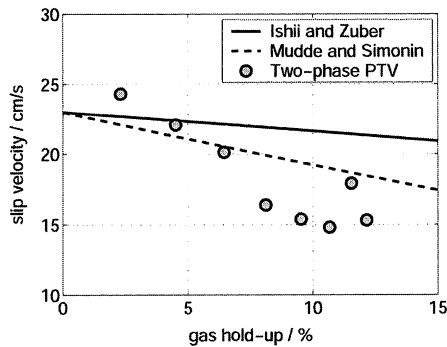


Fig. 9. Bubble slip velocity measured in a homogeneously aerated bubble column 3c) and curves predicted by Ishii and Zuber and Mudde and Simonin [12]

5 Conclusions

LDA and a newly developed two-phase PTV technique were used for detailed measurements of the hydrodynamics in various gas-liquid reactor configurations. The experimental results were used for validation and further development of numerical modeling and simulations of two-phase flow. The image processing technique was successfully validated with LDA results for gas volume fractions up to 13%. In comparison to LDA, PTV provides additional information such as of bubble and liquid velocities and instantaneous flow maps.

References

- [1] **Delnoij E; Kuipers JAM; van Swaij WPM** (1999) A three-dimensional CFD model for gas-liquid bubble columns. *Chem Eng Sci* 54: 2217-2226
- [2] **Lain S; Bröder D; Sommerfeld M** (1999) Experimental and numerical studies of the hydrodynamics in a bubble column. *Chem Eng Sci* 54: 4913-1920
- [3] **Sokolichin A; Eigenberger G** (1995) Gas-liquid flow in bubble columns and loop reactors. Part I: Detailed modeling and numerical simulation. *Chem Eng Sci* 49: 5735-5746
- [4] **Borchers O; Busch C; Sokolichin A; Eigenberger G** (1999) Applicability of the standard k - ϵ turbulence model to the dynamic simulation of bubble columns. Part II: Comparison of detailed experiments and flow simulations. *Chem Eng Sci* 54: 5927-5935.
- [5] **Schlüter M; Rübiger N** (1998) Bubble swarm velocity in two phase flows. *Proceedings ASME Heat Transfer Division* 5
- [6] **Kataoka I; Serizawa A** (1989) Basic equations of turbulence in gas-liquid two-phase flow. *Int J Multiphase Flow* 15: 843-855
- [7] **Martin WW; Adbelmessih, AH; Liska JJ; Durst F** (1981) Characteristics of laser-Doppler signals from bubbles. *Int J of Multiphase Flow* 7: 439-460
- [8] **Brankovic A; Currie IG; Martin WW** (1984) Laser-Doppler measurements of bubble dynamics. *Phys Fluids* 27: 348-355
- [9] **Groen J S; Mudde RF; van den Akker HEA** (1999) On the application of LDA to bubbly flow in the wobbling regime. *Exp in Fluids* 27: 435-449
- [10] **Borchers O** (2002) Zweiphasen-Particle-Tracking-Velocimetry (PTV) zur detaillierten Analyse der Hydrodynamik von Blasensäulenreaktoren. *Fortschritt-Berichte VDI-Verlag, Düsseldorf*
- [11] **Mudde RF; Simonin O** (1999) Two- and three-dimensional simulations of a bubble plume using a two-fluid model. *Chem Eng Sci* 54: 5061-5069

Basic experimental investigations on the hydrodynamics of bubble columns

Günter Brenn, Vladimir Kolobarić, F. Durst

Institute of Chemical Engineering, Chair of Fluid Mechanics, University of Erlangen-Nürnberg, Cauerstraße 4, D-91058 Erlangen, Germany¹

Abstract

The aim of the present work is to investigate experimentally basic properties of the buoyancy-driven two-phase flow in bubble columns. The present report represents results from investigations on the turbulent liquid motion induced by the bubbles. The experimental hardware used was a small-scale bubble column with square-shaped cross section, oriented at the design from the Institute of Chemical Process Engineering (ICVT) of the University of Stuttgart. The capillary aerator produced bubbles with adjustable sizes of up to 5 mm. Gas void fractions up to around 3% were achieved. Measuring techniques employed were PIV/LIF to get information about the gross-scale liquid and bubble motions, and LDA for acquiring data on the turbulent motion of the liquid. Results consist in spatial distributions of the mean velocities of the two phases, turbulence levels in the liquid, and power spectral density distributions at various locations in the flow field. These sets of information together yield insight into the turbulent behavior of this two-phase flow, which is of interest for various fields of process engineering.

Experimental technique and results

The bubble column employed for the investigations had a cross section of 40x40 mm, with a liquid level height of 420 mm. In order to have flow conditions close to real situations, bubbles with a size of approximately 4 mm were produced. The left-hand part of Fig. 1 shows a front view of the column. The aerator used had six capillaries with an internal diameter of 1.1 mm, placed in a hexagon pattern so as to have equidistant bubble streams. The capillary in the center of the hexagon pattern ($y=0$) is optically accessible without disturbances. The flow field in the bubble column, partly shown in the right-hand part of Fig. 1, is described in a coordinate system (x,y,z) , with the z axis pointing upwards and the y axis pointing to the right in the bottom horizontal plane of the front view of the column.

¹ Present address of G. Brenn: Institute of Fluid Mechanics and Heat Transfer, Graz University of Technology, Inffeldgasse 25/F, 8010 Graz, Austria

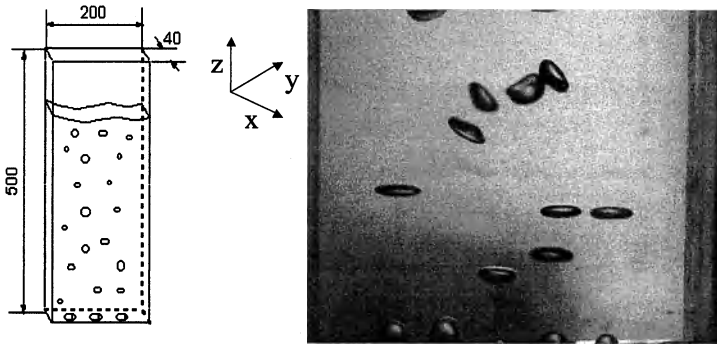


Fig. 1. Left: sketch of the bubble column employed for the experiments. Right: Bubbles with volume-equivalent size of 3.7 mm in the water-air system close to the aerator exit.

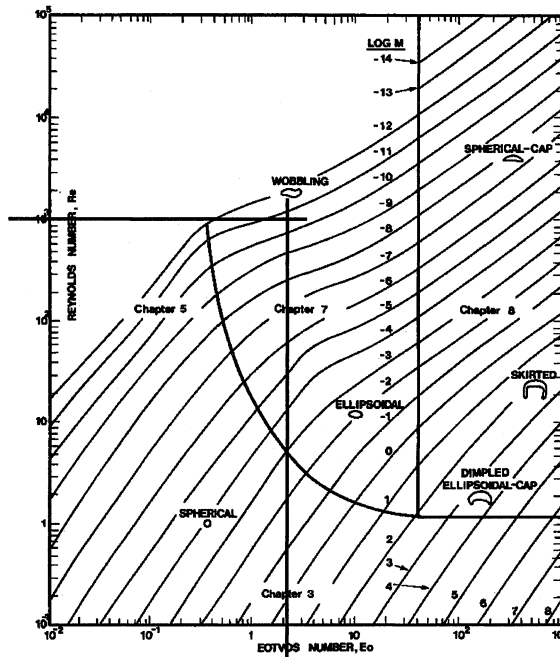


Fig. 2. Bubble regime in the E_o/Re diagram (Clift et al 1978)

In the y direction the column was confined to a length of 40 mm in our experiments. According to the shape diagram shown in Fig. 2, adopted from Clift et al (1978), the shape of 4 mm bubbles in water-air systems belongs to the wobbling regime. The bubbles shown on the right in Fig. 1 confirm this.

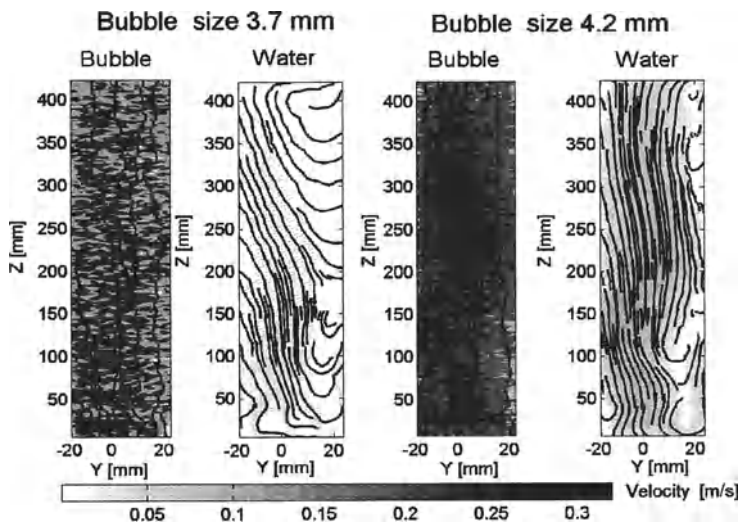


Fig. 3. PIV/LIF measurement results of the time-average two-phase flow field in the bubble column for two different bubble sizes

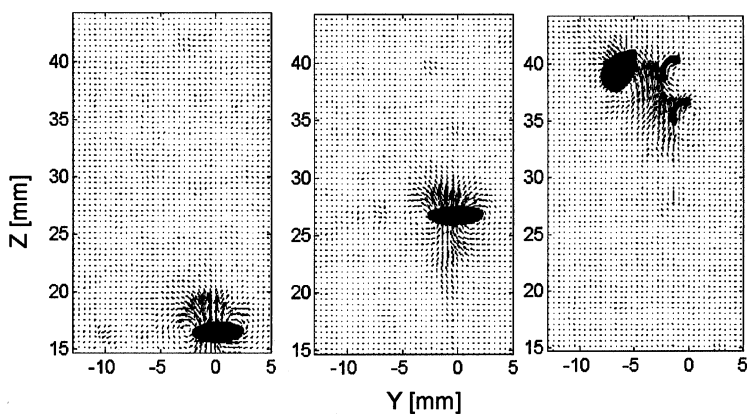


Fig. 4. The bubble shape with the vector field of the induced water velocity for the bubble diameter of 3.4 mm. The vortex motion in the wake is clearly seen in the third image.

In order to examine the gross-scale velocity field of the two-phase flow in the bubble column, PIV/LIF measurements were carried out. The results for two bubble sizes presented in Fig. 3 were obtained by averaging the results from 500 PIV images. On the left-hand side of each pair of diagrams the bubble velocity is shown; the right-hand diagrams show the water velocity fields. The solid lines in

the figures represent the bubble and water path and streamlines. For both bubble sizes, the bubble velocities are considerably higher than the mean induced water velocities. It was of interest for the present investigations to measure the liquid velocity field around the bubbles, even for strongly deformed bubbles, as shown in Fig. 4. For this investigation, the PIV/LIF equipment was used. In order to enable the visualization of the bubble shape during the PIV/LIF measurements, the flow field was back-lighted with white light. In order to eliminate this light for the PIV/LIF measurements, the optical unit was modified by inserting a blue filter mask. The results show that the bubbles rise along rectilinear paths with almost constant shape, until they reach a level of approximately $z=30$ mm above the aerator exit. At this level, a transition to a spiraling path occurs. At the same time, the bubble shape starts to oscillate. In addition, a wake instability is observed, which points the formation of two counter-rotating filaments. This wake structure is characteristic for the spiraling motion of bubbles (Brücker 1999). It was one aim of the present investigations to draw a link between the bubble shape (and its oscillations) and the frequency spectrum of turbulent velocity fluctuations in the liquid. In order to find the dominant oscillation mode of the bubbles, which could affect the velocity fluctuation power spectrum, the shape of the bubbles was analyzed by expanding its radial extension r in Legendre polynomials P_i according to $r(\theta)=a_0+\sum a_i P_i(\cos\theta)$. Figure 5 represents the values of the expansion coefficients a_i for different positions of the bubbles above the aerator and show the dominant role of the second and fourth oscillation modes. All other modes investigated yield small values of the expansion coefficients. These results also represent the change in the shape behavior of the bubbles as the z coordinate exceeds the value of 30 mm.

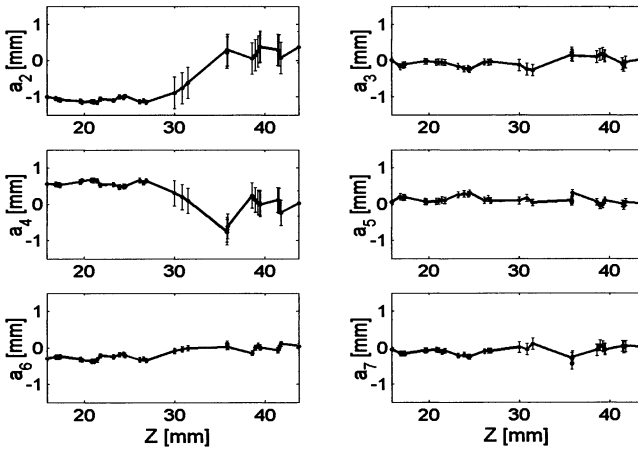


Fig. 5. Bubble shape analysis by expansion in Legendre polynomials – the expansion coefficients as functions of the bubble position z

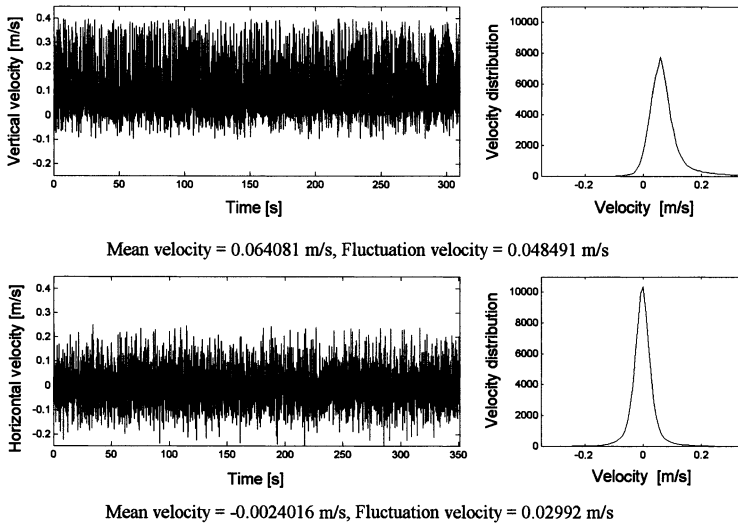


Fig. 6. Time series of liquid velocities measured with LDA at the bubble formation frequency of 25 Hz, bubble size 4 mm, at the location $z=240$ mm above the central capillary.

The properties of the turbulent liquid flow field were examined with laser-Doppler anemometry at different gas void fractions and different positions in the two-phase flow field. The LDA provides information about the liquid flow field in the form of time series of the velocity. The results shown in Fig. 6 reveal that both the average value of the velocity and the fluctuation level are higher for the vertical than for the horizontal component. From measured time series, the power spectrum of the velocity fluctuation frequency is calculated in order to find dominant frequencies and the slope of the power spectrum in the developed regime. Typical results for two positions downstream from the central capillary in the flow field are presented in Fig. 7. The vertical solid lines mark the bubble formation frequency. The dashed lines represent the second-mode oscillation frequency. For the bubble size of 4.2 mm, the second-mode oscillation frequency is 48 Hz. As mentioned before, in the region below $z=30$ mm the bubbles rise rectilinearly, without shape oscillations. Correspondingly, we do not find 48 Hz as a characteristic frequency in the spectrum for the location $z=13$ mm. Instead, the bubble formation frequency of 39 Hz clearly appears in the power spectrum, which can only be expected at locations where the bubbles pass the probe volume periodically in time with the frequency of bubble formation. At distances beyond 30 mm from the aerator, i.e. for spiraling rise path, there are no dominant frequencies found in the spectrum. Also, frequencies corresponding to the dominant oscillation modes of the bubbles are not observed. The slope of the power spectrum in the developed regime in all measurement points varied between -1 and $-4/3$, which is a behavior similar to what was observed by other researchers (e.g., Mudde et al, 1997), and different from the $-5/3$ law found by Kolmogorov for single-phase turbulence. The low power spec-

trum slope is in agreement with the findings of Lance and Bataille (1991), who interpret the values as caused by the bubbles which continuously maintain the small-scale structures in the flow. The frequency analysis of velocity time series measured with LDA above the central capillary at the bubble formation frequency of 11 Hz (Fig. 8.) again shows the dominance of the bubble formation frequency below $z=30$ mm. This is, of course, in agreement with results from PIV measurements and observations with a high-speed camera.

Comparison with theory

The levels of bubble-induced pseudo turbulence were calculated from the velocity time series measured with LDA at various positions in the flow field. The pseudo turbulence level, non-dimensionalised with the square of the terminal bubble velocity, is presented in Fig. 9 as a function of the gas void fraction α . The measurement results are compared with the result from the calculation by Lopez de Bertodano et al (1994) based on the potential theory, which reads

$$k/U_t^2 = \frac{1}{2} \cdot \alpha \cdot \rho_1 \cdot C_{vm} \quad (1)$$

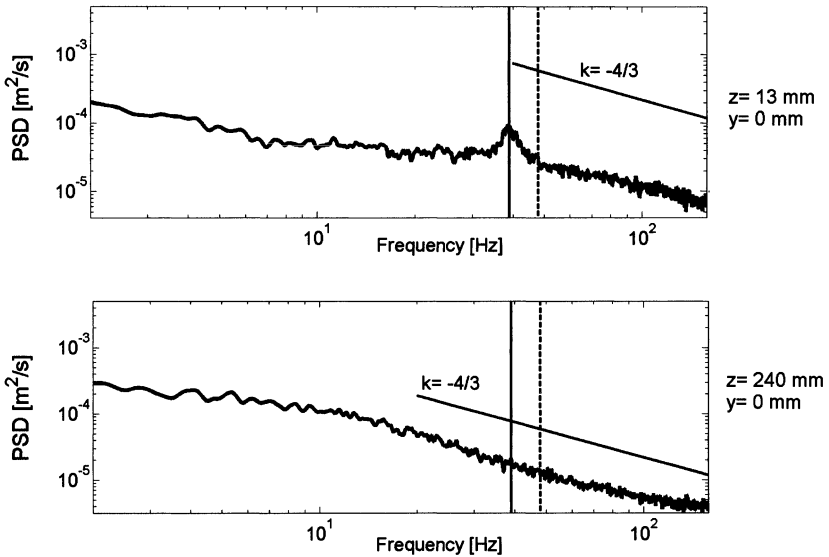


Fig. 7. Velocity fluctuation frequency spectra above the central capillary at the bubble formation frequency of 39 Hz. The bubble size is 4.2 mm.

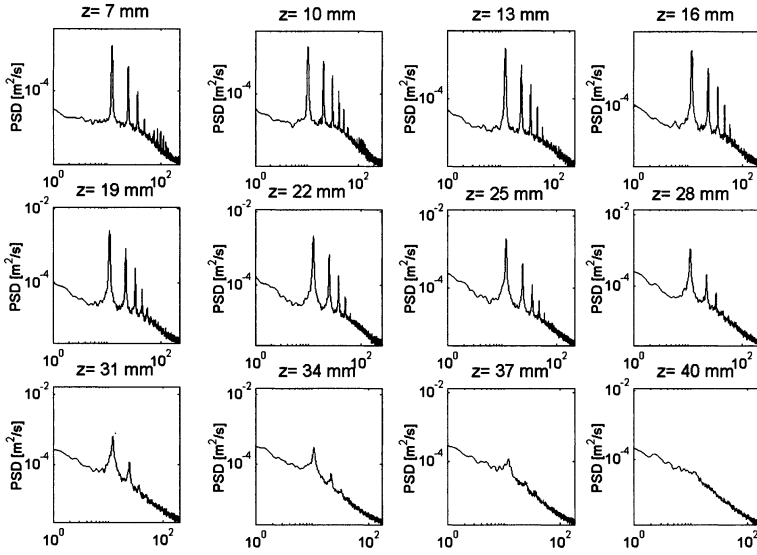


Fig. 8. Vertical velocity fluctuation power spectra above the central capillary ($y=0$) at varying distance z for the bubble size of 3.7 mm

In this equation, k is the turbulent kinetic energy induced by the bubbles, U_T the terminal bubble velocity, ρ_l the liquid density, and C_{vm} the virtual mass coefficient. The virtual mass coefficient for spherical bubbles is 1/2, but for ellipsoidal bubbles moving on spiral paths it is considerably higher (Lopez de Bertodano et al 1994). The correction of the virtual mass coefficient according to the bubble size and shape is given by the equation

$$C_{vm} = Q(\lambda) C_{vm,sph} \quad (2)$$

where $C_{vm,sph}$ is the virtual mass coefficient of a spherical bubble, λ the aspect ratio of the ellipsoid (ratio of longer to shorter axis lengths), and Q is the correction coefficient. For an oblate spheroid, the coefficient Q is described as a function of λ per (Milne-Thomson 1968; van Wijngaarden 1998)

$$Q(\lambda) = 2 \frac{(\lambda^2 - 1)^{1/2} - \cos^{-1}\lambda - 1}{\cos^{-1}\lambda - 1 - (\lambda^2 - 1)^{1/2} / \lambda^2} \quad (3)$$

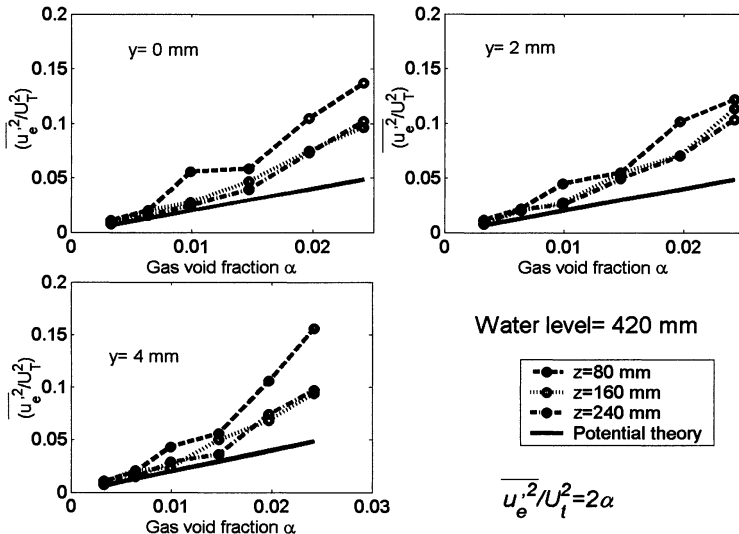


Fig. 9. Bubble-induced turbulence level as a function of the gas void fraction for various locations in the flow field

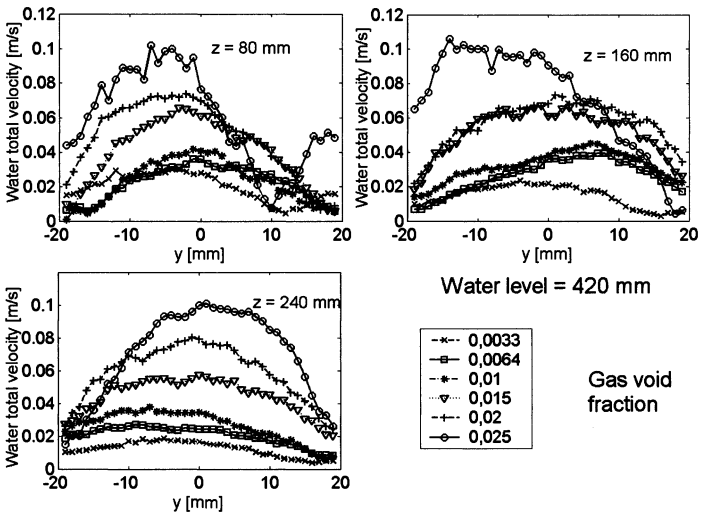


Fig. 10. Spatial mean liquid velocity distribution for various gas void fractions at three levels z

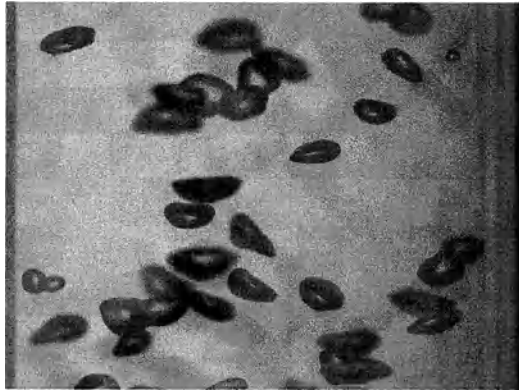


Fig. 11. Bubble distribution at void fraction $\alpha=0.025$, $z=240$ mm above the central capillary for a bubble size of 4.2 mm

In our measurements, the average aspect ratio λ of the bubble shape is 2.75. An oblate spheroid of this shape would yield $C_{vm}=1.51$. Our bubbles, however, were not spheroids; for our calculations we therefore set $C_{vm}=2.0$, which leads to the equation

$$\frac{\overline{u_e'^2}}{U_t^2} = 2 \cdot \alpha \quad (4)$$

for the pseudo turbulence level (otherwise called excess turbulence level in cases, where a pedestal due to a (pressure driven) liquid flow field is also present), where $\overline{u_e'^2}$ is the mean sum of the squares of all three components of fluctuation velocities. In this work the assumption of equal values of the x and y velocity fluctuation levels is adopted. The results of our measurements in comparison with the computational results are presented in Fig. 9. Measurement and calculation are in good agreement at low gas void fractions below 1.5%, and at positions far enough away from the plane of the aerator, i.e. in the present case at $z \geq 160$ mm. At higher gas void fractions, the non-dimensional turbulent energy grows progressively, i.e. more rapidly than predicted by the linear potential theory. The spatial profiles of the mean liquid velocity shown in Fig. 10 indicate that, at higher gas void fractions, the bubble and mean velocity distributions are not homogenous. A typical non-uniform bubble distribution in the flow for $\alpha=2.5\%$ is shown in Fig. 11. A uniform distribution of the bubbles in the flow field, however, is a basic assumption of the calculation that leads to Eq. (4). A departure from this assumption leads to an increase of the virtual mass coefficient (Zenit et al 2001). Also, at high void fractions, mutual interactions between the bubbles become important. These effects contribute to the discrepancy between measurement result and calculation

from Eq. (1) observed in Fig. 9. A solution to this problem would be a computational approach that accounts for the mutual influences of the bubbles on the velocities they induce in the flow field when modeled as dipoles in the potential theory.

Summary and conclusions

In the first part of our project, not reported here in detail, basic information on model bubble column flows was obtained by means of detailed measurements with PDA (Brenn et al 2002). The combined application of image processing, PIV/LIF, and LDA provide detailed information about the water velocity field, the vorticity distribution, and bubble contour. During the transition from a linear to a spiraling bubble rise path, instability of the wake occurs, which is indicated by the formation of counter-rotating vortex filaments characteristic for spiraling rise paths. In the fluctuation velocity frequency spectra calculated close to the aerator, the expected cascades are observed, which occur due to the strictly periodic formation of the bubbles. Outside the bubble path, and in the spiraling regime, there is no dominant frequency, and the frequency spectrum exhibits slopes of -1 or $-4/3$ due to the bubbles maintaining small-scale structures in the flow, thus leading to slopes smaller than the value of $-5/3$ known from the single-phase case. The non-dimensional turbulent kinetic energy in the water depends linearly on the gas void fraction for $\alpha < 1.5\%$ and agrees with the equation from potential theory.

References

- Brenn G, Braeske H, Durst F (2002) Investigation of the unsteady two-phase flow with small bubbles in a model bubble column using phase-Doppler anemometry. *Chem Eng Sci* (in press)
- Brücker C (1999) Structure and dynamics of the wake of bubbles and its relevance for bubble interaction. *Phys Fluids* 11:1787-1796
- Clift R, Grace JR, Weber ME (1978) *Bubbles, Drops and Particles*, Academic Press, New York
- Lance M, Bataille J. (1991) Turbulence in the liquid phase of a uniform bubbly air-water flow. *J Fluid Mech* 222: 95-118
- Lopez De Bertodano M, Lahey RT Jr, Jones OC (1994) Phase distribution in bubbly two-phase flow in vertical ducts. *Int J Multiphase Flow* 20:805-818
- Milne-Thomson LM (1968) *Theoretical Hydrodynamic*, Macmillan & CO LTD, London
- Mudde RF, Groen JS, Van Den Akker HEA (1997) Liquid velocity field in a bubble column: LDA experiments. *Chem Eng Sci* 52:4217-4224
- van Wijngaarden L (1998) On Pseudo Turbulence. *Theoret Comput Fluid Dynamics* 10:449-458
- Zenit R, Koch DL, Sangani AS (2001) Measurement of the average properties of a suspension of bubbles rising in a vertical channel. *J Fluid Mech* 429: 307-342

Examination of bubble collisions and coalescence in bubbly flows

D. Bröder and M. Sommerfeld

Mechanische Verfahrenstechnik, Fachbereich Ingenieurwissenschaften, Martin-Luther-Universität Halle-Wittenberg, D-06099 Halle (Saale), Germany

Abstract. In order to allow more reliable modelling of coalescence processes in turbulent bubbly flows, detailed experiments in a double loop reactor were performed. Narrow, essentially monomodal bubble size distributions in the range between 2 to 4 mm were produced by capillary aerators. For simultaneous measurements of bubble size, bubble velocity and liquid velocity a combined system of PIV and PTV was developed and applied. It was possible to determine bubble size distributions and mean, but also fluctuating velocities for both phases. The spatial changes of the bubble size distribution due to the influence of bubble coalescence was analyzed and coalescence rates were calculated.

1. Introduction

For the analysis of bubble coalescence in general two experimental approaches have been established. One is the injection of bubbles with and without a tracer gas and analysis of the composition of individual bubbles in different distances to the sparger, which was for example used by Prince & Blanch (1990), and the other methods are based on the determination of bubble size or bubble volume distributions. The later one for example was used by Kamp et al. (2001) for the analysis of coalescence in a pipe flow but also for the analysis of bubble break-up in a turbulent jet by Martínez-Bazán et al. (1999). The measurement of the bubble size distributions is often performed by the evaluation of photographic images or high speed recordings, but simultaneous measurements of the size and velocity of bubbles and the surrounding liquid are rare. Kirkpatrick & Lockett (1974) analyzed the influence of the approach velocity of bubbles to the water surface on the coalescence time, but up to now experimental investigations about the collision behaviour of bubbles in a swarm and the influence on coalescence are still missing.

Modern camera optical measurement techniques like particle image velocimetry (PIV) and particle tracking velocimetry (PTV) are able to realise complete planes of a flow and together with methods of digital image processing techniques it is possible to provide velocities of both phases and also information about size, shape and position of bubbles. A big problem for the application of

standard PIV to bubbly flows is the strong absorption of the penetrating laser light sheet by scattering on the surface of the bubbles at higher void fractions. Because the intensity of the light scattered by bubbles is several decades larger than the scattering intensity of conventional tracer particles, many investigators used fluorescing tracer particles and a phase separation by the different wavelengths of the light source and the fluorescing dye in the tracers (Deen et al. 2000, Bröder and Sommerfeld 2002). Such an approach however requires the use of two CCD-cameras. Since a light sheet is used for illumination it is very difficult to obtain the bubble size with this approach (Diaz & Riethmuller 1998). In order to obtain a planar image of the bubble contour a shadow imaging may be used (Lindken & Merzkirch 1999, Borchers 2002). A combination of this shadow imaging with PIV again requires additionally a light sheet and a second CCD-camera. In order to avoid strong light scattering on the bubble surface again the use of fluorescing tracer is necessary (Fujiware et al. 2001).

The application of two or more cameras and light sources result in quite extensive experimental equipment and time consuming measurement and evaluation procedures. Therefore, an efficient system with background illumination and only one CCD-camera was developed (Bröder and Sommerfeld 2002). The system allowed for online measurements and was applied to analyse the hydrodynamic interactions and coalescence of bubbles in a laboratory airlift reactor.

2. EXPERIMENTAL

2.1 Test Facility

The experimental facility was a rectangular container of Plexiglas[®] with the inner dimensions 2300 x 300 x 100 mm. The apparatus (Fig. 1) was aerated from the middle part by two capillary aerators and each of these aerators was connected to a single flux controller. The capillaries had a diameter of 0.4 and 0.6 mm and each aerator consisted of 50 capillaries. The aerators generated narrow bubbles size distributions in the range of 1.9 to 2.3 mm in case of the 0.4 mm capillaries and 2.7 to 3.1 mm for the 0.6 mm capillaries. Between the aerators a splitter plate was installed which kept the two bubbly flows separated up to a height of 1100 mm from the bottom of the container. Downstream of the end of the splitter plate the different bubbly flows were mixed so that the two bubble populations could interact. Two more plates separated the up-comer in the middle of the apparatus from the two outer down-comer channels. Two weirs in the upper part of the apparatus were used to reduce the liquid velocity in the two loops and to control the turbulence intensity in the mixing zone. As the internal water level would decrease during long measurements periods, it was kept constant by an electronic level controller.

A CCD-camera and a pulsed LED array as light source were mounted on a CNC traversing system allowing to perform fully automated measurements at all positions inside the airlift facility. This traversing system was also used as a camera lifter to follow rising bubbles with a high-speed camera. All components of the measurement system and the CNC traverse system were controlled by the image processing PC (Intel Pentium III 700 MHz) to allow fully automated online measurements for both phases of the bubbly flow. The synchronization of the CCD-camera and the pulsed LED-array, as well as the pulse duration and the delay time between the pulses were performed by a timer card, which was also installed in the image processing PC. The processing time for filtering a double image, detecting the bubbles and performing a PTV took around 1 s, while the processing time for filtering and performing a PIV for the liquid phase took around 5 s. The typical overall measurement time for a combined measurement of both phases at 5 measurement positions was 12 to 15 h.

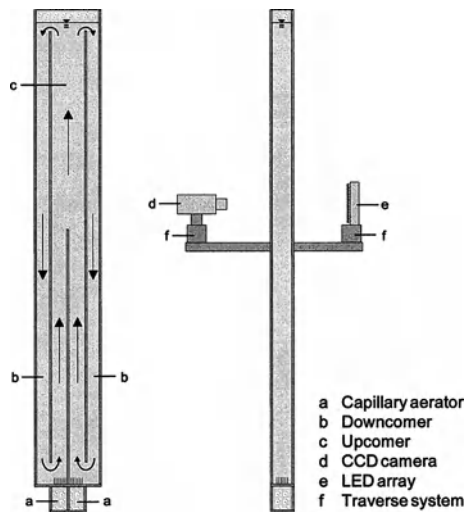


Fig. 1: Airlift facility with CCD camera, pulsed LED array and CNC traverse system

2.2 Image acquisition

The images of the two-phase flow were acquired by a double shutter camera (PCO SensiCam) which allowed to acquire two images with a resolution of 1280 by 1024 pixel within a very short time delay. A background illumination was realised using a pulsed LED-array consisting of 91 high performance LED's with a total area of 100 x 75 mm. In order to produce a thin vertical plane wherein images of bubbles and tracer were detected the CCD-camera was equipped with a macro lens having a small depth of field. The typical duration of the light pulses was 200 μ s,

while the time delay between two successive pictures was adjusted to the local flow velocity in a range from 1 to 3 ms. The images were transferred in a digital way from the CCD-camera to the controlling and image processing PC. The evaluation of the images and all controlling tasks were performed by an in-house developed software. In a first image processing step the images were transformed from the camera's 12 bit format to a 8 bit format grey value image. The histogram of the grey values of each image was analysed and from this histogram a contrast optimized lookup table for the transformation was created.

In order to allow measurements of the liquid velocity fields, the flow was seeded with polyamide tracer particles with a mean diameter of 50 μm and a density of 1050 kg/m^3 . The phase discrimination between bubbles and tracer particles was performed in the evaluation procedure using digital image filters. Because of the small depth of field of the macro camera optics ($< 4 \text{ mm}$) it was possible to discriminate also between bubbles and tracer particles inside and outside of the camera's depth of focus by the gradient of grey values. Sharply depicted objects in the focus have high gradients, while blurred objects out of focus have low gradients of grey values.

2.3 Bubble detection

In order to perform an automatic bubble detection, the recorded images needed to be optimised by a set of digital filters before an object recognition for the bubbles was applied. The tracer particles and small scale noise was deleted from the images by a non-linear 5x5 median filter and the gradient of the contours of sharply depicted bubbles was calculated by an edge-detecting Sobel filter. During the object recognition for the bubbles the gradient of the grey values at the contours of the bubbles, i.e. the sharpness, was used as a criterion for the validation. Additionally, the continuity of the contours was used as a validation criterion. As overlapping bubbles in the images resulted in incomplete contours, it was necessary to reconstruct missing contour points by a cubic spline interpolation. The information about the contour points of the bubbles were used to calculate projection areas, centroids, area equivalent diameters and the longest and shortest chord length.

2.4 Estimation of bubble volumes and coalescence rates

For analysing coalescence processes the knowledge of the bubble volumes is required. Most of the investigations performed with cameras acquire only one projection of the bubbles, which allows to determine a number of geometrical parameters like projection areas, chord lengths, perimeter and orientation of the main axis, but no precise determination of the bubble volumes is possible. Accurate bubble volume measurements could be realized by two perpendicular projections to gain additional information about the spatial extent of a bubble. But a simultaneous registration of two projections of one bubble is unlikely to occur even at low void fraction and impossible to realise in the described apparatus for void

fractions higher than 4 %. Therefore, the information of only one projection provides an estimation of the bubble volume and the accuracy of the volume determination will be better for small rigid and spherical bubbles than for large bubbles with strong shape oscillations. The simplest way to estimate the bubble volume V_B is to determine a bubble diameter D_A which is area equivalent to the projection area A_{Pro} of a detected bubble:

$$A_{Pro} = \frac{\pi}{4} AB = \frac{\pi}{4} D_A^2 \quad (1)$$

The bubble volume corresponds to the volume of a sphere with this area equivalent diameter. However, bubbles with larger area equivalent diameters than 2 mm have a ratio between the length of the major axis larger than 2 (Duineveld 1994) and differ considerably from a sphere. These bubbles can be described as oblate spheroids (Fig. 2) with the volume given by:

$$V_{Sph} = \frac{\pi}{6} ABC \quad (2)$$

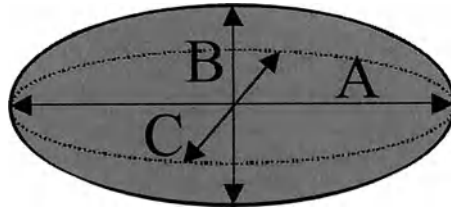


Fig. 2: Oblate spheroid with main axes

Both horizontal major axes A and C are approximately equal and larger than the vertical major axis B . By substitution of the missing major axis C with the longest chord length of the bubble contour A , an estimation of the bubble volume V_B is provided by the following equation:

$$V_B = \frac{\pi}{6} A^2 B = \frac{\pi}{6} D_A^2 * A \quad (3)$$

Evaluations of high speed recordings for bubbles of an area equivalent diameter $D_A = 3.8$ mm have shown a relative deviation of 12 % for the volume determination following equation (3) and a relative deviation of 16 % following equation (2).

The present investigations were performed in water purified by a reverse osmosis purification system. The system water/air was analysed by many authors (Oolman and Blanch 1986, Zahradník et al. 1995) with regard to coalescence behaviour in a stagnant liquid. For the investigated bubble size and the low turbulence intensity in the apparatus, the occurrence of bubble break-up can be neglected. Moreover, the test section was not long enough to allow for the formation of very large bubbles which might again break-up. Therefore, changes of the bubble size were caused by coalescence of bubbles and the change of the hydrostatic pressure along the rise of bubbles. In order to quantify the coalescence, the proper-

ties of the bubbles and the continuous phase were measured at 5 horizontal profiles along one of the risers up to the end of the splitter plate. The coalescence rate Γ_T was determined from the change of the bubble volume distribution between two measurement profiles following Prince und Blanch (1990):

$$\Gamma_T = \frac{c_B}{t_r} \frac{V_{gc}}{V_{gT}} \frac{\bar{V}_b}{\bar{V}_{bc}} \quad (4)$$

The bubble concentration c_B was calculated with the mean bubble velocity of the measured profiles, the bubble volume distribution and the superficial gas velocity. The residence time t_r was also calculated by the mean bubble velocity of the profiles and the distance between the measurement profiles. The coalesced volume V_{gc} corresponds to the positive integral area of the difference between two volume distributions. The mean bubble volume of coalesced bubbles \bar{V}_{bc} is also calculated from this area, while the mean bubble volume \bar{V}_b results from the total volume of gas V_{gT} . Bubble volumes from different measurement positions have to be corrected by the ideal gas law because of the volume expansion due to the change of the hydrostatic pressure.

2.5 Bubble velocity measurements (PTV)

The velocities of the bubbles were determined by the application of the Particle Tracking Velocimetry (PTV) and the described bubble detection algorithm for two consecutive images. Corresponding bubble pairs were found by the criterion of overlapping bubble contours and the closest neighbour in the direction of bubble rise. The bubble velocity was calculated from the translation of the centroids of the bubbles within both images, the time delay and the magnification factor. The translations of the centroids of the bubbles and the information extracted by the bubble detection were stored together for later post-processing of the data.

2.6 Liquid velocity measurements (PIV)

The velocities of the continuous phase were determined by the application of the Particle Image Velocimetry (PIV) to the extracted images of the tracer particles by using several filter operations (Fig.3). This extraction was performed with an edge filter proposed by Marr and Hildreth (1980) which is often called Laplacian of Gaussian (LoG). After the application of the LoG edge detector the images of the tracer particles, but also the contours of sharply depicted bubbles were kept inside the images. Therefore, an additionally image operation was used to remove these bubble contours. A median filtered image was created which contained only large objects like bubble contours but no tracer particles (Image C). This median filtered image with the bubble contours was subtracted from the image filtered by the LoG edge detector (Image B) and so the resulting image (Image D) was prepared for the PIV evaluation containing only the tracer particles.

The evaluation of the filtered images was performed by a PIV with iterative refinement of the interrogation areas following an approach of Scarano et al. (1999). The determination of the tracer displacement was based on a combination of the Minimum Absolute Difference Method (MAD) and the Minimum Quadratic Difference Method (MQD) developed by Gui et al. (1997). Further details about the applied PIV can be found in Bröder and Sommerfeld (2002). By recording and evaluating a large number of images (i.e. typically 500 per measurement plane) it was possible to determine instantaneous but also mean and fluctuating velocities fields for the continuous phase within the bubble swarm in all areas of the described apparatus.

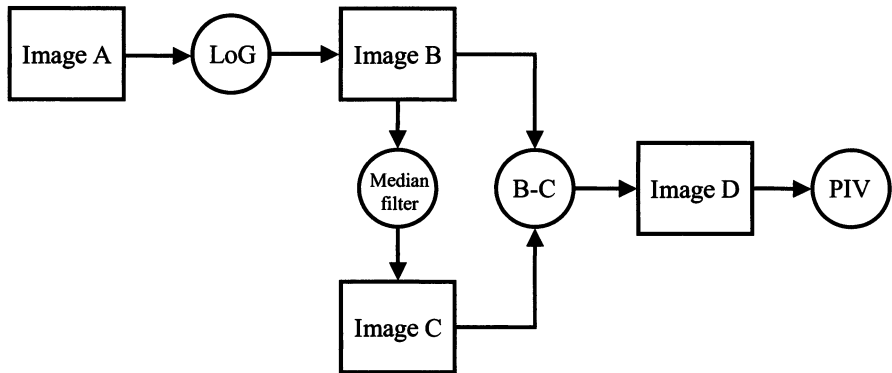


Fig. 3: Schematic diagram of the filter structure for the phase discrimination of the liquid by extracting the images of tracer particles from the pictures of the two-phase flow.

3. RESULTS

3.1 Shear layer development

The presented measurements were done in the riser channel of the apparatus. The measurements in the lower section (i.e. right and left of the splitter plate) are restricted to interactions of approximate equal sized bubbles and were used as initial conditions for the numerical calculations in the area above the splitter plate where interactions of different sized bubbles were investigated. The main operating conditions of the measurements are the superficial gas velocities of 0.44 cm/s in the left riser channel and 0.22 cm/s in the right one and the superficial water velocities of 17.06 cm/s in the left riser channel and 1.27 cm/s in the right one. The void fraction for this case was about 1 %.

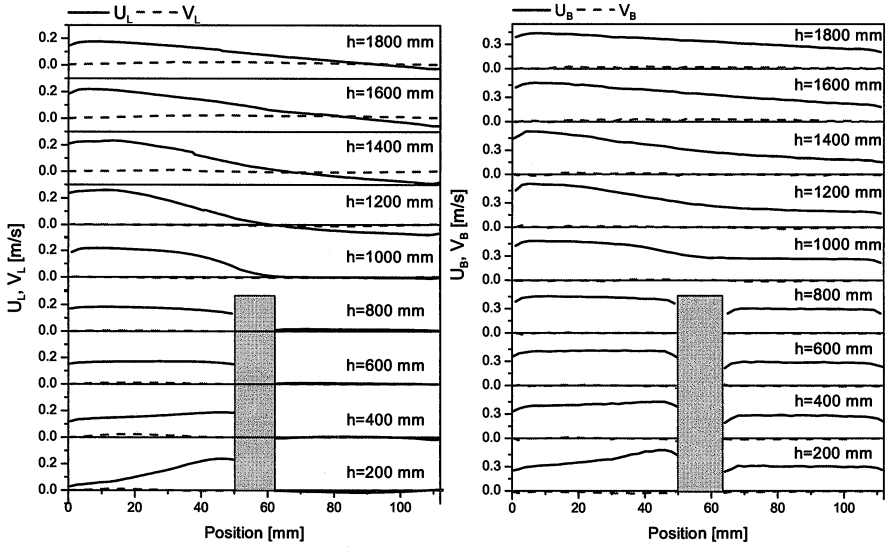


Fig. 4: Profiles of the mean velocity components of the liquid (U_L , V_L) and the bubbles (U_B , V_B) measured at different heights in the riser channel. (U: vertical component, V:horizontal component)

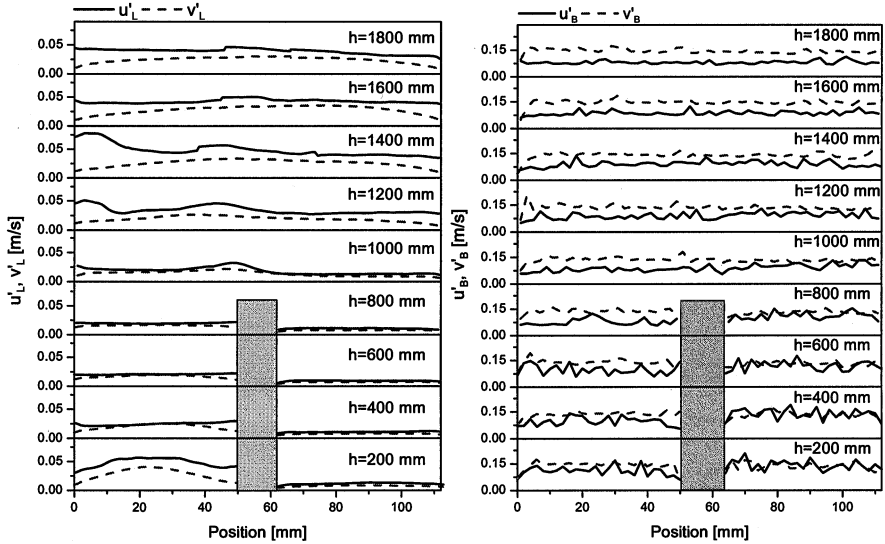


Fig. 5: Profiles of the fluctuating velocity components of the liquid (u'_L , v'_L) and the bubbles (u'_B , v'_B) measured at different heights in the riser channel. (u: vertical component, v: horizontal component)

The profiles of the mean and fluctuating velocities of the liquid were determined by averaging the information of 500 PIV vector fields per profile. The measurements of the velocities of the continuous phase showed, up to a height of 800 mm, no completely developed flow, because of the short length of the riser channels. This is revealed by the mean velocity profiles of the left riser channel, presented in Fig. 4, which are not symmetric.

Above the end of the splitter plate the profiles of the mean liquid velocity show a large-scale circulation in the riser channel caused by the different superficial water velocities in the two lower riser channels. The shear layer extends along the entire test section (i.e. from the end of the splitter plate up to 1800 mm) and at the end of the test section an almost constant shear rate over the entire cross-section of the riser is established. The profiles of the mean bubble velocities are similar to the profiles of the mean liquid velocities but, due to the relative velocity between the phases of about 0.28 m/s, the profile of the vertical bubble velocity show no negative values. The horizontal component of the bubble velocity shows a lateral transport of bubbles by the large-scale circulation of the liquid flow.

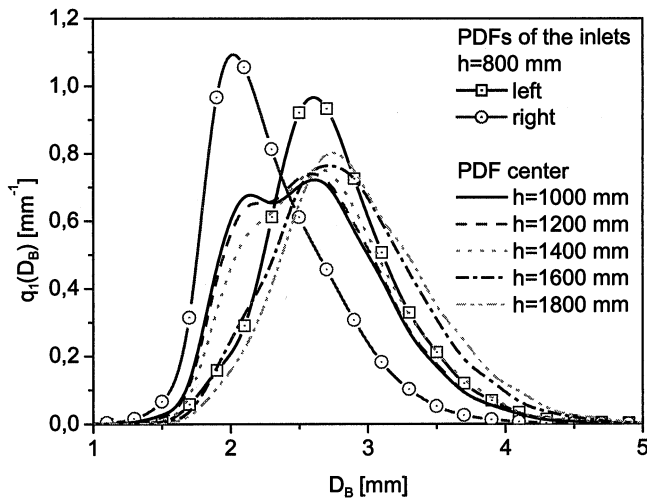


Fig. 6: Evolution of the bubble size distribution along the shear layer (data are collected in a region with a width of 50 mm in the center of the riser) and initial size distributions in the right and left channel

The fluctuating velocities, presented in Fig. 5, show a strongly anisotropic character of turbulence and bubble motion. With the exception of the bubbles in the right lower riser channel, the velocity fluctuations of the bubbles in vertical and horizontal direction are strongly anisotropic. The reason for the large horizontal fluctuations are the strong horizontal oscillations of the bubbles with a size in the range from 2 to 4 mm. This behaviour is quite different to the fluctuating velocities of the liquid as the horizontal components of the liquid are smaller than the vertical ones. The bubbles in the right lower riser channel had a mean bubble di-

iameter of 2.1 mm and therefore this bubbles show an almost isotropic fluctuating behaviour.

Within the shear layer above the splitter plate a peak in the profiles of the fluctuating velocities of the liquid develops, which also shows a lateral shift to the left by the flow circulation and flattens in stream wise direction. As expected, the bubble fluctuating velocities are considerably higher than those of the liquid. The strong oscillations in the profiles of the bubble fluctuations indicate that the number of collected images is not yet sufficient.

The development of the bubble size distribution in the centre of the channel above the splitter plate is shown in Fig. 6. The initial bubble size distribution in the left and right channel were obtained at $h = 800$ mm giving a number mean diameter of 2.30 mm in the left channel and 2.74 mm in the right one, respectively. Within the shear layer, both bubble populations interact and the resulting size distributions are a consequence of the mixing of the two streams and the coalescence between bubbles. The latter is indicated by the fact that the population of large bubbles increases while that of the smaller bubbles is reduced.

3.2 Coalescence rates

The analysis of the coalescence rates was done in one of both risers from just above the aerator up to the end of the splitter plate, since here the change of bubble size distribution is solely governed by bubble coalescence. However, it should be noted that this region does not have a fully developed flow.

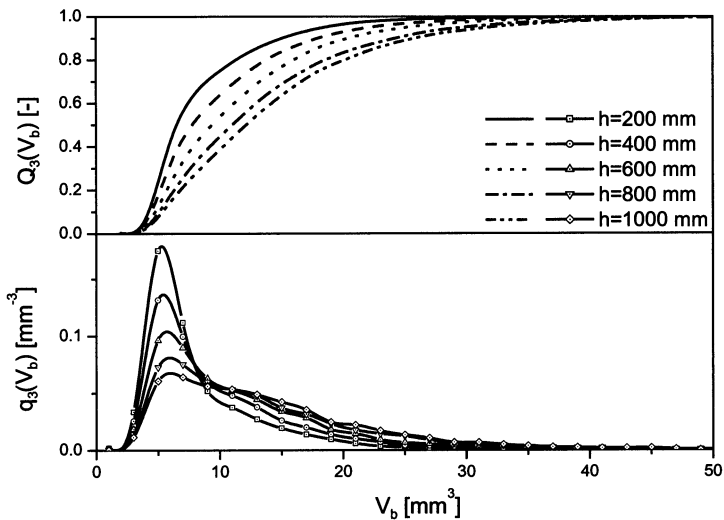


Fig. 7: Changes of the bubble volume distribution in one of the riser channels for a void fraction of 0.96 %.

For this purpose at least 30,000 bubbles were recorded over the entire width of the channel at different vertical positions. The considered height for each cross-section was 40 mm. The change of the bubble volume distribution due to coalescence for a case of 0.96 % void fraction is showed in Fig. 7. The basic bubble population has a peak at about 7 mm³ which decreases with the height of the measurement position, while a second wider peak with twice the volume of the basic population grows at approximately 14 mm³. Thereby, the volume distribution becomes more and more bimodal. The coalescence rates for this experiment decrease with the height of the measurement position, since a larger fraction of the basic population has already coalesced in the lower part of the channel and therefore the bubble number concentration has decreased.

3.3 Collision rates

Bubble coalescence may be separated into three sub-processes namely: collision of bubbles, drainage of the liquid film between the bubbles, break-up of the film and finally merging of two bubble fractions *i* and *j*. Collisions between bubbles may be caused essentially by three phenomena namely: turbulence induced collisions, buoyancy-driven collisions and collisions due to laminar shear (Prince and Blance, 1990). Mostly measurements do not provide all the properties to determine these different collision rates. However, the present imaging measurements provide the velocities of both phases as well as the bubble size. The collision rate due to the turbulent motion of bubbles is given by:

$$\theta_{i,j}^T = 2^{3/2} \pi^{1/2} n_i n_j (r_{bi} + r_{bj})^2 \cdot (\bar{u}_{ii}^2 + \bar{u}_{jj}^2)^{1/2} \quad (8)$$

Where, S_{ij} is the collision cross-section specified below, n_i, n_j are the local number densities of the two bubble fractions and $\bar{u}_{ii}^2, \bar{u}_{jj}^2$ are the local averaged fluctuating velocities of the bubbles which are mostly not available. Therefore, estimations of these values are based on the theory of homogeneous isotropic turbulence and determined as a function of energy dissipation. But such estimations cannot account for the anisotropic motion behaviour of bubbles rising in typical “zigzag” or helical path. The buoyancy-driven collision rate results from the difference in the rise velocity of bubbles with different size:

$$\theta_{i,j}^B = n_i n_j \cdot S_{i,j} \cdot |u_{ri} - u_{rj}| \quad (9)$$

The rise velocities of the two fractions (u_{ri} and u_{rj}) are often expressed through empirical correlations like the ones specified in Clift et al. (1978). However, the bubble rise velocity is not only depending on the bubble size, but also strongly affected by the properties of the liquid and possible impurities. The collision rate due to laminar shear is:

$$\theta_{i,j}^{LS} = n_i n_j \cdot \frac{4}{3} \cdot (r_{bi} + r_{bj})^3 \cdot \left(\frac{d\bar{U}_l}{dR} \right) \quad (10)$$

Here $d\bar{U}_l/dR$ is the average shear rate, which for a bubble column is usually determined from empirical correlations for the liquid velocity profile.

With the applied new measurement system all relevant information for a detailed analysis of different collision rates could be obtained for the first time. In combination with the determination of the coalescence rate additionally an overall coalescence efficiency could be obtained. The large number of sampled bubbles (~30.000) per measurement position resulted in a good statistical reliability which was high enough to determine local size-dependent bubble properties, like the mean rise velocity $u_r(d_A)$ but also the mean fluctuating velocities of the bubbles $\bar{u}_i(d_A)$.

The measured mean and fluctuating velocities for the case of a very low superficial water velocity in one of the lower up-comer channels is shown in Fig. 8. The mean bubble rise velocity follows the trend of the well known rise velocity of single bubbles with a maximum for 1.3 mm bubbles and a decreasing rise velocity with growing bubble diameter. Since this experiment was performed with a low void fraction of 1 % and a low superficial water velocity of 0.01 m/s, the difference between the bubble rise velocity and the rise velocity of single bubbles is small. The fluctuating velocities of the bubbles are almost isotropic up to an area equivalent bubble diameter of 2 mm. With the onset of strong shape oscillations for bubbles larger 2 mm, especially the vertical component of the fluctuating velocity decreases strongly.

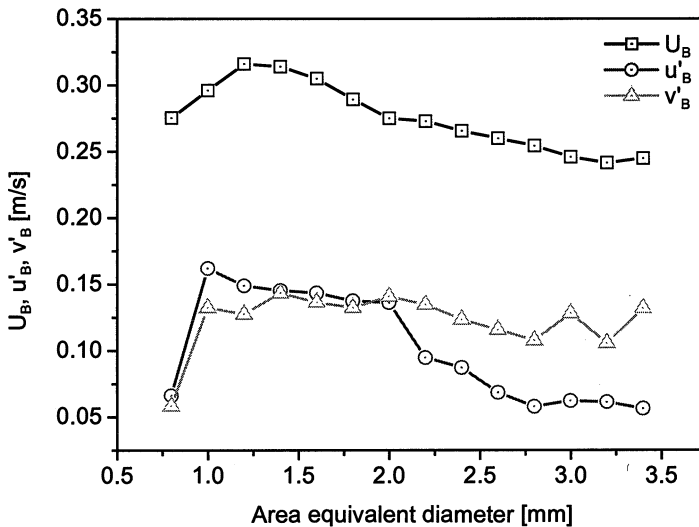


Fig. 8: Mean bubble rise velocity and fluctuating components of the bubble motion as a function of the area equivalent bubble diameter. Measurements were performed in one of the riser channels for a void fraction of 0.96 %.

From the two components of the fluctuating bubble velocities an fluctuating velocity $\overline{u'_i}(d_A)$ averaged over the entire cross-section of the channel was calculated in the following way:

$$\overline{u'^2}(d_A) = \frac{1}{3}(\overline{u_B'^2}(d_A) + 2\overline{v_B'^2}(d_A)) \quad (11)$$

The overall turbulent collision rate was calculated from that averaged fluctuating velocity of the different bubble size classes, the concentrations of the size classes n_i, n_j and the collision cross-sectional area S_{ij} of the bubbles defined by:

$$S_{i,j} = \pi \cdot (r_{bi} + r_{bj})^2 \quad (12)$$

The overall turbulent collision rate is then given by:

$$\theta^T = \frac{1}{2} \sum_i \sum_j 2^{3/2} \pi^{1/2} n_i n_j (r_{bi} + r_{bj})^2 \cdot (\overline{u_{ii}^2} + \overline{u_{jj}^2})^{1/2} \quad (13)$$

For the buoyancy-driven collision rate the bubble rise velocity averaged across the channel for each bubble size fraction $\overline{U_r}(d_A)$ was used and the overall buoyancy-driven collision rate is then given by:

$$\theta^B = \frac{1}{2} \sum_i \sum_j n_i n_j \cdot S_{i,j} \cdot | \overline{U_{ri}} - \overline{U_{rj}} | \quad (14)$$

In case of the laminar shear collision rate, the averaged shear rate of the liquid flow was calculated from the vertical component of the liquid velocity profiles measured by the PIV. Also for the laminar shear collision rate an overall value was calculated:

$$\theta^{LS} = \frac{1}{2} \sum_i \sum_j n_i n_j \cdot \frac{4}{3} \cdot (r_{bi} - r_{bj})^3 \cdot \overline{\left(\frac{dU_l}{dR} \right)} \quad (15)$$

The collision rates along one of the lower up-comer is shown in Fig. 9 for a case with a void fraction of 0.96 % and an initial number mean bubble diameter of 2.1 mm. All collision rates decrease in flow direction due to flow development and the reduction of bubble number density as a result of coalescence. The turbulent collision rate shows the highest values as bubbles in the diameter size range from 1 to 3 mm show the strongest fluctuations in their motion (Fig. 8). Due to the fact that the bubble size distribution was relatively narrow, the difference in the rise velocities of different bubble classes was small, whereby the buoyancy-driven collision rate is one order of magnitude smaller than the turbulent collision rate. The lami-

nar shear collision rate is two orders of magnitude smaller than the turbulent collision rate and therefore negligible. The coalescence rate Γ_T was about two orders of magnitude smaller than the sum of all collision rates, which means that even in the highly coalescing system of purified water a bubble undergoes around 100 collisions before a coalescence process happens. As the investigated bubble size distributions were narrow and initially monomodal, it can be assumed that the coalescence efficiency is almost constant over the entire bubble size distribution. Therefore, an overall coalescence efficiency can be determined from the overall coalescence rate and the sum of the three collision rates in the following way:

$$\lambda = \frac{\Gamma_T}{\theta^T + \theta^B + \theta^{LS}} = e^{-\frac{t}{\tau}} \quad (16)$$

The overall coalescence efficiency was about 0.03 which corresponds to a ratio between coalescence time t and contact time τ of about 3.5.

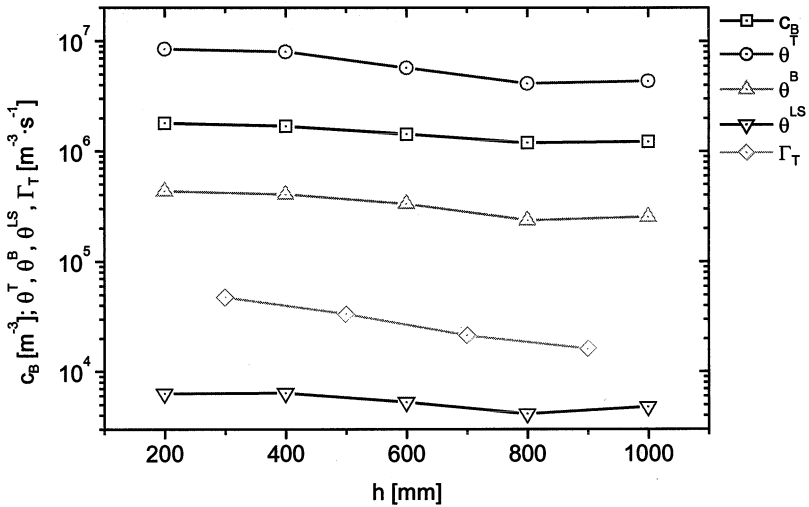


Fig. 9: Collision rates and coalescence rate along one of the lower riser channels (number mean bubble size 2.1 mm, volume fraction 0.96%).

CONCLUSIONS

The described measurement system, combining imaging PIV and PTV, is able to acquire all important parameters in a bubbly two-phase flow. Therefore, it provides a potential to create detailed datasets for validating numerical simulations. Additionally, further analysis of the hydrodynamic interactions of bubbles in a swarm was possible. The simultaneous measurements of bubble size, bubble velocity and liquid velocity allow a sophisticated post-processing of the collected data in order to analyse important phenomena such as, collision rates, coalescence rates and collision efficiencies. The obtained results will be used to improve a bubble collision and coalescence model developed in the frame of the Euler/Lagrange approach and eventually for the validation of the numerical results.

ACKNOWLEDGEMENTS

The financial support of the present studies by the Deutsche Forschungsgemeinschaft under contract number SO 204/19 is gratefully acknowledged.

REFERENCES

- Borchers, O. (2002) *Zweiphasen-Particle-Tracking-Velocimetry (PTV) zur detaillierten Analyse der Hydrodynamik von Blasensäulenreaktoren*, Fortschr. Ber. VDI Reihe 3 Nr. 753, VDI Verlag, Düsseldorf
- Bröder, D. and Sommerfeld, M. (2002) "An advanced LIF-PLV system for analysing the hydrodynamics in a laboratory bubble column at higher void fractions", *Exp. in Fluids*, 33, 826-837.
- Bröder, D. and Sommerfeld, M. (2002) "Experimental studies of bubble interaction and coalescence in a turbulent flow by an imaging PIV/PTV system", *Proceedings of the 11th International Symposium Application of Laser Techniques to Fluid Mechanics*, Lisbon
- Deen, N.G., Hjiertager, B.H., Solberg, T. (2000) Comparison of PIV and LDA measurement methods applied to the gas-liquid flow in a bubble column, 10th Int. Symp. Applications of Laser Techniques to Fluid Mech., Lisbon, Portugal, 1-12
- Diaz, I. and Riethmuller, M.L. (1998). "PIV in two-phase flows: Simultaneous bubble sizing and liquid velocity measurements." 9th Int. Sym. on Applications of Laser Techniques to Fluid Mechanics, Lisbon, Portugal.
- Fujiwara, A., Takahashi T., Tokuhiko A. Hishida, K. (2001) *Turbulent Microscale Structure in Bubbly Channel Flow*. Proceedings of the ICMF, New Orleans.

- Gui, L., Lindken, R. and Merzkirch, W. (1997) "Phase-separated PIV Measurements of the Flow Around systems of Bubbles Rising in Water", ASME-FEDSM97-3103.
- Kamp, A.M., Chesters, A.K., Colin, C., Fabre, J. (2001) Bubble coalescence in turbulent flows: A mechanistic model for turbulence-induced coalescence applied to microgravity bubbly pipe flow, *Int. J. Multiphase Flow*, Vol. 27, 1363-1396
- Kirkpatrick, R.D., Lockett, M.J. (1974) The influence of approach velocity on bubble coalescence, *Chem. Eng. Sci.*, Vol. 29, 2263-2273
- Lindken, R., Merzkirch, W. (1999) Phase separated PIV and shadow-image measurements in bubbly two-phase flow, *Proc. of the 8th Int. Conf. Laser Anemometry Advances and Applications*, Rome, Italy, 165-171
- Marr, D. and Hildreth, E. (1980). "Theory of edge detection", *Proceedings of the Royal Society of London*, B 207, pp. 187-217.
- Martínez-Bazán, C., Montanés, J.L., Lasheras, J.C. (1999) On the breakup of an air bubble injected into a fully developed turbulent flow. Part 2. Size PDF of the resulting daughter bubbles, *J. Fluid Mech.*, Vol 401, 183-207
- Oolman, T. O. and Blanch, H. W. (1986) "Bubble Coalescence in Stagnant Liquids", *Chem. Eng. Comm.*, Vol. 43, pp. 237-261.
- Prince, M. J. and Blanch, H. W. (1990) "Bubble Coalescence and Break-Up in Air-Sparged Bubble Columns", *AIChE Journal*, 36, pp. 1485-1499.
- Scarano, F. and Riethmuller, M. L. (1999) "Iterative multigrid approach in PIV Image processing with discrete window offset", *Experiments in Fluids*, Vol.26, pp. 513-523.
- Zahradník, J., Fialova, M., Kaštánek, F., Green, K.D. and Thomas, N.H. (1995) "Effect of Electrolytes on Bubble Coalescence and Gas Holdup", *Trans IChemE*, Vol.73, Part A.

PIV-Study on bubble interaction and wakes in multiphase flows

Ch. Brücker, W. Schröder

Aerodynamisches Institut der RWTH Aachen
Wüllnerstr. zw. 5 u. 7, D-52062 Aachen, Germany
Tel: +49.241.80-95429, Fax: +49.241.80-92257
E-mail: bruecker@aia.rwth-aachen.de

Abstract.

The flow in the wake of single bubbles and bubble swarms freely rising in water is studied experimentally using Digital-Particle-Image-Velocimetry (DPIV) in combination with high-speed recording. The experiments focus on ellipsoidal bubbles of diameter of about 0.4 – 0.8 cm which show spiraling, zigzagging and rocking motion during their rise in water, which was seeded with small tracer particles for flow visualization. Under counter-flow conditions in the vertical channel, the bubbles are retained in the center of the observation region, which allows the wake oscillations and bubble interaction to be observed over several successive periods. By simultaneous diffuse illumination in addition to the light-sheet, we were able to record both the path and shape oscillations of the bubble, as well as the wake structure in a horizontal and vertical cross-section. The results demonstrate the wake dynamics and its importance on bubble interaction.

1. Introduction

For a long time, the motion of bubbles rising in liquids has drawn the attention of researchers because of the bubbles fascinating variety of motion patterns and instabilities. In bubbly two-phase flows, the bubbles have the shape of spheres, ellipsoids or spherical caps and they rise in rectilinear, spiraling, zigzagging, or rocking motion, depending on the characteristic numbers of the system for example, the bubble diameter and the properties of the liquid (see the review given in Clift et al. (1978) and the recent paper of Maxworthy et al. (1996). In addition, various kinds of shape oscillations can be observed (Lunde & Perkins 1998). Early studies from the beginning of this century had already highlighted the importance of the wake structure for the path instabilities of solid spheroids and speculated

that the same held for bubbles (Hirsch 1923). Saffman (1956) studied zigzagging and spiraling bubbles and concluded that the zigzag motion is possibly related to an oscillation of the wake or a periodic discharge of vorticity from behind the bubble. Moreover, the bubble wake is also one of the most significant factors contributing to turbulence production, which is important for most industrial applications in which bubbly flows occur (Fan & Tsuchiya 1990). The formation of bubbles in clusters and their dynamics is another area in which the individual wakes play an important role. Therefore, the understanding of the nature of the wake of freely rising bubbles is of fundamental importance in improving models for simplified simulations of those mainly three-dimensional and unsteady multiphase flows. However, detailed quantitative studies of the evolution of the flow in the wake of bubbles and swarms are extremely difficult. Our current work attempts to describe the structure of the wake of free rising bubbles and its effect on bubble interaction in a more detailed way. Therefore, in the experiments described herein, we used Digital-Particle-Image-Velocimetry (DPIV) in combination with a digital high-speed camera to obtain the temporal evolution of the flow field in the near wake. These preliminary studies were done for flow parameters and bubble sizes, for which ellipsoidal bubbles with a more or less regular spiraling or zigzagging motion could be observed. This allows comparison of the nature of the vortex shedding behind bubbles and solid spheroids. The size of a typical bubble in the experiments was about 0.4 – 0.8 cm in diameter. After a description of the experimental method (Section 2), the results of the radial and axial flow within the wake are given (Section 3) and discussed. Finally, the mechanism responsible for the observed wake-induced bubble interaction is presented in Section 4.

2. Experimental Method

2.1 Flow channel

The bubble wakes were studied in a vertical water channel, in which the bubbles were released from the bottom and were held stationary in vertical position by an imposed counter-flow, Fig. 1. The test section of transparent acrylic plates had a cross-section of $10 \times 10 \text{ cm}^2$ and was 1.2 m high. The flow was driven by the constant head of water in the settling chamber at the top of the channel and was controlled by a valve located at the right-hand side bottom end of the test section. A uniform flow with low turbulence level was achieved by a contraction passage with a contraction ratio of 5, which is located upstream of the inlet into the test section. Demineralized water was used as the test liquid. Small tracer particles (Vestosint, mean diameter of $30 \text{ }\mu\text{m}$, $\rho = 1.02 \text{ g/cm}^3$) were added to the fluid upstream in the water basin and were homogeneously distributed. From measurements of the rise velocity of the bubbles and comparison with the values in literature (Clift et al. 1978) for the same size of ellipsoidal bubble we concluded that

the contamination with the tracer particles let the bubbles behave like in impure water systems.

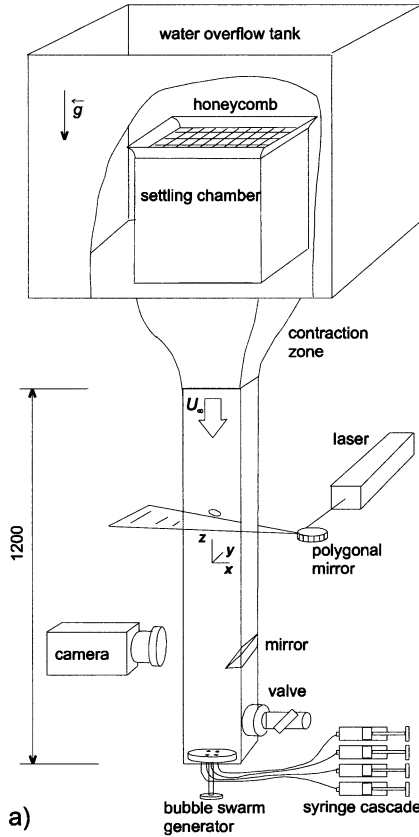


Fig. 1. Flow channel and optics

Experiments were performed either with single bubbles or with the simultaneous release of a few bubbles, in order to study their interaction in relation to wake dynamics. The bubbles were released from the bottom plate of the tank, initially into quiescent fluid. The bubble generator resembled the one used by Stewart (1995) and consisted of a rotating plate with 8 holes, which was placed between two fixed plates for which the top represents the release plate and the bottom the filling plate. In the filling position, each hole in the rotating plate was connected via the bottom plate with a small tube to a syringe and could be filled with a defined gas volume using a proportioning screw. In the release position, the chambers were simultaneously opened at the top and bottom and the pressure difference drove the bubbles out of the generator. Thus, we were able to release in a controlled manner, a maximum of 8 bubbles with a defined volume. Shortly before the bubbles entered the bottom edge of the observation region, the downstream

control valve was opened such that the bubbles - after a short transient phase - remained approximately stationary in a vertical position. In bubbly flows, the Reynolds-number Re_r , often used is based on the equivalent radius of the gas bubbles which is calculated from the gas volume contained. In the following however, the Reynolds-number is defined as $Re = U_T D/\nu$ based on the total speed U_T of the bubble and the mean major diameter D of the spheroid, for reasons of direct comparison with the definition typically used for solid bodies like spheres or discs. The total speed of the bubble is calculated with the vertical rise speed w and the lateral speeds u and v in x - and y -direction.

2.2 Measurement methods

Our investigation focused on the spatial structure and dynamics of the vortices in the wake of the bubbles. The flow field in the bubble wake was recorded with a digital high-speed camera and evaluated frame-by-frame with the method of Digital-Particle-Image-Velocimetry (DPIV). The DPIV set-up was first arranged to measure the velocity field in a horizontal cross-section, downstream of the bubbles, (see the optical arrangement in Fig. 1) in order to obtain the streamwise component of the vorticity vector from the results. This is of importance for the understanding of the lateral motion of the bubble which has to leave a distinct pattern of the streamwise vorticity in the wake. The beam of a continuous Ar^+ laser was expanded with a rotating polygonal mirror to form an intense virtual light-sheet in a horizontal cross-section of the channel. A digital high-speed video camera (Weinberger GmbH, Germany, resolution: 512×512 pixel; maximum frame rate: 1000 Hz, number of frames: 512) was used to record the flow, synchronized with the polygonal mirror so that each frame corresponds to a single sweep of the laser beam. Within the horizontal light-sheet plane (x - y plane, see the coordinate system in the channel as defined in Fig. 1), the in-plane velocity components were obtained from cross-correlation of successive images in small interrogation windows with a size of 32×32 pixel. The results represent a two-dimensional data set, in form of velocity vectors on a grid with 31×31 equidistant nodes over a squared cross-section area of $3 \times 3 \text{ cm}^2$. In addition to the light-sheet, diffuse light was used to illuminate the bubble upstream of the light-sheet. The intensity was adjusted such that the contour of the bubble could be clearly seen from the reflections but did not overexpose the particle images in the light-sheet. With some image enhancement and contour processing, the position and shape of the bubble could be determined from these images. A frame rate of 400 Hz was found to be sufficient to resolve the time scales of bubble and wake oscillations. The recording period of the camera was limited to a maximum of 512 frames in each run.

In supplementary experiments, the light-sheet was oriented in the vertical position (y - z -plane) and the camera was placed to record the vertical motion of the bubbles. However, it turned out to be impossible to achieve successful experiments in which the freely moving bubble was within the plane of the light sheet. Therefore, a multi-planar extension of classical PIV using a scanning light-sheet was used (see Brücker 1999 for details). The scanning light-sheet technique en-

sured that we would obtain at least one plane which would be close to the bubble center within each scan. The scanning light-sheet was generated with a rotating drum by a helical arrangement of mirrors on its surface. With continuous rotation of the drum, the laser beam illuminates the flow in vertical light-sheets staggered in depth. The total scanning width was 2.4 cm in 5 planes, each of which was separated by 0.6 cm so that the sampling in depth was small enough to have one light-sheet close to the bubble center. The 2-D velocity field was again determined by cross-correlation between successive images in each plane; the temporal resolution of the flow in each of the 5 planes is 200 frames/sec when the scanning rate is 1000 planes/sec. To capture a larger extent of vertical motion of the bubbles we enlarged the observation area to a height of 6 cm at the expense of resolution. The results presented here represent a two-dimensional data set in the form of velocity vectors on a grid with 21×41 equidistant nodes over a cross-sectional area of $3 \times 6 \text{ cm}^2$. Simultaneously, the bubble motion was recorded in three dimensions using a stereoscopic viewing arrangement (for a more detailed description see Brücker 1999).

3. Wake of a zig-zagging bubble

3.1 Flow structure in the horizontal cross-section

The measurements were carried out for bubbles with a shape of oblate spheroids between a minimum of 0.5 cm and a maximum of 0.7 cm in diameter. The diameter of the bubble is defined here as the major diameter of the spheroid and has been determined from the images of the projection of the bubble as shown later. They showed a regular zigzag rise path in our experiments with water. The path oscillations were observed to be more or less unidirectional and quite regular in time. Several runs of experiments had to be done to achieve optimum boundary conditions for the measurements, i.e. that the bubble was in the middle of the imaging field and could be retained at the desired vertical distance relative to the predefined position of the horizontal light-sheet. From these well-posed experiments for reasons of simplicity, we have chosen one exemplary experiment in which the zigzag motion was aligned closely in the y-direction (the bubble moved approximately in a plane zigzag with less than maximum 2% motion in the x-direction compared to that in the y-direction). The bubble in this experiment with a diameter of $D = 0.6 \text{ cm}$ had a mean aspect ratio E of 0.66 ($E = \text{maximum vertical dimension}/\text{maximum horizontal dimension}$) and a bubble rise speed of about $w = 20 \text{ cm/s}$ - this equals the imposed counter-flow velocity - which is quite well predicted by the correlation for air bubbles rising in contaminated water (see equation 7-20 in Clift et al 1978 , p. 181). For one complete “zig” and “zag” motion we measured a frequency of 4.2 Hz and a maximum lateral velocity in the horizontal plane of about $v = 10 \text{ cm/s}$. The Reynolds-number based on the maximum total

velocity of the bubble and the bubble diameter D results to $Re \approx 1320$ and the Strouhal-number calculates to $Sr = 0.11$ with $Sr = f D/U_T$. Fig. 2 shows the variation of the position of the bubble centroid in the horizontal plane during the complete measuring period of approximately 0.3 s. The zigzag motion of the bubble is clearly seen as a sinusoidal function of the y -coordinate over time with an amplitude of $1.3 D$ which is about 1 cm.

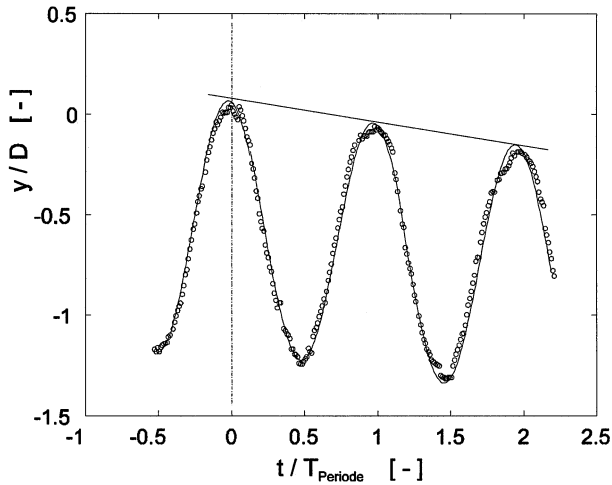


Fig. 2. Motion of a zigzagging bubble of diameter $D \approx 0.6$ cm over time in the zigzag plane along the y -axis



Fig. 3. Wake visualization for a rocking bubble at $Re \approx 1500$ (Lunde & Perkins 1995)

Before the results of the flow field measurements are discussed, we anticipate a qualitative picture of the global wake structure to support interpretation of the quantitative results of only one single plane within the wake. Refer therefore to the flow visualization picture recently taken by Lunde and Perkins (1995), reproduced in Fig. 3. It shows the wake structure of a freely rising bubble at a Reynolds-number of $Re \approx 1500$ which is similar to the one in our experiments (the Reynolds-number they used is likewise based on the total speed of the bubble UT and the major diameter of the spheroidal bubble D). The bubble was released into a water tank in which the bottom layer was colored with dye. During the initial phase of bubble rise, dyed fluid was trapped into the wake which acted as a flow marker after the bubble left the bottom layer and enters the region with clear water. The visualized pattern in the wake of the irregular zigzagging bubble shows a hairpin-vortex whose legs are attached to the base of the bubble while the head points downstream to the left. Note, that due to self-induction the head of the hairpin-vortex is already strongly deformed. In the radial cross section in the near wake region we can therefore expect to see in our measurements regions of concentrated streamwise vorticity which represent cuts through the legs of the hairpin-vortices; in the vertical cross-sections, the vorticity regions would represent cuts through the head.

For the flow studies in the radial cross-section of the wake, we retained the bubbles in the counter-flow approximately 1 cm upstream of the light-sheet. At this distance from the bubble base (roughly a factor of 1.5 of the bubble diameter) we can assume that the coherence of the vortex structures is not yet affected by self-induction and that the measuring plane is already out of the attached part of the wake. In Fig. 4, the flow field is given in the left column with the additional information of the bubble contour taken at the moments A-F. Note, that we have therein corrected for the time, which the vortex structures need to travel from the bubble base to the light-sheet. We therefore assumed that they move downstream with the velocity equal to the free-stream velocity. The flow fields were then taken at the moments corrected by the convection time. This allows us to draw conclusions about the correlation between bubble position, shape and the flow field being created at the bubble base at this moment. The right-hand column shows regions of concentrated streamwise vorticity which are calculated from the determined velocity field by central difference schemes.

The flow field in the cross-section exhibits the alternate generation of a pair of counter-rotating vortices close to the bubble base. As explained above, regions of concentrated streamwise vorticity represent the legs of hairpin-like vortex structures. At the beginning of the cycle in Fig. 4A, a stagnation point exists in the cross-flow at the left-hand side of the bubble which indicates the high-pressure side of the bubble. The flow field to this moment resembles a dipole-like vector field (a sink and a source in the cross-flow along the y -axis). The bubble is positioned near the left-hand stagnation point. In Fig. 4B, this critical point has been split up into two foci which indicate the centers of streamwise vortices. The splitting process hints that the head of the hairpin-vortex has passed the plane and left its legs which correspond to the pair of streamwise vortices seen in the cross-section. The location of the vortex pair in the horizontal plane is clearly shifted

towards the left-hand side of the bubble in positive y -direction and the former weak vorticity concentration at this location (Fig. 4A) has been established in strength towards the dominant pattern (Fig. 4B). A strong cross-flow in the positive y -direction can be observed which is a consequence of the induction effect of the vortex pair (see Fig. 4B). Due to this asymmetry of the cross-flow and the effect on the flow around the bubble, the highest total flow velocity on the bubble equator will occur at a location diametral to the plane of the vortex pair as also concluded by Lunde and Perkins (1995).

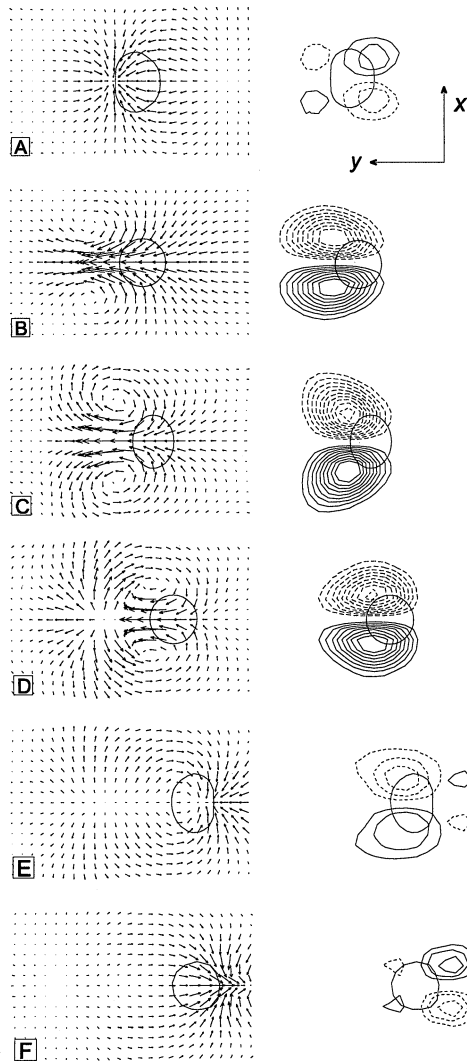


Fig. 4. Evolution of the velocity field and streamwise vorticity distribution in a horizontal plane 1 cm downstream of the zigzagging bubble

This region of highest total velocity - this is also the region of lowest pressure - is therefore located at the right-hand side in the equatorial plane of the bubble. Hence, a net lift force acts to the right in the negative y -direction, which explains the lateral drift of the bubble to the right. In this phase, the attached vortex pair moves with the bubble without any topological change of the flow in the cross-section.

Thereafter, the vortices become progressively weaker and the lateral motion of the bubble begins to decelerate. A new counter-rotating pair is generated at the right-hand side of the bubble, (as seen in Fig. 4E; compare this also to the diametrical situation in Fig. 4A). Once again, the cross-flow shows a vector field with a dipole-like character. In the next instant (Fig. 4F), the stagnation point on the right (Fig. 4E) has been split up, indicating the passing of the next hairpin-vortex now at the right-hand side of the bubble (the centers of the vortices are out of the displayed area). The newly generated counter-rotating pair with alternate circulation increases rapidly in strength, replaces the former pair and establishes the dominant vortex pair, now located at the right-hand side of the bubble. Consequently, the bubble reverses its motion and starts to drift to the left by the associate lift force, for the same reason as explained above. This accounts for the zigzag of the bubble driven by the alternate generation of a pair of longitudinal vortices of alternate circulation and the associated lift force. Note that the flow fields presented in Fig. 4 show only a short extract of the complete recording period which contains a total of 3 cycles.

3.2 Flow structure in the vertical cross-section

The experiments described in this section focus on the evolution of the bubble wake in the vertical cross-section. Measurements of the vertical flow field are necessary for a more complete description of the three-dimensional flow field and vorticity distribution. The vertical cross-section contains important information about the induced vertical flow field and its role for bubble interference. Among others, the observation studies by Stewart (1995) in which he used clusters of few bubbles, revealed that these interactions exclusively occurred after a trailing bubble entered the wake downstream of a larger leading bubble. In the following, this is called the wake capture process. To obtain both the dynamic evolution of the wake of a free rising bubble in the vertical plane and the effects leading to wake capturing, experiments with two interacting bubbles were recorded. To ensure that the wake of the leading bubble was not significantly affected by the presence of the trailing one, the typical diameter of the trailing bubble was chosen about half the diameter of the leading one. In the following, we first describe the wake structure of the leading bubble in the initial phase of the observed period. Over most of the period, the fourth plane in the scan was the closest to the centroid of the leading bubble. Fig. 5 shows two characteristic pictures of measured flow fields in this plane within the cycle of the rocking motion. The velocity field represents the flow structure in the oscillation plane of the bubble at a): the right-hand side inver-

sion point (Fig. 5a), and b): close to the left-hand side inversion point 0.1s later (Fig. 5b). The path oscillation frequency was calculated to be 5 Hz, which is in accordance with the left-right discharge of vortex packages. Note that for the presentation of the vector field, the vertical velocity component of the imposed counter-flow (ca. 20 cm/s) has been subtracted. The bubble featured in Fig. 5a was taken a short moment before it changed its orientation and started to move to the left side. Regions of concentrated circumferential vorticity can be seen at the locations of maximum surface curvature of the bubble, i.e. at the equatorial edges (for the values close to the bubble surface we have interpolated the velocity field into the inner region of the bubble). A second local maximum of circumferential vorticity can be found in the wake, on the left-hand side. This region corresponds to a vortex center in the vector field marked as “L” and indicates a cut through the head of a shed hairpin-vortex whose head points to the left (the path of the legs is indicated by the thick dashed-dotted line in the plots).

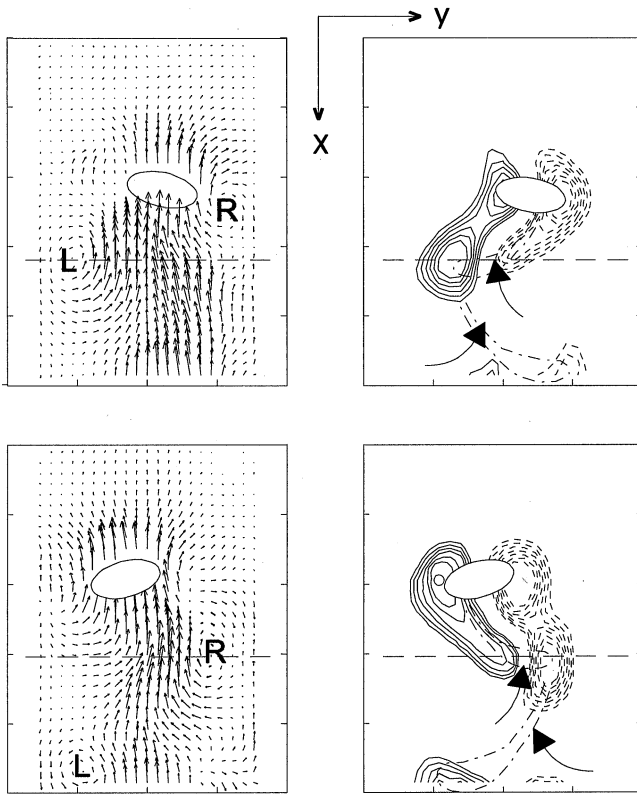


Fig. 5. Flow field in a vertical plane through the wake of a rocking bubble at two characteristic moments within the cycle (the vertical velocity component of the imposed counter-flow has been subtracted).

On the right-hand side the negative vorticity extends downstream from the edge of the bubble in the shape of a tongue-like region. At the next instant of the cycle, the situation is approximately reversed. The bubble is tilted to the left and a new hairpin-vortex has been generated, of which the head now points to the right, see the vortex center in the vector field marked at “R” in the vector field. This center was located at the earlier moment as seen in Fig. 5a, originally at the right-hand side of the bubble edge and was separated from the wake coupled with the tilting of the bubble at the inversion point. In addition, the head of the previously shed hairpin-vortex marked as “L” has moved 1.5 cm downstream with the mean flow. The inner of the loop-like heads and between the legs of the hairpin-vortices demonstrate strong lateral and upwards motion, which is the consequence of the induction effect of the vortex structures. For clarification, the direction of induced flow is indicated in the plots by arrows. As shown later, these areas of strong local induction prove to be the important factors involved in the wake capturing effect.

4 Wake drafting and bubble collision

Note that the two characteristic moments given in Fig. 5 repeat in a similar way over approximately three oscillation cycles until shortly before collision. To visualize the complete sequence in a single plot a spatio-temporal reconstruction of the vorticity field was created. From the obtained distribution of the vorticity field in the vertical plane, the vorticity values along the horizontal line 1 cm downstream of the bubble (see the dashed horizontal lines in Fig. 5) were taken, and stacked line by line vertically in a data array over the complete series of PIV results in the recorded period. The resulting data matrix, displayed as a contour plot in Fig. 6a, gives the spatio-temporal evolution of the component of circumferential vorticity at a stationary location within the wake of the leading bubble. Only regions of values exceeding 50% of the absolute maximum vorticity value are shown, in order to highlight the centers of the head loops of the hairpin-vortices containing the maximum of circumferential vorticity. Note that because of fluctuations in time, the contour lines in the spatio-temporal reconstruction are not as smooth as for a single instantaneous flow picture. The global pattern of the reconstruction however already demonstrates the nature of the wake as a chain of alternately tilted vortex structures with a zigzag orientation. The sideward adjacent regions with contour lines of positive and negative circumferential vorticity represent therein the orientation of the heads of the hairpin-vortices. For clarification, we have indicated the corresponding positive and negative contour lines by dashed ellipses. Note that these structures actually do not represent closed vortex rings. The part closer to the vertical centerline is of a lower maximum vorticity and represents the tip of the tongue-like extended region as seen in Fig. 5, while the outer vorticity regions actually represent the cut through the head of the hairpin-vortices. Recognize also the strong coherence of left-right alternation which demonstrates the near periodic creation and discharge of the vortices. Therefore, the vertical coordinate in Fig. 6a can be interpreted either as the time coordinate or alternatively as the

vertical coordinate in a frozen picture of the wake. A rough sketch of the skeleton of the vortex structures in such a frozen picture is displayed in Fig. 8a on the right-hand side beneath the vorticity reconstruction. The sketch indicates the location and orientation of the head-loops of the hairpin-vortices, consistent with the reconstruction pattern. This allowed us to recognize the wake as a chain of oppositely-oriented hairpin-vortices (the connection between the hairpins is as yet not clear). However, self-induction effects will disintegrate the coherence further downstream leading to more complex vortex patterns in the far wake. In conclusion, these quantitative results clearly confirm that the wake of bubbles within this range of Reynolds numbers consists of a chain of vortex loops with alternate circulation and orientation.

Collisions were observed exclusively after wake capture (this is in agreement with the findings of Fan and Tsuchiya, and Stewart) as also seen in the presented results. The trailing bubble is first captured in the wake and thereafter accelerates until it collides with the leading bubble. Fig. 6b shows the vertical coordinates of both bubbles over the recording period. Note, that the rise velocity of the bubbles is reduced by the imposed counterflow velocity. The motion of the trailing bubble - which was initially zigzagging - is strongly influenced by the wake of the leader while the leader bubble remains nearly unaffected until shortly before collision. A two-fold capturing event of the trailing bubble into the wake of the leading bubble occurs in the recorded period (in the time span $0.25s < t < 0.32s$ and $0.5s < t < 0.7s$ in Fig. 6b). The trailing bubble is initially 1 cm further downstream on the right-hand side of the leading one and shows an irregular zigzagging motion with an oscillation amplitude of 0.5 cm (the bubble's coordinates in the horizontal plane are not displayed here). At the moment when $t \approx 0.26s$ (marked as 'A' in Fig. 6b) the bubble is suddenly accelerated in vertical direction and approaches in a progressive curve the bubble ahead within a distance of 0.5 cm. During the approach, the bubble orientates strongly towards the vertical plane. However, the bubble is once again repelled (marked as 'A*'). A moment later, the bubble is captured for the second time in the wake of the leading one when $t \approx 0.5s$ (marked as 'B') and then collides with the leading bubble when $t \approx 0.7s$ (marked as 'C'). Both bubbles are then pushed apart from each other within a sideward distance of 1.5 cm, in nearly the same vertical position. After this collision event they once again re-establish their individual path oscillation.

Correlating the bubble interaction and the wake flow field is possible by comparing the characteristic events in the vertical coordinates of both bubbles in Fig. 6b, and the corresponding flow field in Fig. 6a. Note that due to the change of position of the trailing bubble relative to the leading bubble, the time marks of these events in Fig. 6b cannot be exactly transferred to the time scale in Fig. 6a, as the reconstruction reflects only the location 1 cm downstream of the leader bubble. Therefore, an additional shift in the positive time axis is necessary if the trailing bubble approaches the leader. At the moment of wake capture initiation, the smaller trailing bubble is located at the right-hand side of the leading bubble, as indicated by an arrow in the sketch in Fig. 6a, at mark 'A' or mark 'B'. The arrows at mark 'A' and 'B' indicate the direction of the flow field induced by the hairpin-vortex ahead at these moments. It is suggested that the horizontally in-

wards induced flow component is responsible for the trailing bubble being driven from the side into the wake. It seems that the necessary conditions for wake capture to take place are, on one hand, that the bubbles are within a critical distance at a particular moment and, on the other hand, that the trailing bubble is then at the right place with respect to the induced flow field in the wake of the leader.

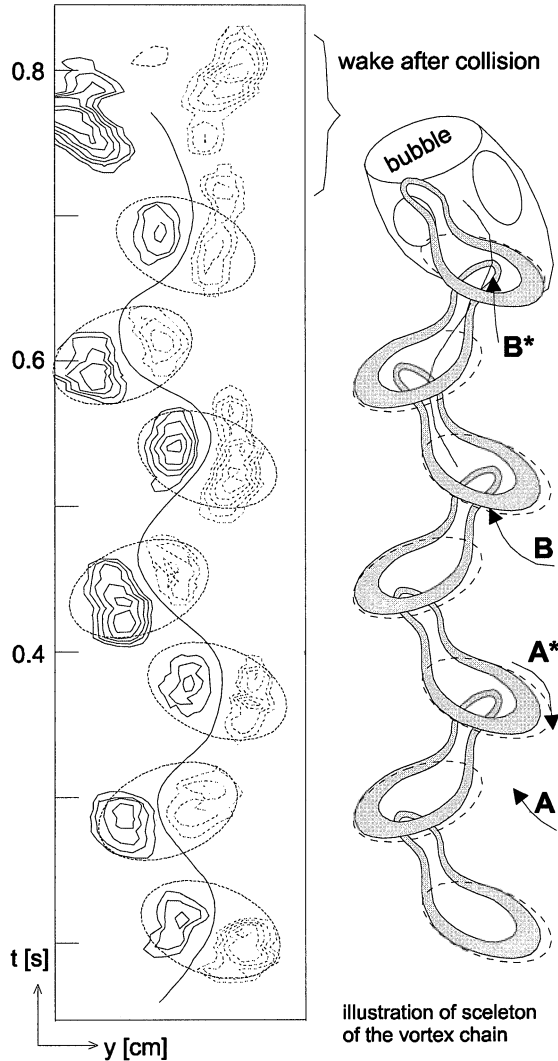


Fig. 6a. Spatio-temporal reconstruction of the distribution of circumferential vorticity 1 cm downstream of the bubble over a period of 3 rocking cycles until the moment of collision

In the first wake capture cycle ($0.26s < t < 0.32s$) the trailing bubble is captured at 'A' from the side, into the wake and is attracted to a distance very close to the leader. However, the immediate following release of the head of the next hairpin-vortex from the right-hand side from the bubble ahead seems to be the reason for the bubble being repelled again, marked here as 'A*'. The second capture process shows two successive "jumps" of the trailing bubble until it collides with the leader. The bubble motion in the vertical plane is not continuous, but the bubble is alternately accelerated ($t > 0.5s$), decelerated ($t > 0.55s$) and accelerated again ($t > 0.6s$). Careful inspection of the shedding cycle in the wake of the leader by means of Fig. 6a reveals that the acceleration and deceleration phase of the trailing bubble is coupled in time to the passing of the head of a shed hairpin-vortex. If one considers a propelling vortex ring as a simplified structure of the head-loop of the hairpin-vortex, the flow on the axis would be accelerated in front of the approaching vortex ring and decelerated behind it, and this would explain the observed bubble behavior.

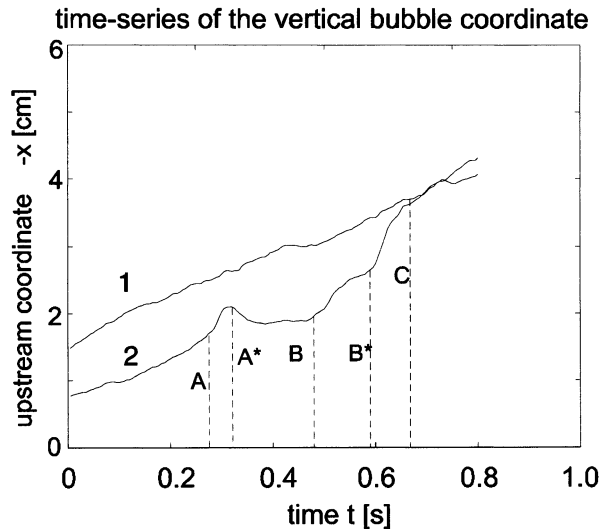


Fig. 6b. Rise pattern of the two interacting bubbles within the counter-flow.

In addition, depending on how far the trailing bubble has been attracted to the center of the wake, the passing by of the next hairpin-vortex either accelerates or decelerates the bubble again. This is due to the change of the induced flow field at the right-hand side of the vortex chain from where the trailing bubble approaches the wake. The induced velocity at the considered location varies with the alternate orientation and zigzag arrangement of the hairpin-vortices. However, in the second capture cycle, the first "jump" at 'B' brings the bubble directly into the inner region of the still attached vortex-structure at 'B*', so that it is accelerated immediately into the attached wake and is not repelled as in case 'A*'. This illustrates how the trailing bubble can "jump" from one hairpin-vortex to the next, and is

therein continuously accelerated (this is seen in the profile of the vertical coordinate which shows a steeper slope in the second jump in comparison to the first). The final approach velocity relative to the leader is about 10 cm/s. Interestingly, the collision and repulsion of the bubbles thereafter leads to a considerable blow-up of the wake region for a short moment (see the top region in the reconstruction in Fig. 6a) which indicates the amplification of turbulent energy production by the collision process.

Discussion and Conclusions

The present study was undertaken with the objective of a more detailed quantitative analysis of the evolution of the flow field in the wake of bubbles and its correlation to shape and path oscillations. Another focus of investigation, closely related to the wake, was the mechanism of wake-driven interaction between bubbles under these conditions. The results for a single zigzagging bubble clearly showed a pair of counter-rotating streamwise vortices within the near wake which is alternately generated on opposite sides of the bubble with alternate circulation. The motion and deformation of the bubble is strongly correlated with the generation of these vortices. As a result, the motion of the bubble in the horizontal plane was always in the direction opposite to the induced velocity between the vortices. Supplementary measurements in the vertical plane corroborate that the overall shape of the generated vortices resembles a hairpin-like structure as observed from flow visualization experiments by Yabe & Kunii (1978). The legs are represented by the measured centers of streamwise vorticity in the cross-section and the head is seen by the circular vorticity segment being shed in the vertical plane from the outer edge of the bubble.

In addition to the influence of the wake on the path instabilities, the wake dynamics was found to play a major role in bubble-bubble interaction. These interactions of zigzagging and rocking bubbles in our experiments exclusively occurred between a leading bubble and a trailing bubble, the later been captured in the wake by several 'jumps' of 2-3 diameters of vertical distance. These 'jumps' could be related to the periodic shedding of the hairpin-vortices in the wake of the bubble ahead and the induced strong upwards flow in the inner center. During this period the bubble motion in the vertical plane is not continuous as the bubble is alternately accelerated and decelerated in response to the passing of the head-loops of the hairpin-vortices. Overall, the results demonstrate that the shedding of vortices in the wake of bubbles trigger the probability of collision. These observations could possibly help to develop a more accurate statistical model of bubble interaction in multiphase flows. In addition, the collision process was found to amplify the turbulent energy production which is another important aspect, not included in cloud dynamics models based on potential flow interactions.

Acknowledgements

The authors gratefully acknowledge the support of the DFG in the Focus-Research-Program "Analyse, Modellierung und Berechnung mehrphasiger Strömungen", Kr 387/35.

References

Clift, R., Grace J.R. and Weber E., "Bubbles, drops and particles," Academic Press, New York, (1978).

Maxworthy T., Gnann C., Kurten M. and Durst F., "Experiments on the rise of air bubbles in clean viscous liquids," J. Fluid Mech. 321, 421 – 441 (1996).

Lunde K., Perkins R.J., "Shape oscillations of rising bubbles," Applied Sci. Res. 58, 387-408 (1998).

Hirsch, P., "Über die Bewegung von Kugeln in ruhenden Flüssigkeiten," Z. Angew. Math. Mech. 3, 93 (1923).

Saffman, P.G., "On the rise of small air bubbles in water," J. Fluid Mech. 1, 249 – 275 (1956).

Fan L.S. and Tsuchiya K., "Bubble wake dynamics in liquids and liquid-solid suspensions," In Butterworths-Heinemann Ser. in Chem. Eng., Butterworths, Boston, (1990).

Stewart C. W., "Bubble interaction in low-viscosity fluids," Int. J. Multiphase Flows 21(6), 1037-1046 (1995).

Yabe K. and Kunii D., "Dispersion of molecules diffusing from a gas bubble into a liquid," Int. Chem. Eng. 18, 666-671 (1978).

Brücker, Ch, "Structure and dynamics of the wake of bubbles and its relevance for bubble interaction," Physics of Fluids 11 (7), 1781-1796 (1999).

Dynamics of the Flow in Bubble Column Reactors

S. Godo, K. Junghans, A. Lapin¹, A. Lübbert²

Institut für Bioengineering, Martin-Luther-Universität Halle-Wittenberg

Abstract:

Bubble columns are modelled by means of an Euler-Lagrange-type model based on the Navier-Stokes equation system. It is shown that the model can not only be used to describe typical situations in the bubble column flow but also to explain atypical operational modes. Model parameters that cannot yet be determined to sufficient accuracy with well accepted theories, e.g. the apparent viscosity of the turbulently flowing dispersion or the bubble path dispersion coefficient were determined by fitting the model to experimental data. The parameter values determined in this way for one flow mode of the bubble column are shown to be applicable for modelling the other flow modes considered as well. The modelling results were validated by measurement data.

Introduction

Bubble columns are used in chemical and biochemical industries for reactions in which species dissolved within a continuous liquid phase are converted with components that are continuously supplied in form of a gas. Typical are halogenation- and oxidation reactions. In biotechnology, these reactors are important for large-scale aerobic fermentations, where the supply of microorganisms with oxygen is of primary importance. Bubble columns outperform the standard stirred tank reactors where the energetic efficiency of the mass transfer is of decisive importance provided the mass transfer requirements can be covered. In industrial practice, bubble columns are thus used for cheap mass products, e.g., baker's yeast production, or for biological waste water treatment, to name just two important applications.

In order to optimize big production processes, full reactor models are desirable. However, up to now a very small number of realistic models is available. This paper summarises a series of investigations performed in order to improve dynamic modelling of bubble column reactors. It also reports about the corresponding model validation with experimental data.

¹ Current adress: Institut für Bioverfahrenstechnik, Universität Stuttgart.

² Corresponding author: Andreas.Luebbert@iw.uni-halle.de

Numerical Approach

Full reactor models are generally based on mass, momentum and energy balances. When we first focus on the velocity pattern $\mathbf{u}(\mathbf{r},t)$, which dominates the transport properties, particularly mixing of the species in the bioreactor, it is straightforward to use the extended Navier-Stokes equation system, i.e., the continuity equation:

$$\frac{\partial \rho}{\partial t} = \frac{\partial}{\partial \mathbf{r}}(\rho \mathbf{u}) \quad (1)$$

and the momentum balance:

$$\frac{\partial(\rho \mathbf{u})}{\partial t} + \frac{\partial}{\partial \mathbf{r}}(\rho \mathbf{u} \mathbf{u}) = - \frac{\partial}{\partial \mathbf{r}}(p) + \frac{\partial}{\partial \mathbf{r}}(\mathbf{T}) + \rho \mathbf{g} \quad (2)$$

where \mathbf{T} is the stress tensor, in components defined as

$$T_{ij} = \mu_{eff} \left(\frac{\partial u_i}{\partial x_j} + \frac{\partial u_j}{\partial x_i} - \frac{2}{3} \delta_{ij} \frac{\partial u_n}{\partial x_n} \right) \quad (3)$$

Although of simple structure, these equations are difficult to solve to a sufficient accuracy with practically relevant initial and boundary conditions. With respect to the boundary conditions, bubble column reactors are the most simple gas-liquid reactors, hence, computational fluid dynamic approaches are most easy to handle for this reactor type. Solutions of the Navier-Stokes equation system, considering technically relevant initial and boundary conditions were developed by Lapin and Lübbert (1994), Sokolichin et al. (1997), as well as by Lapin et al. (2001, 2002).

Relative to the size of the numerical grid elements achievable in current 3D computational fluid dynamics studies, the mean bubble size in real dispersions is very small. Hence, Lapin and Lübbert (1994) considered the fluid in large bubble columns as a quasi-single-phase fluid with variable fluid density $\rho(\mathbf{r},t)$. In this case, the density is primarily dependent on the local gas hold-up $\varepsilon(\mathbf{r},t)$.

There are three essential quantities in these equations, which vary both, spatially and temporally. These are the effective fluid density $\rho(\mathbf{r},t)$, the apparent viscosity $\mu_{eff}(\mathbf{r},t)$, and the local pressure $p(\mathbf{r},t)$.

In order to accurately determine the local variations of the fluid density ρ , the local gas-holdup ε is determined by following the individual bubbles or bubble clusters through this dispersion. The apparent viscosity μ_{eff} is much more difficult to describe, as it depends on the fluid dynamic state of the reactor, particularly on

the local energy dissipation rate. Finally, the local pressure p is not only dependent on the liquid height (static pressure), but especially on the local fluid flow conditions.

The bubbles are considered to move at a velocity \mathbf{u}_{slip} relative to the surrounding liquid, which is flowing with the velocity \mathbf{u}_l . Their motion is assumed to be drawn by pressure gradients ∇p and decelerated by their flow resistances. These effects are taken into account in the following equation of motion (Lapin et al. 2001):

$$c_{vm}\rho_L \frac{d\mathbf{u}_{slip}}{dt} = -\nabla p - c_d\mathbf{u}_{slip} \quad (4)$$

where c_{vm} is the virtual mass coefficient. According to Schwarz and Turner (1988), the flow resistance force is proportional to the slip velocity, c_d is the corresponding drag coefficient.

One point which proved to be necessary to improve the simple model for the bubble motion was to consider additional random fluctuation of the bubble motion, which physically is due to bubble wake effects and interactions between the bubble and eddies of smaller scales, not yet considered in the computations. This was done by means of an additional submodel for the i -th Cartesian component of the positions $\mathbf{r}^{(b)}$ of the bubbles at time t (Sokolichin et al. 1997):

$$r_i^{(b)}(t) = r_i^{(b)}(t) + \text{ran} \sqrt{2D_b\Delta t} \quad (5)$$

where ran is a random number taken from the interval $[0, 1]$, Δt the time increment in the computations, and D_b a “bubble path dispersion coefficient”.

The bubble velocity \mathbf{u}_b , measured in the laboratory coordinate system, is simply related to these two velocity values by

$$\mathbf{u}_b = \mathbf{u}_l + \mathbf{u}_{slip} \quad (6)$$

Even with the coarse resolutions to which fluid flow simulation are currently restricted (about half a million points on the numerical grids) these fluid dynamical calculations involve several million unknowns and solutions take days of turn-around-times on available workstations.

In order to correctly consider the concentrations of the gaseous components dissolved in the liquid phase, the simulation also considers the gas-liquid mass transfer. Typically, the mass transfer resistances are assumed to be exclusively on the liquid-side, in the boundary layers around the bubbles. In the simulations, the mass m of gas (e.g., oxygen) transferred per unit of time into the continuous liquid phase is modeled by

$$\frac{dm}{dt} = k_L A (C_g^* - C_g) \quad (7)$$

where k_L is the mass transfer constant, A is the interfacial area and $(C_g^* - C_g)$ the driving concentration difference, i.e. the difference between the solubility C_g^* assumed at the physical interface and the local concentration C_g dissolved in the liquid bulk. Since we are dealing with a slow chemical reaction, the influence of the consumption of gas on the mass transfer coefficient can be neglected.

The change of concentration of the dissolved gas in the liquid bulk with time is described by:

$$\frac{\partial C_g}{\partial t} + (\mathbf{u} \nabla) C_g = D_{eff} \Delta C_g - S_C + S_{mt} \quad (8)$$

Besides the diffusive and convectional transport of the dissolved gas within the liquid, a source (S_{mt}) and a consumption term (S_C) have to be considered in this equation. According to general similarity assumptions, the effective diffusivity, effective viscosity and effective temperature conductivity were assumed to be linear functions of the gas-holdup and are practically equal to each other. The gas consumption takes place during the chemical reaction. It is described by a kinetic expression of the form:

$$S_C \sim C_g^a C_e^b f(T) \quad (9)$$

where C_e is the concentration of the liquid educt. The exponents a and b as well as the parameters of $f(T)$, an Arrhenius term, were known beforehand. The source term corresponds to the mass transfer rate:

$$S_{mt} \sim k_L A (C_g^* - C_g) \quad (10)$$

Mixing in the liquid phase is also of importance for the liquid educt. This is treated in roughly the same way as the mixing of the dissolved gas, the essential difference being that there is no mass transfer term.

$$\frac{\partial C_e}{\partial t} + (\mathbf{u} \nabla) C_e = D_{eff} \Delta C_e - S_C \quad (11)$$

The corresponding consumption rate is of course apart from the stoichiometric constants the same as discussed before for the dissolved gas.

Reactions we are usually considering in bioreactors produce heat which is being removed via the heat exchanger jackets. The energy balance used to model the temperature behavior of the dispersion is:

$$\frac{\partial T}{\partial t} + (\mathbf{u} \nabla) T = K_{eff} \Delta T + S_T \quad (12)$$

where K_{eff} is the effective temperature conductivity. The source term, the heat production rate, is considered proportional to the chemical reaction rate:

$$S_T \sim S_C \quad (13)$$

In addition, the heat transfer as well as the subsequent temperature increase within the cooling jackets are considered.

A typical result from such calculations for a pilot-scale bubble column yeast fermenter (1 m diameter) is shown in Figure 1. The graphs on the left show snapshots of the velocity vector field and the dissolved oxygen concentration (Lapin and Lübbert 2000). The latter was determined for an actively growing yeast culti-

vation. The flow is computed in three dimensions Obviously, the flow patterns on single planes can be shown only. Here they are depicted in a plane through the axis of the reactor. Both patterns, the velocity and the dissolved oxygen concentration patterns change steadily with time, even if the reactor is in a quasi-stationary state.

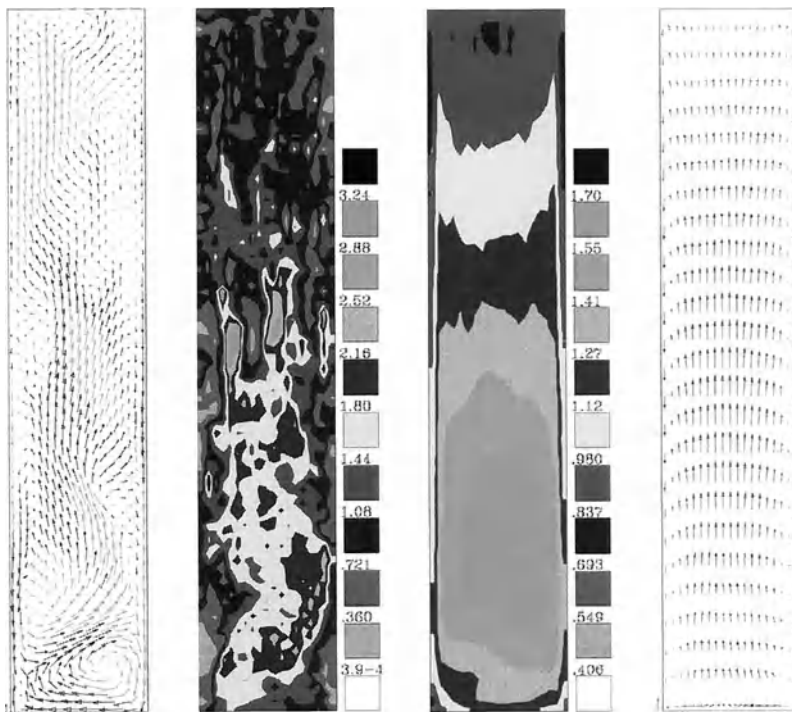


Figure 1: Typical results of a CFD simulation of a pilot-scale bubble column reactor for yeast cultivation with 1 m column diameter. The arrows in the left graph depict flow velocity vectors taken from a snapshot of the dynamically varying velocity pattern. The plot to its right shows the corresponding dissolved oxygen concentrations. The plots on the right show the corresponding long time averaged profiles (taken from Lapin and Lübbert 1999).

It is evident from such a snapshot representation of the fluid velocity pattern that the flow pattern is characterized by randomly distributed eddies, as expected for turbulent flows. The transient pattern of the dissolved oxygen distribution also exhibits a chaotic character. In reality, in such a reactor, a uniform oxygen distribution is never achieved under realistic input and boundary conditions.

In order to become sure that the computations are correct, such transient computational results with time increments of 0.5 s were averaged over real time intervals of 30 minutes.

On the right hand side of Figure 1, long-term averages over the two transient profiles are shown. The averaged flow velocities (shown on the rightmost graph in Figure 1.) are typical of the profiles commonly presented in the textbook literature (e.g., Doran 1997). The time-averaged concentration data show pronounced oxygen concentration profiles in both axial and in radial directions, consistent with experimental data, which are also time averages. With respect to bioreactor performance optimization, this point is particularly worth noting: the vessel content is inhomogeneous with respect to oxygen concentration.

Hydrodynamic calculations in three dimensions are extremely time-consuming even on the fastest computers available. However, it is essential to note that two-dimensional calculations, which are much less time consuming, do not provide sufficiently accurate approximations, since turbulence is a truly three-dimensional flow phenomenon. Recently, Sokolichin and Eigenberger (1999) showed a comparison of two- and three-dimensional calculations with experimental data giving additional evidence to this well known fact.

Identification of the model parameters

Fluid dynamical models as chemical and biochemical process models in general can not yet be established from first principles alone. Hence some of the model parameters must be obtained from measurement data. As the decisive model parameters, such as the apparent viscosity μ or the bubble path dispersion coefficient D , cannot be measured directly, they must be obtained by fitting the model to measurable variable patterns.

For the fluid dynamical part of the reactor model, predominantly fluid flow velocity measurements are needed. Two fundamental problems appear in this respect. First, at practically relevant superficial gas velocities, the flow velocities in the dispersion are chaotically fluctuating. Second, at relevant gas throughputs, the gas hold-up is rather high, so that liquid flow velocities are very difficult to determine in pilot or production-scale bubble columns.

Bubble velocity distributions, however, can be measured at single points with the ultrasound-Doppler-anemometer (Bröring et al. 1994). As bubble velocities and their modelled values considerably fluctuate with time, it is only possible to compare long-time averages. In the particular case reported, an averaging time of 15 minutes proved to be required to obtain reproducible results.

The particular case which was considered for parameter identification was a pilot scale bubble column of 30 cm diameter and 5 m height, aerated with sparger consisting of a rubber plate into which holes were drilled with a 0.5 mm drill bit in a regular scheme covering the entire bottom of the column. The bubble column allowed measurements of radial profiles of the mean bubble velocities at heights of 75, 125, and 175 cm above the sparger.

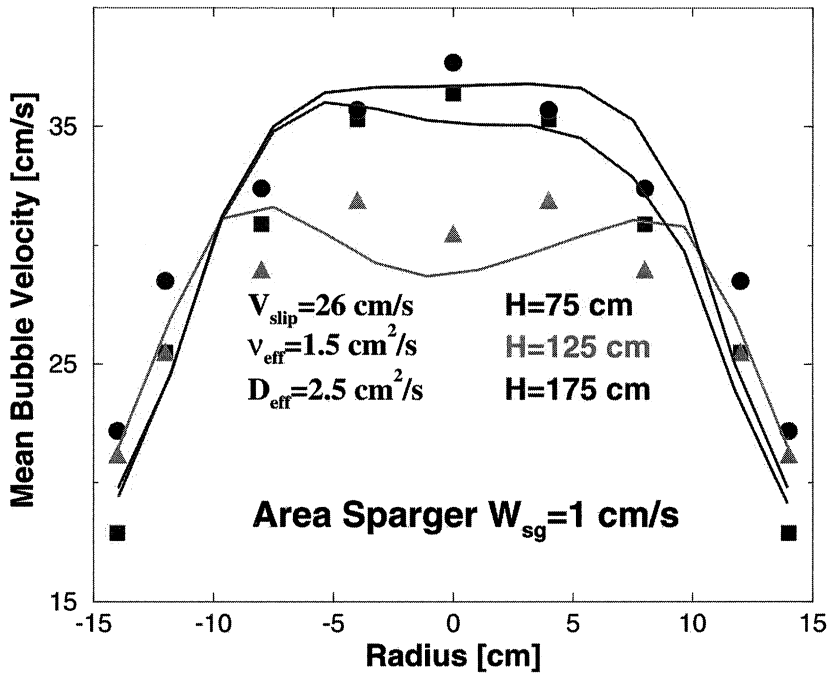


Figure 2: Radial bubble velocity profiles measured (symbols) in and computed (lines) for a bubble column aerated with an aerator covering the entire bottom of the bubble column. The column was operated at a superficial gas velocity of 1 cm/s. Measurements were performed at three different heights indicated with the symbols.

The corresponding results are shown in Figure 2. The computed profiles follow the measurement results fairly well. The parameters in the model varied in the course of the identification were apparent viscosity μ_{eff} , slip velocity of the bubbles v_{slip} , and the bubble path dispersion coefficient D_b . The values obtained were:

$$\begin{aligned}
 \mu_{eff} &= 1.5 \quad [\text{cm}^2/\text{s}] \\
 u_{slip} &= 26 \quad [\text{cm}/\text{s}] \\
 D_b &= 2.5 \quad [\text{cm}^2/\text{s}]
 \end{aligned}$$

All these parameters were considered constant across the entire reactor.

Validation measurements

Models receive their credibility by validation against measurement data from the processes under consideration. In the sense of cross validation only those data can be used for that purpose that have not been used for model identification. Needless to say that the model must be able to describe the same process under slightly different operational conditions.

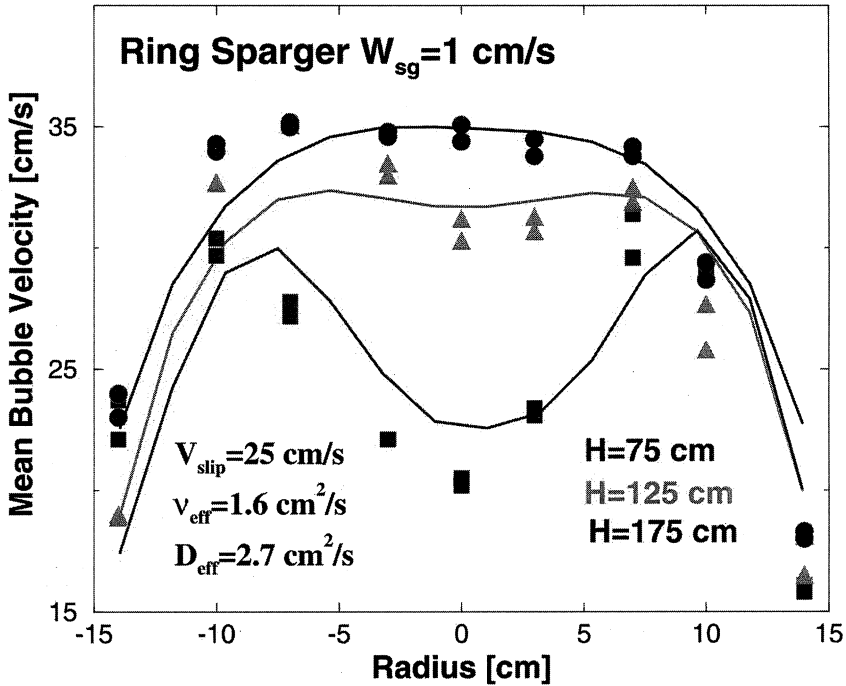


Figure 3: Radial bubble velocity profiles measured at three different heights above the sparger of the bubble column (symbols) together with the corresponding computational results (lines). The measurements were performed twice at each point.

To obtain validation measurement results, the pilot-scale bubble column was operated with a large-diameter ring sparger, i.e. a sparger with a diameter shortly below the column diameter.

The fit of the model to these data resulted in practically the same parameter values as obtained for the bubble column aerated with aeration of the entire bottom. The results are shown in Figure 3. Again, the agreement between measure-

ment and computation is fairly good. Hence we can assume that the model is able to describe this situation as well, a fact that supports the validity of the model.

Flow within tilted bubble columns

Point measurements of mean liquid velocities in gas-liquid two-phase flows are difficult as the liquid velocity is not defined if the measurement point is covered by a gas bubble. As it is not possible with most of the measurement devices to make use of the measurement values they deliver when the sensors are within bubbles, the entire signal cannot just be averaged to obtain a reliable value for the liquid velocity within the dispersion. Early investigators tried to solve that problem by numerically processing the data records. They developed algorithms that detect segments within the records that are due to bubble influences and removed them numerically. This is a cumbersome method particularly with signals measured in turbulent flows, where it is not easy to detect bubble influences in the anemometer signals. Thus, an alternative technique was developed in the project reported here.

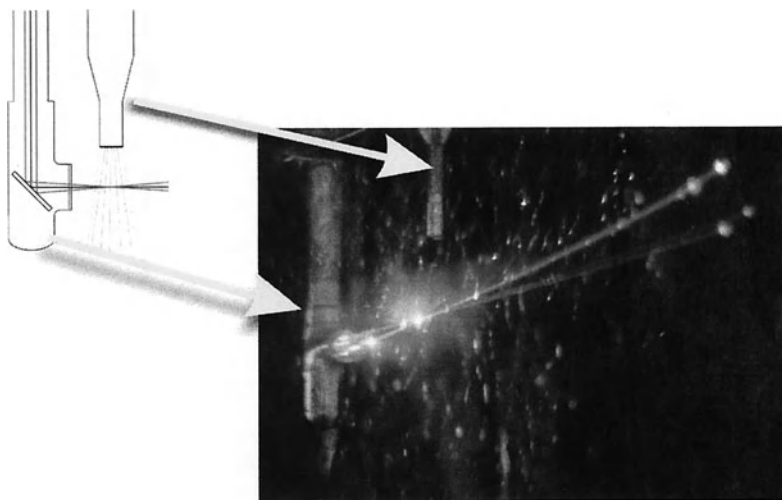


Figure 4: Measurement set-up combining laser Doppler anemometry with ultrasound Doppler anemometry in order to measure both mean liquid and mean bubble velocity distributions simultaneously at the same measurement point.

As the ultrasound Doppler technique already used to measure local bubble velocity distributions proved to reliably detect bubbles, it was combined with a laser Doppler anemometer (LDA). The measurement volume of the ultrasound Doppler was chosen in such a way that it completely covered the smaller measurement volume of the LDA. Every time the ultrasound device detects a bubble, it electronically switches the signal from the LDA to zero. In this way it was possible to

measure the mean liquid velocity more reliably. The entire measurement set up is sketched in Figure 4.

With this measurement arrangement, another feature of bubble columns was investigated, namely the influence of a small misalignment of bubble columns on their flow pattern. For this purpose a bubble column of 40 cm diameter and 3 m height, aerated with a sparger, the holes of which covered the entire bottom, was tilted by 1 degree against the vertical. The other operational conditions were the same as for the examples discussed before.

In order to characterize the dispersion, liquid velocity profiles were measured with the combination of a LDA and an UDA. Measurements were performed at different heights and with different orientations with respect to the plane within which the column was inclined. The results are shown in Figure 5.

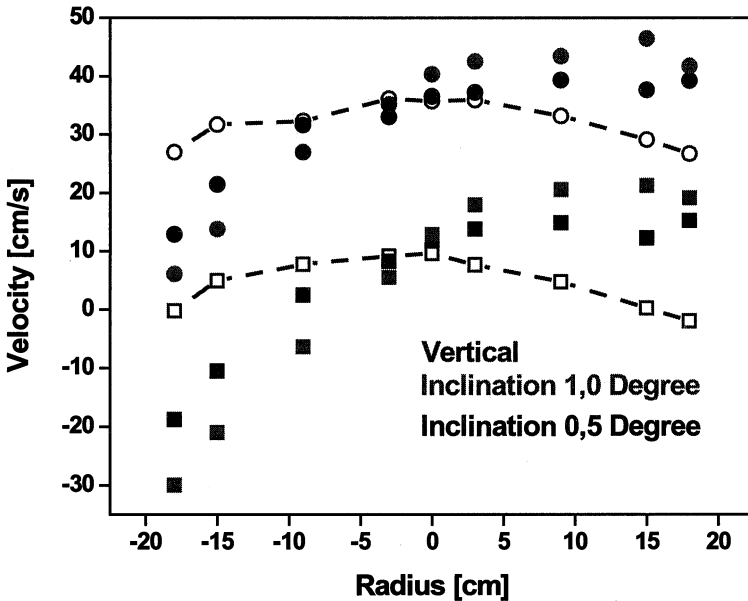


Figure 5: Mean liquid velocity profiles in a bubble column tilted against the vertical by 0.5 and 1.0 degrees. The measurement points connected by the dashed lines were measured in the direction perpendicular to the other one, showing that these profile remain symmetrical with respect to the column axis. The measurements were performed at 1 cm/s superficial gas velocity.

The results in Figure 5 show that the mean velocity profiles are drastically changing with the misalignment even at very small angles of the tilt against the vertical.

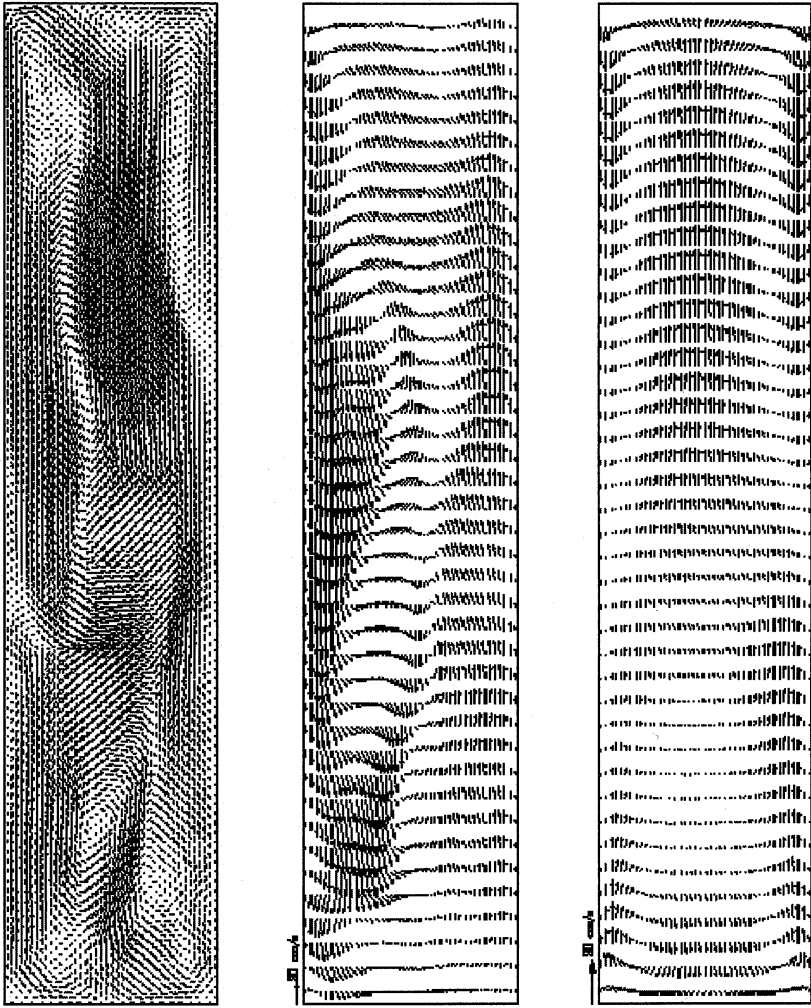


Figure 6: Velocity patterns in a bubble column tilted by 1 degree. The left graph shows a transient velocity patterns resolving large scale eddies within the column, the graph in the middle and to the right hand side depict long time averages, averaged over 25 min real time.

Qualitatively the same effect was observed at different heights above the sparger, although the deviations from the symmetric profiles observed with a correctly aligned column are different at different heights.

The patterns computed with the software used for the examples already discussed reveal the decisive change as compared with the vertically aligned column (Figure 1 and 6). Although the transient patterns again depict a chaotic eddy motion that cannot easily be distinguished from the one obtained for the vertical column, the long-time averages show a completely different flow mode. Instead of the mode observed with a vertical column, a circulation flow appears that, in the plane within which the column is turned, rises on one side of the column and comes down at the wall on the other side. In the perpendicular plane, the flow profiles remain essentially symmetric as shown in the graph on the right side in Figure 6.

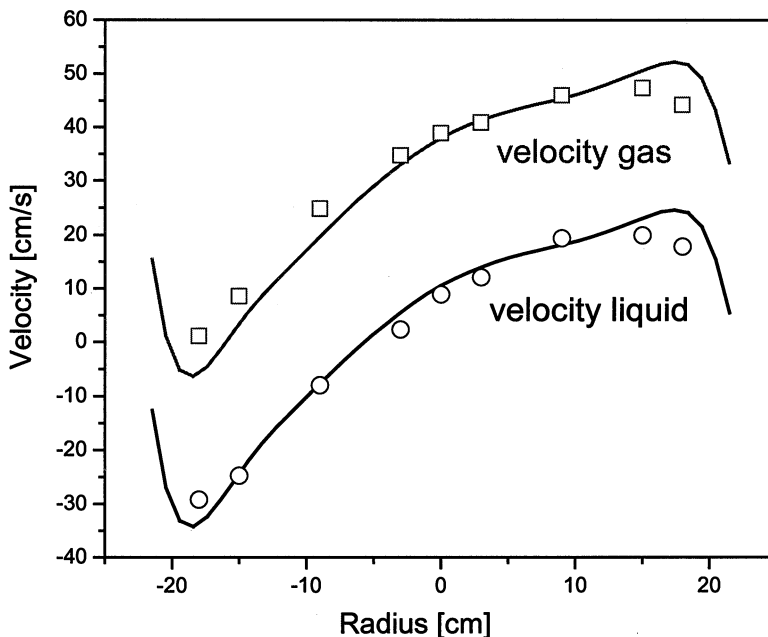


Figure 7: Comparison between computation (lines) and measurement (symbols) results for a bubble column tilted by 1 degree against the vertical. Two quantities were measured: (i) the mean vertical bubble velocity and (ii) the mean vertical liquid velocity.

Again, the computations match the measurement values fairly well as shown in Figure 7. With respect to the computations, the most important point to mention is that the parameters used for the computations were the same as those used for the examples discussed before. Hence, this investigation can be viewed as another validation measure for the computational fluid dynamical model used.

Conclusions

Two-phase gas-liquid flows in bubble columns can fairly well be described and simulated with models based on the Navier-Stokes equation system. As shown in this article, the Euler-Lagrange representation of such a fluid flow model is able to capture some main features of the two-phase gas-liquid flow in the so-called large eddy approximation. The parameters of such models, which are influenced by the flow behaviour on the smaller scales that can not yet be considered in such flow simulations can be obtained by fitting the model to measurement data. The critical parameters are particularly the apparent viscosity of the fluid, the bubble slip velocity and the bubble path dispersion.

As it will not be possible in the near future to perform computations for industrial-scale bubble columns or airlift reactors on a sufficiently fine scale that can consider all fluid flow motions, it is strongly recommended to generally determine these parameters by fitting the model to measurement data. The investigation performed here and in Lapin et al. (2000, 2001) showed that this leads to a good description of the overall behaviour of bubble columns even in the case of chemical reactions taking place in these reactors.

It was shown that this model is not only able to describe standard situations of the flow in bubble columns but also some higher order effects such as aeration with unconventional sparger designs or the flows in not perfectly aligned bubble columns. All the results could be cross-validated with additional measurement data, not used during the identification of the model parameters.

Acknowledgements

We gratefully acknowledge the financial support of the Deutsche Forschungsgemeinschaft (DFG). Numerous discussions and exchanges of data were held with the fluid dynamics group of Professor G. Eigenberger, University of Stuttgart and others taking part in the project.

References

- Lapin, A., Maul, C., Junghans, K., Lübbert, A. (2001), Industrial-scale bubble column reactors: gas-liquid flow and chemical reaction, *Chem.Eng.Sci.*, 56, 239-246
- Sokolichin, A., Eigenberger, G., Lapin, A., Lübbert, A. (1997), Dynamic numerical simulation of gas-liquid two-phase flows: Euler-Euler versus Euler-Lagrange, *Chem.Eng. Sci.*, 52, 611-626
- Lapin, A., Lübbert, A. (1994), Numerical simulation of the dynamics of two-phase gas-liquid flows in bubble columns, *Chem.Eng.Sci.*, 49, 3661-3674

- Lapin, A., Paaschen, T., Junghans, K., Lübbert, A. (2002), Bubble column fluid dynamics: Flow structures in slender columns with large-diameter ring-spargers, Chem.Eng.Sci., 57, 1419-1424
- Sokolichin, A., Eigenberger, G. (1999), Applicability of the standard k-e turbulence model to the dynamic simulation fo bubble columns: Part I: Detailed numerical simulations, Chem.Eng.Sci., 54, 2273-2284

Improved model for the calculation of homogeneous gas-liquid flows

S. Scheid, S. John, O. Bork, H. Parchmann, M. Schlüter, N. Rübiger

Institute of Environmental Process Engineering, University of Bremen

Abstract

The research project presented below gives a detailed explanation of the phenomenon of an increased relative velocity between gas and liquid phase in bubbly flows. It points out the conditions under which classical models for the description of two-phase flows tend to predict higher gas hold-ups than those determined experimentally, and explains the underlying physical relations. The cause for the increased relative velocity is an interactive effect of the bubble wakes on the shapes and trajectories of other bubbles. The experimental facilities of this research project which allowed the simultaneous observation of integral and local effects under a broad range of operating conditions are described in detail.

A model for the calculation of the relative velocity in homogeneous bubbly two-phase flows is presented. It overcomes deficiencies of classical models which do not consider the mutual effects of swarm turbulence, gas hold-up, bubble shape and size on the relative velocity. Based on observations of the shape and trajectories of single bubbles under swarm conditions an extension to the model, which includes further parameters of the liquid phase, is proposed.

Nomenclature

A_L	cross-sectional area of liquid phase	m^2
A_R	cross-sectional area of the reactor	m^2
A_T	cross-sectional area of the de-gassing tank	m^2
C_1, C_2	fitting parameters of the drift flux model	-
d_{eq}	equivalent bubble diameter	m
d_p	seeding particle diameter	μm
f	wake shedding frequency	Hz
h	Liquid height during the experiment	m
h_0	Liquid height at the start of the experiment	m
m, n	exponent to describe flow conditions	-
p	pressure	Pa
T	temperature	$^{\circ}C$

V_R	Reactor volume	m^3
w_B	bubble velocity (local)	$cm\ s^{-1}$
w_G^0	superficial gas velocity	$cm\ s^{-1}$
w_L	liquid velocity (local)	$cm\ s^{-1}$
w_L^0	superficial liquid velocity	$cm\ s^{-1}$
w_{Rel}	relative velocity $w_B - w_L$ (local)	$cm\ s^{-1}$
w_S	single bubble velocity (terminal velocity)	$cm\ s^{-1}$
w_{Slip}	slip velocity (averaged)	$cm\ s^{-1}$
w_{Swarm}	swarm velocity (averaged)	$cm\ s^{-1}$
x	horizontal position	cm
y	vertical position	cm
Θ	inclination of bubble trajectory to vertical	$^\circ$
ε_G	gas hold-up	Vol.-%
ε_P	particle hold-up	Vol.-%
η	viscosity	mPa s
σ	surface tension	mN m^{-1}

Introduction

A detailed knowledge on the behavior of multiphase flows is necessary to satisfy the increasing demand for the computer-aided design of reactors for chemical, food and pharmaceutical industries as well as for biological wastewater treatment. Increasing customer pressure for inexpensive yet highly reliable production facilities forces plant manufacturers to drastically reduce costs. This goal can only be achieved by cutting experimental tests of the plant performance in favor of computer aided simulations, thus requiring very exact numerical descriptions of all processes, including hydrodynamics (CFD).

Most current models for the description of gas-liquid two-phase flows, which is one of the most important subsets of multiphase flows, rely on the behavior of single bubbles under different conditions with empirical corrections which are supposed to account for the effects of flow structures, turbulence effects and boundary layers. Unfortunately, these empirical equations tend to be valid only for limited operating conditions as they are based only on integral parameters, such as superficial gas and liquid velocities, and gas hold-up. An application for a liquid with different properties requires a new set of time-consuming and expensive experiments to determine the empirical parameters. An exact calculation of the behavior of multiphase flows can be achieved by means of direct numerical simulation (DNS) which requires solving the Navier-Stokes-Equations at a very detailed level. The computational power required for DNS limits its application to small-scale local phenomena since complete reactors cannot be simulated within a reasonable period of time.

This project aims at a more general description of the behavior of two-phase flows under typical operating conditions formulated as a model which can be implemented into commercially available CFD-codes.

Current models

In two-phase flows one has to distinguish between two major flow regimes which are characterized mainly by the behavior of the gas bubbles. Consider a flow channel reactor with a given cross sectional area A_R filled with liquid which has a constant superficial velocity w_L^0 . Gas is dispersed at the bottom of the reactor with a superficial velocity w_G^0 resulting in an overall gas hold-up ε_G . Since every bubble transports a volume of liquid in its wake, the resulting transport has to be counteracted by some flow in the opposite direction to ensure the conservation of mass. In the homogeneous flow regime, the gas hold-up is so small that the cross sectional area taken up by the liquid

$$A_L = (1 - \varepsilon_G) \cdot A_R \quad (1)$$

is sufficient for a compensating recirculation for every individual bubble. Consequently, the bubbles exhibit rather continuous, although not necessarily linear, trajectories with very few disturbances. The size of the turbulent vortices in the liquid generated by the phase interaction are in the order of the bubble size.

The behavior of homogeneous two-phase flow regimes is often described by the two-fluid model

$$w_{\text{slip}} = \frac{w_F^0}{1 - \varepsilon_G} \pm \frac{w_G^0}{\varepsilon_G} \quad (2)$$

which is based on integral measurements only. It considers the gaseous and the liquid phases independently and uses one or more empirical parameters to describe the interaction of the phases, for example as

$$w_{\text{swarm}} = w_{\text{slip}} \cdot (1 - \varepsilon_G^m)^n \quad (3)$$

(Richardson and Zaki 1954 with $m=1$, Zehner 1985). In this equation, which was originally derived from the observation of the sedimentation behavior of solid particles, n is assigned different values by various researchers (Richardson and Zaki 1954; Bridge et al. 1964; Davies and Taylor 1966; Wallis 1969; Ishii and Zuber 1979; Zehner 1985 to mention but a few).

With increasing superficial gas velocity w_G^0 , the increasing gas hold-up ε_G reduces the cross sectional area of the liquid to a value smaller than the required space for homogeneous recirculation. As a consequence, bubbles start to cluster and rise together as a loose agglomerate with a lower resistance value since the surrounding liquid flows around the whole rising agglomerate instead of every single bubble. Through this agglomeration of bubbles, the distribution of gas and liquid in any cross sectional area of the reactor becomes very uneven or heterogeneous. The recirculating liquid flows faster past the bubble agglomerates resulting in vortices similar in size to the reactor diameter.

These flow conditions are often described by the drift-flux model

$$\frac{w_G^0}{\varepsilon_G} = C_0 \cdot (w_G^0 + w_L^0) + C_1, \quad (4)$$

based on the two-fluid model, which was presented first by Zuber and Findlay (1965). In this equation the empirical parameters C_0 and C_1 are derived from experiments resulting in several different correlations depending on the experimental apparatus or operating conditions (Zuber and Findlay 1965; Wallis 1969; Clark and Flemmer 1985, Joshi et al. 1990).

Motivation for this research project

Earlier research projects showed a deviation of the slip velocity in different types of gas-liquid reactors (jet-zone loop reactor and jet driven loop reactor) under certain operating conditions (Fig. 1) which were not taken into account by common empirical models. The aim of this project was to investigate the physical reasons for the observed phenomena in order to provide a more detailed description of two-phase flows for the design and layout of reactors with or without the aid of computational fluid dynamics (CFD).

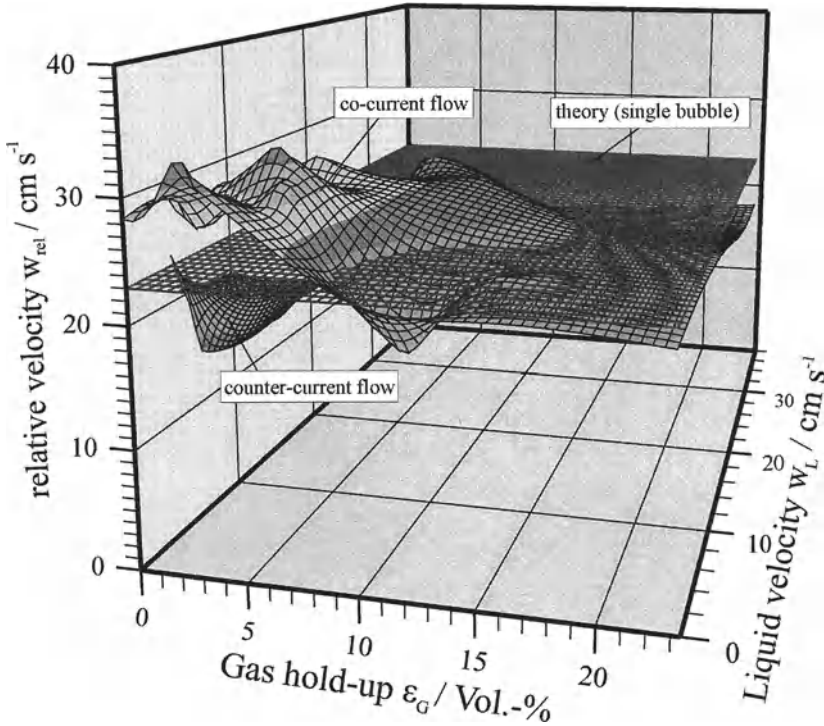


Fig. 1. Experimental results from different two-phase reactors indicating a dependency of the relative velocity on gas hold-up as well as direction and strength of the superficial liquid velocity.

Experimental set-ups

Unit A, the first experimental set-up (Fig. 2), consists of a frequency-controlled centrifugal pump which circulates liquid (usually deionized tap water) through a 4 m-high perspex column with an inner diameter of 190 mm. By means of a set of valves, the speed and direction of the liquid flow can be controlled, allowing the reactor to be operated under co- and counter-current conditions with a superficial liquid velocity up to $w_L^0 = 0.3 \text{ m s}^{-1}$, as well as an airlift reactor or bubble column. At the bottom of the reactor different types of gas spargers, such as sinter plates or rings spargers can be installed in to influence the bubble size distribution. The pressurized oil-free air is fed into the reactor at a superficial velocity $0 \leq w_G^0 \leq 5 \text{ cm s}^{-1}$. In the case of co-current operation the bubbly air-liquid mixture flows to the top of the reactor into the de-gassing tank where the liquid is slowed down sufficiently for all bubbles to be discharged into the atmosphere. The liquid drawn from the de-gassing tank into the pipe leading back to the centrifugal pump is thus virtually free of gas bubbles.

After filling the reactor from the storage tank at the beginning of each experimental run, the liquid level h_0 in the de-gassing tank is measured using the pressure transducer at the bottom of the tank. During the experiment, the displacement of liquid through gas introduced into the flow channel can be measured as an increased liquid height h , and is correlated to the cross sectional area of the de-gassing tank A_T and the reactor volume V_R to calculate the integral gas hold-up

$$\varepsilon_G = \frac{A_T \cdot (h - h_0)}{V_R}. \quad (5)$$

The superficial gas and liquid velocities are measured by means of a gas mass-flowmeter based on hot-film anemometry, and a magneto-inductive flow meter, respectively. During the experimental run the liquid temperature is constant at $T = 20 \pm 1 \text{ }^\circ\text{C}$.

The electro-diffusion measurement technique (EDM, John et al. 1999) was used to measure the liquid velocity in a layer vertical to the probe tip at several positions across the flow channel.

Gas phase parameters such as bubble number density n_B , specific surface a and bubble velocity w_B are measured by ultrasound bubble analysis (UBA, Guder 1997).

While the mentioned intrusive measuring techniques are applied at high gas hold-ups which are consequently inaccessible to visual measurements, a 3D particle-tracking velocimetry (3D-PTV) can be used at low gas hold-ups. To minimize optical distortions from the round perspex tube, it is enclosed into a square perspex casing filled with water, allowing the detailed observation of rising bubbles from two rectangular-oriented CCD-cameras. Using this system the speed, shape and 3D trajectory of individual bubbles within a swarm can be measured at a frequency of up to 200 Hz. The major advantage of the 3D-PTV is the exact analysis of the bubble size, especially when the bubble shape is highly dynamic.

Unit B, the other experimental set-up (Fig. 3), is used to obtain detailed information on local effects in bubble swarms by optical means. Since liquids with higher gas hold-ups are usually inaccessible to visual measurements – due to the high optical density – special care has to be taken to observe single bubbles under conditions similar to those in a bubble swarm.

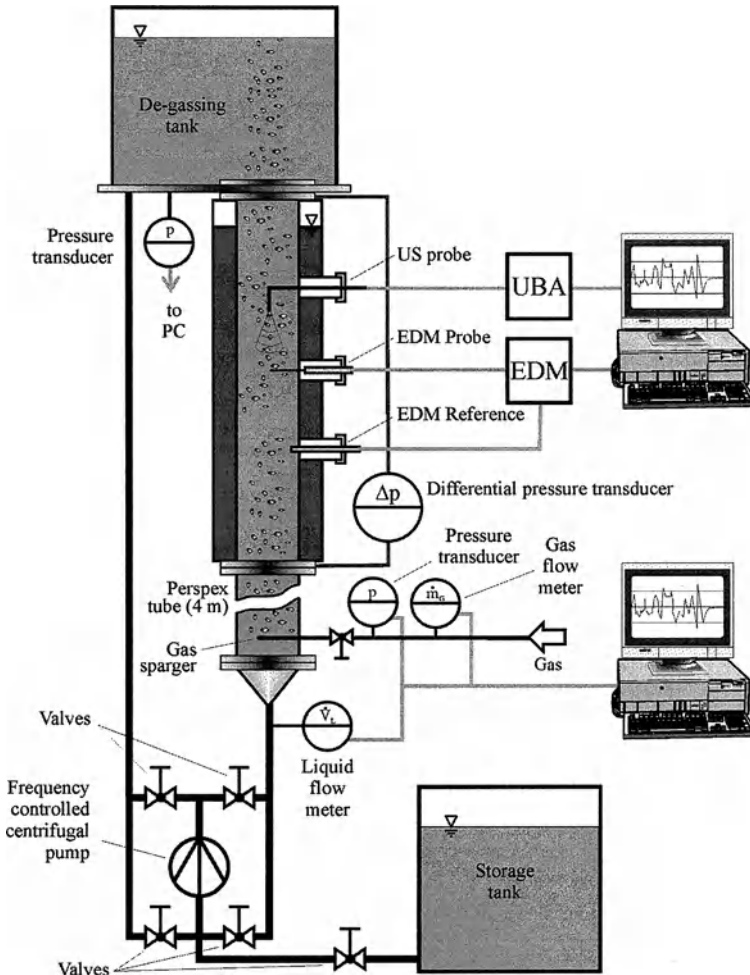


Fig. 2. Unit A: Experimental set-up to examine the correlation between local and integral phenomena

To achieve this, a particle grid (Fig. 4) was built of body-centered cubic, ellipsoidal particles with an equivalent diameter of 9 mm. The application of such a particle arrangement as a model of a bubble swarm was suggested first by Zehner (1985). The particles are arranged in groups of 9 or 16, with a distance of 20 mm in orthogonal, horizontal layers, which is equivalent to a particle hold-up of $\epsilon_p = 11$ Vol.-%. With the aid of thin steel rods, the layers are fixed vertically at a dis-

tance of 18 mm. One layer of particles is left out to allow optical observation of a single bubble moving through the particle grid while at the same time ensuring a homogeneous flow field.

A bypass-controlled centrifugal pump is used to set up a downward flow of up to $w_L^0 = 0.08 \text{ m s}^{-1}$ through the particle grid generating a flow field similar to the conditions found in a particle swarm. Single bubbles are generated by pressurized air – pumped with the aid of a syringe – through a glass capillary mounted below the particle grid. This device provided the means to exactly control the volume of the bubbles, independently of any effects of surface tension.

In a first step, the relationship between the artificially generated bubble swarm flow-field and the bubble motion the flow field in the flow channel, and in the empty horizontal layer of the particle grid respectively, is examined by standard Particle Image Velocimetry (PIV). A vertical light sheet with a thickness of 1 mm is generated by a 7.5 W Ar-Ion laser, and set of mirrors and lenses. The liquid flowing through the particle grid is seeded with tracer particles ($d_p = 10 \mu\text{m}$) with negligible inertia. The position of the particles through the light sheet is captured twice by a PIV camera to calculate a momentary 2D vector flow map from the position offset during the interval between the two photographs. A quasi-static flow map is generated by averaging several individual PIV flow maps. Since the length and direction of the liquid velocity vector at every position of the flow map can be interpolated, it is possible to derive the average local vertical liquid velocity w_L .

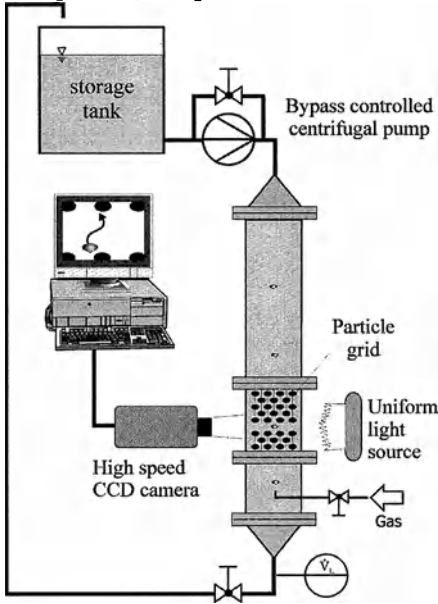


Fig. 3. Unit B: Experimental set-up to examine the correlation between bubble shape and motion and the liquid flow field around it (PIV system not pictured)

In a second step, a single bubble is generated at a glass capillary with the help of a syringe and rises through the flow channel including the particle grid. This method of bubble generation aims at a constant bubble size to avoid unwanted side effects from the surfactant used (Räbiger 1984, Räbiger and Schlüter 2002).

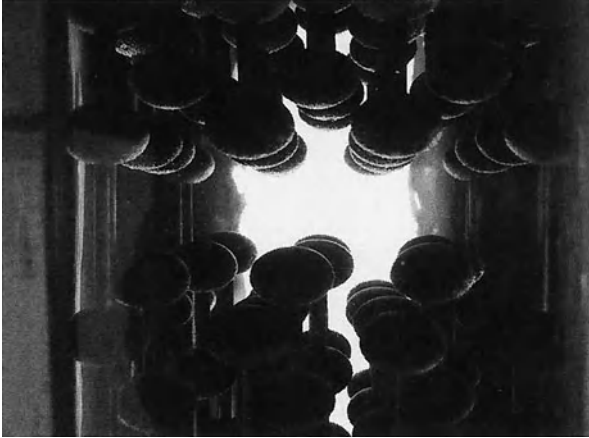


Fig. 4. Photograph of the observation region in the particle grid

The liquid viscosity was not influenced by the addition of surfactant and remained constant at $\eta = 1.02 \pm 0.04$ mPas as control measurements showed. The bubble is photographed by a high speed CCD camera with a 312 x 256 pixel resolution at 500 Hz while fully visible in the particle-free layer (Particle Tracking Velocimetry, PTV). A control camera positioned at a right angle to the optical axis of the high-speed CCD camera is used to verify that the bubble rises in the 2D plane defined by the PIV measurement previously. By means of a calibration beforehand, the exact size as well as the 2D trajectory of the bubble during its residence time in the particle-free layer can be calculated. The momentary vertical speed of the bubble w_B is calculated from the change in position of the center of area of the bubble during the known time interval between two images.

Finally, the local relative velocity

$$w_{\text{Rel}} = w_B - w_L \quad (6)$$

is calculated, which can be averaged with all instantaneous measurements taken during the time of observation of the specific bubble.

Results and discussion

A comparison of dependencies between gas hold-up and superficial gas velocity using different spargers shows the influence of bubble diameter distribution and relative velocity (Fig. 5).

While the sinter plate produces very small bubbles with a narrow diameter distribution, the ring sparger with a 1 mm hole diameter produces larger bubbles with

a broad size distribution. Due to different flow conditions, the transition region between homogeneous and heterogeneous regime changes, as does the dependency between gas hold-up and superficial gas velocity. According to equation 2, this leads to different slopes of the gas hold-up vs. superficial gas velocity curves, which are predicted fairly accurately by the two-fluid model in Eq. 3 (Richardson and Zaki 1954), if the dependency of terminal velocity of single bubbles w_s on bubble diameter d_{eq} is considered as well (thin dashed, and dotted lines in Fig. 6 showing a zoom of the homogeneous region data from Fig. 5).

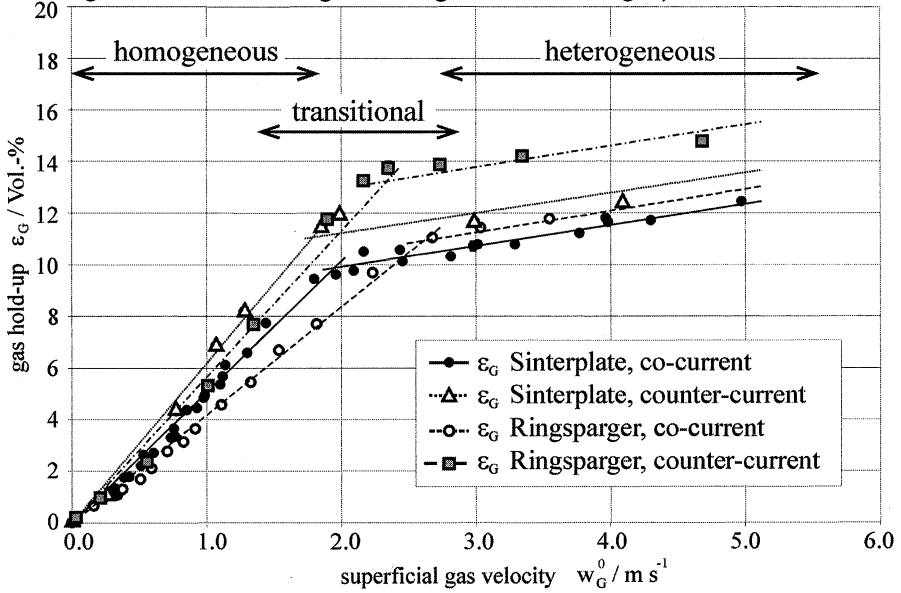


Fig. 5. Comparison of the impact of liquid flow direction and sparger type on gas hold-up

Nevertheless, there is a significant overestimation of gas hold-up in the range of superficial velocities between 0.3 and 1.0 cm s^{-1} by the two-fluid model, under considering the diameter and relative velocity of single bubbles. This phenomenon can be explained by looking at local measurements of relative velocities in homogeneous flow with 3D-PTV for lower gas hold-ups, and EDM/UBA measurements at higher gas hold-ups. The results exhibit a dependency between relative velocity, gas hold-up and liquid velocity as presented before (Schlüter and Rübiger 1998, Schlüter et al. 2001, Schlüter 2002).

Influences on momentum transfer due to bubble wakes force bubbles in swarms onto more narrow helical trajectories than single bubbles, and cause deviations in relative velocity as a function of gas hold-up, which can be calculated by a recently developed model (Schlüter 2002).

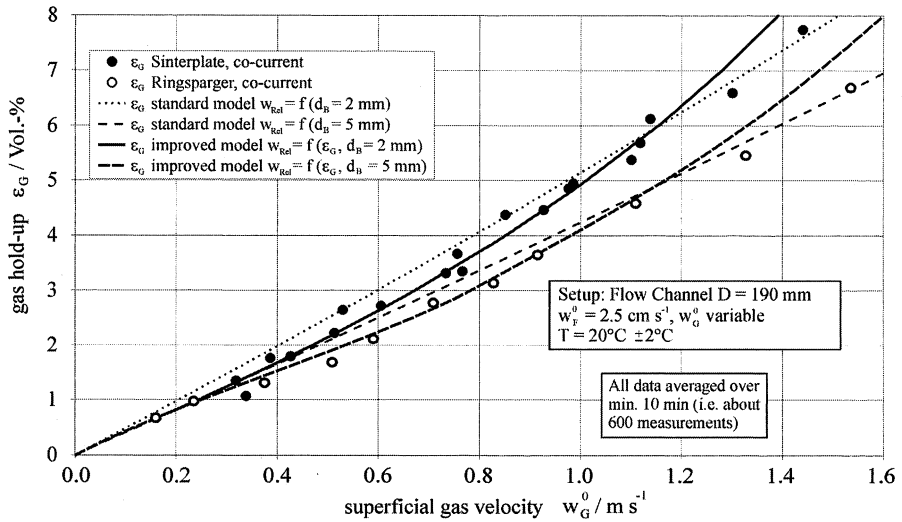


Fig. 6. Comparison between standard and improved model to predict the gas hold-up

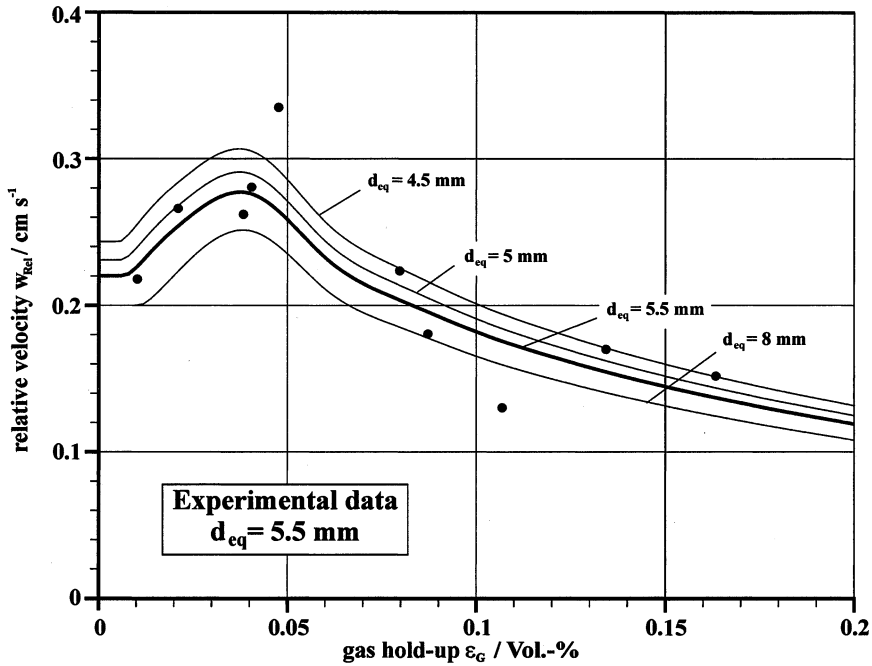


Fig. 7. Comparison of calculated vs. measured relative velocities. The influence of the bubble diameter on the relative velocity calculated by the improved model is indicated.

This model takes into account the terminal velocity of the single bubble w_s , the gas hold-up ϵ_G and the changes in the trajectory of bubbles in a swarm represented

by the slope angle Θ and the Strouhal number Sr . The relative velocity of bubbles in swarms can be predicted by the correlation

$$w_{\text{Rel}} = \sqrt{w_s^2 + \left[\frac{\pi}{2} \cdot w_s \cdot (\tan \Theta - Sr \cdot (2.28 \cdot \varepsilon_G^{-1/3} - 8)) \right]^2} \quad (7)$$

with

$$Sr = \frac{f \cdot d_{\text{eq}}}{w_{\text{Rel}}} \quad (8)$$

in the range of

$$\tan \Theta \geq Sr \cdot (2.28 \cdot \varepsilon_G^{-1/3} - 8) > 0. \quad (9)$$

Taking into account different bubble diameters and the effect of the gas-hold up Eq. 7 leads to a much better prediction of relative velocities under swarm conditions (Fig. 7). Consequently, the accuracy of the calculation of gas hold-ups up to $\varepsilon_G \leq 6$ Vol.-% is improved compared to common equations (continuous and broad dashed plot lines in Fig. 6).

This investigation points at the importance of local bubble dynamics for calculating two-phase flows. The close dependency between the flow field around a bubble and its surface dynamics is almost unknown. Nevertheless, the presented model is a first step taking into account local bubble dynamics.

One of the most important links between the surrounding flow field and the bubble surface dynamics is the gas/liquid interfacial tension. To study its influence on the movement of bubbles, the interfacial tension was lowered to $\sigma = 46.6$ mN m^{-1} by the addition of Triton X-100, a non-ionic surfactant, which had no discernible effect on the liquid viscosity. The behavior of single bubbles was studied in counter-current flow with $w_L^0 = 8$ cm s^{-1} in the experimental unit B (Fig. 3), with and without the additional influence of swarm turbulence generated by the particle grid (Fig. 4).

The quasi-static liquid velocity data from the time-averaged PIV measurements is displayed in Fig. 8. While the vector field indicates both direction and absolute velocity of the liquid, the color-coded background indicates the vertical velocity component, with darker colors corresponding to higher velocities. As expected, the turbulent flow field ($Re = 8000$) in the perspex pipe with an inner diameter of 100 mm is very homogeneous, resulting in an evenly colored background.

The dots represent the trajectories of several single bubbles which were measured by 2D PTV during independent experimental runs, the color of the dots representing the local relative velocity of the bubbles according to Eq. 6.

All of the bubbles moving in purified water with a surface tension of $\sigma = 72.4$ mN m^{-1} exhibit typical helical trajectories with a wake shedding frequency around $f = 5$ Hz, which are to be expected for ellipsoidal bubbles in the range $0.67 \leq d_{\text{eq}} \leq 0.87$ cm (Fan 1990). Apart from the large-scale motion, many smaller deviations in the bubble motion can be observed which are very irregular in respect to occurrence and extent.

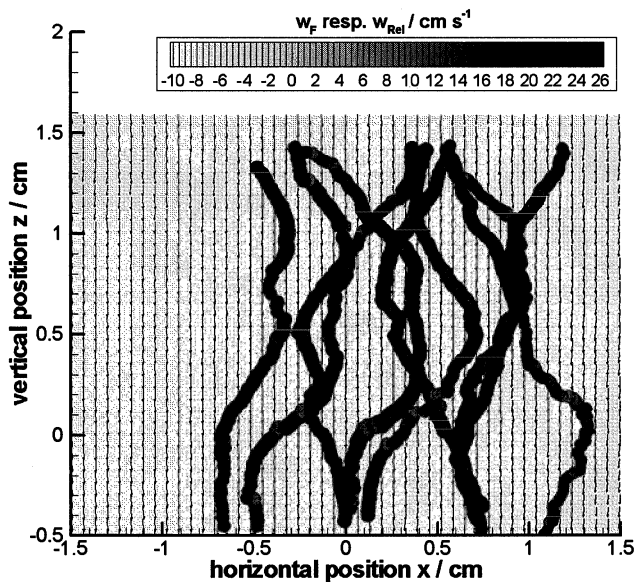


Fig. 8. Trajectories of single bubbles rising in counter-current flow with $w_L^0 = 8 \text{ cm s}^{-1}$ and without influence of the particle grid. The liquid is purified water with $\sigma = 72.4 \text{ mN m}^{-1}$. Background and dot colors indicate vertical liquid, and relative bubble velocities, resp.

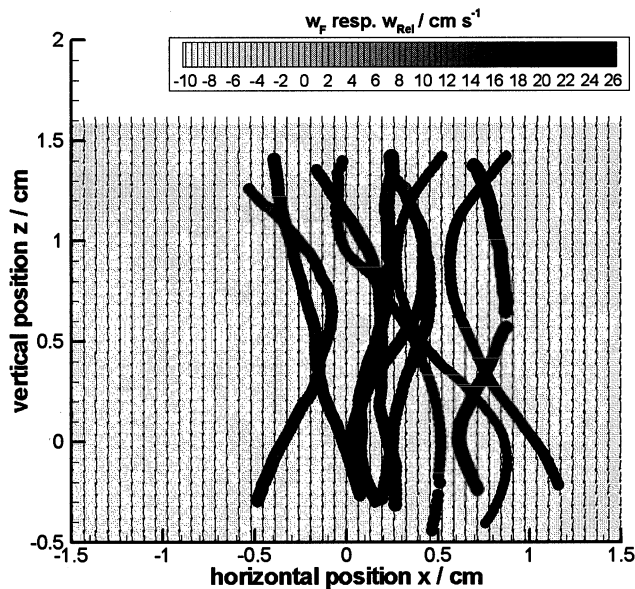


Fig. 9. Similar to Fig. 8, but the liquid is a water-surfactant solution with $\sigma = 46.6 \text{ mN m}^{-1}$

In contrast, Fig. 9 displays the trajectories of similar sized bubbles ($0.55 \leq d_{eq} \leq 0.77$ cm), moving in the counter-current flow of a water-surfactant solution with a surface tension of $\sigma = 46.6$ mN m⁻¹. The trajectories show stable helices with very few and minor irregularities. Generally the wake-shedding frequencies are higher with $f > 6$ Hz.

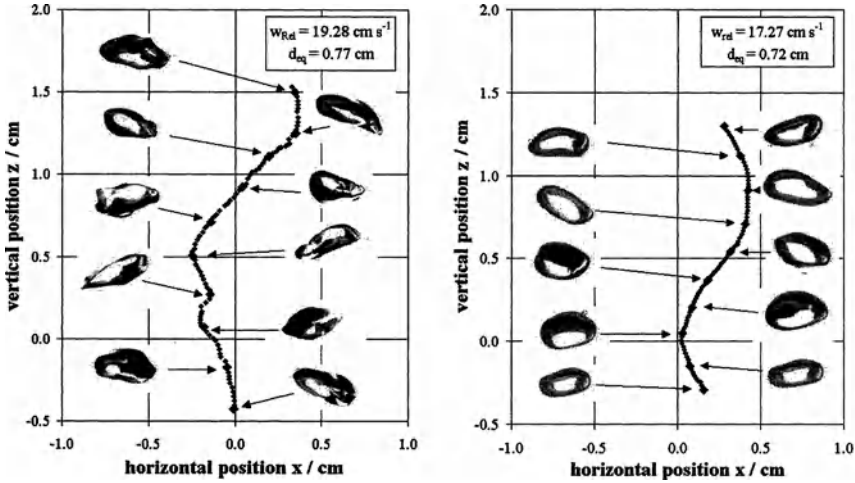


Fig. 10. Trajectories of exemplary single bubbles from Figs. 7 (left) and 8 (right). The photographs indicate the shape of the bubbles at specific times.

The reason for the different behavior of bubbles moving in water and in a water-surfactant solution becomes obvious in Fig. 10 which shows photographic images of two exemplary bubbles from the 2D PTV-system. The bubble on the left in Fig. 10 is moving in purified water and shows a very irregular shape. Minor turbulent disturbances from the surrounding liquid cause deformations of the bubble surface which then changes the bubble's path and disturbs the formation of the bubble wake region.

The bubble moving in a water-surfactant solution with a lowered surface tension (Fig. 10 right) shows a very stable shape with only few deformations. Consequently, the trajectory is closer to the ideal helix with large-scale horizontal motion. Given a constant terminal bubble velocity, Eq. 7 results in a lower average relative velocity $w_{Rel} = 17.27$ cm s⁻¹, compared to $w_{Rel} = 19.28$ cm s⁻¹ for the exemplary bubble moving in purified water, whose horizontal motion is disturbed by the stochastic shape distortions. This corresponds well with literature data for the motion of bubbles in contaminated water (Levich 1962, Brauer 1971, Maxworthy et al. 1996). The physical reason for the stable bubble shape can be seen in the locally increased viscosity through the adsorption of surfactant molecules at the bubble surface (Agrawal and Wasan 1979).

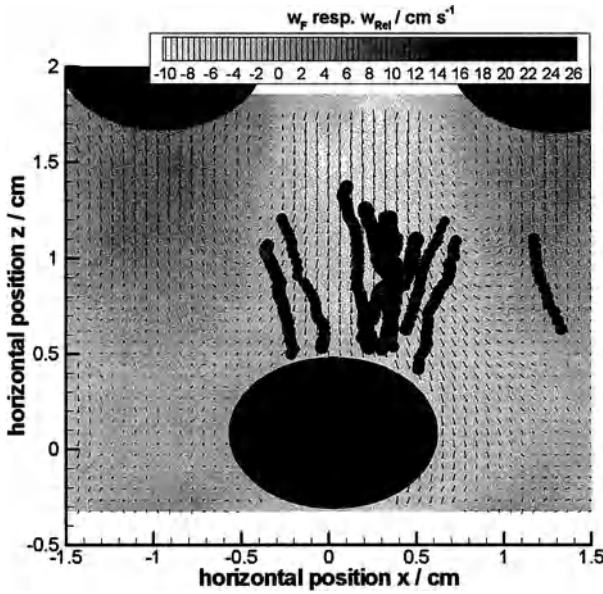


Fig. 11. Similar to Fig. 8, but with liquid flow influenced by the particle grid. The liquid is purified water with a surface tension of $\sigma = 72.4 \text{ mN m}^{-1}$. The size and position of the grid particles are indicated as black ellipsoids.

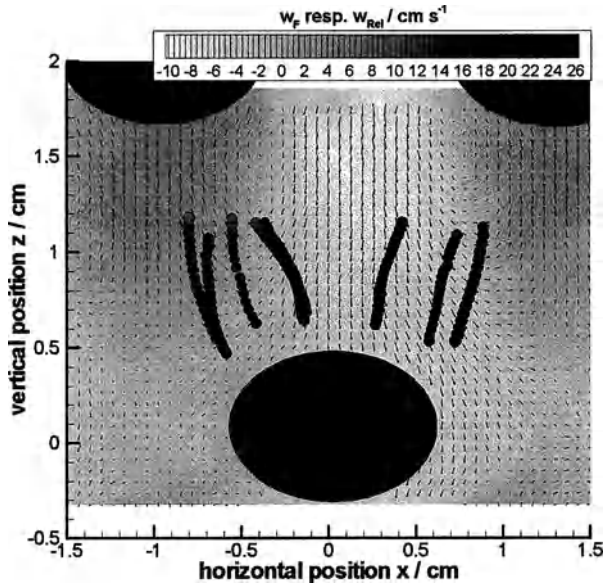


Fig. 12. Similar to Fig. 11, but the liquid is water-surfactant solution with $\sigma = 46.6 \text{ mN m}^{-1}$

The experiment was repeated with the particle grid (Fig. 4) installed. The resulting flow field is shown in Figs. 10 and 11. The large black ellipsoids show the position of particles which limited the range of vision for optical measurements. The vector map as well as the color-coded vertical components of the liquid velocity indicate wake regions with darker colored zones of upward flow below the solid particles, as well as the lighter colored regions of increased downward velocities between them.

In case of purified water with a surface tension of $\sigma = 72.4 \text{ mN m}^{-1}$ as the continuous phase, the bubble trajectories plotted in Fig. 11 appear stretched and do not show the large scale helical motion. Nevertheless, the stochastically appearing, small-scale irregularities are still visible.

When the observed bubble is moving in surfactant solution with a surface tension of $\sigma = 46.6 \text{ mN m}^{-1}$, again, the stochastic changes in the trajectory are absent in Fig. 12, in this case as well as the large-scale horizontal motion usually caused by the helical motion.

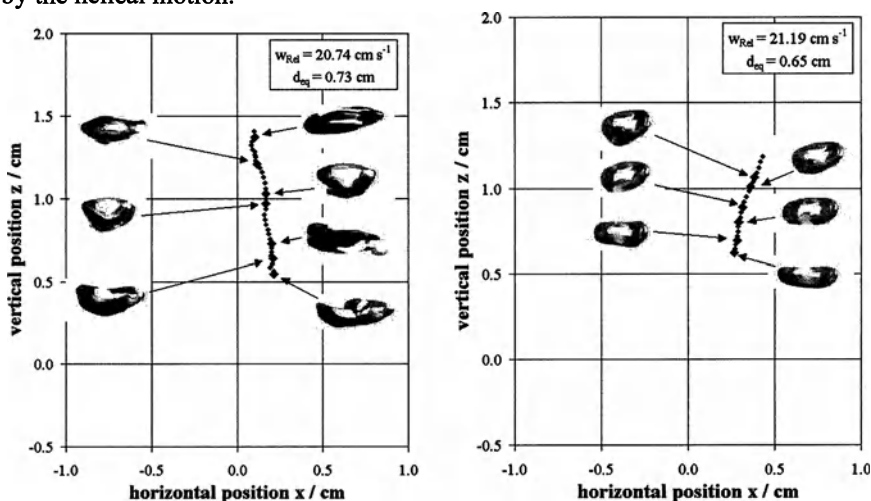


Fig. 13. Trajectories of exemplary single bubbles from Figs. 10 (left) and 11 (right).

A comparison of the bubble shapes in Fig. 13 which shows a bubble moving in purified water on the left and a bubble moving in surfactant solution on the right, shows that there are again significant differences in the bubble shapes. While the bubble moving in purified water is still distorted and continuously changing its shape, the bubble moving in surfactant solution is very stable.

These observations indicate that the turbulence structure generated by the particle grid, similarly to the turbulence generated by a freely moving bubble swarm, has an effect on the formation of the bubble wake responsible for the large-scale helical motion of the bubble. In agreement with the model of Schlüter (2002) in Eq. 7, the vertical component of the bubble motion, which is relevant for the calculation of the relative velocity w_{Rel} , is increased, if the horizontal motion of the bubble is reduced. In case of bubbles moving in undisturbed turbulent pipe flow,

the lowered surface tension favors the helical motion by stabilizing the bubble shape and thus, reducing the effect of shape deformations. Consequently the relative velocity is lowered by the surfactant.

The turbulence generated by the particle grid (or by a bubble swarm) prevents the helical motion of a bubble to a large degree by disturbing a regular wake formation, resulting in a generally accelerated vertical motion of the bubbles. Since the remaining stochastic deformations of a bubble moving in purified water still cause some horizontal motion, they cause a lower relative velocity compared to a bubble moving under the influence of swarm turbulence in a water-surfactant solution: here, both helical and stochastic horizontal motions are more or less suppressed.

Since the effect of swarm turbulence is already accounted for in Eq. 7, an extension of the model such as

$$w_{\text{Rel}} = \sqrt{w_s^2 + \left[\frac{\pi}{2} \cdot w_s \cdot (\tan \Theta - \text{Sr} \cdot (2.28 \cdot \varepsilon_G^{-1/3} - 8)) \cdot f(\varepsilon_G, \sigma) \right]^2} \quad (10)$$

is necessary and will be added in future work.

Recommendations

As a recommendation for the calculation of relative velocities in gas-liquid flows, it is important to consider the susceptibility of gas bubbles towards deformation depending on their equivalent diameter d_{Eq} . While very small bubbles with $d_{\text{Eq}} \leq 2$ mm are inherently spherical, very large ones with $d_{\text{Eq}} \geq 6$ mm are shapeless (Fan 1990). The relative velocities of both bubble size classes are hardly influenced by swarm turbulence effects.

At very low gas hold-ups $\varepsilon_G \leq 0.5$ Vol.-%, the distance between the bubbles is usually too small for a significant effect of the swarm turbulence on the relative velocity. In this case bubbles with a surfactant-stabilized shape would rise on a more pronounced helical trajectory, and thus lowered relative velocity compared to bubbles rising in pure water.

At high gas hold-ups $\varepsilon_G \geq 5$ Vol.-%, the high degree of momentum exchange between the bubbles tends to stabilize the two-phase mixture.

In the frequently found case of intermediately sized bubbles at medium gas hold-ups, the influence of liquid phase parameters, such as viscosity and surface tension on the swarm effect, have to be considered. While an increased liquid viscosity speeds up the decay of turbulence, and hence limits the range of influence of the swarm turbulence, a lowered surface tension stabilizes the bubble shape.

This necessity is upheld even if these conditions are found only in a small space within a complete reactor, since a changed relative velocity affects the operating conditions of the whole unit. A model which considers most of the effects was presented in Eq. 7, with a suggested extension to include further parameters in Eq. 10. The details of this extension are the focus of a continuing research program.

References

- Agrawal S K, Wasan D T (1979) Einfluss der Grenzflächenaktivität auf die Bewegung von Tropfen und Blasen. *Chem Eng J* 18:215-223
- Brauer H (1971) Grundlagen der Einphasen- und Mehrphasenströmungen. Verlag Sauerländer, Aarau, Frankfurt am Main
- Bridge A G, Lapidus L, Elgin J C (1964) The mechanics of vertical gas-liquid fluidised systems I: Countercurrent flow. *AIChE J* 10:819-826
- Clark N N, Flemmer R L (1985) Gas-Liquid Contacting in Vertical Two-Phase Flow. *Ind Eng Chem Process Des Dev* 24:231-236
- Davies R M, Taylor G I (1950) The mechanics of large bubbles rising through extended liquids and through liquids in tubes. *Proc Roy Soc A* 200:375-390
- Fan L, Tsuchiya K (1990) Bubble Wake Dynamics in Liquids and Liquid-Solid Suspensions. Butterworth-Heinemann, Boston, London, Singapore, Sydney, Toronto
- Guder R (1997) Fluidodynamik von Dreiphasenströmungen in Treibstrahlschlaufenreaktoren. Fortschritt-Berichte VDI Verlag Düsseldorf
- Ishii M, Zuber N (1979) Drag coefficient and relative velocity in bubble, droplet or particulate flows. *AIChE J* 25:843-855
- John S, Wilfer R, Rübiger N (1999) Messung hydrodynamischer Parameter in Mehrphasenströmungen bei hohen Dispersphasengehalten mit Hilfe der Elektrodiffraktionsmesstechnik. In: H.-M. Prasser (ed) Wissenschaftlich-Technische Berichte. FZR-281 Forschungszentrum Rossendorf
- Joshi J B, Ranade V V, Gharat, S D, Lele S S (1990) Sparged Loop Reactors. *Can J Chem Eng* 68:705-741.
- Levich, V G (1962) Physicochemical hydrodynamics. Prentice Hall, Englewood Cliffs, New York
- Maxworthy T, Gnann C, Kürten M, Durst F (1996) Experiments on the rise of air bubbles in clean viscous liquids. *J Fluid Mech* 321:421-441
- Rübiger, N (1984) Blasenbildung an Düsen sowie Blasenbewegung in ruhenden und strömenden Newtonschen und nicht-Newtonschen Flüssigkeiten. Fortschrittsberichte VDI, Nr. 625, Düsseldorf
- Rübiger N, Schlüter M (2002) Bildung und Bewegung von Tropfen und Blasen. VDI-Wärmeatlas, 9 edn, Springer Verlag, Heidelberg
- Richardson J F, Zaki W N (1954) Sedimentation and fluidization: part 1. *Trans Instn Chem Engrs* 32:35-53.
- Schlüter M, Bork O, Scheid S, Hövelmann S, Rübiger N (2001) New Aspects of Hydrodynamics and Mass Transfer in Multiphase Flows. Proceedings of the ICMF-2001 Tulane University
- Schlüter M (2002) Blasenbewegung in praxisrelevanten Zweiphasenströmungen. Ph.D. Thesis, University of Bremen
- Schlüter M, Rübiger N (1998) Bubble swarm velocity in two-phase flows. *HTD-Vol. 361 Proceedings of the ASME Heat Transfer Division, vol 5, ASME*
- Wallis G B (1969) One-dimensional two-phase flow. McGraw Hill, New York
- Zehner P (1985) Beschreibung der Fluidodynamik von gleichmäßig fluidisierten Kugelschwärmen. *Chem Eng Process* 19:57-65
- Zuber N, Findlay J A (1965) Average volumetric concentration in two-phase flow systems. *ASME J Heat Transfer* 87:453

Experimental and theoretical investigation of bubble break-up and coalescence in bubbly flows

O. Gnotke, R. Jeschke and R. Loth

Technische Universität Darmstadt, FB Maschinenbau, FG Energietechnik und Reaktoranlagen

Petersenstr. 30, 64287 Darmstadt, Germany

E-Mail: dept@eur.tu-darmstadt.de, Tel.: +49-6151-16 2191, Fax: +49-6151-16 5685

Abstract

The population balance equation considers the change of the bubble size and the bubble number density due to coalescence and break-up in bubbly flows. Although a number of theoretical models exist for coalescence and break-up rates, nearly no experimental data for the validation of these models exist for turbulent flow with high void fraction. To overcome this lack, vertical air-water pipe flows were examined. The validation concept consists of two steps: The observation of single coalescence and break-up events with a high-speed video system and the measurement of time averaged influence parameters such as number density and liquid turbulence. For measuring the number density a combination of single and double fibre optical probes was used that could be applied in high void fraction flows. X-Hotfilm probes were used to measure the liquid flow turbulence.

The observation of single events gave information about the efficiency of collisions leading to coalescence. Based on these observations, the coalescence model of Prince was modified using a critical Weber number to calculate the coalescence efficiency. The break-up model of Luo was corrected because comparison of calculated with measured turbulent spectra showed that this model overestimates the turbulent kinetic energy for large eddies. The number density was obtained from the solution of the one-dimensional conservation equation and was compared with measured data. Good agreement between measured and calculated values within the error range could be obtained. That proves the applicability of the adapted models for coalescence and break-up rates.

Introduction

In gas-liquid flows the knowledge of bubble sizes and the interfacial area concentration is needed for a proper calculation of mass, momentum and heat transfer between the phases. In a technical apparatus these parameters are time and space dependent due to coalescence and break-up. A general way to take these processes into account is the solution of the population balance equation together with the conservation equations for mass, momentum and energy (Randolph 1964; Kocamustafaogullari 1995).

$$\frac{\partial f(v)}{\partial t} + \nabla \cdot (f(v) \vec{u}_B) = \underbrace{B_{Break-Up} + B_{Coalescence}}_{\text{Birth}} + \underbrace{D_{Break-Up} + D_{Coalescence}}_{\text{Death}} \quad (1)$$

The population balance equation describes the change of the number density distribution function in time and space. Equation (1) shows its general form for an adiabatic, non-reacting system. Evaporation and condensation as well as pressure changes have not been taken into consideration. From the number density distribution function the number density of bubbles $n(v)$ in a certain volume class of width dv can be determined as $f(v)dv$. The source terms of the right-hand side denote birth and death of bubbles caused by coalescence and break-up.

The formulation of the source terms is quite sophisticated and has been subject to some, mostly theoretical investigations (Kolev 1993; Hibiki 1999; Kataoka 1999). The physical properties of the gas and the liquid, the number density, the bubble volume and the turbulence of the liquid phase have been identified as main influence parameters. But there exists still a large uncertainty in the formulation of the source terms due to lacking experimental data especially for turbulent gas-liquid flows with high void fraction and large bubbles. Most of the experiments concerning coalescence and break-up were carried out with single bubbles or very low void fraction (Drogaris 1982; Martinez-Bazan 1998; Hesketh 1990).

According to the most common models the birth and death terms are formulated analogous to the principles of molecular collisions. Bubbles collide with other bubbles and they may coalesce with a certain efficiency (Prince and Blanch 1990; Millies and Mewes 1999). Break-up is modeled as result of a collision between bubbles and eddies if the energy of the eddies is sufficiently high (Luo and Svendsen 1996). Here only turbulence induced collisions shall be taken into consideration since the focus of the investigations is highly turbulent flow.

$$D_{Coalescence} = - \int_0^{\infty} \underbrace{\frac{\pi}{4} (d + d^*)^2 u'_{B,rel}}_{\text{Collision rate}} \underbrace{f(v) f(v^*)}_{\text{Efficiency}} \eta_C dv^* \quad (2)$$

$$B_{Coalescence} = - \int_0^{v/2} \underbrace{S(v-v^*, v^*) u'_{B,rel} f(v-v^*) f(v^*)}_{\text{Collision rate}} \underbrace{\eta_c}_{\text{Efficiency}} dv^* \quad (3)$$

To model the coalescence rate, the collision rate between bubbles is expressed through the collision cross-section, the relative fluctuating bubble velocity and the number densities of the bubble volume classes (see Eq. (2)). Here the collision cross section is correctly defined using the diameters of the colliding bubbles and not their radii that were used by Prince. The collision rate is strongly dependent on the turbulence in the liquid phase. Though it is difficult to measure, the dissipation rate ε of turbulent kinetic energy is used as characteristic parameter of the liquid phase turbulence. The coalescence efficiency represents the probability of a collision leading to coalescence. According to Lehr coalescence occurs, if the bubble relative velocity is smaller than a critical relative velocity (Lehr and Mewes 2001). Assuming a Normal-distributed fluctuating relative bubble velocity the efficiency is modeled according Eq. (4).

$$\eta_c = e^{-u'_{B,rel}/u'_{crit}} \quad (4)$$

The fluctuating relative bubble velocity is determined by the liquid turbulence and the bubble diameter.

$$u'_{B,rel} = \sqrt{2} u'_{rms} (d_{eq}) = \sqrt{2} \cdot 1.4 (\varepsilon d_{eq})^{1/3} \quad (5)$$

A similar expression for the efficiency is shown by Prince who used as exponent the ratio of coalescence time and the contact time. However these values are difficult to obtain experimentally. Models for the coalescence time have only been validated for stagnant liquids and cannot be applied for turbulent flows. The critical relative velocity is derived from a critical Weber number,

$$We_{crit} = \rho d_{eq} u'_{crit} / \sigma, \quad (6)$$

that is determined via experimental investigations of single coalescence events.

The break-up rate is formulated analogous to the coalescence rate. Bubbles of volume v collide with eddies of diameter λ . The probability for a break-up to take place after such a collision is expressed through a break-up efficiency term according to Luo (see Eq. (7)). For the application of this model additional information about the number density of eddies and the kinetic turbulent energy of an eddy with diameter λ is required. These informations are deduced from turbulent spectra. Isotropic turbulence and the existence of an inertial subrange is often assumed.

$$D_{Break-up} = - \int_{\lambda_{min}}^{\lambda_{max}} \underbrace{\frac{\pi}{4} (d + \lambda)^2 u'_{rel,\lambda} f(v) n(\lambda)}_{\text{Collision rate}} \underbrace{\eta_B}_{\text{Efficiency}} d\lambda$$

(7)

$$B_{Break-up} = - \int_{\lambda_{min}}^{\lambda_{max}} \underbrace{\frac{\pi}{4} (d(2v) + \lambda)^2 u'_{rel,\lambda} f(2v) n(\lambda)}_{\text{Collision rate}} \underbrace{\eta_B}_{\text{Efficiency}} d\lambda$$

(8)

The break-up efficiency is based on energetic considerations. According to Luo break-up occurs if the kinetic energy of the colliding eddy is higher than the energy that is needed to create the new interface. The kinetic energy is calculated from the size of the eddy and its fluctuating velocity. Assuming a Normal Distribution for the eddy energies, the following expression is obtained for the break-up efficiency:

$$\eta_B = e^{-E_\sigma/E_\lambda} \quad \text{with} \quad \frac{E_\sigma}{E_\lambda} = \frac{c_f \sigma \pi d^2}{\frac{1}{2} m_\lambda u_\lambda'^2}$$

(9)

The energy that is needed to create the new surface is expressed as a fraction of the original bubble surface. The parameter c_f that represents the surface increase fraction is still subject of research. It is assumed to be a function of the bubble form and its deformation and of the daughter bubble size distribution (Hesketh 1990). In this article only the break-up into two equal sized daughter bubbles shall be investigated. For a spherical bubble that breaks into two equal sized spherical daughter bubbles the parameter c_f is theoretically set to 0.26. Single break-up events should be observed to quantify the efficiency experimentally.

To simplify the population balance equation, the one-dimensional conservation equation of the total number density shall be examined as proposed by Millies. All bubbles are assumed to have the same velocity.

$$\frac{\partial \langle n_{tot} \rangle}{\partial t} + \frac{\partial (\langle n_{tot} \rangle u_B)}{\partial x} = Y \langle n_{tot} \rangle^2 + \Omega \langle n_{tot} \rangle$$

(10)

It yields from the population balance equation by integrating it over all bubble volumes and area-averaging. The cross-sectional averaged total number density (in angled brackets) is used as variable. The total number density represents the first statistical moment of the number density distribution function and can also be expressed through the void fraction and the mean bubble volume (see Eq. (13)). Y and Ω are the kernel functions for coalescence and break-up, respectively.

$$Y = \frac{1}{\langle n_{tot} \rangle^2} \int_0^{\infty} (B_{Coalescence}(v) - D_{Coalescence}(v)) dv$$

(11)

$$\Omega = \frac{1}{\langle n_{tot} \rangle} \int_0^{\infty} (B_{Break-up}(v) - D_{Break-up}(v)) dv$$

(12)

$$n_{tot} = \int_0^{\infty} f(v) dv = \frac{\alpha}{\bar{v}}$$

(13)

The effort to solve only one differential equation of the number density conservation equation is relatively low compared to that one solving the complete population balance equation. The integrals in Eqs. (11, 12) can be solved and stored independently as proposed by Gharaibah (Gharaibah and Polifke 2002). Therefore it would be feasible to implement this conservation equation into a CFD Code.

Validation concept

The focus of the presented investigations lies in the measurement of those parameters that influence coalescence and break-up in turbulent flows with low and high void fraction. The validation concept consists of two steps. The first step comprises the observation and evaluation of single coalescence and break-up events in flows with low void fraction. As described above, such experiments can be used to quantify the efficiency of bubble/bubble or bubble/eddy collisions leading to coalescence and break-up, respectively. Especially the bubble sizes and velocities have to be determined from high video speed sequences.

The second step of the validation concept comprises the validation of the results of the number density conservation equation (Eq. (10)). For that the axial development of the number density in bubbly flow was measured. Additionally, all relevant hydrodynamic parameters, such like liquid turbulence and bubble velocities, were determined.

With all these informations, it can be checked if the underlying models concerning the collision rates and efficiencies for coalescence and break-up, respectively, are valid. Additionally, the consistency of the solution process of the number density conservation equation is shown.

Measuring system

The experiments were carried out in an adiabatic air-water test facility at ambient conditions. Deionized water was used. The test section comprised a 90 mm diameter and 7 m long vertical transparent pipe. About 2.5 m upstream of the mixing chamber (see figure 1), at the water inlet to the pipe, a flow stratifier is situated. The mixing chamber contains a built-in exchangeable turbulence grid. Via needles above the grid air is injected into the turbulent water flow. Four turbulence grids with different obstructed area were used to modify the inlet turbulence (for details see Benk 2001). They modified specifically the inlet bubble diameter distribution of a flow immediately downstream of the grid due to turbulent forces that enhance the bubble break-up. It was possible to produce a homogenous and defined turbulence field in the developed flow region over a certain cross-section of the pipe and to study the effect of different bubble diameters and number densities on coalescence and break-up even for equal air and water flow rates. In this report results for two different grids are presented. Different air and water superficial velocities can be adjusted to produce different flow regimes ranging from dispersed small bubbles to large, irregularly shaped bubbles.

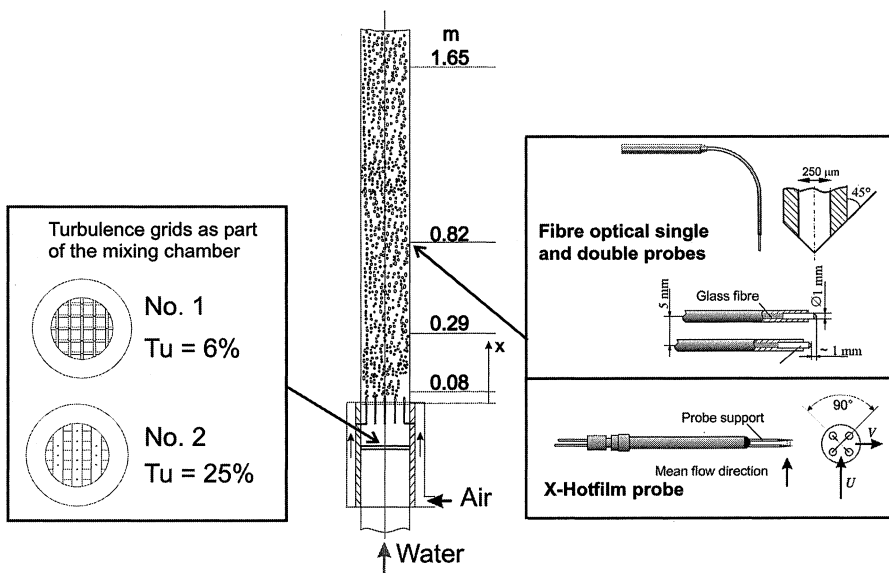


Fig. 1. Experimental setup of the test section

The probes - fibre optical probes and X-Hotfilm probes - were positioned in different radial and axial measurement points. In order to get information about the liquid flow parameters, the mean liquid velocity and the turbulent fluctuations were measured with X-hotfilm-probes (TSI -1240W). These probes are also applicable in flows with high void fractions. Detailed information concerning the measuring system can be found by Benk (Benk 2000, 2001). A signal processing pro-

cedure is used to separate the liquid signal from the gas signals of the probes to determine correctly the liquid turbulence. Fibre optical probes were used to measure void fraction, velocity, diameter distribution and number density of the bubbles. A detailed description of the used measuring system and the signal processing can be found by Rinne (Rinne 1996). The local void fraction is obtained by dividing the total gas detection time by the total measuring time t . The mean bubble velocity in flow direction is determined by the cross-correlation of the two signals of a double-probe consisting of two conical fibre tips separated by 10 mm. Now the penetration time or chord length, respectively, of each bubble can be calculated. In the following step all chord lengths are assigned to finite chord length intervals and so a discrete chord length PDF is obtained. This chord length distribution can further be transformed into a diameter distribution according to a method of Clark (Clark et al. 1996). The procedure to determine the number density distribution function is described by Gnotke (Gnotke 2002).

In order to obtain the one-dimensional development of the flow parameters, measurements with all probes have been performed at 16 radial points. The cross-sectional area averaged value of all flow parameters (i.e. void fraction, velocity, turbulence, size distributions) was determined.

A digital High-Speed Camera (Vosskühler HCC 1000) was used to observe the coalescence and break-up events. The frame rate was up to 1800 frames per second with a maximum image size of 1024x1024 pixel. This time-resolving measurement method allowed to determine the bubble sizes and velocities immediately before and after the coalescence or break-up event. Also the coalescence time could be determined. The image processing comprised an automatic blob analysis to get the bubble sizes. The software package Impuls VISON XXL was used. The procedure to detect the bubbles comprised image enhancement, finding the borderlines via a Sobel operator and binarization of the image. Due to the fact that the borderline of the detected bubbles was in some cases not closed, the form and area of the bubbles were not always correctly determined. The Feret diameter gives then the most accurate result for the bubbles size. The bubble velocity vector was manually determined by measuring the bubble displacement from two succeeding images. The images were taken with a small depth of focus to get a quasi two-dimensional view. For the illumination of the flow a diffusive backlight from a strobe light was used.

Observation of coalescence events

For checking the physical boundary conditions during coalescence events about 50 single events were evaluated in a low void fraction flow region at $x = 0.29$ m ($j_l = 0.5$ m/s ; $j_g = 0.05$ m/s ; $\alpha = 6\%$; $Tu = 10$ %). In this region directly downstream of the mixing chamber most of the coalescence events take place. To show which bubble sizes contribute most on coalescence within a certain flow, characterized by its size distribution according to the left diagram of figure 2, the size distribution of the coalescing bubbles is shown at the right diagram. The horizontal Feret-

Diameter distribution for all bubbles ranges up to about 8 mm. In contrast, the size distribution for bubbles that were involved in coalescence ranges only up to a maximal bubble diameter of about 3 mm. This observation indicates that for flows of this kind the coalescence efficiency decreases with increasing bubble sizes. However, further observations have to be made to get statistically significant data.

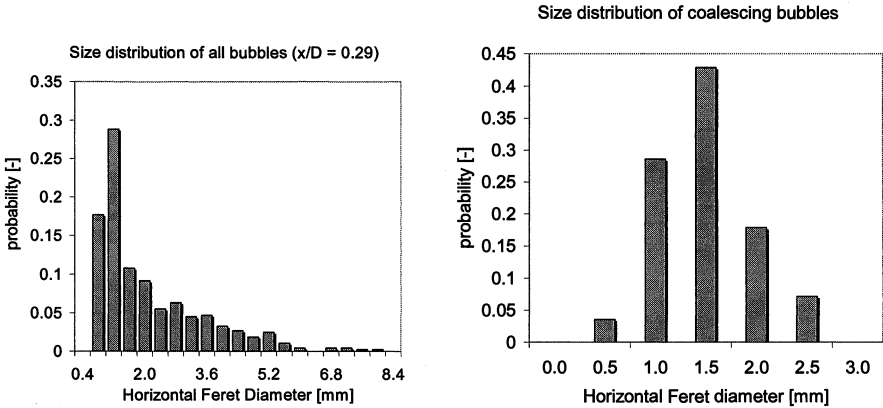


Fig. 2. Bubble diameter distributions from digital image processing

For all coalescence events the vector of the relative bubble velocity was determined immediately before the moment of coalescence. Its alteration shows clearly that the efficiency decreases with increasing relative velocity and supports the model assumption that for coalescence a critical relative velocity must exist.

According to Hagesæther (Hagesæther 2002) the coalescence efficiency is also dependent on the collision angle β in the moment of coalescence. It may be defined as the angle between the relative velocity vector and the difference position vector corresponding with the colliding bubbles (see Fig. 3).

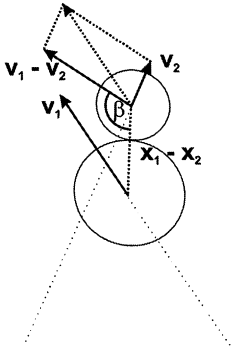


Fig. 3. Geometry of bubble collision

The most probable collision angles observed were 30 and 60 degree. This means that most of the collisions that lead to coalescence were non-central. One can assume that the mobile surfaces of the bubbles deform already before they collide and the bubbles push each other apart. These surface deformations will influence the contact time or the critical velocity, respectively. The larger the collision angle the shorter is the critical velocity. From the images with high speed sequences also the coalescence time could be estimated. It was defined as period of time that elapses from the first contact (no more liquid could be distinguished between the interfaces) to the film rupture. The mean coalescence time was five milliseconds for the investigated flows. With this information the critical Weber number could be quantified to 0.12 and equation (4) can be solved. The resulting coalescence efficiency is shown in the left diagram of Fig. 6.

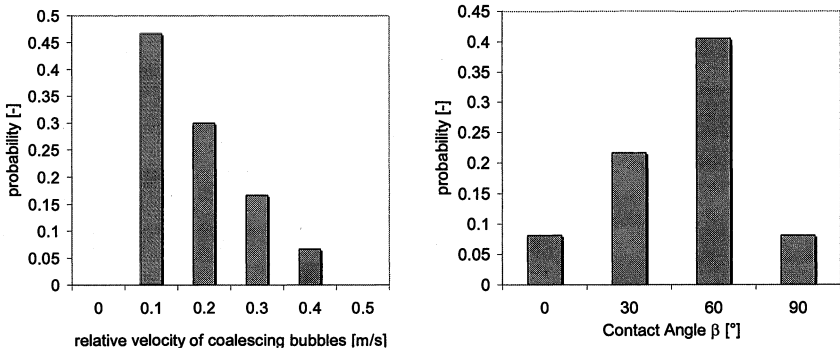


Fig. 4. Relative velocity and contact angle of coalescing bubbles

Break-up efficiency

Luo's model for the kinetic energy of the eddies assumes the existence of an inertial subrange. To check his model, turbulent spectra were measured. The measured data (see Fig. 5) show that the turbulent spectra for a flow with low Re-Number of turbulence ($Re_{Tu} = u' \lambda / \nu$), that go along with small bubbles, do not have a distinct inertial subrange. For high turbulent flows, as it was observed for high void fractions, a good agreement was obtained between measured and calculated kinetic energies within the inertial subrange. The model of Luo, however, overestimates the turbulent kinetic energy for eddies larger than the macroscale. So, the macro-length should be considered in the calculation of the turbulent kinetic energy.

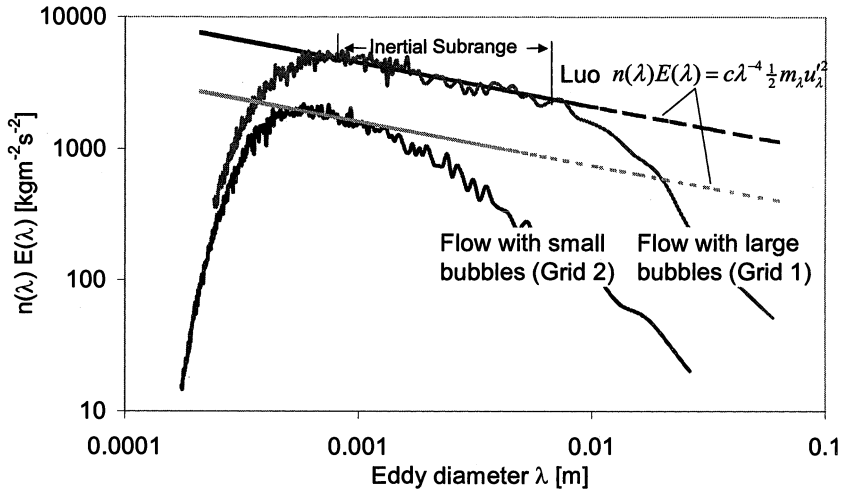


Fig. 5. Energy spectra from X-Hotfilm in developed flow at $x = 0.82$ m ($j_1 = 1$ m/s ; $j_g = 0.2$ m/s ; $\alpha = 10\%$)

The attained efficiency curve is shown in the right diagram of figure 6. It shows the break-up efficiency for a collision between a bubble and an eddy of the same size, i. e. $\lambda = d$. The parameter c_f was chosen based on the observation of break-up events. Before the break-up occurs, the bubbles are strongly deformed and elongated. The axis ratio was 5 for most of the events. If an rotational ellipsoid is assumed, the surface of such a bubble is 1.4 times larger than that of a spherical bubble with the same volume, resulting in the coefficient $c_f = 0.4$.

The break-up efficiency increases with increasing bubble diameter. As already mentioned the model was corrected for eddy sizes larger than the macro-length. For this, the energy $E(\lambda)$ of a single eddy was kept constant, leading to a steeper decrease of the total turbulent kinetic energy $n(\lambda)E(\lambda)$. This leads to a decrease of the efficiency if the diameter of the bubble exceeds the macro-length. In this case the surface energy increases faster than the eddy energy.

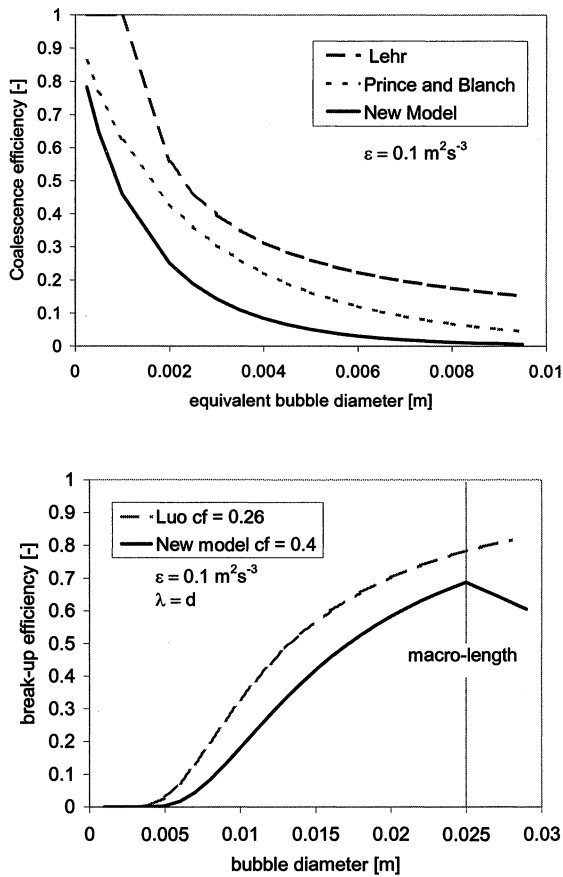


Fig. 6. Coalescence efficiency for two equal sized bubbles and break-up efficiency (with macro-length = 25 mm)

Comparison of calculated and experimentally determined number densities

Experiments were performed within a wide range of boundary conditions concerning superficial gas (j_g) and liquid velocities (j_l) and inlet turbulence levels. The axial development of the area averaged number density was recorded based on a procedure described by Gnotke. The presented new models were implemented in the number density conservation equation which was then solved numerically. To solve the integrals in the Eqs. (11/12), the diameter-pdf has to be known. For sim-

plification a Gamma-pdf was used to approximate the measured data. The results are compared to the experimental data.

Figure 7 shows the results for Grid 2 that produces high inlet turbulence and therefore small bubbles. The mean bubble diameter ranged from 1.5 to 2.5 mm. According to a We-number criterion no break-up is assumed to occur in such flows. Thus, only coalescence takes place and the experimental results can directly be used to validate the coalescence rate model. As can be seen from Fig. 7 good agreement between experimental and calculated data was reached. For higher number densities the deviation becomes larger. This is due to the fact, that the small bubbles have a size similar to the fibre optical probe tip and they cannot be detected correctly anymore. The error of the measured number density was quantified to be 15 percent of the measured value. Also the model of Lehr is able to predict reasonably the measured data except for high number density, i.e. small bubbles, where it overestimates the coalescence rate. The reason for the deviation lies in the higher coalescence efficiency in the model of Lehr. However a slightly different calculation of the collision frequency of bubbles is used that reduce the coalescence rate.

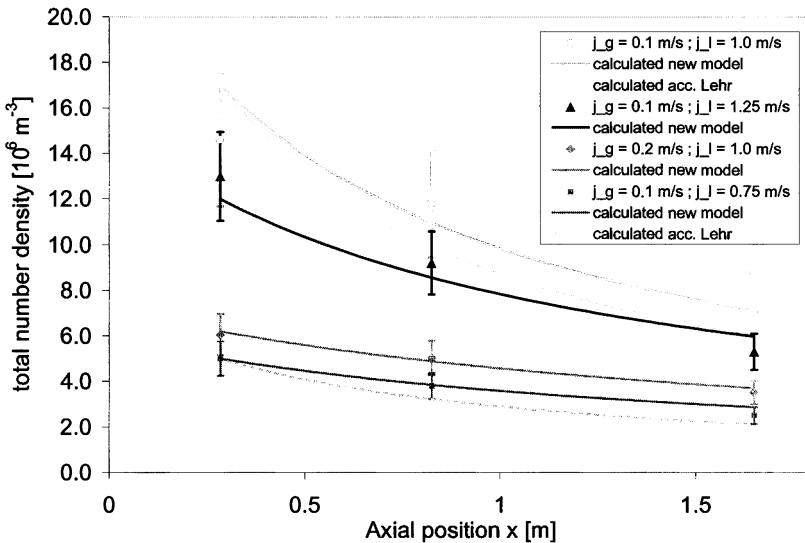


Fig. 7. Axial development of the total number density for Grid 2

In Fig. 8 the results are shown for Grid 1 that produces low inlet turbulence and a flow with both small and large bubbles. An equilibrium of coalescence and break-up is nearly reached within a short distance downstream of the gas distributor where almost a fully developed flow region exists. The new coalescence and break-up rate models are capable to correctly predict the equilibrium state and good agreement is also reached for these flows with the experimental data. It should be emphasized that all calculations were done with the same model parameters.

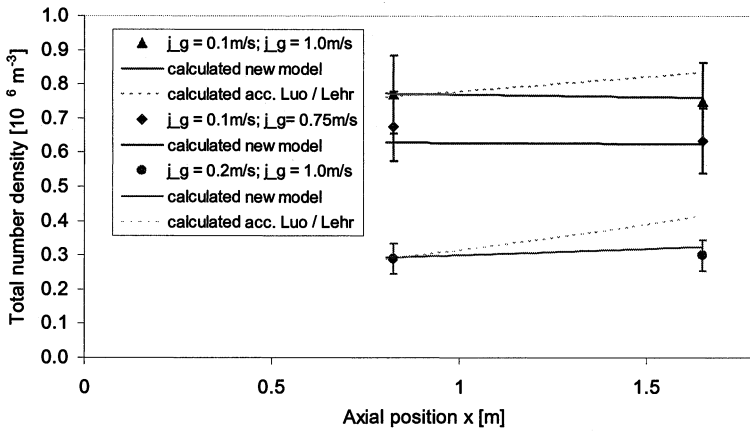


Fig. 8. Axial development of the total number density for Grid 1

Conclusions

Frequently used models, the coalescence model of Prince and the break-up model of Luo, have been improved by quantifying their parameters through experimental investigations of two-phase pipe flow. Single coalescence and break-up events were observed with a High Speed Camera and first results were obtained for the coalescence and break-up efficiency. Digital image processing was applied to get the relevant information. Further investigations are needed here to get statistically significant data. The liquid flow turbulence was measured with a X-hotfilm probe in order to use in the break-up model a more correct dependency of the turbulent kinetic energy from the eddy size. The total number density of the bubbles and the bubble sizes were measured with fibre optical probes. The conservation equation of the total number density can be solved without high numerical effort. Good agreement between calculated and measured total number densities could be achieved for all investigated boundary conditions. Thus, the new models have been proven for turbulent systems with small and large bubbles (>20 mm) and high local void fractions α ranging from 5 to 25 percent. The data will be further used to validate in detail the population balance equation to calculate the bubble size distribution.

Nomenclature

Symbol	description	unit
B	Birth term	$m^{-6} s^{-1}$
D	Death term	$m^{-6} s^{-1}$
$E(\lambda)$	Kinetic turbulent eddy energie	$kgm^2 s^{-2}$
$f(v)$	number density distribution function	m^{-6}
j	superficial velocity	ms^{-1}
M_λ	mass of eddy with diameter λ	kg
n_{tot}	total number density	m^{-3}
S	cross sectional area	m^2
Tu	turbulence intensity ($= u'/u_L$)	-
U'	fluctuating velocity	ms^{-1}
u_B	Mean bubble velocity	ms^{-1}
v	bubble volume	m^3
Ω	Break-up kernel	s^{-1}
Y	coalescence kernel	$m^3 s^{-1}$
α	void fraction	-
β	collision angle	°
ε	dissipation rate	$m^2 s^{-3}$
λ	eddy diameter	m
ρ	density	kgm^{-3}
σ	surface tension	Nm^{-1}

References

- Benk, H., Loth, R. (2000) Investigations of the Interactions Between the Dispersed and Continuous Phase in Air/Water Two-Phase Flow with Grid Turbulence, 3rd European Thermal Sciences Conference, Heidelberg, Germany
- Benk, H. (2001) Zum Turbulenzeinfluss auf die Phasenwechselwirkungen im Ausbildungsbereich vertikaler Gas/Flüssigkeits-Zweiphasenströmungen, PhD Thesis, Tech. Universität Darmstadt, Germany
- Clark, N. N., Liu, W. and Turton, R (1996) Data Interpretation Techniques for Inferring Bubble Size Distribution from Probe Signals in Fluidized Systems, Powder Techn. 88, 179-188
- Drogaris, Georgios (1982) Koaleszenz von Gasblasen in wässrigen Lösungen, PhD Thesis, Universität Dortmund, Germany
- Hesketh, R.P., Etschells, A.W. and Russel, T.W.F. (1990) Bubble Breakage in Pipeline Flow, Chem. Engng. Sci. 46(1), 1-9
- Hibiki, T. and Ishii, M. (1999) Experimental Study on Interfacial Area Transport in Bubbly Two-Phase Flows, Int. J. Heat Mass Transfer, 42, 2711-2726
- Kataoka, I. and Serizawa, A. (1999) Interfacial Area Concentration in Bubbly Flow, Nucl. Engng. Design 120, 163-180
- Kocamustafaogullari, G. and Ishii, M. (1995) Foundation of the Interfacial Area Transport Equation and its Closure Relations, Int. J. Heat Mass Transfer 38(3), 481-493

- Kolev, N. I. (1993) Fragmentation and Coalescence Dynamics in Multiphase Flows, *Exp. Thermal and Fluid Sci.* 6, 211-251
- Lehr, F. and Mewes, D. (2001) A Transport Equation for the Interfacial Area Density Applied to Bubble Columns, *Chem. Engng. Sci.*, 56, 1159-1166
- Luo, Hean and Svendsen, Hallvard F., (1996) Theoretical Model for Drop and Bubble Breakup in Turbulent Dispersions, *AIChE J.* 42(5)
- Martinez-Bazan, C., Lasheras, J.C. and Montanes, J.L. (1998) Splitting and Dispersion of Bubbles by Turbulence, *Third International Conference on Multiphase Flows, ICMF98*
- Millies, M., Mewes, D. (1999) Interfacial Area Density in Bubbly Flow, *Chemical engineering and processing* 38, 307-319
- Prince, M. J. and Blanch, H. W (1990) Bubble Coalescence and Break-Up in Air-Sparged Bubble-Columns, *AIChE J.* 36, 1485-1499
- Randolph, A.D. (1964) A Population Balance for Countable Entities, *American Potash and Chemical Corporation*
- Rinne, Achim and Loth, R. (1996) Development of Local Two-Phase Flow for Vertical Bubbly Flow in a Pipe with Sudden Expansion, *Int. J. Exp. and Therm. Fluid Sci.* 13, 152-166
- Gharaibah, E. and Polifke, W. (2002) Numerical Model for the Simulation of Dispersed Two Phase Flows based on Presumed Shape Number Density Functions, *Proceedings of the 10th Workshop on Two-Phase Flow Predictions, Merseburg, Germany*
- Gnotke, O., Benk, H. and Loth, R. (2002) Experimental study on the influence of the number density distribution function on coalescence and break-up in bubbly flows, submitted to *Experimental Thermal and Fluid Science Journal*, August 2002
- Hagesæther, L. (2002) Coalescence and break-up of drops and bubbles, *PhD Thesis, Trondheim, Norway*

Experimental investigation and modeling of air/water flows in vertical pipes

D. Lucas, E. Krepper, H.-M. Prasser

Forschungszentrum Rossendorf e.V., Institute of Safety Research, P.O.Box
510 119, 01454 Dresden, Germany

Abstract

CFD codes are more and more used for practical applications as the design and optimization of technical facilities, e.g. in process industry or in nuclear power plants. For most cases this limited to single phase flows. To qualify CFD codes for two-phase flows, they have to be equipped with constitutive laws describing the interaction between the gaseous and the liquid phases. In the case of bubble flow this particularly concerns the forces acting on the bubbles and bubble coalescence and break-up. To obtain detailed experimental data, an electrode wire-mesh sensor was used, which enables the measurement of the phase distribution with high resolution in space and in time. Air-water flow at ambient conditions in a vertical pipe (51.2 mm inner diameter) is investigated to have well defined boundary conditions. Local bubble size distributions are calculated from the data. The measurements were done in different distances from the gas injection device. As a result the development of bubble size distributions and the development of the radial gas fraction profiles can be studied. It was found, that the bubble size distribution as well as local effects determine the transition from bubble flow to slug flow. The data are used for the development of a model, which predicts the development of the bubble size distribution and the transition from bubble flow to slug flow in case of stationary flow in a vertical pipe.

1 Introduction

World-wide great efforts are made to develop CFD codes for two-phase flows in complicated three-dimensional geometries. In case of bubble flow, and especially for the correct prediction of the flow pattern transition from bubble to slug flow, constitutive laws describing the interaction between the gaseous and the liquid phases in a more detailed way than the wide-spread assumption of mono-disperse bubble flow are needed. Recently attempts were made to solve this problem by the

introduction of additional equations for the bubble density or similar variables like bubble diameter, bubble volume or interfacial area. Rates for bubble coalescence and frequencies for bubble break-up, which form the source terms in these equations, have to be calculated as local quantities. They depend on local parameters of turbulence as well as on the local bubble size distribution. In order to reflect the fact, that bubbles of different sizes develop different spatial distributions, it is necessary to introduce multi-bubble-size models. The main challenge is to find model equations for quantifying the interaction between these bubble-size classes.

Gas-liquid flow in vertical pipes is a very suitable object for studying the corresponding phenomena. Here, the bubbles move under simple boundary conditions, resulting in a shear field of nearly constant structure where the bubbles rise for a comparatively long time. This allows to study the lateral motion of the bubbles in a shear flow by comparing distributions measured at different heights. It was shown, that the radial distribution of bubbles strongly depends on their diameter. For a vertical upflow smaller bubbles tend to move towards the wall, while large bubbles are preferably found in the centre. This was initially observed for single bubbles (Tomiya 1998). In an air-water system at ambient conditions the change of the direction of the lift force in the shear field occurred at a bubble diameter of about 5–6 mm. We could confirm this also for multi-disperse flow (Prasser et al. 2002). This is very important for the evolution of the flow because the local bubble size distributions may differ significantly from those averaged over the cross section.

For this reason detailed investigations of gas-liquid flows in vertical tubes including the transition from bubble flow to slug flow along the flow path were performed. The change of the bubble size distribution along the pipe as well as the changing radial profiles of the gas fraction represented by bubbles of different size were measured by fast wire-mesh sensors developed by the Research Centre Rossendorf. A model was developed to simulate the development of the flow along the flow path for the special case of vertical pipe flow. This allows to test the models for the forces acting on a bubble perpendicular to the flow path as well as models for bubble coalescence and break-up and to adjust them according to the experimental data.

2 Experiments

2.1 Experimental setup and instrumentation

The evolution of the bubble size distribution was studied in a vertical tube of 51.2 mm inner diameter supplied with air-water mixture at 30°C. Different gas injection devices were used. The distance between sensor and air injection was varied from 0.03 m to 3.03 m (inlet lengths 0.6 - 60 L/D). Gas and liquid superficial velocities were varied in a wide range. Stationary flow rates of air and water were

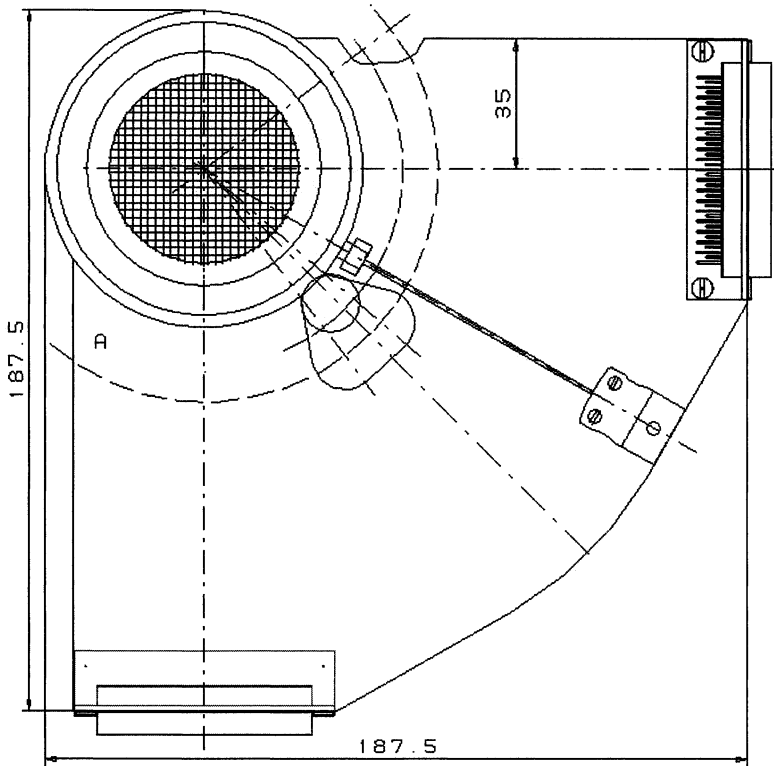


Fig. 1. Scheme of the wire-mesh sensor

used. About 150 combinations of the superficial velocities were considered. They include stable bubble flow, finely dispersed bubble flow, slug flow and annular flow at the upper end of the pipe. Transitions between the flow regimes were observed within the pipe.

Data were obtained by an electrode wire-mesh sensor (Fig. 1) performing measurement of the instantaneous conductivity distribution (Prasser et al. 1998). Two electrode grids with 24 electrode wires each (diameter 120 μm) are placed at an axial distance of 1.5 mm behind each other. During signal acquisition, the electrodes of the first grid (transmitter wires) are supplied with short voltage pulses in a successive order. The currents arriving at the second grid (receiver wires) are digitalized by ADCs and stored in a data acquisition computer. Two sensors were put in a distance of 36 mm behind each other to measure velocities, too. For this sensor assembly, a time resolution of 2500 frames per second was achieved. The spatial resolution is given by the pitch of the electrodes and equals 2 mm.

The sensor delivers a sequence of two-dimensional distributions of the local instantaneous conductivity, measured in each mesh formed by two crossing wires i and j . Local instantaneous gas fractions are calculated assuming a linear dependence between gas fraction and conductivity. The result is a three-dimensional data

array i,j,k where k is the number of the instantaneous gas fraction distribution in the time sequence. A special procedure, described in (Prasser et al. 2001) allows the identification of single bubbles and the determination of their volume and the equivalent bubble diameter. Using this procedure, bubble size distributions as well as gas fraction profiles for bubbles within a predefined interval of bubble sizes can be calculated, the latter by using the method described in (Prasser et al. 2002).

2.2 Test matrix for the investigations on the transition from bubble to slug flow

A detailed experimental database concerning the development of the flow along the flow path, including the transition from bubble to slug flow was obtained. A description of the database and selected results can be found in (Lucas et al. 2002). The gas injection device used, consists of 19 capillaries, which are equally distributed over the cross section of the pipe. 89 combinations of gas and liquid volume flow rates and 10 different gas flow rates in case of stagnant liquid were investigated. The air superficial velocity varies from 0.0025 m/s up to 0.53 m/s and the maximum water superficial velocity is 4 m/s. The measurements were conducted for up to 10 different distances from the gas injection ($L/D = 0.6, 1.6, 2.5, 4.5, 8.4, 16.2, 29.9, 39.6, 49.4, 59.2$). The measuring time was always 10 s, what results in a matrix of raw data with the dimension of $24*24*25.000$ for each sensor. From these data total and local bubble size distributions as well as radial gas fraction profiles decomposed according to the bubble size were calculated.

2.3 Experimental results

Tomiyama found a correlation for the bubble lift force by investigations of the behavior of single bubbles within a well defined shear field (Tomiyama 1998). It changes sign at a bubble diameter of about 5.5 mm in air-water flow at ambient conditions. This was confirmed by our own experiments in a multi-dispersed flow. (Figure 3 gives an example.)

Stable bubble flow was only observed for high water superficial velocities and low air superficial velocities. In this case a stable sharp wall peak of the gas fraction was found. In all cases with a core peak, the development of the bubble size distributions along the pipe indicates, that the coalescence rate exceeds the break-up rate. Although at $L/D \cong 60$ the transition to slug flow is not yet completed in many cases, it can be expected at larger distances. This is also evident by the comparison of experiments for the same superficial velocities, but different gas injection devices. If the initially generated bubbles are larger than the critical bubble diameter of about 5.5 mm, slug flow is established for many combinations of superficial velocities, whereas bubble flow is observed in case of an initial bubble diameter less than 5.5 mm. The experiments clearly show, that the transition from wall to core peak leads to a transition to slug flow somewhere upwards in the pipe, if the length is sufficient.

Titel:

Graphics produced by IDL

Erstellt von:

IDL Version 5.3.1 (Win32 x86)

Vorschau:

Diese EPS-Grafik wurde nicht gespeichert mit einer enthaltenen Vorschau.

Kommentar:

Diese EPS-Grafik wird an einen PostScript-Drucker gedruckt, aber nicht an andere Druckertypen.

Titel:

Graphics produced by IDL

Erstellt von:

IDL Version 5.3.1 (Win32 x86)

Vorschau:

Diese EPS-Grafik wurde nicht gespeichert mit einer enthaltenen Vorschau.

Kommentar:

Diese EPS-Grafik wird an einen PostScript-Drucker gedruckt, aber nicht an andere Druckertypen.

Fig. 2. Bubble size distributions (upper picture) and radial gas volume fraction profiles (lower picture) for different distances from the gas inlet. Superficial velocities: $j_1 = 1.0$ m/s, $j_g = 0.14$ m/s.

<p>Titel: Graphics produced by IDL Erstellt von: IDL Version 5.3.1 (Win32 x86) Vorschau: Diese EPS-Grafik wurde nicht gespeichert mit einer enthaltenen Vorschau. Kommentar: Diese EPS-Grafik wird an einen PostScript-Drucker gedruckt, aber nicht an andere Druckertypen.</p>	<p>Titel: Graphics produced by IDL Erstellt von: IDL Version 5.3.1 (Win32 x86) Vorschau: Diese EPS-Grafik wurde nicht gespeichert mit einer enthaltenen Vorschau. Kommentar: Diese EPS-Grafik wird an einen PostScript-Drucker gedruckt, aber nicht an andere Druckertypen.</p>
<p>Titel: Graphics produced by IDL Erstellt von: IDL Version 5.3.1 (Win32 x86) Vorschau: Diese EPS-Grafik wurde nicht gespeichert mit einer enthaltenen Vorschau. Kommentar: Diese EPS-Grafik wird an einen PostScript-Drucker gedruckt, aber nicht an andere Druckertypen.</p>	<p>Titel: Graphics produced by IDL Erstellt von: IDL Version 5.3.1 (Win32 x86) Vorschau: Diese EPS-Grafik wurde nicht gespeichert mit einer enthaltenen Vorschau. Kommentar: Diese EPS-Grafik wird an einen PostScript-Drucker gedruckt, aber nicht an andere Druckertypen.</p>

Fig. 3. Radial volume fraction profiles decomposed for different bubbles sizes at four different distances from the gas inlet. Superficial velocities: $j_1 = 1.0$ m/s, $j_g = 0.14$ m/s.

In pipes of a larger diameter the effects have still to be investigated, since there is a maximum pipe diameter for the establishment of slug flow (Taitel et al. 1980).

The transition from wall to core peaking is demonstrated at Figure 2. The upper picture shows the bubble size distributions for different distances from the gas inlet. Starting from an initial bubble diameter of about 4.7 mm more and more larger bubbles are generated by coalescence. The lower picture shows the corresponding gas fraction profiles. Very close to the gas injection device ($L/D = 0.6$) still the individual injection nozzles (19 nozzles, equally distributed over the cross section) determine the radial profile. The small bubbles migrate quickly to the wall and form a wall peak of the gas fraction ($L/D = 16.2 - 29.9$). With a further increase of the distance from the gas inlet a transition to core peaking is observed ($L/D = 59.2$).

Figure 3 shows again gas fraction profiles for different distances from the inlet, but here they are subdivided according to the bubble diameter. Only few bubbles exceeding 5.5 mm are generated by the air injector. They appear due to coalescence at higher positions and migrate to the core of the pipe. These large bubbles form a clear core peak at $L/D = 59.2$, while the small bubbles show a wall peaking also for this distance.

Titel:

Graphics produced by IDL

Erstellt von:

IDL Version 5.3.1 (Win32 x86)

Vorschau:

**Diese EPS-Grafik wurde nicht gespeichert
mit einer enthaltenen Vorschau.**

Kommentar:

**Diese EPS-Grafik wird an einen
PostScript-Drucker gedruckt, aber nicht
an andere Druckertypen.**

Titel:

Graphics produced by IDL

Erstellt von:

IDL Version 5.3.1 (Win32 x86)

Vorschau:

**Diese EPS-Grafik wurde nicht gespeichert
mit einer enthaltenen Vorschau.**

Kommentar:

**Diese EPS-Grafik wird an einen
PostScript-Drucker gedruckt, aber nicht
an andere Druckertypen.**

Fig. 4. Bubble size distributions (upper picture) and radial gas volume fraction profiles (lower picture) for different distances from the gas inlet. Superficial velocities: $j_1 = 0.4$ m/s, $j_g = 0.34$ m/s.

For other combinations of superficial velocities the transition from bubble to slug flow was observed. The process of transition is very fast, if a sufficient fraction of bubbles with a diameter between 10 mm and 15 mm is generated by coalescence. Figure 4 shows a typical evolution of the bubble size distribution and the radial gas fraction profile in case of the transition. Bubbles larger than 10 mm in diameter coalesce with a high rate and form slugs. Consequently, a transition to a bi-modal bubble size distribution is observed.

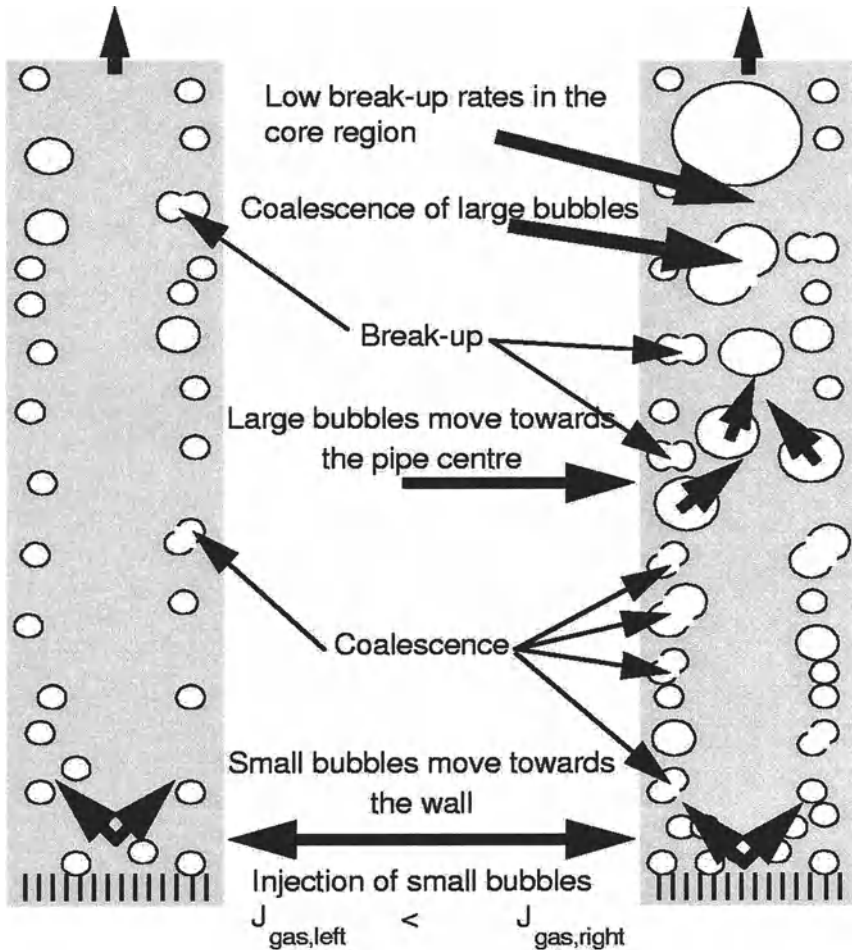


Fig. 5. Development of the flow pattern for different gas volume flow rates (superficial velocities). Small bubbles are injected in both cases. For low gas volume flow rates (left) an equilibrium of bubble coalescence and break-up leading to a stable bubbly flow is established. For large volume flow rates (left) large bubbles coalesce at the pipe center at low break-up rates, what leads to a transition to slug flow.

3 THE TRANSITION FROM BUBBLE TO SLUG FLOW

As the experimental data advice, the transition from bubble to slug flow along the flow path in case of an co-current flow within a pipe is influenced by local effects depending on the bubble size. Bubble coalescence and bubble break-up, which cause the transition, depend on the local bubble densities n as well as on the dissipation rate of the turbulent kinetic energy ε (Prince and Blanch 1990):

$$\text{Coalescence rate:} \quad \Gamma_{i,j} = f(d_i, d_j, \varepsilon) * n_i * n_j$$

$$\text{Break-up rate:} \quad \Omega_i = f(d_i, d_j, \varepsilon) * n_i$$

i and j indicate the bubble class. The lift force found by Tomiyama (1998) causes, that small bubbles (diameter < ca. 5.5 mm in case of air-water flow) can be found preferably in the wall region, while larger bubbles are accumulated in the core region.

Another important fact is, that the dissipation rate of turbulent energy is larger in the near wall region than in the core flow in most cases. The consequences for the transition to slug flow can be explained by help of Figure 5. An upward air-water flow is considered. In both considered cases small bubbles (diameter < 5.5 mm) are injected. In the left side of the figure a low superficial gas velocity was assumed. The small bubbles tend to move towards the wall. The local gas fraction in the wall region is larger than the averaged gas fraction, but it is still low. In this case bubble coalescence and break-up are in equilibrium and an stable bubble flow is established.

If the gas superficial velocity is increased (Figure 5, right side), the equilibrium between bubble coalescence and break-up is shifted towards a larger bubble diameter, because the coalescence rate increases with the square of the bubble density, while the break-up rate is proportional to the bubble density. The bubble break-up rate strongly increases with the bubble diameter.

By a further increase of the gas superficial velocity, more and more large bubbles (diameter > 5.5 mm) are generated. They start to migrate towards the pipe centre. If enough large bubbles are generated by coalescence in the wall region, some of them can reach the core region without break-up. Because of the lower dissipation rate of turbulent energy they can then growth up by further coalescence at much lower break-up rates, typical for the low shear in the centre. This mechanism is the key for the transition from bubble to slug flow. That means, for an appropriate simulation of the transition a number of bubble classes as well as radial gas fraction profiles for each bubble class have to be considered.

4 Modeling

4.2 Basic idea of the model

According to the importance of the local bubble size distributions and the dependence of the parameter on the radial position, a model, which considers a large number of bubble classes and resolves the parameter on the radial position was developed. Because this model is explained in detail in (Lucas et al. 2001b), only the basic idea of the model is presented here.

The radial profiles of the bubble density are the result of the non drag forces, acting perpendicularly to the flow direction. They are caused by the liquid shear flow, turbulence and no-slip boundary at the tube wall. The radial profiles of the liquid velocity, of the turbulent energy and of the dissipation rate of turbulent energy are calculated on basis of the model from Sato et al. (1980) and the balance equation for the turbulent energy (Lucas et al. 2001a). Using these data, the model calculates the radial gas fraction profiles for each bubble class on the basis of a balance of the non drag forces. In the result local bubble size distributions for all radial positions are available. Simple models for bubble coalescence and break-up calculate from these data rates for bubble coalescence and break-up for each bubble class and each radial position.

The model does not resolve the parameters over the height of the pipe. Instead a bubble velocity, which is equal for all bubble sizes and radial positions is assumed. This allows the approximate evaluation of the flow pattern over the height of the pipe in case of stationary flows by introducing a dependence on time. Because of the assumed uniform bubble velocity the time corresponds to a height position within the pipe. Starting from an initial bubble size distribution for each time step radial profiles and new bubble size distributions are calculated.

For the non drag forces the model assumes an equilibrium. The transient behaviour of the radial gas fraction profiles is modelled by a relaxation. For situations with stable flow conditions a good agreement between predicted and measured radial gas fraction profiles is observed, but deviations occur especially in the region of the transition from bubble to slug flow. The model is up to now not able to simulate the time dependence of the shift of the large bubbles, generated by coalescence in the near wall region, to the centre of the pipe. For this reason it is planned to consider the velocity of the bubble migration in future versions of the model.

First calculations were made using simplified assumptions for coalescence and break-up rates. Starting with the bubble size distribution and the radial profile of the gas fraction measured at the inlet of the test pipe the development of the bubble size distribution was calculated. After adjusting the model parameters a good agreement with the experimental data at the upper end of the pipe was achieved (Lucas et al. 2001b). The transition from bubble to slug flow was reproduced by the model. It has to be remarked that the model adjustment is independent from the flow rates, i.e. the model has a generalising capability. The models for the non-

drag bubble forces and the rates for coalescence and break-up can be applied in one-dimensional codes as well as in CFD-codes.

4.2 Comparison with experimental results

The new database, shortly characterised in 2.2, will be used for the further improvement of the model. As a first step the model described above was applied on the new experimental data. The only extension of the model is, that it now also considers the decreasing pressure along the flow path, which is connected with an increase of the total gas fraction.

Measured total bubble size distributions and radial gas fraction profiles close to the gas injection device ($L/D = 0.6$) were taken as an input of the model. Starting from these data, the model calculates the radial gas fraction profiles and the bubble size distributions along the flow path. Figures 6 to 8 compare the measured and calculated bubble size distributions at the upper end of the pipe ($L/D = 60$) for different combinations of gas liquid superficial velocities. From Fig. 6 to Fig. 8 the liquid superficial velocity is increased from 0.40 m/s to 0.64 m/s and 1.0 m/s. The gas superficial velocities were chosen in a way, that cases with bubble flow as well as with slug flow at the upper end of the pipe are included.

In general the flow pattern for $L/D = 60$ is well predicted by the model. However there are deviations in the radial gas fraction profiles as well in the bubble size for other distances from the gas inlet. For this reason it is necessary to include the transient radial migration of the bubbles and more sophisticated models for bubble coalescence and break-up into the model. This will be done on basis of the new experimental database.

5 Conclusions

The experimental data clearly show, that the transition from bubble to slug flow is determined by effects depending on the bubbles sizes as well as on local effects. For an adequate modelling a large number of bubble classes (e.g. 25) has to be considered. There are very different conditions for bubble coalescence and break-up in the core region of the pipe compared to the near wall region. This fact has also to be considered by the models for the simulation of the development of the flow pattern along the pipe. The experimental data obtained in vertical pipes are useful for the development of generalised models for the non-drag bubble forces as well as for local bubble coalescence and break-up. These models can be used by one-dimensional codes as well as 2- or 3-dimensional CFD-codes. The simplified approach is a powerful tool for the model development for CFD codes, since it allows to test model correlations in a very efficient manner.

Titel:
Graphics produced by IDL
Erstellt von:
IDL Version 5.3.1 (Win32 x86)
Vorschau:
Diese EPS-Grafik wurde nicht gespeichert
mit einer enthaltenen Vorschau.
Kommentar:
Diese EPS-Grafik wird an einen
PostScript-Drucker gedruckt, aber nicht
an andere Druckertypen.

Titel:
Graphics produced by IDL
Erstellt von:
IDL Version 5.3.1 (Win32 x86)
Vorschau:
Diese EPS-Grafik wurde nicht gespeichert
mit einer enthaltenen Vorschau.
Kommentar:
Diese EPS-Grafik wird an einen
PostScript-Drucker gedruckt, aber nicht
an andere Druckertypen.

Titel:
Graphics produced by IDL
Erstellt von:
IDL Version 5.3.1 (Win32 x86)
Vorschau:
Diese EPS-Grafik wurde nicht gespeichert
mit einer enthaltenen Vorschau.
Kommentar:
Diese EPS-Grafik wird an einen
PostScript-Drucker gedruckt, aber nicht
an andere Druckertypen.

Fig. 6. Experimental bubble size distribution at the gas inlet and experimental and calculated bubble size distributions at the upper end of the test section. Superficial velocity of the liquid: $j_l = 0.4$ m/s.

Titel:
Graphics produced by IDL
Erstellt von:
IDL Version 5.3.1 (Win32 x86)
Vorschau:
Diese EPS-Grafik wurde nicht gespeichert
mit einer enthaltenen Vorschau.
Kommentar:
Diese EPS-Grafik wird an einen
PostScript-Drucker gedruckt, aber nicht
an andere Druckertypen.

Titel:
Graphics produced by IDL
Erstellt von:
IDL Version 5.3.1 (Win32 x86)
Vorschau:
Diese EPS-Grafik wurde nicht gespeichert
mit einer enthaltenen Vorschau.
Kommentar:
Diese EPS-Grafik wird an einen
PostScript-Drucker gedruckt, aber nicht
an andere Druckertypen.

Titel:
Graphics produced by IDL
Erstellt von:
IDL Version 5.3.1 (Win32 x86)
Vorschau:
Diese EPS-Grafik wurde nicht gespeichert
mit einer enthaltenen Vorschau.
Kommentar:
Diese EPS-Grafik wird an einen
PostScript-Drucker gedruckt, aber nicht
an andere Druckertypen.

Fig. 7. Experimental bubble size distribution at the gas inlet and experimental and calculated bubble size distributions at the upper end of the test section. Superficial velocity of the liquid: $j_1 = 0.64$ m/s.

Titel:
Graphics produced by IDL
Erstellt von:
IDL Version 5.3.1 (Win32 x86)
Vorschau:
Diese EPS-Grafik wurde nicht gespeichert
mit einer enthaltenen Vorschau.
Kommentar:
Diese EPS-Grafik wird an einen
PostScript-Drucker gedruckt, aber nicht
an andere Druckertypen.

Titel:
Graphics produced by IDL
Erstellt von:
IDL Version 5.3.1 (Win32 x86)
Vorschau:
Diese EPS-Grafik wurde nicht gespeichert
mit einer enthaltenen Vorschau.
Kommentar:
Diese EPS-Grafik wird an einen
PostScript-Drucker gedruckt, aber nicht
an andere Druckertypen.

Titel:
Graphics produced by IDL
Erstellt von:
IDL Version 5.3.1 (Win32 x86)
Vorschau:
Diese EPS-Grafik wurde nicht gespeichert
mit einer enthaltenen Vorschau.
Kommentar:
Diese EPS-Grafik wird an einen
PostScript-Drucker gedruckt, aber nicht
an andere Druckertypen.

Fig. 8. Experimental bubble size distribution at the gas inlet and experimental and calculated bubble size distributions at the upper end of the test section. Superficial velocity of the liquid: $j_l = 1.0$ m/s.

Nomenclature

d_i	Bubble diameter of the bubble class i
D	Inner diameter of the pipe
j_g	Gas superficial velocity
j_l	Liquid superficial velocity
n_i	Bubble density of the bubble class i
Γ_{ij}	Rate of coalescence of bubbles from the bubble class i with bubbles from the bubble class j
ε	Dissipation rate of turbulent energy
Ω_i	Break-up rate for bubbles of the bubble class i

References

- Lucas D., Krepper E., Prasser H.-M. (2001a) Prediction of radial gas profiles in vertical pipe flow on basis of the bubble size distribution. *International Journal of Thermal Sciences* 40: 217-225
- Lucas D., Krepper E., Prasser H.-M. (2001b) Development of bubble size distributions in vertical pipe flow by consideration of radial gas fraction profiles. 4th International Conference on Multiphase Flow, New Orleans, May 27 - June 1, 2001, Conference-CD, Paper 378
- Lucas D., Krepper E., Prasser H.-M. (2002) Experimental high-resolution database for co-current air-water flow in a vertical pipe. 40th European Two-Phase Flow Group meeting, Stockholm, Sweden, June 10-13, 2002, paper C4
- Prasser H.-M., Böttger A., Zschau J. (1998) A new electrode-mesh tomograph for gas-liquid flows. *Flow Measurement and Instrumentation* 9: 111-119
- Prasser H.-M., Scholz D., Zippe C. (2001) Bubble Size Measurement using Wire-Mesh Sensors. *Flow Measurement and Instrumentation* 12: 299-312
- Prasser H.-M., Krepper E., Lucas D. (2002) Evolution of the two-phase flow in a vertical tube - decomposition of gas fraction profiles according to bubble size classes using wire-mesh sensors. *International Journal of Thermal Sciences* 41: 17-28
- Prince J.P., Blanch H.W. (1990) Bubble coalescence and break-up in air-sparged bubble columns. *AIChE Journal* 36: 1485-1499
- Sato Y., Sadatomi M., Sekoguchi K. (1981) Momentum and heat transfer in two-phase bubble flow. *International Journal on Multiphase Flow* 7: 167-177
- Taitel Y., Bornea D., Dukler A.E. (1980) Modelling Flow Pattern Transitions for Steady Upward Gas-Liquid Flow in Vertical Tubes. *AIChE Journal* 26: 345-354
- Tomiyama A. (1998) Struggle with computational bubble dynamics. Third International Conference on Multiphase Flow, ICMF'98, Lyon, France, June 8-12, 1998

Experimental and theoretical investigation of instationary bubble flow and mass transfer in a bubble column

D. Schmitz, D. Mewes

Institute of Process Engineering, University of Hannover, Callinstrasse 36, 30167 Hannover, Germany

Abstract

In many chemical processes, chemical reactors and storage vessels are used under high pressure and temperature conditions. In case of a sudden decrease of the pressure a large amount of steam and gas is generated by flashing of the liquid and re-volatilisation of dissolved gaseous substances. As a result, the liquid level inside the vessel swells and a two-phase blowdown from the vessel may occur. In the present work a water-carbon dioxide system is examined. The time dependent pressure, the axial profile of the void fraction and its distribution over the cross sectional area at different axial positions are measured by electric tomography. For the simulation of the pressure relief an improved mathematical model compared to common calculation methods for pressure relief systems is used. A new method for calculating the maximum possible mass flow of the liquid at the entrance of the blowdown pipe is developed. The calculated values of the pressure and the two-phase mass flow rate agree well with the experimental data.

1 Introduction

In recent years standard practices in the chemical industry regarding safety, environmental protection, energy consumption, quality assurance and complexity of the products have developed significantly, necessitating more complex and detailed measurement techniques for the design and control of chemical plants and transportation systems. During this development, the use of tomographic measurement techniques has become increasingly popular. The advantage of tomographic measurements in contrast to local measurements is the imaging, by simultaneous or near-simultaneous measurements, of the complete cross sectional area of the measured object once at a time. This is in contrast to local probes which provide only local information. For the measurement of the radial void distribution in bubble columns one-point conductivity probes have been used by e.g. Menzel (1990), resistivity probes have been used by e.g. Idogawa et al. (1986).

The application of tomographic measurement techniques for process or chemical engineering applications is, in comparison to the medical sector, relatively new. Nevertheless, the use of electrical, x-ray or NMR tomographic techniques is now widely spread. The advantage of x-ray tomography is its high spatial resolution. The time resolution varies depending on the sensor system used. Very fast and expensive systems can reach measurement times of 0.5 ms with a spatial resolution of 2 mm² (cp. Hori et al. 1997). Most of the used systems have imaging times of several seconds or minutes and therefore they are not applicable for investigations on non steady state multiphase flows. Kumar et al. (1997) have measured the gas-hold up in bubble columns. Toye et al. (1994) have investigated steady state flows in trickle bed reactors, measuring the liquid distribution in the packing. Sederman et al. (1997) use NMR for the imaging of the pore structure within packed beds. With the NMR technique the distribution of density and velocity are measured simultaneously. The NMR technique is restricted to non-ferromagnetic materials due to the magnetic field used for the measurements. Hence this technique cannot be used for steel pressure vessels but for glass vessels.

Electrical capacitance tomography (ECT) has been used for the investigation of pulsing flow in trickle bed reactors by Reinecke and Mewes (1991). They developed a 16 electrode sensor for the measurement of the phase distribution in reactors filled with ceramic spheres as packing material. Investigations on three phase flow have been carried out by Johansen et al (1996) using mixtures of oil, water and gas. The time resolution in these applications are in the range of 100 frames per second. The spatial resolution depending on the diameter of the pipe is about 10 % of the cross sectional area. The tomographic measurement technique presented in this paper combines a high measurement frequency with good spatial resolution.

2 Experimental setup

The experimental setup consists of two pressure vessels, which can be operated with pressures of up to 1.6 MPa. In the first vessel, tap water is saturated with carbon dioxide. In the next step the saturated water is pumped into the second vessel which is shown in **Fig. 1**. This vessel is 2100 mm in height, 315 mm in diameter and has a volume of 160 l. It is built from several cylindrical segments. The tomographic sensor is mounted between the cylindrical segments in the vessel at various heights to measure void fraction distributions over the height of the column.

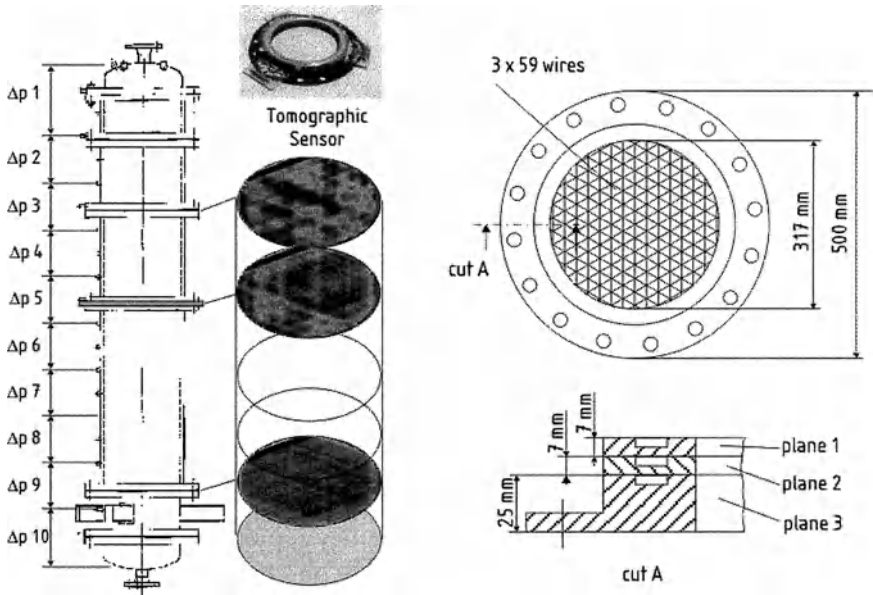


Fig. 1. Drawing of the column, tomographic Sensor

In addition to the tomographic measurement of the void fraction, the axial profile of the gas holdup is determined from 9 differential pressure transducers mounted in equal distances from the bottom to the top of the column. The blow-down is started by opening the ball valve at the top of the vessel. The pressure in the vessel decreases rapidly and the liquid starts bubbling. The surface of the liquid rises until it reaches the top of the vessel. A two phase flow through the vent-line is established. It takes about one minute until the pressure reaches the ambient pressure, depending on the liquid viscosity and the filling level at the beginning of the depressurization. In addition to the void fractions the temperatures at the top and the bottom as well as the pressures at the top of the vessel are measured.

3 Tomographic measurement technique

For the measurement of the local void fractions a conductive tomographic measurement technique is used. It provides a spatial resolution of 5.3 mm and a time resolution of 100 measurements per second. The tomographic sensor consists, as shown in **Fig. 1**, of three planes of parallel wires. The inner diameter is set equivalent to the vessel diameter. The wires have a diameter of 0.18 mm and are spaced 5.3 mm to each other. In every plane 59 wires are stretched across the sensor, resulting in 58 integral measurement values. The individual planes are rotated 120° to each other in such a way that 4722 isosceles triangles are obtained. Between each two adjacent wires within each plane the electrical conductance is measured.

This value is directly proportional to the liquid fraction in the area between the wires. From the measured conductances the void fraction of each triangle is calculated by using the ART-Algorithm (Algebraic Reconstruction Technique). The computation is performed in an adapted coordinate system, as suggested by Reinecke et al. (1997). Further details of the measurement technique and reconstruction-algorithm are also described by Reinecke et al (1998).

4 Experimental results

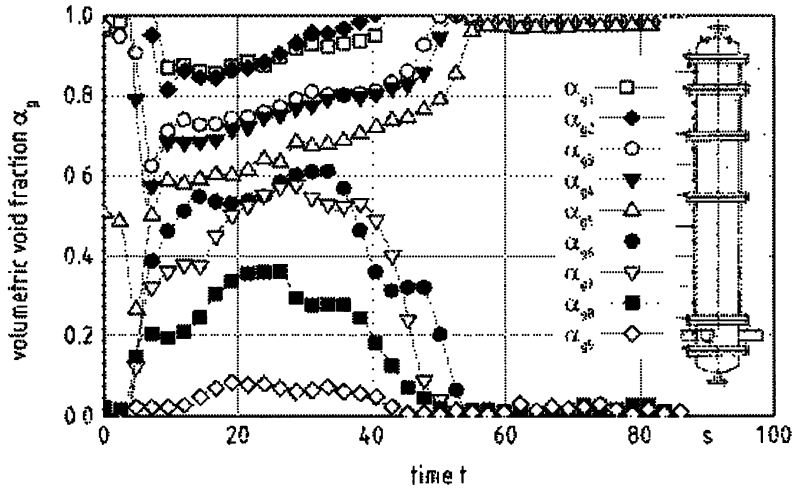


Fig. 2. Void fraction at different axial positions

In Fig. 2 the volumetric void fraction is plotted as a function of time at different vessel heights. In this case the void fraction is measured with the differential pressure transducers. The initial liquid level is 50 % and the initial pressure is 1.28 MPa. At the beginning of the pressure relief the pressure transducers are located either above the liquid level or beneath the liquid level, the void fraction is either 1 or 0. Only pressure transducer No. 5 gives a void fraction of 50 % due to the gas-liquid interface which is in between the two pressure taps of the differential pressure transducers. The void fraction rises rapidly within the first 7 seconds after the start of the de-pressurisation and reaches a maximum value. The measured void fractions for the pressure transducers No.1-4 fall to approximately 80 %. The void fractions measured by the pressure transducers No. 5-9 are increasing from bottom-up, according to the gas volatilisation during blowdown.

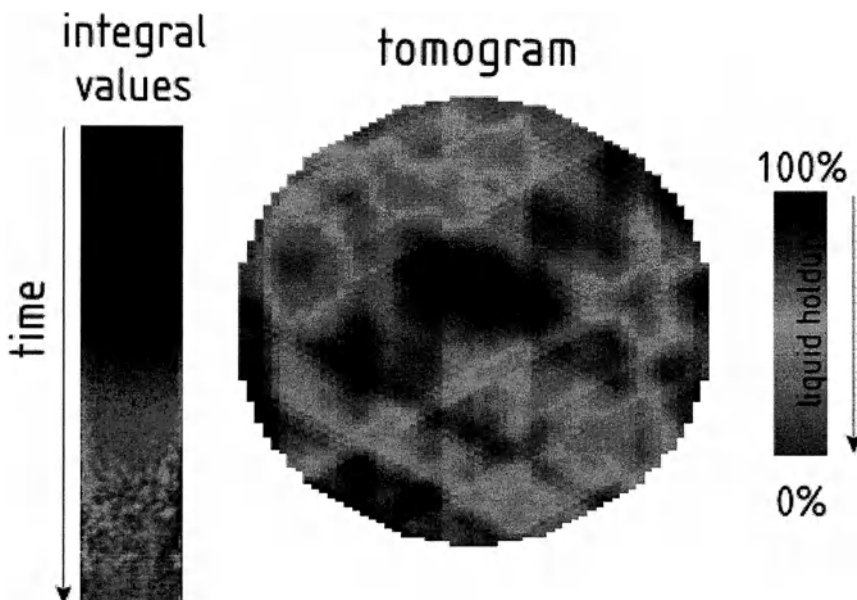


Fig. 3. Tomographic reconstruction

A sample tomographic measurement of the void fraction distribution in the cross sectional area of the column is shown in **Fig. 3**. On the left side the measured integral values of the electrical conductivity is shown for one of the projections as a function of time. The void fraction is scaled according to the table on the right side. The time scale starts at the top. The measurement frequency is 100 frames per second. Beside the results from the integral measurements a tomogram is given at the right side. The tomogram is measured approximately 12 s after the starting of the blowdown. The level of the liquid is located at beginning of the blowdown at 65 % of the vessel height. After 2.5 s the carbon dioxide starts to desorb, as indicated by the change of the colors. More and more the void distribution becomes inhomogeneous. Areas with a high gas-holdup can be distinguished from others with a low.

In a separate series of experiments the ball valve at the top of the vessel is controlled by one of the differential pressure transducers to avoid the two phase flow in the vent-line. As a result the liquid remains in the vessel. The control-loop is shown in **Fig. 4**. If the two-phase flow reaches the maximum level in the vessel the ball valve is closed. The pressure in the vessel increases again and the two phase flow mixture collapses. The ball valve is opened again when the two-phase flow mixture reaches the lower limit of the control mechanism. This is repeated until the pressure in the vessel reaches the ambient pressure.

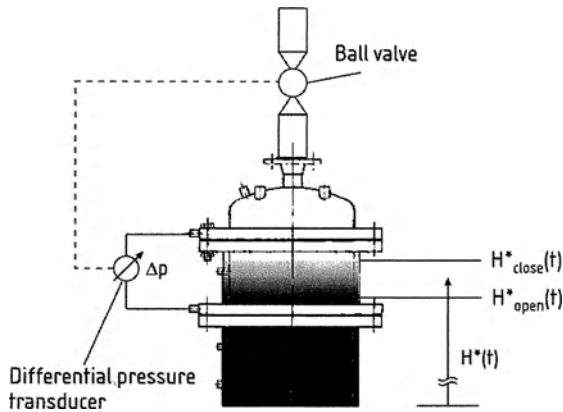


Fig. 4. Control of the ball valve

5 Simulation of the blowdown

The aim of the theoretical investigations is to calculate the time dependent values of pressure and two-phase mass-flow rate during the pressure-relief. The calculations are carried out for carbon-dioxide as the dissolving component. The bubble production takes place within the whole liquid volume. The bubble production is caused by growing of small bubbles already suspended within the liquid after filling the vessel.

Details of the conducted numerical calculations and the applied equations would exceed the limits of this publication by far. A detailed listing and derivation of the numerical model can be found in Schmitz et al. (2001). The calculated parameters include transient level swell, pressure in the vessel, dissolution rate, local void fractions, mass flow out of the vessel, and others. The superficial gas velocity is calculated by the Drift-Flux model of Zuber and Findlay (1965). For calculating the unsteady bubble flow in the liquid, the breakup and coalescence of bubbles is taken into account, cp. Millies and Mewes (1996). The interfacial mass transfer rate is calculated according to Calderbank (1967).

5.1 Comparison with experiments

In **Fig. 5** the calculated void fraction at the entrance of the orifice is shown as a function of time. The initial dimensionless liquid level is $h_0^* = 90\%$. The initial pressure is $p_0 = 12.8 \cdot 10^5$ Pa, the initial temperature $T_0 = 10^\circ\text{C}$. After 2.2 s the liquid level reaches the top of the reactor, a two-phase flow occurs. This yields to a sudden decrease of the void fraction. The void fraction decreases from its initial value of 1 to a minimum value of about 0.4.

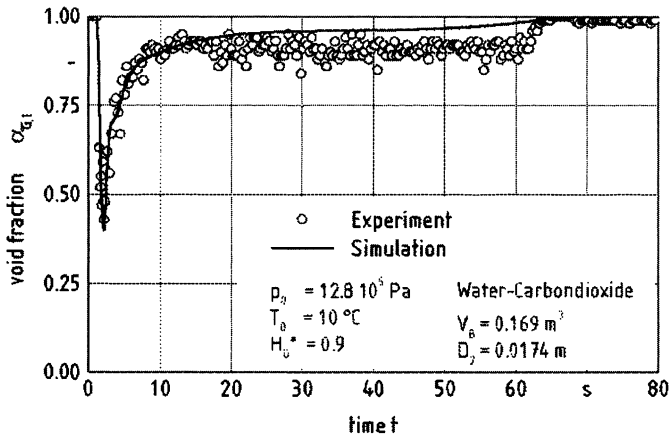


Fig. 5. Void fraction in front of orifice

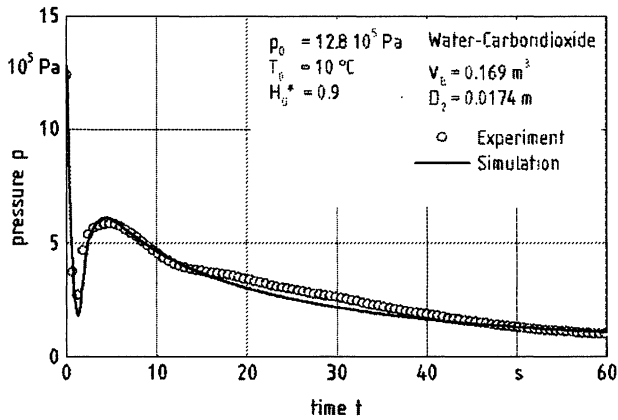


Fig. 6. Calculated pressure in the pressure vessel

In Fig. 6 the calculated value of the pressure is compared to experimental data for the initial liquid level of $h_0^* = 0.9$. Initially the pressure decreases very fast because of the high volumetric flow rate of the single-phase gas flow. With the beginning bubble growth the liquid level begins to swell. The speed of depressurisation decreases until the pressure reaches a minimum value. After this time the mass of gas which is produced due desorption is bigger than the gas mass leaving the vessel, causing an increase of the pressure. While the pressure is increasing the level of the two-phase mixture within the vessel reaches the entrance of the blow-down pipe. The lower the initial liquid level is the longer it takes for the level to reach the top of the vessel.

In Fig. 7 the calculated axial void distribution is compared to experimental results for a elapsed time of 5s after the start of the de-pressurisation. The void fraction profile develops due to the production of gas and the rise of the bubbles.

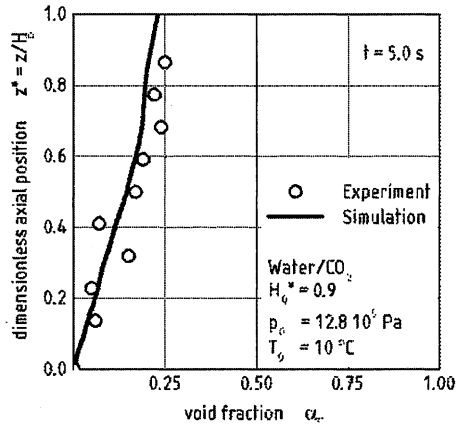


Fig. 7. Local void fraction in the pressure vessel

All experiments described above have been carried out without a control of the ball valve at the top of the column. This leads in all cases to a two-phase outflow in the vent line. To prevent environmental contamination with liquid, experiments are conducted with the use of the described control mechanism. By consecutive opening and closing of the ball valve the liquid is kept in the column. Both the results for the numerical simulation and experimental results are shown in Fig. 8.

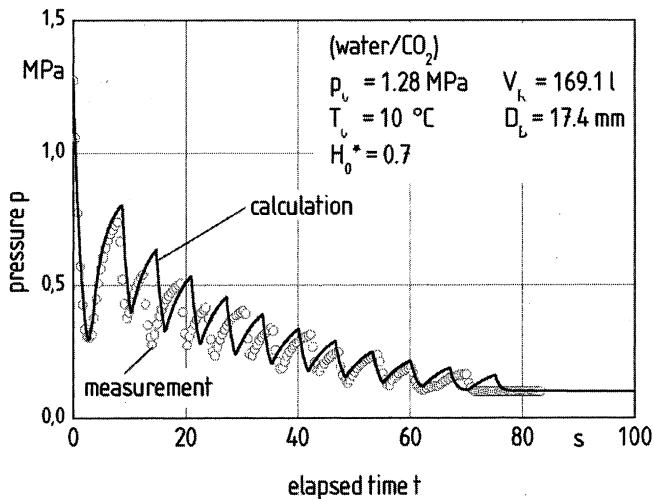


Fig. 8. Controlled pressure relief

6 Conclusion

Electrical tomography is used to measure the phase distribution during the blow-down of a pressurised vessel. The high time resolution allows to measure the alteration of the void fraction during the pressure relief process. The sensor is mounted in various axial positions in the column in order to gain the void fraction distribution in axial direction. For calculating the pressure and the mass-flow rate during blowdown an improved mathematical model is developed. By controlling a valve at the vessel outlet a maximum flowrate out of the vessel can be achieved, resulting in short blowdown times without liquid overflow.

Acknowledgements

The authors wish to thank the German Research Foundation (DFG) for financial support.

References

- Calderbank P (1967) Gas absorption from liquids. *Chem. Eng.* 212: 209-233
- Hori K, Fujimoto T, Kawaniski K, Nishikawa H (1997) Advanced high speed X-ray CT scanner for measurements and visualization of multiphase flow. *Proc. OECD/CSNI Specialist Meeting, Santa Barbara, CA, Mar. 1997*
- Idogawa K, Ikeda K, Fukuda T, Morooka S (1986) Behaviour of bubbles of the air-water system in a column under high pressure. *Int. Chem. Eng.* 26: 468-474
- Johansen GA, Froenstien T, Hjertaker BT, Olsen O (1996) A dual sensor flow imaging tomographic system. *Meas. Sci. Technol.* 7: 297-307
- Kumar SB, Moslemian D, Dudukovic MP (1997) Gas-holdup measurements in bubble columns using computed tomography. *AIChE J.* 43: 1414-1425
- Menzel T (1990) Die Reynolds-Schubspannung als wesentlicher Parameter zur Modellierung der Strömungsstruktur in Blasensäulen und Airlift-Schlaufenreaktoren (in German). VDI-Verlag, Düsseldorf, Germany
- Millies M, Mewes D (1996) Phasengrenzflächen in Blasenströmungen, Teil 1: Blasensäulen (in German). *Chem.-Ing.-Tech.* 68: 660-669
- Reinecke N, Mewes D (1991) Tomographic imaging of trickle-bed reactors. *Chem. Eng. Sci.* 51: 2131-2138
- Reinecke N, Petritsch G, Mewes D (1997) Reconstruction of limited view problems by using adapted coordinates. *Proc. Fluid Engineering Division Summer Meeting, Vancouver, Aug. 1997*
- Reinecke N, Boddem M, Petritsch G, Mewes D (1998) Tomographic imaging of the phase distribution in two phase slug flow. *Int. J. Multiphase Flow* 24: 617-634
- Sederman AJ, Johns ML, Bramley AS, Alexander P, Gladden LF (1997) Magnetic resonance imaging of liquid flow and pore structure within packed beds. *Chem. Eng. Sci.* 52: 2239-2250

- Toye D, Marchot P, Crine M, L'Homme E (1994) The use of large scale computer assisted tomography for the study of hydrodynamics in trickling filters. *Chem. Eng. Sci.* 49: 5271-5280
- Zuber N, Findlay J (1965) Average volumetric concentration in two-phase flow systems. *Journal Heat Transf.* 87: 453-463

Publications during this project (chronological order)

- Reinecke N, Petritsch G, Schmitz D (1997) Tomographische Meßverfahren - Visualisierung zweiphasiger Strömungsfelder (in German); *Chem. Ing. Technik* 69: 1379-1394
- Petritsch G, Schmitz D, Mewes D (1998) Influence of the fluid properties on the void-fraction distribution in a bubble column. 2nd Int. Symp. Measuring Techniques for Multiphase Flows, Beijing, China
- Schmitz D, Petritsch G, Mewes D, Moser F (1998) Tomographic Measurement of the liquid hold-up in a structured packing; *ASME Mech. Engng. Int. Congr. & Expos. (IMECE 98)* Anaheim, USA
- Schmitz D, Petritsch G, Mewes D (1998) Tomographic imaging of the void distribution in bubble columns during blowdown; *Proc. of ICMF 98, 3. Int. Conf. Multiphase Flow*, Lyon, France
- Reinecke N, Petritsch G, Schmitz D, Riest K, Mewes D (1998) Tomographic measurement techniques for multiphase flow applications; *ACHEMASIA 98, Int. Meeting on Chem. Eng. and Biotechn.*, Beijing, China
- Schmitz D, Mewes D (1999) Tomographic imaging of transient multiphase flow in bubble columns; *Chem. Engng. J.* 77: 99-104
- Lörcher M, Schmitz D, Mewes D (1999) Tomographic measurement techniques - Visualization of multiphase flows. In: *Machine Graphics & Vision 8*, Polish Akad. of Sciences, Warsaw, Poland
- Schmitz D, Petritsch G, Mewes D (1999) Tomographic Image of the Void Distribution in Bubble Columns during Blowdown, 1st World Congress on Industrial Tomography, Buxton, England
- Lörcher M, Schmitz D, Mewes D (1999) Tomographic measurement techniques - Visualisation of multiphase flows. *Euromech 406*, Warszawa, Poland
- Mewes D, Schmitz D (1999) Tomographic methods for the analysis of flow pattern in steady and transient flows, *Proceedings of the 2nd Int. Symposium on Two-Phase Flow*
- Brodhagen A, Schmitz D, Mewes D (1999) Experimental and theoretical investigation on blowdown of pressurized vessels. *Proceedings of the 2nd Int. Symposium on Two-Phase Flow Modelling and Experimentation*, Pisa, Italy
- Brodhagen A, Schmitz D, Mewes D (1999) Stoffübergang und spezifische Phasengrenzfläche während schneller Druckänderungen in Blasensäulen (in German). *GVC-Jahrestreffen der Verfahreningenieure*, Leipzig, Germany, *Chem. Ing. Technik* 71: 1036
- Mewes D, Schmitz D (2000) Analysis of the flow patterns in pipes and packings using tomographic methods. 2000 ASME Fluids Engng. Summer Conf., Boston, USA, FEDSM 2000-11341 (invited paper)

- Schmitz D, Brodhagen A, Mewes D (2000) Dynamic simulation of the pressure relief of chemical reactors. Two-Phase-Flow-Group-Meeting, Karlsruhe, Germany
- Schmitz D, Brodhagen A, Mewes D (2000) Two-phase flow in pressure relief and blow-down systems. 2nd Japanese-European Two-Phase-Flow Group Meeting, Tsukuba, Japan
- Schmitz D, Brodhagen A, Mewes D (2001) Experimental investigation and numerical simulation of pressure relief in chemical reactors. 10th Int. Symp. Loss Prevention & Safety Promotion in the Process Industries, Stockholm, Schweden
- Schmitz D (2002) Tomographische Messungen in gasentlösenden Systemen (in German). Ph.D. thesis, University of Hannover, Germany

X-ray Based Particle Tracking Velocimetry for Bubble Columns with High Void Fraction

Seeger, A., Kertzscher, U., Affeld, K., Goubergrits, L., Wellnhofer, E.

Biofluidmechanics Lab, Charité, Spandauer Damm 130, 14050 Berlin, Germany

German Heart Institute Berlin, Augustenburger Platz 1, 13353 Berlin, Germany

1 Introduction

Bubble columns are liquid filled vertical tubes which are aerated - usually from the bottom. They are widely used in biotechnology and chemical engineering, e.g., for yeast production and wastewater treatment. Despite their widespread application, the flow phenomena in these apparatus is not yet fully understood. Velocity measurements are required for a better understanding of the fluid mechanics as well as for the development of mathematical models for the computational fluid dynamics (CFD) (Pfleger & Becker, 2001, Dudukovic, Larachi, & Mills, 1999). The problems of the current methods available for the measurement of the liquid velocity are briefly described below.

All optical methods based on visible light (Laser Doppler Velocimetry, Particle Image Velocimetry, Particle Tracking Velocimetry) face the problem of reflection and refraction of light at the gas-liquid boundaries (Larue de Tournemine, Roig, & Suzanne, 2001; Chen et al., 1994, Borchers & Eigenberger, 2000; Mudde, Groen, & Akker, 1998). These methods can therefore only be applied when bubbles are not obscuring the path of the light. This means that these methods are only applicable for a bubble column with a small void fraction. Larue de Tournemine, Roig, & Suzanne (2001) report that void fraction in bubble columns should be below 5 % when optical methods are to be applied. This value also depends on the bubble size distribution and the length of the optical path. Other authors like Mudde, Groen, & Akker (1998) made averaging measurements with Laser Doppler Velocimetry (LDV) at 25 % void fraction. However, the data acquisition rate was low (e.g. with a length of the optical path of 75 mm the data acquisition rate was 0.1 Hz). LDV yields only limited information - point measurement - about the flow. Time dependent flow structures cannot be measured.

Hot Film Velocimetry (Franz et al., 1984) and the electrodiffusion method (Pauli, 1991) can be applied, to a large extent, independently from the void fraction. Like LDV, Hot Film Velocimetry allows only point measurements. An additional disadvantage of this method is that the probes disturb the flow itself.

Another method is the of Computer Aided Radioactive Particle Tracking (CARPT). A radioactive particle with a diameter of 2.38 mm is added to the flow (Chen et al., 1999). Radioactive radiation penetrates the flow in straight lines. The radioactive particle represents the flow of the liquid phase and is tracked. This measurement technique is very time and money consuming (measurement time: approximately 20 hours).

The only multi-point measurement method which works independently from the void fraction is X-ray based Particle Tracking Velocimetry (XPTV). X-rays penetrate a multi-phase flow in straight lines. They are neither refracted nor reflected at phase boundaries. The method is a three-dimensional, three component method. It enables us to obtain a mean velocity field of the region of interest within 20 seconds (Seeger et al., 2001, Seeger et al., 2002). This method is presented here.

2 Method

The liquid is seeded with X-ray absorbing particles. These particles have the same density as the liquid. It is assumed that the particles represent the liquid velocity (see section about the particles). Therefore, the liquid motion itself can be derived from the particle motion.

X-rays penetrate a gas-liquid interface in straight lines. Thus the problems described above, i.e. those of an observation using visible light - refraction and reflection - do not occur.

The experimental set-up is shown in figure 1. Two X-ray-sources S1 and S2 generate X-rays, which are directed through the bubble column onto the image intensifiers. The image intensifiers convert X-rays into visible light and intensify it. Digital cameras behind the image intensifier record the images. An X-ray absorbing particle, represented by point P, is mapped on the two image intensifiers I1 and I2, generating the points P1 and P2. The straight lines G1 and G2, which connect P1 and P2 and the X-ray sources are calculated and the point of their nearest distance is the reconstructed point P. By recording a series of images, the motion of a particle can be observed. The velocity of the particle can be obtained by its displacement and the time difference between the images. By the observation of many particles (in this case between 50 and 80) over a defined period, a vector field can be calculated. The method resembles optical 3D-PTV.

2.1 Device

A medical X-ray device (Philips Integris BH 3000) was used for the experiments. It is clinically used for the flow visualization in human coronary blood vessels. The German Heart Center in Berlin (DHZB) provided this device.

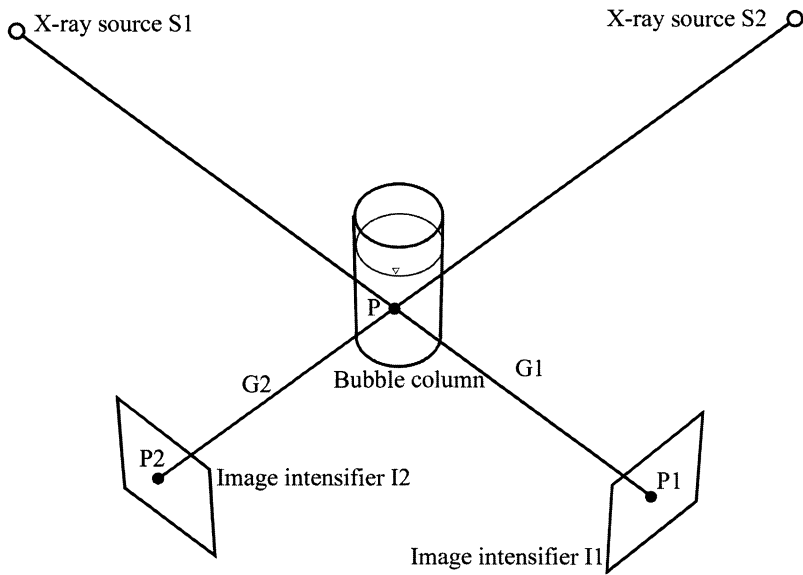


Fig. 1. Experimental set-up

The input screens of the image intensifiers had a diameter of 23 cm. The image intensifiers had a resolution of 1024x1024 pixel. The digital cameras behind the image intensifiers transformed the X-ray intensities into digital 8 bit grayscale images. A digital camera had a resolution of 512x512 pixels. X-ray flashes were generated and images were recorded every 20 ms alternating between each X-ray system, thus 25 image pairs per second were recorded. The time delay between the first and second image made the three-dimensional reconstruction difficult. On one hand it limited the number of traceable particles (50-80) and on the other hand it limited the maximum traceable velocity. The time delay between the two images was not adjustable. A time delay between the images is necessary, because X-rays from source S1 are scattered at the bubble column and the scattered X-rays would greatly reduce the image quality in the image intensifier I2. Image series of up to 1000 images (500 image pairs) can be recorded. The volume under analysis had a size of about 104 mm x 104 mm x 104 mm.

2.2 Particles and liquid

Particle Tracking Velocimetry (PTV) is based on the observation of particles that move with the liquid in question. The particles have to have the same density as the liquid - in this case glycerin. In addition, they must be able to absorb X-rays. Particles were manufactured at the Biofluidmechanics Lab according to these requirements. They have a cubic shape with the dimensions of $2.1 \times 2.1 \times 2.1 \text{ mm}^3$. The cubic shape was chosen due to fabrication reasons. The particles were made

of polyurethane foam with a cylindrical insert of a lead alloy with a length of 2.1 mm and a diameter of 0.5 mm. The alloy absorbs X-rays, whilst the foam makes the cubes buoyant. Despite their size, it was possible to measure flow structures accurately by the use of these particles, because they were small in comparison with the typical flow structures in our flow system. The reason for this is that the experiments are performed with glycerin as a liquid, which is highly viscous compared with water. Glycerin was used because it led to a slower flow, therefore making the particle velocity lower and the particle tracking easier.

The performance of the particle in a vortex was investigated theoretically to prove that the particles represent the liquid flow. The particle was assumed to be in a vortex 10.00 mm away from its center. The vortex had a velocity of five revolutions per second. The calculation returned that the distance of the particle from its initial position after one revolution was small. It was about 10.03 mm. This indicates that the particle follows a glycerin flow very well.

2.3 Software

The software works with the following steps:

1. Particle recognition: The first step recognizes the particles on the grayscale images. The algorithm enables us to detect whether a pixel is much darker than its surroundings. If this is so, it could be the case that the pixel may belong to the particle itself. A second step helps us decide whether the pixel belongs to a particle or not. If a selected area of pixels, which may possibly belong to a particle, has a size of between 10 and 45 pixels, this area is generally recognized as a particle.
2. Distortion correction: The distortion correction is necessary because the image intensifier works with a curved input screen, leading to what is known as pin-cushion distortion. This step enables us to correct the distortion.
3. Particle Tracking: The particles are tracked two-dimensionally with a standard next neighborhood-algorithm (resembling the one of Guezennec et al. (1994))
4. Isocenter correction (see below)
5. Reconstruction of the three-dimensional trajectories: Both orthogonal two-dimensional trajectories are combined to obtain the three-dimensional trajectories.
6. Calculation of a velocity field: The velocity field is calculated assuming that the flow during the measurement time is stationary (see also results section).

All algorithms are described in detail in Seeger et al. (2001). However, the isocenter correction used has been improved since then, allowing us to increase the number of reconstructed particles by up to 50 %. This is described here in more detail.

The isocenter correction rectifies the insufficient positioning of the two "X-ray source - image intensifier" units. If straight lines connect the centers of the image intensifiers and the corresponding X-ray sources, ideally they should touch each other at the so-called isocenter. However, in reality they do not.

To correct this error, the isocenter correction is performed. Images of about 300 randomly distributed points in space are taken. A grid with X-ray absorbing, non-moving particles are placed in different positions of the investigation area to do this. It is essential to know which point on image intensifier I1 corresponds with which point on image intensifier I2. Straight lines between the mapped points on the image intensifiers and the X-ray sources were calculated. The corresponding lines should touch each other - in reality, they do not. Therefore, the distance between the corresponding lines was calculated. A virtual change of the positions of the image intensifiers and of the X-ray sources minimized this distance. However, it had to be considered that: (1) The virtual position change of the X-ray sources and the image intensifiers have to be small. (2) It is necessary to yield a true scale.

The latter is possible since the distances among the randomly distributed points in space are known. The algorithm yielded the new coordinates of the X-ray sources and the image intensifiers. The mean initial distance between the straight lines was 16 mm. The mean distance was 1.8 mm after the isocenter correction. One has to consider that the points in space are recognized by a particle recognition algorithm, which has, as well as the distortion correction, an influence on the accuracy of the algorithm. The whole algorithm reconstructs between 59 % and 76 % of the recognized particles in the three-dimensional space.

2.4 Bubble column

The method was applied to a cylindrical bubble column. It had an inner diameter of 104 mm and a filling height of 100 mm. 91 hypodermic needles with an inner diameter of 0.34 mm were used as gas dispersers. The use of these needles made the gas distribution uniform. A disc was mounted at the tip of the needles to prevent any possible flow between them (see figure 2).

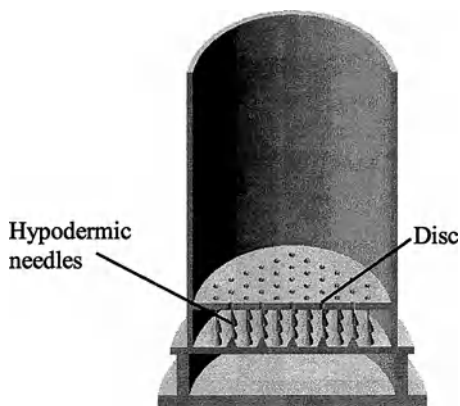


Fig. 2. Bubble column. It has an inner diameter of 104 mm. 91 hypodermic needles with an inner diameter of 0.34 mm are used as gas dispersers.

3 Results

3.1 Accuracy analysis and validation

Images from non-moving X-ray absorbing particles in the form of an X-ray absorbing tin grid (mesh width: 10 mm) were taken in different positions in order to calculate the accuracy of the 3D-reconstruction. The particle recognition algorithm recognizes the particles. Their position is rectified by the distortion correction and they are reconstructed in the three-dimensional space by the reconstruction algorithm. Therefore, all algorithms could be verified except the particle tracking algorithm.

The mean distance between the straight lines yielded by the connection of the mapped points on the image intensifiers and the X-ray sources (G1 and G2 in figure 1) was calculated. It was 1,8 mm (standard deviation: 1,7 mm).

Since the geometry of the tin grid is known, the scale accuracy could be calculated. For a distance of 10 mm, the error was 0,02 mm (standard deviation: 0,43 mm). The angular error was $2,1^\circ$ (standard deviation: $1,5^\circ$). These values are comparable with results from other authors (Cheriet & Meunier, 1998).

The method was validated in a bubble column with a rectangular cross section. The vertical velocity was measured in a height of 9 cm by three methods: LDV (Laser Doppler Velocimetry), optical PTV (Particle Tracking Velocimetry) (Borchers and Eigenberger, 2000), and XPTV (X-ray based Particle Tracking Velocimetry). The results obtained by the new XPTV method showed a strong similarity with the results measured by LDV and PTV. Moreover, the standard deviation of the vertical velocity was also found to be very similar. The detailed results are published in Seeger et al. (2001).

3.2 Measurements in a cylindrical bubble column

The measurements in the cylindrical bubble column were taken under different conditions. One example is shown here. The superficial gas velocity was set to 3 mm/s. The void fraction was about 8 %. The left-hand image of figure 3 shows a photo of the flow. The right-hand image of figure 3 shows the bubble column with a paper grid in the middle of the bubble column. The grid is visible only at the edges, which shows that optical methods cannot be applied in this case.

Particle trajectories consisting of 18607 velocity vectors were obtained by the algorithm. Some of them are shown in figure 4. A velocity field was calculated from the trajectories, which is shown in figure 5. It is a mean value of 470 image pairs. Since 25 images were taken per second, the recording time was about 18.6 s.

The visualization was performed with AMIRA (Indeed - Visual Concepts GmbH, Berlin), a software package for the visualization of three-dimensional data.

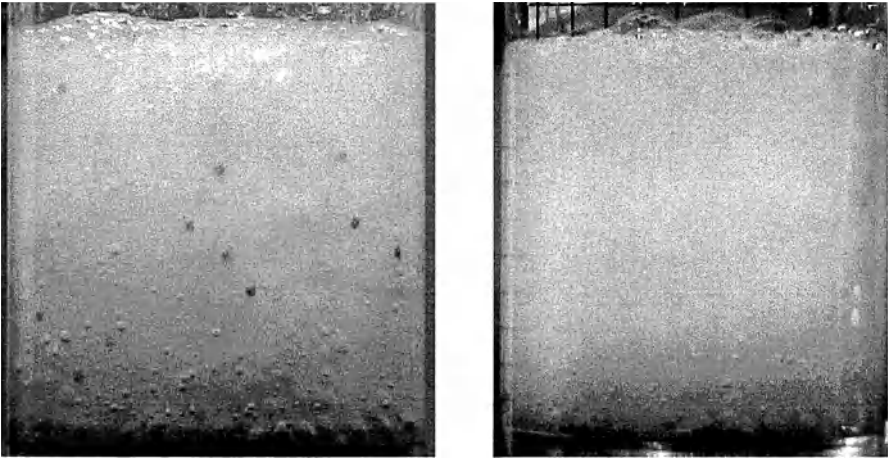


Fig. 3. Photo of the flow (left-hand side) and paper grid in the middle of the bubble column (right-hand side).

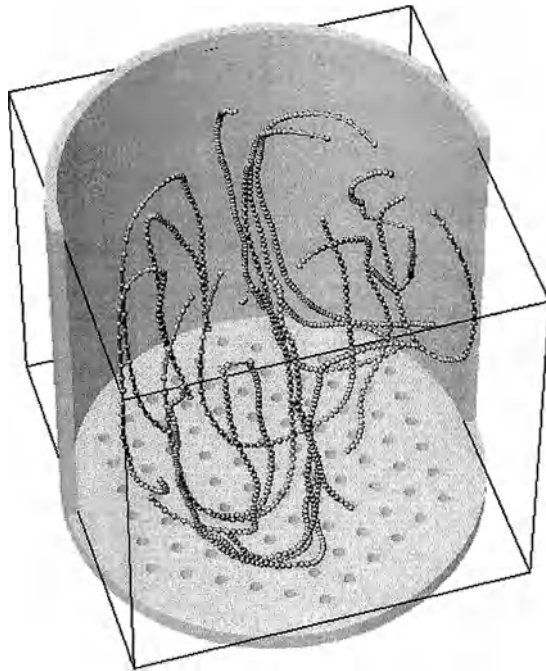


Fig. 4. Particle trajectories. The dots on the surface of the trajectories indicate the three-dimensionally reconstructed points belonging to a trajectory. The box represents the investigated area.

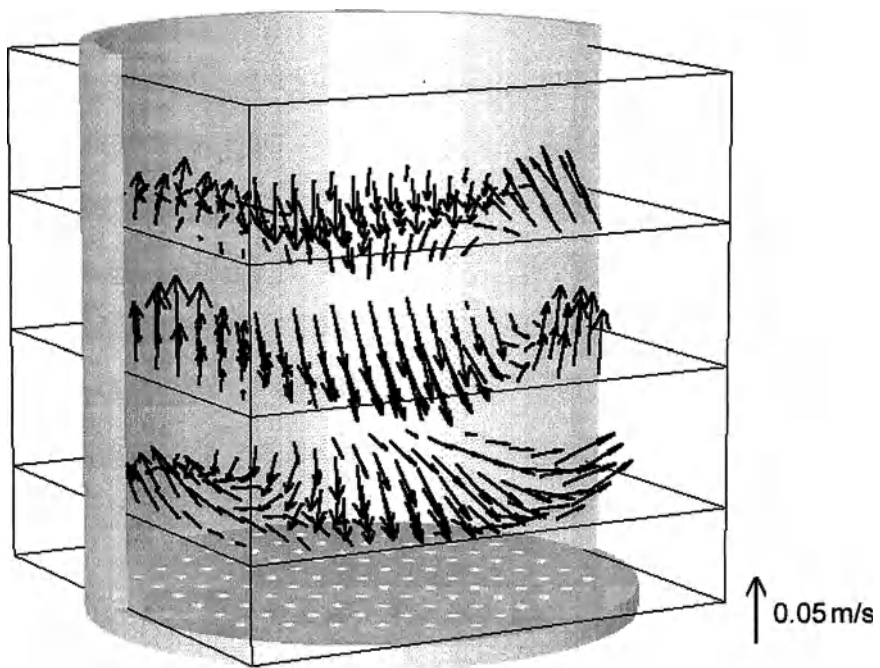


Fig. 5. Velocity field - calculated from the trajectories assuming a stationary flow.

To evaluate whether the velocity field was changing during the measurement, a velocity field was calculated for the first set of 235 images (image series 1) and the second set of 235 images (image series 2) separately. To do this, the trajectories were calculated separately for the two cases. 9480 velocity vectors in the trajectories were found in image series 1 and 9168 velocity vectors in the trajectories were found in image series 2. Again, velocity fields were calculated and they looked alike. The mean velocity in image series 1 was 22.7 mm/s and in image series 2 23.2 mm/s. The mean standard deviation in the investigated area was 26.5 mm/s and 30.2 mm/s respectively.

4. Discussion

X-ray based Particle Tracking Velocimetry proved to be suitable for the measurement of the three-dimensional velocity of the liquid phase of a bubble column. The main advantages of this technique are:

1. Reflection and refraction at the phase boundaries pose no problem - the application of this method is not limited by a large void fraction or by opaque fluids.
2. The method is a 3-dimensional, 3-component method.
3. It is a non-intrusive technique - the flow is not disturbed by probes.

4. The method is also applicable to regions with no optical access.
5. The time required for the acquisition of a 3-dimensional velocity field is small. In this case, it was 20 seconds. However, using a faster system would allow measurement times of less than 1 second (see below). This means that time dependent structures in bubble columns with water as liquid could be measured.
6. The method can also be applied to a three-phase flow (gas, solid, liquid), where the X-ray absorbing particles represent either the liquid or the solid phase. It is also possible to measure the velocity of the liquid and the solid phase simultaneously (see paper: Kertzscher et al.: "Measurement of the local liquid and the local solid velocity simultaneously" in this book).

The disadvantages of this method are:

1. The image frequency is small (25 image pairs per second).
2. Due to the fact that the particles have to be recognized on the pictures, the minimum particle size is limited.
3. The particle seeding density is low.
4. The use of X-rays is hazardous. However, this problem can be solved by the use of adequate precautions

Using a measurement system specially designed for two-phase flows - instead of the medical system - can reduce the first three problems. Such a system would apply:

- smaller particles with a smaller X-ray absorbing area to prevent particle overlapping (1 dimension smaller than the one used here - depending on the image resolution, the size of the investigated area etc.)
- 2 cameras taking 500 images per second, resolution 1024x1024 pixels
- 2 X-ray generators, 500 flashes/s
- 2 fast X-ray image intensifiers

Such a system can be composed for the price of a PIV systems including the laser. In the following paragraph, an estimation of the recording time for the measurement of a 3D-flow field is given:

It is assumed that a cubic vector field is to be calculated. There are 10 grid points in each direction. It is furthermore assumed that five trajectory vectors at these grid points are necessary to calculate a mean velocity field. The trajectory vectors are distributed so that five vectors are at each grid point. The seeding consists of 500 X-ray absorbing particles. With the help of the theoretical investigation of Guezennec et al. (1994), the necessary number of images for the calculation of the velocity field can be determined. In our case, it is 24 images. This corresponds to a recording time of 48 ms (at the maximal recording frequency of 500 image pairs per second). This is, of course, only a theoretical number and the real recording time would be longer. However, it shows, that XPTV can be extended to become a powerful technique for velocity measurements in multi-phase flows.

6 References

- Borchers O, Eigenberger G (2000) Particle Tracking Velocimetry for simultaneous investigation of liquid and gas phase in bubbly flow. 9th International Symposium of Flow Visualisation, Edinburgh
- Chen JAK, Al-Dahhan MH, Dudukovic MP, Lee, DJ, Fan LS. (1999) Comparative hydrodynamics study in a bubble column using computer-automated radioactive particle tracking (CARPT) / computed tomography (CT) and particle image velocimetry (PIV). Chem Eng Sci 54: 2199-2207
- Chen RC, Reese J, Fan LS (1994) Flow structures in a three-dimensional bubble column and three-phase fluidized bed. AIChE J 40: 1093-1104
- Cheriet F, Meunier J (1998) Self-calibration of a biplane X-ray imaging system for an optimal three dimensional reconstruction. Computerized Medical Imaging and Graphics 23: 133-141
- Dudukovic MP, Larachi F, Mills PL (1999) Multiphase reactors - revisited. Chem Eng Sci 54: 1975-1995
- Franz K, Borner T, Kantorek HJ, Buchholz R (1984) Flow structures in bubble columns. Germ Chem Engng 7: 365-374
- Guezennec YG, Brodkey RS, Trigui N, Kent JC (1994) Algorithms for fully automated three-dimensional particle tracking velocimetry. Exp Fluids 17: 209-219
- Larue de Tournemine A, Roig V, Suzanne C (2001) Experimental study of the turbulence in bubbly flows at high void fraction. Proceedings of the 4th International Conference on Multiphase Flow, New Orleans, U.S.A., May 27 – June 1, 2001
- Mudde RF, Groen JS, Van Den Akker HEA (1998) Application of LDA to bubbly flows. Nucl Eng and Des 184: 329-338
- Pauli J (1991) Einsatz der Elektrodifusionsmeßtechnik in Gas-Flüssigkeitsströmungen mit Sauerstoff als Polarisator. VDI-Fortschrittsberichte Reihe 3 no 278
- Pfleger D, Becker S (2001) Modelling and simulation of the dynamic flow behaviour in a bubble column. Chem Eng Sci 56: 1737-1747
- Raffel M, Willert C, Kompenhans J (1998) Particle Image Velocimetry. Springer, Berlin Heidelberg New York
- Seeger A, Affeld K, Goubergrits L, Kertzsch U, Wellnhofer E (2001) X-ray-based assessment of the three-dimensional velocity of the liquid phase in a bubble column. Exp Fluids 31: 193-201
- Seeger A, Affeld K, Goubergrits L, Kertzsch U, Wellnhofer E, Delfos R (2002) X-ray based flow visualization and measurement: Application in multi-phase flows. Annals of the New York Academy of Science 972: 247-253

Multi-Level Modelling of Dispersed Gas-Liquid Two-Phase Flows

M. van Sint Annaland, N.G. Deen and J.A.M. Kuipers

Fundamentals of Chemical Reaction Engineering,
Faculty of Science and Technology, Twente University,
P.O. Box 217, NL-7500 AE Enschede, The Netherlands

1. Introduction

Dispersed gas-liquid two-phase flows are encountered in a variety of industrial processes such as the large-scale production of synthetic fuels and base chemicals employing bubble column reactors. Despite their widespread industrial application the detailed understanding of the fluid mechanics prevailing in bubble column reactors is unfortunately lacking (Tomiya, 1998), which can be related to the inherent complexity of the underlying physical phenomena in (dense) bubbly flows such as bubble-liquid interaction (including turbulence) and bubble-bubble interaction (including coalescence and break-up).

Flows encountered in bubble columns are inherently unsteady (Sokolichin and Eigenberger, 1994) and display a wide range of time and length scales and as a direct consequence therefore we adopted a multi-level modelling approach consisting of several levels (see Fig. 1) each with its own particular strong point. At the lowest level (*i.e.* the smallest time and length scale) we use the Front Tracking (FT) approach originally developed by Tryggvason and co-workers (Unverdi and Tryggvason, 1992) to study the behaviour of a single bubble or a few (interacting) bubbles. The idea is that simulations

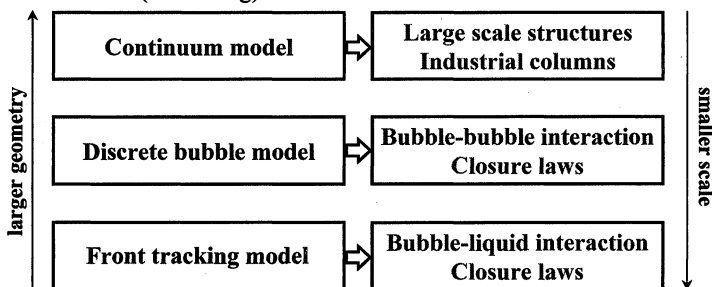


Figure 1. Multi-level approach for modelling of dispersed gas-liquid two-phase flow. For each level of modelling the typical application area is indicated.

using the FT approach should generate insight in the behaviour of a single rising gas bubble or the behaviour of a few rising gas bubbles and provide closures for bubble-liquid interaction. At the intermediate level (*i.e.* the intermediate time and length scale) we use the Euler-Lagrange (EL) or discrete bubble approach, which is particularly suited to account for bubble-bubble and/or bubble-wall encounters. Because, contrary to the FT approach, the flow field at the scale of an individual bubble is not resolved, closure laws for bubble-liquid interaction (drag, lift and added mass) have to be provided. At the highest level (*i.e.* the biggest time and length scale) we use the Euler-Euler (EE) or continuum approach, which is particularly suited to model bubbly flows in industrial scale bubble columns. Similar to the EL approach closures for bubble-liquid and bubble-bubble interaction have to be provided.

Subsequently the three levels of modelling will be discussed in more detail together with some illustrative computational results, which have been obtained from the respective models.

2. Front Tracking model

To model complex multiphase free surface flows a Front Tracking method based on direct numerical simulation has been introduced by Univerdi and Tryggvason (1992). Contrary to other numerical models developed to simulate multiphase flows, like the Level Set or Marker and Cell methods (Welch *et al.*, 1965) and Volume of Fluid methods (Nichols and Hirt, 1971; Youngs, 1982, 1987), the Front Tracking method uses an unstructured dynamic mesh to represent the interface surface and tracks this interface explicitly by the interconnected marker points. The Lagrangian representation of the interface avoids the necessity to reconstruct the interface from the local distribution of the fractions of the phases and, moreover, allows a direct calculation of the surface tension forces without the inaccurate numerical computation of the interface curvature, as is required in the Continuum Surface Force-method (CSF) introduced by Brackbill *et al.* (1992).

For incompressible bubbly flows the Navier-Stokes equations describing the fluid motion inside and outside the bubbles can be combined into a single vector equation for the fluid velocity \vec{u} in the entire domain when accounting for the local volumetric surface tension forces \vec{F}_σ , since the transport equation for the colour function F , indicating the local instantaneous liquid fraction, can be reduced to a passive scalar equation. Thus, the governing conservation equations for unsteady, incompressible, immiscible, Newtonian, two-fluid flow systems are given by:

$$(\nabla \cdot \vec{u}) = 0 \tag{2.1}$$

$$\frac{\partial}{\partial t}(\rho \bar{u}) + (\nabla \cdot \rho \bar{u} \bar{u}) = -\nabla p + \rho \bar{g} + \left(\nabla \cdot \mu \left[(\nabla \bar{u}) + (\nabla \bar{u})^T \right] \right) + \bar{F}_\sigma \quad (2.2)$$

where the local averaged density ρ and viscosity μ are evaluated from the local distribution of the indicator function F . For the local average density linear weighing of the gas and liquid densities is used:

$$\rho = F \rho_l + (1 - F) \rho_g \quad (2.3)$$

Usually the local average dynamic viscosity is also obtained via linear averaging of the gas and liquid dynamic viscosities. In this work an alternative, more fundamental approach recently proposed by Prosperetti (2001) has been applied, where the local average viscosity is calculated via harmonic averaging of the kinematic viscosities:

$$\frac{\rho}{\mu} = F \frac{\rho_l}{\mu_l} + (1 - F) \frac{\rho_g}{\mu_g} \quad (2.4)$$

The Navier-Stokes equations have been solved with a finite volume technique on a staggered rectangular three-dimensional grid using a two-step projection-correction method with an implicit treatment of the pressure gradient and explicit treatment of the convection and diffusion terms. A second order flux delimited Barton-scheme (Centrella and Wilson, 1984) has been used for the discretisation of the convection terms and standard second order central finite differences for the diffusion terms. In order to be able to simulate systems with very large density ratios, the Navier-Stokes equations have been rewritten in their non-conservative form using the total continuity equation,

$$\rho \left[\frac{\partial \bar{u}}{\partial t} + (\nabla \cdot \bar{u} \bar{u}) \right] = -\nabla p + \rho \bar{g} + \left(\nabla \cdot \mu \left[(\nabla \bar{u}) + (\nabla \bar{u})^T \right] \right) + \bar{F}_\sigma \quad (2.5)$$

where the density in the term on the left hand side has been discretised explicitly in time.

The local distribution of the indicator function F is computed from the location of the triangulated interface by solving a Poisson-equation, following the method proposed by Univerdi and Tryggvason (1992):

$$\nabla^2 F = \nabla \cdot \sum_m D(\bar{x} - \bar{x}_m) \bar{n}_m \Delta s_m \quad (2.6)$$

where the summation is carried out over all markers m representing the interface, using \bar{n}_m to denote the outwardly pointing normal on interface element m and Δs_m its surface area. The function D represents a numerical approximation of the Dirac-function

normalised to the cell volume. In this work volume weighing proved to be sufficiently stable, but a distribution function as suggested by Peskin (1977) could be applied to smoothen the interface, however, at the expense of a significantly increased size of the computational stencil, thus requiring more Eulerian grid cells. A robust Incomplete Cholesky Conjugate Gradient (ICCG) algorithm has been used to solve the Poisson equation for the F -field.

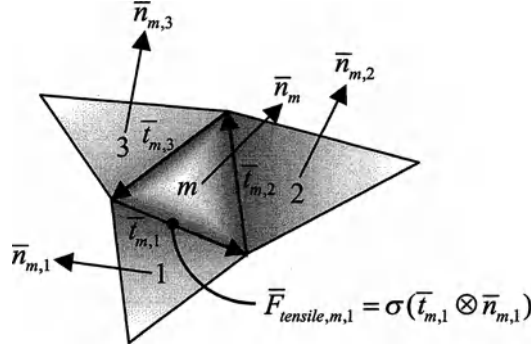


Figure 2. Schematic representation of the calculation of the three tensile forces acting on the three edges of interface marker m .

The surface tension forces are computed from the tensile forces on the three edges ℓ of all interface markers m (see Fig. 2), which are subsequently distributed to the Eulerian grid via volume weighing.

$$\bar{F}_\sigma = \sum_m \sum_\ell D(\bar{x} - \bar{x}_{m,\ell}) \sigma(\bar{t}_{m,\ell} \otimes \bar{n}_{m,\ell}) \quad (2.7)$$

where $\bar{t}_{m,\ell}$ denotes the tangential vector to edge ℓ of marker m . Note that in this work the normal and tangent vectors of the edges of the elements are used, which can be obtained directly from the interface marker data, in contrast to the method used by Tryggvason *et al.* (2001), where a polynomial fit for the interface is constructed from which the normal and tangent vectors to the elements are calculated.

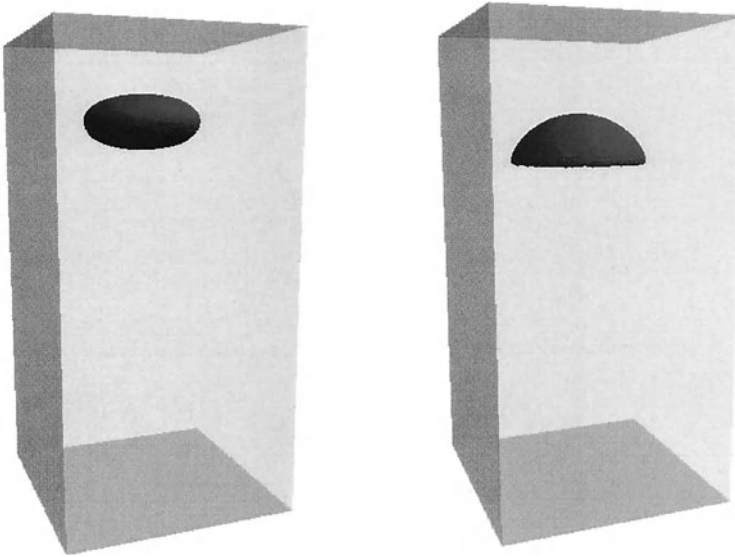
The Lagrangian handling of the interface marker points deforms the triangular surface elements. To maintain an adequate resolution of the interface, the elements are reshaped in case the aspect ratio of the element edges becomes too large and elements are added or deleted in case the length of one of the edges becomes too large or too small compared to the Eulerian grid size, following Univerdi and Tryggvason (1992).

Some computational results with the Front Tracking model for a few selected cases will be shown to illustrate the capabilities of the model.

Results Front Tracking model

With the Front Tracking model the shape of a bubble and the bubble rise velocity can be calculated as a function of the physical properties of the bubble and continuous phase and the bubble volume. In Fig. 3 the final bubble shape computed with the Front Tracking model for a single initially spherical bubble released in an initially quiescent liquid in a small column is given for two different sets of physical properties listed in Table 1. For the first case (Fig. 3a) a very high density and viscosity ratio and a very high surface tension coefficient were selected to demonstrate the capabilities of our implementation of the Front Tracking model to handle these systems that often give rise to numerical problems. For this case an ellipsoidal bubble shape was calculated, while for the second case (Fig. 3b) with the main difference a much lower surface tension coefficient, a spherical-cap bubble shape was finally obtained, as expected because of the lower surface tension forces (see Grace, 1973). For the second case the initially spherical bubble changes into a bubble with a large indentation at the bottom of the bubble, while the top of the bubble remains perfectly smooth and convex. Then, the bubble shape slowly changes into a hemisphere with an almost perfectly flat bottom. For these calculations typically about 10^4 markers were used and after about 0.2 s simulation time about 10^5 markers were added and a similar number of markers deleted. The bubble volume was conserved typically within a few %. The computed terminal bubble Reynolds-numbers compared very well with experimental results summarized by Grace (1973): 84 vs. 90 for the first case and 51 vs. 60 for the second case (see Table 1). Increasing the column width and depth compared to the bubble size, obviously at the cost of larger computational times, can even further decrease the small discrepancy in the terminal rise velocities.

Also the interactions of bubble wakes on other bubbles can be investigated with the Front Tracking model. Results of a sample calculation, where three initially spherical bubbles were released in an initially quiescent liquid in a small column, are shown in Fig. 4. Firstly, the two lower bubbles on the left and right side are accelerated in the wake of the top bubble and almost catch up with the bubble in the centre (at $t=0.15$ s). Then, the two bubbles on both sides are pushed towards the free-slip walls, where they are again slowed down due to the downwards flowing liquid ($t=0.25$ s).



(a) Case I (at $t = 0.16$ s)

(b) Case II (at $t = 0.20$ s)

Figure 3. Final bubble shape of an initially 0.02 m diameter spherical bubble in an initially quiescent liquid in a square column of 0.05 m x 0.05 m x 0.10 m released at position (0.025 m, 0.025 m, 0.025 m), calculated with the Front Tracking model using a 50 x 50 x 100 grid and a time step of $1.0 \cdot 10^{-4}$ s, for two cases with different physical properties for the bubble and continuous phase (listed in Table 1). (Free-slip boundary conditions.)

Table 1. Physical properties used for the numerical simulations of the final bubble shape (shown in Fig. 2) and terminal Re-number computed with the Front Tracking model and compared with experimental data taken from Grace (1973).

		Case I	Case II
Bubble phase	Density ρ_g	(kg/m^3)	1.0
	Viscosity μ_g	($\text{kg/m}\cdot\text{s}$)	$1.0 \cdot 10^{-5}$
	Bubble diameter d_b	(m)	0.02
Continuous phase	Density ρ_l	(kg/m^3)	1000
	Viscosity μ_l	($\text{kg/m}\cdot\text{s}$)	0.1
	Surface tension σ	(N/m)	1.0
	$Eo (= g\Delta\rho d_b^2/\sigma)$	(-)	3.9
	$M (= g\mu_l^4\Delta\rho/\rho_l^2\sigma^3)$	(-)	$9.8 \cdot 10^{-7}$
	Computed $Re_b (= \rho_l u_b d_b / \mu_l)$	(-)	84
	Experimental $Re_b (= \rho_l u_b d_b / \mu_l)$	(-)	~ 90
			~ 60

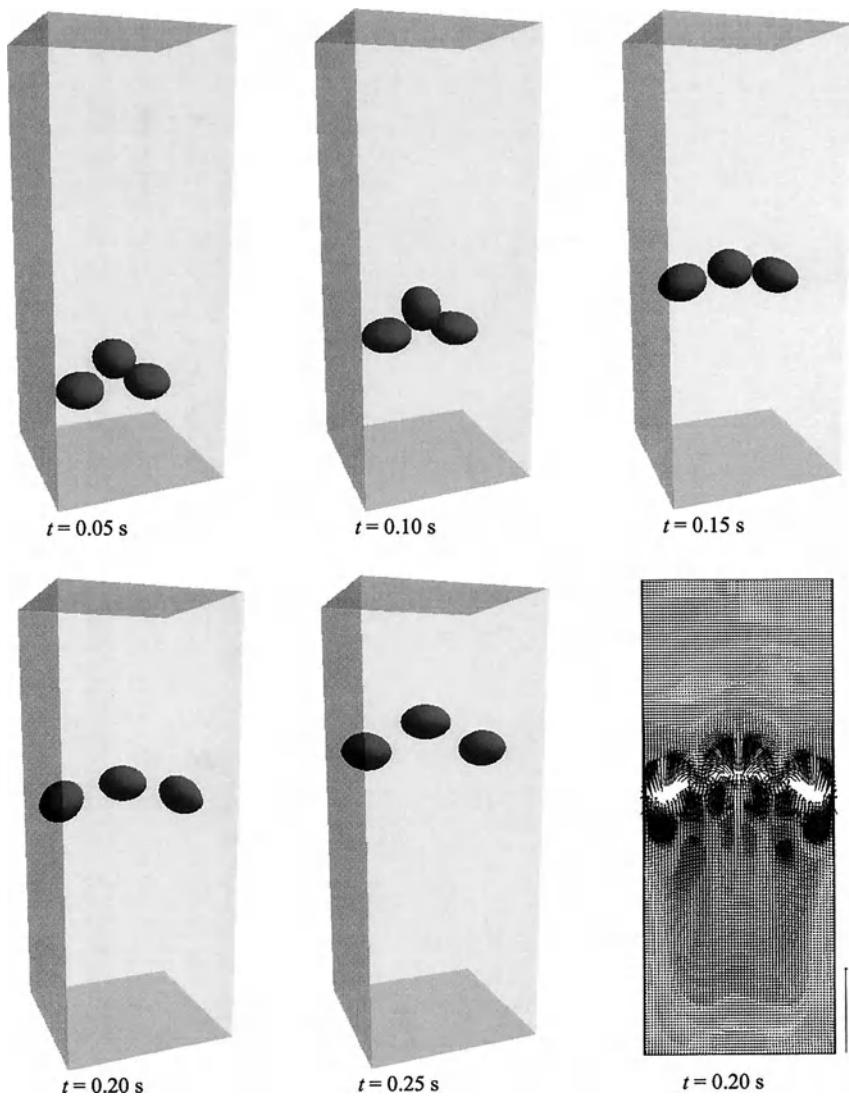


Figure 4. Snapshots at different times of three initially spherical bubbles of 0.016 m diameter released at positions (0.015 m, 0.030 m, 0.015 m), (0.045 m, 0.030 m, 0.015 m) and (0.030 m, 0.030 m, 0.025 m) in an initially quiescent liquid in a square column of 0.05 m x 0.05 m x 0.10 m, calculated with the Front Tracking model using a 60 x 60 x 150 grid and a time step of $1.0 \cdot 10^{-4}$ s. Also the velocity field at the central plane at $t=0.20$ s is shown (reference vector: 1.0 m/s). (Physical parameters: $\rho_g = 10 \text{ kg/m}^3$, $\mu_g = 0.001 \text{ kg/m}\cdot\text{s}$, $\rho_l = 1000 \text{ kg/m}^3$, $\mu_l = 0.1 \text{ kg/m}\cdot\text{s}$, $\sigma = 1.0 \text{ N/m}$). (Free-slip boundary conditions.)

3. Euler-Lagrange model

Our Euler-Lagrange model is based on volume-averaged continuity and momentum equations given below to compute the liquid phase flow field.

$$\frac{\partial}{\partial t}(\varepsilon_l \rho_l) + (\nabla \cdot \varepsilon_l \rho_l \bar{u}_l) = 0 \quad (3.1)$$

$$\frac{\partial}{\partial t}(\varepsilon_l \rho_l \bar{u}_l) + (\nabla \cdot \varepsilon_l \rho_l \bar{u}_l \bar{u}_l) = -\varepsilon_l \nabla p - (\nabla \cdot \varepsilon_l \tau_l) - \bar{S}_{l \rightarrow b} + \varepsilon_l \rho_l \bar{g} \quad (3.2)$$

The viscous stress in the liquid phase is assumed to obey the general Newtonian form where the shear viscosity consists of the sum of a laminar and a turbulent contribution, where the latter is computed from a simple SGS turbulent viscosity model given by:

$$\mu_{l, \text{turbulent}} = \rho_l (C_s \Delta)^2 \sqrt{S^2} \quad (3.3)$$

where C_s equals 0.1, Δ represents the filter width and S the rate of strain tensor, respectively given by the following expressions:

$$\Delta = (\Delta x \Delta y \Delta z)^{\frac{1}{3}} \quad \text{and} \quad \bar{S}^2 = \frac{1}{2} \sum_i \sum_j \left(\frac{\partial u_i}{\partial x_j} + \frac{\partial u_j}{\partial x_i} \right)^2 \quad (3.4)$$

Two-way coupling is achieved via a source term which can be computed from the positions and velocities of the bubbles. To obtain this information for each individual bubble the equation of motion is solved taking into account the action of external forces due to gravity, pressure, drag, lift and virtual mass:

$$\begin{aligned} \frac{d}{dt}(m_b \bar{w}_b) = m_b \bar{g} - V_b \nabla p + C_D A_b \frac{1}{2} \rho_l |\bar{u}_l - \bar{w}_b| (\bar{u}_l - \bar{w}_b) - C_L V_b \rho_l (\bar{w}_b - \bar{u}_l) \times (\nabla \times \bar{u}_l) \\ - \left[\frac{D}{Dt} (\rho_l V_b C_{VM} (\bar{w}_b - \bar{u}_l)) + \rho_l V_b C_{VM} (\bar{w}_b - \bar{u}_l) \cdot (\nabla \bar{u}_l) \right] \end{aligned} \quad (3.5)$$

For the drag, lift and virtual mass coefficient the following simple closures were used:

$$\text{Re}_b < 1000 \rightarrow C_D = \frac{24}{\text{Re}_b} [1 + 0.15(\text{Re}_b)^{0.687}] \quad \text{with} \quad \text{Re}_b = \frac{\varepsilon_l \rho_l |\bar{u}_l - \bar{w}_b| d_b}{\mu_l} \quad (3.6)$$

$$\text{Re}_b > 1000 \rightarrow C_D = 0.44$$

$$C_L = 0.5 \quad \text{and} \quad C_{VM} = 0.5 [1 + 2.78(1 - \varepsilon_l)] \quad (3.7)$$

In our model it is also possible to account for (possible) encounters between a bubble and another bubble (binary encounter) and a bubble and a solid wall. It should be mentioned here that the processing of the bubble-bubble and bubble-wall encounters is computed using an event driven computational strategy employing efficient techniques (such as the neighbourlist concept) borrowed from the field of Molecular Dynamics (MD) (see Delnoij *et al.*, 1997 and Delnoij, 1999 for further details).

Results Euler-Lagrange model

In this paper the effect of incorporating bubble-bubble interaction on the flow structure in a homogeneously aerated bubble column with a square cross-sectional area will be reported. The results of two simulations in which bubble-bubble encounters were respectively neglected and incorporated will be mutually compared in terms of the time-averaged distributions of the vertical liquid phase velocity and its RMS value. In Table 2 the common conditions used for both numerical simulations are summarized. At the top boundary the free slip condition was applied, whereas at all remaining boundaries the no-slip condition was imposed. The liquid exits the computational domain through four openings located at the top of the four side walls (prescribed pressure condition applied) and the bubbles leave at the top boundary (no collision). Note that the superficial gas velocity U is relatively low in this case which is not due to any fundamental limitation of the EL model.

Table 2. Conditions used for the numerical simulation of a homogeneously aerated square bubble column using the Euler-Lagrange approach.

Gas	air	Column	square
<i>Bubble size</i>	2 mm	<i>Area</i>	0.2 m x 0.2 m
<i>Density</i>	1.2 kg/m ³	<i>Height</i>	0.5 m
<i>Viscosity</i>	2.10 ⁻⁵ kg/(m.s)	<i>Grid</i>	40x40x100
<i>U</i>	1.05.10 ⁻³ m/s	<i>Δx</i>	5 mm
Liquid	water	<i>Δy</i>	5 mm
<i>Density</i>	1000 kg/m ³	<i>Δz</i>	5 mm
<i>Viscosity</i>	0.001 kg/(m.s)	<i>Time step</i>	2.5 ms

In Fig. 5 and 6 the results are shown for respectively the case neglecting the bubble-bubble encounters and the case incorporating the bubble-bubble encounters. In both figures the results are presented in terms of computed bubble configurations (left), liquid phase velocity field (central) and liquid phase velocity field at positions with non-zero bubble

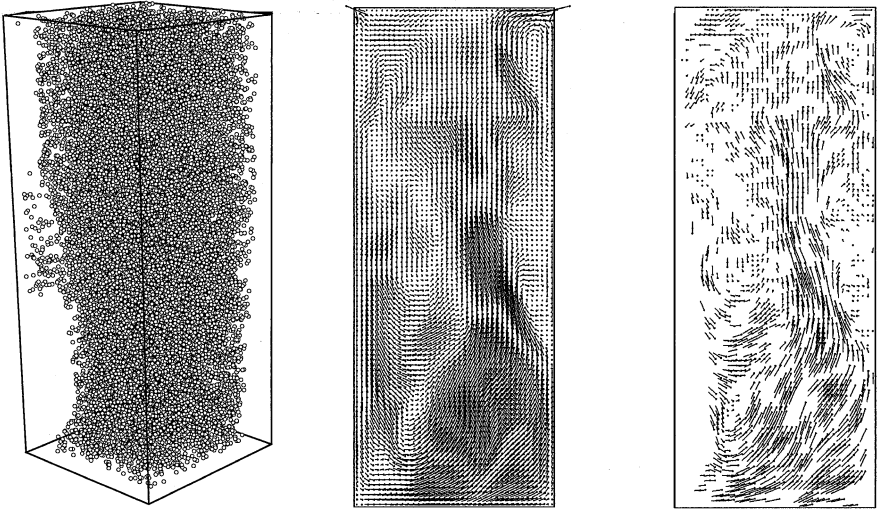


Figure 5. Computed bubble configurations (left), liquid phase velocity field (central) and liquid phase velocity field at positions with non-zero bubble hold-up (right) at the central plane (velocity distribution) of the column at $t=30.0$ s for case without bubble-bubble encounters. Reference vector: 1.0 m/s.

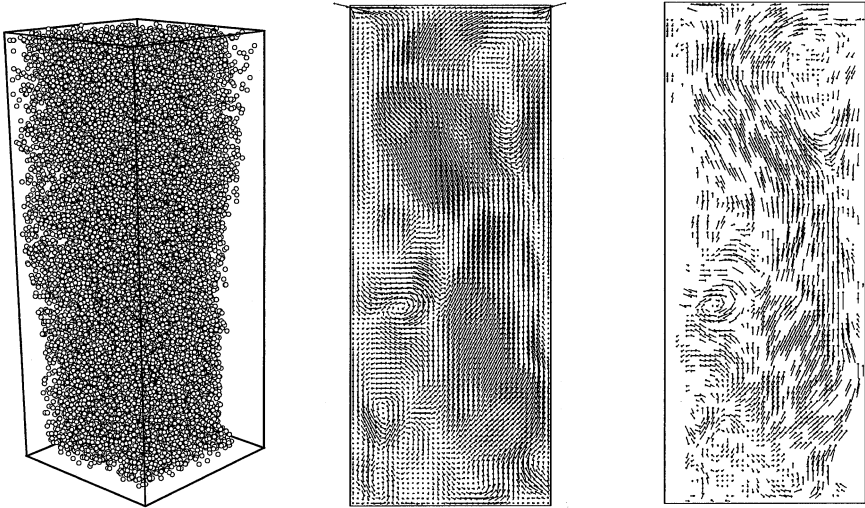


Figure 6. Computed bubble configurations (left), liquid phase velocity field (central) and liquid phase velocity field at positions with non-zero bubble hold-up (right) at the central plane (velocity distribution) of the column at $t=30.0$ s for case with bubble-bubble encounters. Reference vector: 1.0 m/s.

hold-up (right) at the central plane of the square column, all at $t=30.0$ s. In both cases the flow is found to be very dynamic containing many vortical structures of different size

moving in the column. This result is in accordance with results obtained by Sokolichin *et al.* (1997) who compared results obtained from a pseudo Euler-Lagrange and an Euler-Euler approach. When the computed bubble configurations are examined in more detail for both cases it turns out that for the case in which the bubble-bubble encounters were accounted for, the lateral spreading of the bubble plume is more pronounced. This can only be due to the bubble-bubble encounters and seems logical in view of the dispersive nature of bubble-bubble collisions, although it is somewhat surprising that the effect is so clearly noticeable already at the relatively low superficial gas velocity used in our computations. This difference in lateral spreading influences the time-averaged distribution of the vertical liquid phase velocity considerably as can be concluded from Fig. 7, whereas the RMS value of the vertical liquid phase velocity is not significantly affected.

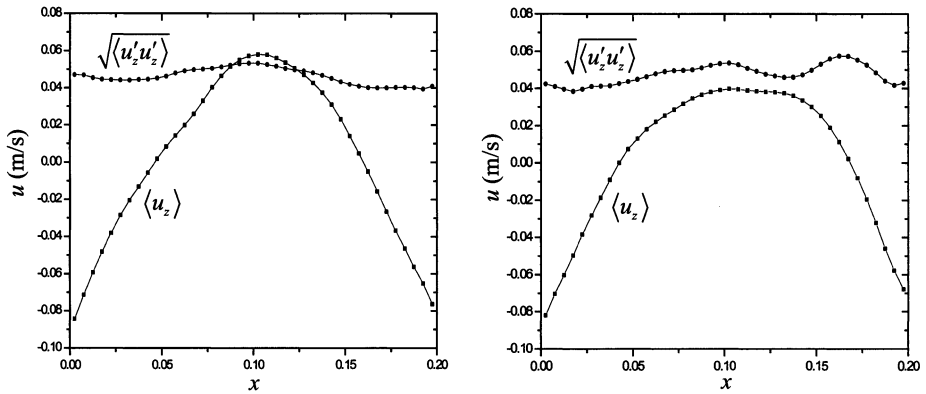


Figure 7. Time-averaged distributions of the averaged (in y -direction) vertical liquid phase velocity and its RMS component after $t=30.0$ s for case without bubble-bubble encounters (left) and case with (right) bubble-bubble encounters.

4. Euler-Euler model

In the two-fluid model the equation of motion of the dispersed gas-phase is ensemble averaged in order to obtain an Euler-Euler description of the two-phase flow. When an ensemble averaging or filtering procedure is applied to the equations of motion, unclosed parts emerge in the stress term and the interface forces. In this work, the unclosed part of the interface forces were neglected. The stress term was closed through an effective viscosity. The effective viscosity of the liquid phase is composed of three contributions:

$$\mu_{eff,l} = \mu_{L,l} + \mu_{T,l} + \mu_{BIT,l} \quad (4.1)$$

Two models were used to incorporate the turbulent viscosity of the liquid phase, $\mu_{T,l}$: the standard $k-\varepsilon$ model, and a LES sub-grid scale model suggested by Smagorinsky (1963).

There are several models available to take account of the turbulence induced by the movement of the bubbles, $\mu_{BIT,l}$. In this study the model proposed by Sato (1975) was used:

$$\mu_{BIT,l} = \rho_l C_{\mu,BIT} \alpha_g d_b \left| \bar{u}_g - \bar{u}_l \right| \quad (4.2)$$

with a model constant $C_{\mu,BIT}$ equal to 0.6.

The calculation of the effective gas viscosity was based on the effective liquid viscosity as follows:

$$\mu_{eff,g} = \frac{\rho_g}{\rho_l} \mu_{eff,l} \quad (4.3)$$

as was proposed by Jakobsen *et al.* (1997).

The interface momentum transfer consists of forces due to drag, lift and virtual mass. In the two-fluid model simulations the drag coefficient for distorted bubbles of Ishii and Zuber (1979) was used:

$$C_D = \frac{2}{3} Eo^{\frac{1}{2}} \quad (4.4)$$

where Eo is the dimensionless Eötvös number ($Eo = g\Delta\rho d_b^2/\sigma$). In this work, a bubble size of 4.0 mm was used, giving $Eo = 2.2$ and $C_D = 1.0$. The bubble size was in accordance with experimental observations by Deen (2001). The coefficients for both the lift and virtual mass force were set equal to a value of 0.5.

The flow in a square bubble column was simulated, using seven different settings, as summarized in Table 3. The effects of both the different interface forces and the different turbulence models were investigated. All simulations were carried out with the commercial

CFD code CFX 4.3 from AEA Technologies. The Smagorinsky model and the averaging routines were implemented in user Fortran. Further details of the numerical implementation of the simulations can be found in Deen (2001).

The simulations are compared with experiments of Deen (2001), who performed two-camera particle image velocimetry (PIV) measurements in a 3-D bubble column filled with distilled water. The column had a square cross-section of $0.15 \times 0.15 \text{ m}^2$ and a height of 1 m. The column was initially filled with water up to a height of 0.45 m. Air was introduced into the centre of the bubble column through a perforated plate at a superficial gas velocity of 4.9 mm/s.

Table 3. Overview of numerical settings for the Euler-Euler simulations.

Case	Grid	Δt (ms)	μ_{eff}	M_I
1	15 x 15 x 45	10	$k-\varepsilon$, BIT	M_D
2	15 x 15 x 45	5	LES, BIT	M_D
3	15 x 15 x 45	5	LES, BIT	$M_D M_L$
4	15 x 15 x 45	5	LES, BIT	$M_D M_{VM}$
5	15 x 15 x 45	5	LES, BIT	$M_D M_L M_{VM}$
6	15 x 15 x 45	5	LES	$M_D M_L M_{VM}$
7	32 x 32 x 45	5	LES, BIT	$M_D M_L M_{VM}$

Results Euler-Euler model

The effect of the different interface forces for the LES can be inferred from Fig. 8a. When only the drag force was incorporated the bubble plume rose straight to the top of the column without transversal spreading. This is in contrast to the experiment, where the bubble plume moves around in the bubble column in a random fashion. Accordingly, the predicted liquid velocity profile shows a strong peak in the centre where the gas is rising, and moderate downflow alongside the plume. When the virtual mass force is included, the behaviour is basically the same. The small effect of the virtual mass force can be explained by the fact that the simulations yield a quasi-stationary state. In a quasi-stationary state there is only little acceleration, so the influence of the virtual mass force is small. When both the drag force and the lift force are incorporated, the plume is spread across the column, due to the nature of the lift force. When also the virtual mass force is added, the differences are small. The velocity profile for case 5 is only slightly lower than for case 3.

In Fig. 9 snapshots of gas fraction iso-surfaces and liquid velocity fields are displayed for cases 1 and 7. We can see a clear difference between the results for the two turbulence models. The LES model resolves much more of the details of the flow. Large vortices are observed alongside the bubble plume. Due to the high turbulent viscosity a quasi-stationary state is obtained for the $k-\varepsilon$ model, *i.e.* the transient details are not resolved but implicitly contained in the turbulent kinetic energy. It is seen that a large stationary vortex

is obtained next to the bubble plume. The presence of this vortex produces an asymmetric solution.

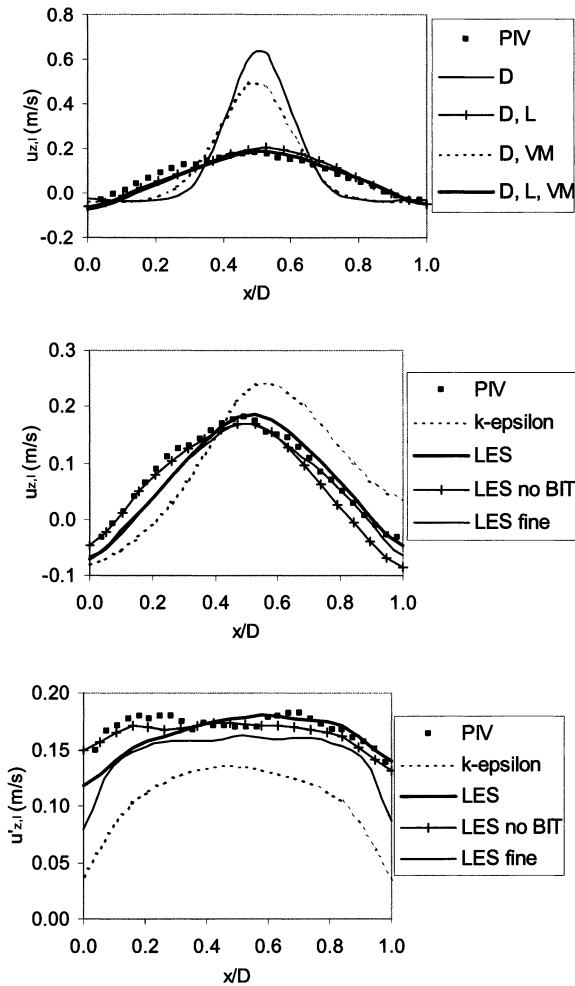


Figure 8. Comparison of simulated and experimental profiles at a height of 0.25 m. a. (top): mean axial liquid velocity for different interface forces. b. (middle): mean axial liquid velocity for different grid sizes and turbulence models. c. (bottom): mean axial liquid velocity fluctuations for different grid sizes and turbulence models.

A more quantitative comparison between the two turbulence models can be obtained from Fig. 8b. This figure shows the averaged axial liquid velocity profile. The predictions with the $k-\varepsilon$ model produce asymmetric results, though in the right order of magnitude. The LES model yields more symmetric velocity profiles. The simulations on both grids predict the same trends. In Fig. 8b the effect of the model for the turbulence induced by the bubbles can also be seen. The differences between the cases with and without bubble-induced turbulence are marginal.

Profiles of the axial fluctuations of the liquid velocity are shown in Fig. 8c. It is noted that the axial velocity fluctuations for case 1 are deduced from the value of k , while in the other cases the axial velocity fluctuations are resolved. It is apparent from Fig. 8c that the assumption of isotropy in the $k-\varepsilon$ model is not valid. The axial fluctuations predicted by the $k-\varepsilon$ model are too low. The LES agrees much better with the experimental data.

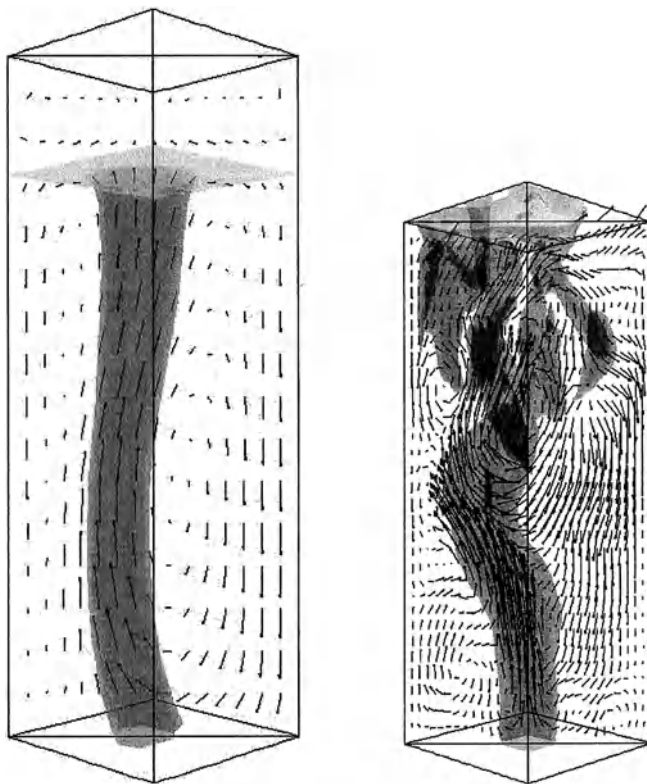


Figure 9. Snapshots of the instantaneous iso-surfaces of $\alpha_g = 0.04$ and liquid velocity fields. Left: $k-\varepsilon$ model (case 1). Right: LES model at the fine grid (case 7).

5. Conclusions

In this paper the multi-level modelling approach for dispersed gas-liquid two-phase flows has been introduced and discussed. The three models constituting this approach, namely the Front Tracking, the Euler-Lagrange and the Euler-Euler model, have been explained and corresponding illustrative computational results have been presented.

To resolve the flow phenomena at the lowest level an improved Front Tracking model has been developed, which can handle systems with very high density ratios and very high surface tension coefficients. Computed bubble shape and bubble rise velocity for a single bubble rising in a liquid compared well with experimental data (Grace, 1973) for two selected cases with different physical properties. Furthermore, results of a sample calculation with three bubbles was shown to demonstrate the capabilities of the Front Tracking model to study bubble-wake interactions.

At the intermediate level the Euler-Lagrange model has been used, which allows to account for bubble-bubble interactions prevailing in dense bubbly flows. Surprisingly it was found that already at low superficial gas velocities the impact of bubble-bubble interactions on the liquid circulation pattern is significant.

At the highest level the Euler-Euler approach has been applied to study the effect of closures for gas-liquid interaction and liquid phase turbulence. It has been shown that interactions due to drag, lift and virtual mass need to be taken into account. Furthermore, with the LES type closure for liquid phase turbulence the strong transient behaviour of the bubble plume could be captured, contrary to the $k-\varepsilon$ model.

References

- Brackbill, J.U., Kothe, D.B. and Zemach, C. (1992). A continuum method for modeling surface tension. *J. Comp. Phys.* **100**, 335-354.
- Centrella, J. and Wilson, J. (1984). Planar numerical cosmology. II. The difference equations and numerical tests, *Astrophysical J. Suppl. Ser.* **54**, 229-249
- Deen, N.G. (2001). An experimental and computational study of fluid dynamics in gas-liquid chemical reactors, Ph.D. thesis, Aalborg University Esbjerg
- Delnoij, E. Lammers, F.A., Kuipers, J.A.M. and van Swaaij, W.P.M. (1997). Dynamic simulation of dispersed gas-liquid two-phase flow using a discrete bubble model, *Chem. Eng. Sci.* **52**(9), 1429.
- Delnoij, E. (1999). Fluid dynamics of gas-liquid bubble columns: A theoretical and experimental study, Ph.D. thesis, Twente University, The Netherlands.
- Grace, J.R. (1973). Shapes and velocities of bubbles rising in infinite liquids. *Trans. Inst. Chem. Eng.* **51**, 116-120.

- Ishii, M. and Zuber, N. (1979). Drag coefficient and relative velocity in bubbly, droplet or particulate flows. *AIChE J.* **25**(5), 843-855.
- Jakobsen, H.A., Sannaes, B.H., Grevskott, S. and Svendsen, H.F. (1997). Modeling of vertical bubble-driven flows, *Industrial and Engineering Chemistry Research* **36**, 4052-4074.
- Nichols, B.D. and Hirt, C.W. (1971). Improved free surface boundary conditions for numerical incompressible-flow calculations, *J. Comp. Phys.* **8**, 434-448.
- Peskin, C.S. (1977). Numerical analysis of blood flow in the heart. *J. Comp. Phys.* **25**, 220-252.
- Prosperetti, A. (2001). Navier-Stokes numerical algorithms for free-surface flow computations: An overview. *Drop Surface Interactions*, 21.
- Sato, Y. and Sekoguchi, K. (1975). Liquid velocity distribution in two-phase bubble flow. *International Journal of Multiphase Flow* **2**, 79.
- Smagorinsky, J. (1963). General circulation experiments with the primitive equations. *Monthly Weather Review* **91**, 99-165.
- Sokolichin, A. and Eigenberger, G. (1994). Gas-liquid flow in bubble columns and loop reactors: part I. Detailed modelling and numerical simulation, *Chem. Eng. Sci.* **49**, 5735.
- Sokolichin, A., Eigenberger, G., Lapin, A. and Lübbert, A. (1997). Dynamic simulation of gas-liquid two-phase flows – Euler/Euler versus Euler/Lagrange. *Chem. Eng. Sci.* **52**, 611.
- Tomiya, A. (1998). Struggle with computational bubble dynamics, Third Int. Conf. Multiphase Flow 1998, 8-12 June, Lyon, France.
- Tryggvason, G., Bunner, B., Esmaeeli, A., Juric, D., Al-Rawahi, N., Tauber, W., Han, J., Nas, S. and Jan, Y.J. (2001). A front tracking method for the computations of multi-phase flow. *J. Comp. Phys.* **169**, 708.
- Univerdi, S.O. and Tryggvason, G. (1992). A front-tracking method for viscous, incompressible multi-fluid flows. *J. Comp. Phys.* **100**, 25-37.
- Welch, J.E., Harlow, F.H., Shannon, J.P. and Daly, B.J. (1965). The MAC method: a computing technique for solving viscous incompressible transient fluid flow problems involving free surfaces. Los Alamos Scientific Laboratory Report LA-3425.
- Youngs, D.L. (1982). Time-dependent multi-material flow with large fluid distortion, In: *Numerical methods for fluid dynamics*, K.W. Morton and M.J. Baines (Eds.), Academic Press, New York, 273

Youngs, D.L. (1987). An interface tracking method for a 3D Eulerian hydrodynamics code. Technical Report AWRE/44/92/35. Atomic Weapons Research Establishment, April 1987.

Nomenclature

A_b	Projected bubble area (m^2)
$C_{\mu,BI}$	Model constant bubble induced turbulence (-)
C_D	Drag coefficient (-)
C_L	Lift coefficient (-)
C_s	Filter constant (-)
C_{VM}	Virtual mass coefficient (-)
d_b	Bubble diameter (m)
D	Numerical approximation to the Dirac function (m^{-3})
Eo	Eötvös number ($= g\Delta\rho d_b^2/\sigma$) (-)
F	Colour-function = liquid fraction (-)
F_σ	Volumetric surface tension force (N/m^3)
g	Gravitational acceleration ($= 9.81 \text{ m}/\text{s}^2$)
k	Turbulent kinetic energy (m^2/s^2)
M	Morton number ($= g \mu_l^4 \Delta\rho/\rho_l^2 \sigma^3$) (-)
m_b	Bubble mass (kg)
n	Outwardly pointing unit normal vector (-)
p	Pressure (Pa)
Re_b	Bubble Reynolds number ($= \rho_l u_b d_b / \mu_l$) (-)
S_{l-b}	Momentum source term due to two-way coupling (N/m^3)
S	Rate of strain tensor (s^{-1})
t	Time (s); Tangential vector (m)
u	Mean or grid scale velocity (m/s)
u'	Fluctuating or sub-grid scale (SGS) velocity (m/s)
U	Superficial gas velocity (m/s)
V_b	Bubble volume (m^3)
w_b	Bubble velocity (m/s)
x_i, x_j	Spatial co-ordinate direction (m)

Greek symbols

α	Volume fraction (-)
Δ	Filter width (m)
Δs	Surface area (m^2)
Δt	Time step (s)
Δx	Grid spacing in x -direction (m)
Δy	Grid spacing in y -direction (m)

Δz	Grid spacing in z -direction (m)
ε	Liquid phase volume fraction (-); Energy dissipation (m^2/s^3)
μ	Shear viscosity ($\text{kg}/\text{m}\cdot\text{s}$)
ρ	Density (kg/m^3)
σ	Surface tension (N/m)
τ	Stress tensor (Pa)

Subscripts and superscripts

b	Bubble
BIT	Bubble induced
D	Drag
eff	Effective
g	Gas phase
l	Liquid phase
L	Lift; Laminar
ℓ	edge
m	marker
s	Sub-grid
T	Turbulent; Transpose
VM	Virtual mass
z	Vertical, axial direction

Direct numerical simulation of mass transfer between rising gas bubbles and water

D. Bothe, M. Koebe, K. Wielage^{*)}, J. Prüss^{#)}, H.-J. Warnecke

Universität Paderborn, Technische Chemie, D-33095 Paderborn, Germany

^{*)} Universität Paderborn, Paderborn Center for Parallel Computing, D-33095 Paderborn, Germany

^{#)} Martin-Luther Universität Halle-Wittenberg, Institut für Analysis, D-06099 Halle, Germany

Abstract

This paper presents numerical simulations of two-phase flow with high-density ratio, taking into account mass transport of a soluble component and its interfacial mass transfer. The mathematical model and the numerical method allow for different solubility of the species in the respective fluid phases, while volume changes due to mass transfer are neglected. The discontinuous changes in species concentrations at the interface are modeled by means of Henry's law. Simulations are carried out with an extended version of the highly parallelized code *FS3D*, which employs an advanced Volume-Of-Fluid (VOF) method. For the examination of mass transfer, single bubbles are held in counter-flow to investigate the transient dissolution of a dilute species. In case of small bubbles with laminar wake a rotational symmetric concentration profile occurs, in agreement with theoretical considerations, while the local mass concentrations in the wake of larger bubbles show complex patterns of varying concentration as it also has been recently observed experimentally.

Nomenclature

c	Concentration	mol m^{-3}
d_B	Bubble diameter	m
D	Diffusion coefficient	$\text{m}^2 \text{s}^{-1}$
f	Marker function	-
g	Acceleration due to gravity	m s^{-2}
H	Henry Coefficient	-

I	Unit tensor	-
J	Molecular flux	$\text{mol s}^{-1}\text{m}^{-2}$
\tilde{M}	Molar mass	kg mol^{-1}
n	Unit normal at interface	-
p	Pressure	N m^{-2}
S	Viscous stress tensor	N m^{-2}
t	Time	s
T	Temperature	K
u	Velocity	m s^{-1}
\tilde{V}	Molar volume	$\text{m}^3 \text{mol}^{-1}$
x	spatial position	m
ϕ	Association factor of solvent	-
ρ	Density	kg m^{-3}
υ	Increment for calculation of diffusion volume	-
σ	Surface tension	N m^{-1}
η	Dynamic viscosity	$\text{kg m}^{-1} \text{s}^{-1}$
κ	Curvature	m^{-1}

Indices

A	Component
B	Bubble, component
l	Liquid
g	Gas
i	Interface

Introduction

Many industrial applications based on two-fluid systems involve mass transfer operations such as extraction, gas scrubbing and waste water treatment in bioreactors. For the design of efficient two-phase mass transfer reactors detailed knowledge of, say, bubble sizes and shapes, rise velocities, internal circulation, swarm behavior, bubble induced turbulence, bubble size distributions (including coalescence and break up) as well as the influence of surfactive species are of fundamental importance. Optimization of mass transfer units additionally requires profound understanding of the underlying mass transport and mass transfer processes. Here, numerical simulations provide a helpful tool to reduce the usually large experimental expenses for reactor design. Due to the increase in computational power, Direct Numerical Simulation (DNS) using mathematical models based on first principles become feasible and prove extremely useful for understanding fundamental processes and phenomena.

The present paper focuses on single gas bubbles rising in water, although the same techniques can be applied to other gas/liquid or liquid/liquid systems. Depending on bubble diameter, this may lead to complicated two-phase flows. For example, bubbles with diameter above 8 mm show dynamic surface deformations that induce turbulence within the liquid phase, which in turn strongly effects interfacial mass transfer. Evidently, the mathematical models fail to admit exact analytical solutions of mass transport and mass transfer which depend on the complex flow patterns. Existing analytical studies rely on approximate solutions of the two-phase Navier-Stokes equations in axisymmetric cases, like axisymmetric Stokes flow around spherical bubbles; see (Brauer 1971, Clift et al. 1978, Sadhal et al. 1999) and the references given there. Even for such known velocity fields, exact solutions of the species equation are not available. Hence rigorous investigation of mass transport and mass transfer requires numerical simulations. In fact, there are several numerical results concerning simulations of mass transfer in such simplified situations, like spherical bubbles/drops or axisymmetric domains, that lead to two-dimensional problems (Mao et al. 2001, Schulze and Kraume 2002, Pfennig 2002, Paschedag et al. 2001). For instance, an interesting recent contribution due to Zhang et al. (2001) investigates the mass transfer of surfactants to the interface of axisymmetric, spherical bubbles and its effect on rise velocity.

On the other hand, experiments by Schlüter et al. (2001) and Borg et al. (2001, 2002) show asymmetric distributions of the dissolved component in the wake of bubbles in case of sufficiently large Reynolds numbers. Consequently, a deeper understanding of mass transfer phenomena in general situations requires three-dimensional numerical simulations of the two-phase balance equations for mass, momentum and additional species equations without simplifying assumptions concerning, e.g., fluid flow or bubble shape.

There are only few papers concerning mass transfer across (strongly) deforming interfaces in two-fluid flow. For instance Sato et al. (2002) perform three-dimensional numerical simulations of single rising LCO_2 droplets in water with unidirectional mass transfer resulting from dissolution of LCO_2 in the continuous phase, taking into account the droplets shrinkage. Within the continuous phase, an advection-diffusion equation describes mass transport of the dissolved species CO_2 . In a recent interesting paper, Davidson and Rudman (2001) studied the depletion of a solute from a rising bubble by means of VOF-simulations. The numerical algorithm employed there computes the species distribution within both fluid phases, with a particular modeling of interfacial mass transfer based on one-dimensional considerations using continuity of concentration at the interface. Simulations given there are in 2D, either with cartesian or with cylindrical coordinates. For further literature concerning numerical studies of heat transfer problems see the references given in Davidson and Rudman (2002).

The VOF method mentioned above is a common current approach that is suitable for accurate computation of the fluid flow within the continuous and dispersed phase, especially if the interface shows complex dynamical behavior. Complemented by additional species equations, this method allows for the computation of interfacial mass transfer as well as mass transport inside the fluid phases.

In contrast to heat transfer problems, species concentrations usually undergo a jump discontinuity at the interface due to different solubility within the respective fluid phases, which leads to additional numerical difficulties. To our knowledge, all previous contributions concerning numerical simulation of mass transfer in situations with complex interface dynamics assume continuous concentration at the phase boundary. While the latter is almost always valid for heat transfer, it means a rather severe restriction in case of mass transfer corresponding to a Henry coefficient equal to 1.

In this paper we present 3D direct numerical simulations of mass transfer between rising gas bubbles and water, performed with an extended version of the highly parallelized code *FS3D*, which employs an advanced VOF method. The mathematical model and the numerical method allow for different solubility of the dilute dissolved component in the respective fluid phases, given that thermodynamical equilibrium at the interface is attained and is determined by Henry's law with a constant Henry coefficient. We also assume that surface tension does not depend on the concentration of the dissolved species.

Mathematical Model and Numerical Method

Throughout this paper we consider isothermal flows of two immiscible Newtonian fluids with constant density. Based on continuum mechanics, balance of mass and momentum inside the phases leads to the Navier-Stokes equations, i.e.

$$\partial_t(\rho \mathbf{u}) + \nabla \cdot (\rho \mathbf{u} \otimes \mathbf{u}) = -\nabla p + \nabla \cdot \mathbf{S} + \rho \mathbf{g}, \quad \nabla \cdot \mathbf{u} = 0 \quad (1)$$

with the viscous stress tensor

$$\mathbf{S} = \mu (\nabla \mathbf{u} + \nabla \mathbf{u}^T), \quad (2)$$

where the material parameters depend on the respective phase. Whenever distinction between the different phases is necessary, *l* (liquid) and *g* (gas) are used as phase indices. At the interface, the additional jump conditions

$$[\rho(\mathbf{u} - \mathbf{u}_i)] \cdot \mathbf{n} = 0 \quad (3)$$

$$[\rho \mathbf{u} \otimes (\mathbf{u} - \mathbf{u}_i) + p\mathbf{I} - \mathbf{S}] \cdot \mathbf{n} = \nabla_i \sigma + \sigma \kappa \mathbf{n} \quad (4)$$

appear, where \mathbf{u}_i is the interfacial velocity, $\nabla_i \sigma$ denotes the surface gradient of the surface tension and

$$\kappa = -\nabla \cdot \mathbf{n} \quad (5)$$

is the sum of the local main curvatures of the interface. Here \mathbf{n} is the unit normal at the interface directed into one of the fluid phases, and the notation

$$[\Psi(x)] = \Psi(x+) - \Psi(x-) \quad (6)$$

stands for the jump of a physical quantity Ψ across the interface.

In the sequel, it is assumed that the two-fluid systems under consideration do not endure phase changes, which leads to continuous normal components of fluid velocities at the phase boundary. Finally, we assume no slip at the interface and constant surface tension. Then the jump conditions simply become

$$[\mathbf{u}] = 0, \quad [p\mathbf{I} - \mathbf{S}] \cdot \mathbf{n} = \sigma \kappa \mathbf{n}. \quad (7)$$

The local concentration c of a dilute chemical species is governed by the balance equation

$$\partial_t c + \nabla \cdot (c\mathbf{u}) + \nabla \cdot \mathbf{J} = 0. \quad (8)$$

If the molecular flux is given by Fick's law,

$$\mathbf{J} = -D \nabla c, \quad (9)$$

with constant diffusivities this leads to the advection-diffusion equation

$$\partial_t c + \mathbf{u} \cdot \nabla c = D \Delta c \quad (10)$$

inside the phases. At the phase boundary, mass balance implies continuity of the fluxes, i.e.

$$[-D \nabla c] \cdot \mathbf{n} = 0. \quad (11)$$

One more constitutive equation is needed to determine the concentration profiles. Here, we assume instantaneous thermodynamical equilibrium at the interface modeled by Henry's law,

$$c_l = c_g / H \quad (12)$$

with fixed Henry coefficient H . For more details about continuum mechanical modeling of two-phase flows see (Ishii 1975, Slattery 1999).

The numerical method employed here is based on the Volume-of-Fluid (VOF) method (Hirts and Nichols 1981). The VOF method solves the Navier-Stokes equations for an incompressible transient two-phase flow. Advection of the dispersed gas phase is governed by an additional transport equation for the volume fraction f of this phase, i.e.

$$\partial_t f + \nabla \cdot (\mathbf{u}f) = 0. \quad (13)$$

Here, the dispersed fluid phase corresponds to regions where the f -function has value one, while the interface is located within grid cells for which $0 < f < 1$. Surface tension is taken into account based on a conservative approximation of Laaurie et al. (1994).

Most numerical methods for convective transport of a passive scalar produce artificial diffusion that leads to smearing of steep gradients, hence are not useful for advection of a discontinuous quantity. On the other hand, due to complicated shapes and dynamics of the interface, specialized higher order schemes that avoid numerical diffusion are hardly applicable or computationally too expensive. Therefore, we exploit the linear structure of (10), (11), (12) to incorporate Henry's law into the concentration itself by considering the new scalar

$$\tilde{c} = \begin{cases} c_l & \text{inside the liquid phase} \\ c_g / H & \text{inside the gas phase} \end{cases} \quad (14)$$

Notice that the interfacial jump in species concentration is thereby shifted to a jump in the normal derivative. More precisely, the evolution of \tilde{c} is governed by

$$\partial_t \tilde{c} + \mathbf{u} \cdot \nabla \tilde{c} = D \Delta \tilde{c} \quad (15)$$

inside the phases and

$$[\tilde{c}] = 0, \quad D_l \nabla \tilde{c}_l \cdot \mathbf{n} = H D_g \nabla \tilde{c}_g \cdot \mathbf{n} \quad (16)$$

at the interface. The numerical solution of (15), (16) is based on the finite volume method with the following additional feature within each time step. Prior to the diffusional step, the values of \tilde{c} in those cells which share part of the interface are computed in such a manner that the resulting diffusional fluxes across the phase boundary will then satisfy (16). Computations are performed with an extended version of the parallelized VOF-code *FS3D*. The latter was developed at the *ITLR* Stuttgart (Rieber and Frohn 1999) and the additional module for computation of mass transfer has been elaborated within the current investigations.

Validation

It has been shown in (Koebe et al. 2002) that *FS3D* is able to render the rise velocities and bubble shapes of air bubbles in water correctly. A first validation of the numerical method for mass transport and mass transfer is done by comparison between simulation results and (approximations of) exact solutions. For this purpose symmetric situations with stationary phase boundary are considered in order to reduce the dimensionality of the problem.

The simplest test case corresponds to a cube of 1cm length under gravity, the lower half filled with water and the upper half with air. No-slip boundary conditions are imposed at the fixed walls, hence due to zero initial velocities the fluids stay at rest. The contact angle between interface and wall is artificially set to 90° such that the phase boundary remains fixed and lies in a horizontal plane at 0,5cm height. Initially, a chemical species is present within the liquid phase, where it is homogeneously distributed with concentration normalized to 1,0. The diffusivity of this species is set to 0,2 cm²/s inside the liquid phase and to 1,0 cm²/s inside the gas phase. Neumann boundary conditions at the walls are used for the species equation. Figure 1 shows results of numerical computations with Henry coefficient equal to 3. The dots correspond to numerical simulation with *FS3D*, while the lines represent the exact solution. Different colors correspond to different times, starting from red (t=0 s) to blue (t=1,14 s). Simulations are done with grid resolution of 256 cells in the vertical direction, but concentration values are only shown for a certain fraction of all cells in Figure 1. Almost no deviation between numerical and exact solution appears although the initial concentration is unphysical. Let us note in passing, that in fact an approximation of the exact solution is

used, since the solution can not be given in closed form. Computation of this approximate solution is based on a one-dimensional model with fixed interface that is adapted to the underlying simple situation.

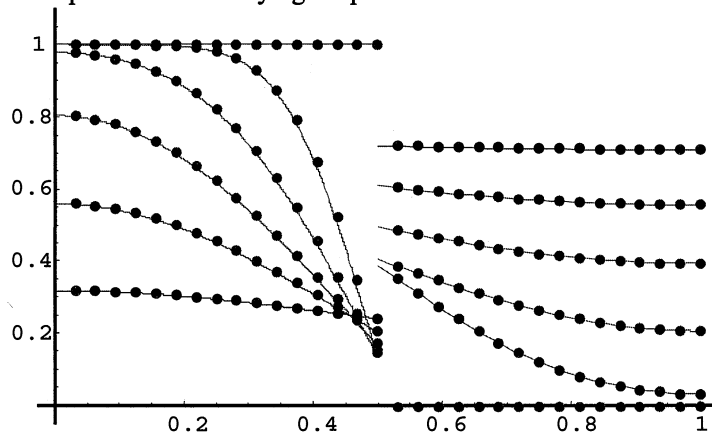


Fig. 1. Concentration profiles along the vertical axis. Comparison between numerical results and exact solutions.

The second test case is in 2D, again with stationary but curved phase boundary. The liquid phase forms a disc of radius 0,8 cm, surrounded by the gas phase and placed in the center of a square with a length of 12,8 cm. To avoid so-called parasitic currents, fluid velocities are set to zero throughout the simulation. As before, initial concentrations are 1,0 inside the liquid and 0,0 inside the gas phase. The diffusivity of the dissolved species is set to 10 cm²/s inside the liquid phase and to 1 cm²/s inside the gas phase. This time the Robin boundary condition

$$\frac{\partial c}{\partial \mathbf{n}} + \frac{\mathbf{x} \cdot \mathbf{n}}{2Dt} c = 0 \tag{17}$$

is used to reduce deviations from the radial symmetric situation. Notice that far from the disc the effect of the initial concentration is close to that of a unit mass placed at the center of the disc, and (17) is satisfied for the fundamental solution of the diffusion equation. Figure 2 shows the simulated concentration profile after 0.25 s for a Henry coefficient of 4. Comparison between numerically calculated radial concentration profiles and exact solutions at different times up to 0,3 s is illustrated by Figure 3. The simulation with *FS3D* is performed on a grid with 512 by 512 cells. As in the 1D test case the exact solution is calculated from a one-dimensional model exploiting radial symmetry. Agreement between numerical and exact solution is very good.

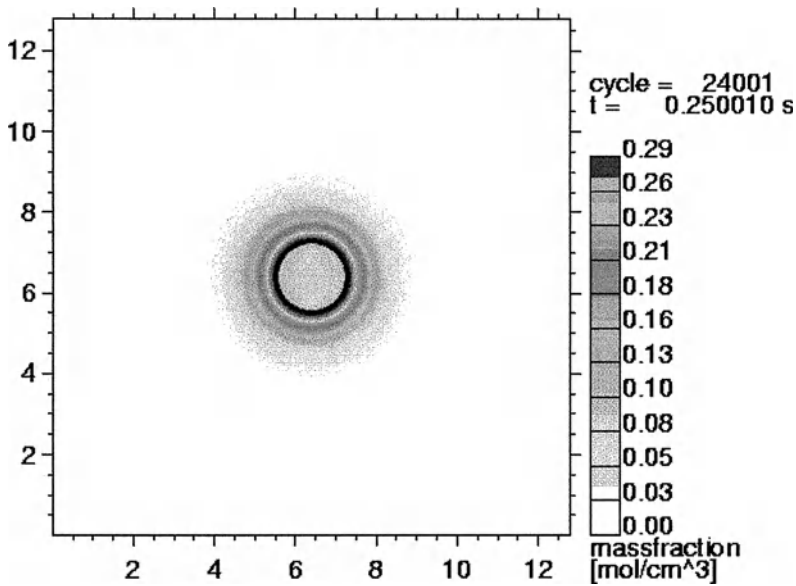


Fig. 2. Mass transfer from a liquid disc into the surrounding gas phase. Concentration distribution after 0.25s.

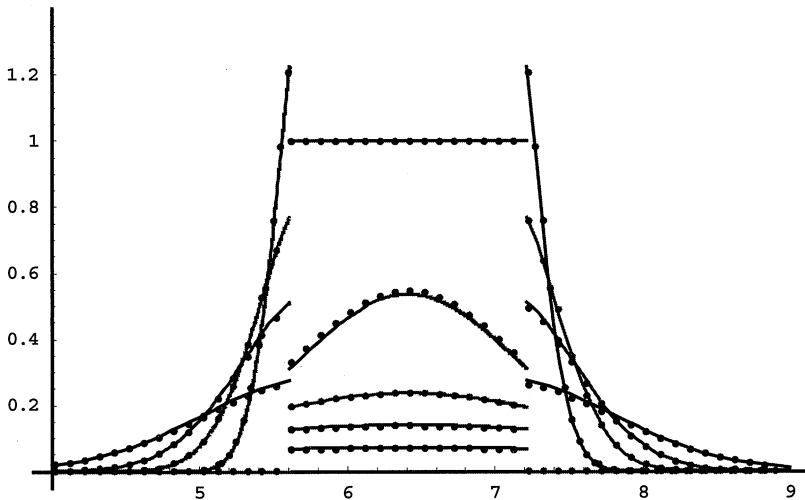


Fig. 3. Radial concentration profiles. Comparison between numerical and exact solutions.

A second type of validation of numerical mass transfer and mass transport uses experimental data. Riethues et al. (1985) determined the oxygen transfer from single air bubbles to liquids using microelectrodes. The air bubbles were fixed with a platinum wire spiral, while the liquid was either stagnant or flowing downwards.

In this set-up, the oxygen concentrations in the vicinity of the interface have been measured at several positions with precise distances to the bubble. Validation of our numerical simulations is done by means of an experiment with an air bubble of 3,94 mm diameter in stagnant N_2 -saturated water.

As mentioned before parasitic currents are a problem in VOF-simulations with very small or zero velocities. To avoid unphysical results, convection is again suppressed by setting all velocities to zero. Consequently, mass transport is only due to diffusion. In the absence of convection, the air bubble remains at its initial position, hence the grid resolution can be increased using three symmetry planes. The correspondingly reduced computational domain is discretized by $128 \times 128 \times 128$ cells and the bubbles diameter is resolved with 32 cells. Figure 4 compares experiment and simulation.

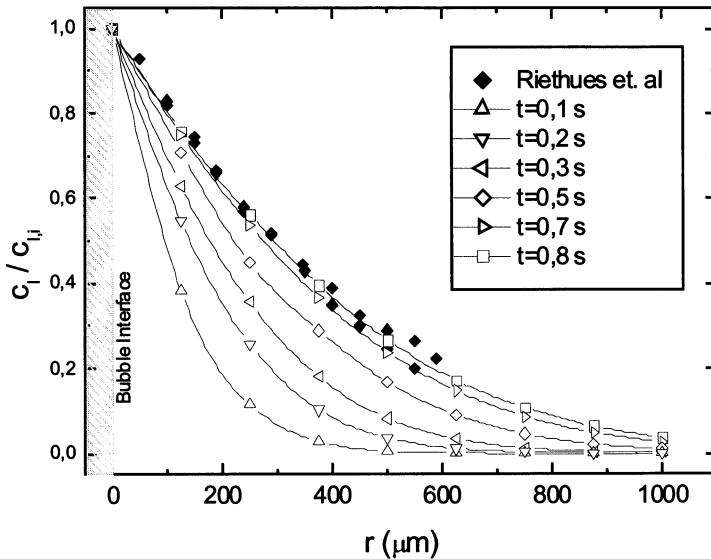


Fig. 4. Temporal evaluation of the normalized oxygen concentration in the liquid phase away from the interface. Comparison between experimental data (Riethues et al. 1986) and numerical simulation.

Considering the evolution in time of the concentration it is evident that after 0,8 seconds the calculated concentration profile agrees very well with the measured one. For low viscosities, Riethues et al. (1986) observed a much steeper concentration gradient near the interface than that calculated by Fick's law of diffusion. Using microscopy they discovered small convective flows – possibly Marangoni convection - which could not be suppressed in the experiment. Lacking information on the absolute concentrations in the liquid phase, Figure 4 compares concentration ratios which match very well. As convection increases mass transfer

tration ratios which match very well. As convection increases mass transfer rates, the absolute mass transfer rates obtained numerically are probably too low.

Numerical Simulation of rising bubbles

For a good approximation of the deforming interface, numerical grids of high resolution are necessary. Therefore, the numerical simulations are performed on a Siemens hpcLine parallel computer with 96 nodes, owning two 850 MHz - *Pentium III* - processors with 512 Mbytes memory each. The results shown here were performed with up to 64 processors and a numerical grid composed of 4 million uniform cubic cells ($\Delta x = \Delta y = \Delta z$).

We chose the systems of air bubbles and oxygen bubbles in water, with the following properties for density, dynamic viscosity and surface tension at room temperature:

Water:	$\rho_L = 998,2 \text{ kg/m}^3$,	$\eta_L = 1002 \cdot 10^{-6} \text{ kg/ms}$,	$\sigma = 0,073 \text{ N/m}$,
Air:	$\rho_G = 1,122 \text{ kg/m}^3$,	$\eta_G = 18,24 \cdot 10^{-6} \text{ kg/ms}$,	
Oxygen:	$\rho_G = 1,314 \text{ kg/m}^3$,	$\eta_G = 20,37 \cdot 10^{-6} \text{ kg/ms}$,	

In previous simulations (Koebe et al. 2002) we investigated rising air bubbles in water without mass transfer. In the literature there are some examples where rising bubbles are only described by means of Reynolds-, Morton-, and Eötvös-number instead of the real material properties. Thereby the density and viscosity ratios can be drastically reduced, keeping the dimensionless numbers fixed. While this approach reduces numerical problems to a big extent, there are other drawbacks. Despite the fact that the terminal velocities can be rendered quite well, the acceleration of the bubbles in the wake of preceding bubbles, say, or bubbles accelerating from nozzles are not reproduced sufficiently well. For example, to take into account this acceleration, the virtual mass coefficient is an important factor. In numerical tests the virtual mass coefficient differs by about 10-15%.

With real properties chosen for the numerical simulation, terminal rise velocities and rise paths of air bubbles with a diameter ranging from 0,5 to 16 mm were examined systematically in (Koebe et al. 2002). For technically relevant bubbles ($d_B = 2-8 \text{ mm}$) agreement with experimental data is very well concerning the terminal velocities. Strong realistic surface deformations can be observed for bubbles larger than 8 mm. In addition, the phenomenon of vortex shedding from the edges of bubbles can be observed. For bubble diameter above 15 mm those bubbles start to disintegrate. Considering the rise paths it should be mentioned that agreement is qualitatively good for helical and zigzag paths, but the rise radii differ by about one order of magnitude compared to experimental data for the same physical domain.

In addition to the material properties mentioned above, diffusion coefficients for each phase are required for numerical simulations of mass transport. There are

different approaches for the gas and liquid phase. For the latter, Wilke and Chang describe the binary diffusion coefficient of a solute A in a solvent B in an infinite dilute solution as

$$D_{A,B} = \frac{7,4 \cdot 10^{-15} (\phi \tilde{M}_B)^{0,5} T}{\eta_B \tilde{V}_A^{0,6}} \quad (18)$$

with molecular weight \tilde{M}_B of solvent B, temperature T, viscosity η_B of solvent B, the molar volume \tilde{V}_A of solute A at its normal boiling temperature, and the association factor ϕ of the solvent. For water Wilke and Chang recommend ϕ to be chosen as 2,26. The simulations were performed for water or water-glycerin solution as solvents with the diffusion coefficients $D_{O_2,H_2O} = 2,01 \cdot 10^{-5} \text{ cm}^2/\text{s}$ and $D_{O_2,\text{solution}} = 2,13 \cdot 10^{-6} \text{ cm}^2/\text{s}$.

For moderately compressed gas mixtures the diffusion coefficient can be determined for nonpolar materials according to Fuller, Schettler and Giddings

$$D_{A,B} = \frac{0,1013 \cdot 10^{-7} T^{1,75} \left[(\tilde{M}_A + \tilde{M}_B) / (\tilde{M}_A \tilde{M}_B) \right]^{1/2}}{p \left[(\sum \nu)_A^{1/3} + (\sum \nu)_B^{1/3} \right]^2} \quad (19)$$

This leads to a value of $D_{O_2,\text{air}} = 0,1915 \text{ cm}^2/\text{s}$. If the gas phase consists of pure oxygen only, the self diffusion coefficient can be calculated as

$$D_{A,A} = D_{273K} \left(\frac{T}{273} \right)^n \quad (19)$$

with $D_{273K} = 0,182 \text{ cm}^2/\text{s}$ and $n=1,92$. This yields $D_{O_2,O_2} = 0,2085 \text{ cm}^2/\text{s}$ at room temperature. Formulas (18), (19), (20) are taken from (Weiss 1986).

For spherical or ellipsoidal bubbles, symmetry planes are taken into account to enlarge the possible grid resolution. A typical result for a 4 mm bubble in a water-glycerin solution (60 / 40% by wt, $\eta_L = 9,45 \cdot 10^{-3} \text{ Pa s}$) is presented in Figure 5. Due to the large Henry-coefficient of 33 there is a great difference in concentrations between the center of the bubble and the liquid phase. To visualize the distribution within the *liquid* phase the concentration scale has been adapted to the maximal concentration inside this phase. The bubble shows a completely symmetric wake and the concentration profiles within the wake are qualitatively very similar to theoretical results from Brauer (1971).

For the examination of non laminar wakes and wobbling surfaces full three dimensional simulations have to be carried out. As an example of our numerical results, Figure 6 shows an 8 mm oxygen bubble in counterflowing water about 0,58 seconds after it was released. In this figure a typical concentration profile inside the liquid phase is depicted together with the corresponding velocity plot, illustrating the strong surface deformation of the wobbling bubble and an open and turbulent wake. The rising bubble induces large-scale turbulence. During its rise, vortices shed frequently into the wake and are advected by the water flow before they

dissipate. In addition to surface deformation this further contributes to turbulence. Let us note in passing that a large amount of oxygen has already been washed out of the computational domain before the bubble leaves its rectilinear path and surface deformation begins. Inside the wake there are asymmetric regions of varying concentrations with steep gradients. Together with bubble induced turbulence this enlarges mixing efficiency.

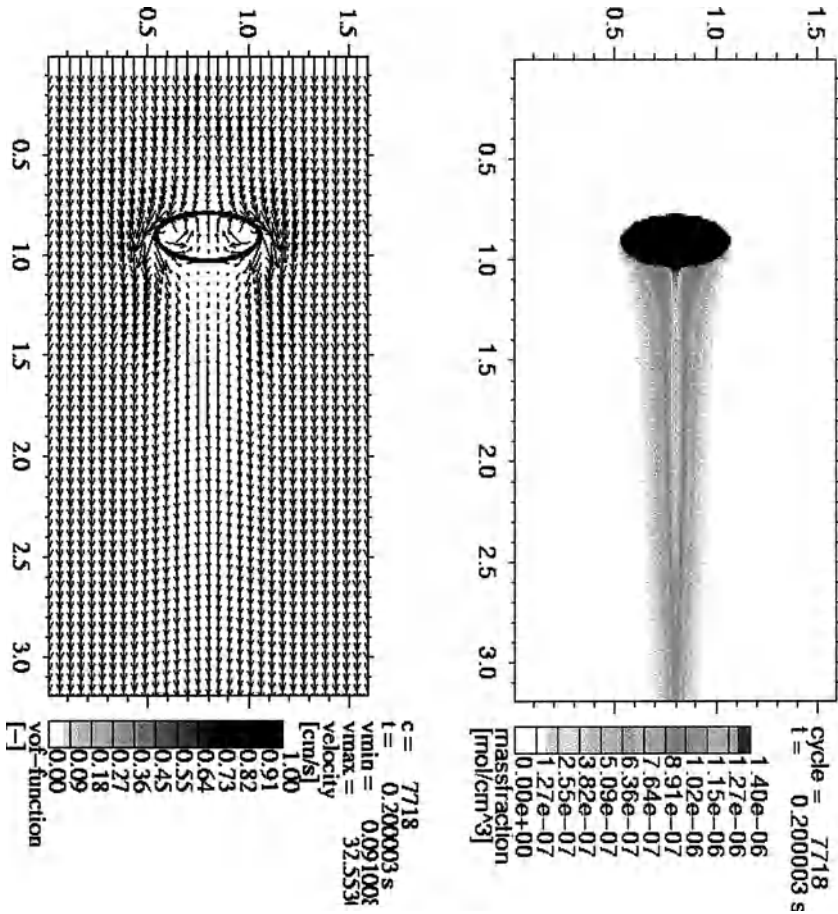


Fig. 5. Velocity vectors in the liquid phase (left) and oxygen concentration (right) for a 4 mm air bubble in a glycerin / water (60 / 40% by wt) mixture with the bubble held in counterflow.

It becomes obvious from Figure 6 that the assumption of a symmetric wake, which is essential for the validity of the existing analytical approximations, cannot be upheld for bubbles of this size. This observation has already been made ex-

perimentally by Schlüter et al. (2001) and Bork et al. (2001, 2002), where laser-induced fluorescence (LIF) is employed to visualize the oxygen concentration in the liquid phase.

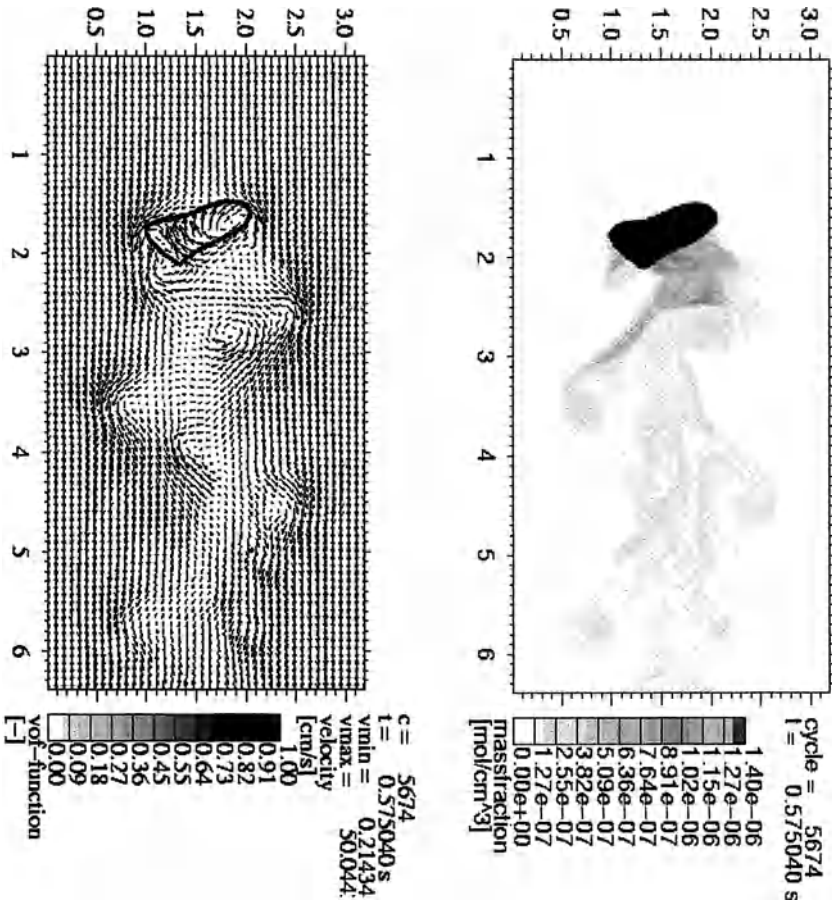


Fig. 6. Velocity vectors in the liquid phase (left) and oxygen concentration (right) for a 8 mm oxygen bubble in water held in counterflow.

To describe the influence of turbulence in the wake, mass transfer coefficients are estimated from three-dimensional numerical simulations. For this purpose, the normalized amounts of oxygen inside bubbles of different size as shown in Figure 7 are extracted from the numerical data. By means of the relation

$$k_L \approx \frac{\Delta n_g / n_g(0)}{a \Delta t}, \quad (21)$$

where a denotes specific interfacial area, the integral mass transfer coefficients until $t=0.25$ seconds are $1,12 \cdot 10^{-4} m/s$ in case of 4 mm bubbles, but $1,28 \cdot 10^{-4} m/s$ for both 6 and 8 mm bubbles. Of course further validations especially concerning the convective transport as well as other improvements, like calculation of ensemble averages for slightly disturbed initial conditions, are required to obtain reliable values for mass transfer coefficients. Nevertheless, the present results already indicate the increase in mass transfer due to turbulent wakes.

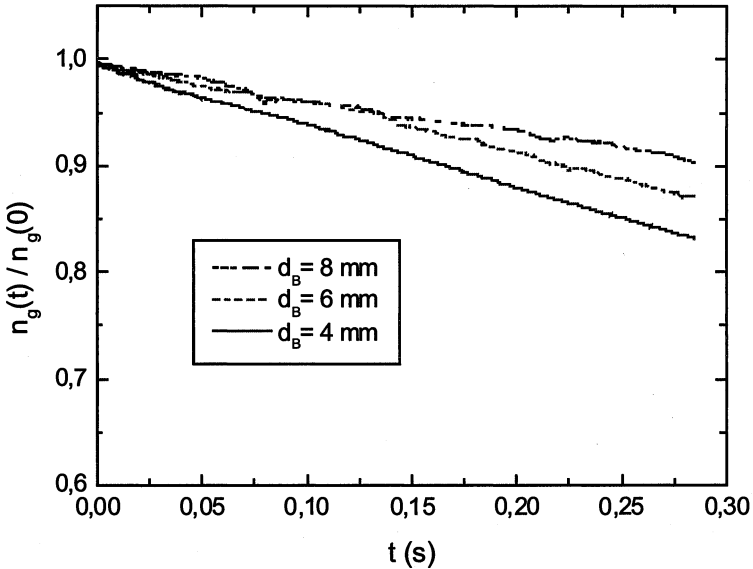


Fig. 7. Normalized amount of oxygen inside bubbles of different size.

Further investigations on local mass transfer effects from rising bubbles will be carried out in cooperation with the Institute of Environmental Process Engineering at Bremen University. These will include mass transfer in Newtonian and non-Newtonian fluids for single bubbles and for bubble chains. Special emphasis will be put on mixing effects in the wake regions.

Conclusion

These investigations show that the VOF method in combination with species balances is a suitable tool for numerical simulations of two-phase fluid systems with mass transport and interfacial mass transfer. This includes the case of jump discontinuities in concentration profiles across the interface, even for distribution coefficients according to Henry's or Nernst's law that are far away from unity. Numerical simulations for gas bubbles rising in water show qualitatively good

agreement with known experimental data and indicate that mass transfer is increased by turbulent wakes. Present work concentrates on further validations, especially in situations with convective mass transport.

References

- Bork O, Schlüter M, Scheid S, Rübiger N (2001) New phenomena of mass transfer in gas/liquid flows. In: Proc. ASME HTD, Fluid-Physics and Heat transfer for Macro- and Micro-Scale Gas-Liquid and Phase Change Flows, New York, pp. 1-6
- Bork O, Schlüter M, Rübiger N (2002) Influence of wake mixing on mass transfer in gas-liquid reactors. In: 15th Int. Congress of Chemical and Process Engineering, CHISA, Prag, Czech Republic
- Brauer H (1971) Stoffaustausch einschließlich chemischer Reaktionen. Verlag Sauerländer, Aarau und Frankfurt a. M.
- Clift R, Grace J R, Weber M E (1978) Bubbles, Drops and Particles. Academic Press, New York
- Davidson M R, Rudmann M J (2002) Volume-of-fluid calculation of heat or mass transfer across deforming interfaces in two-fluid flow. Num. Heat Transfer B 41: 291-308
- Hirts C W, Nichols B D (1981) Volume of Fluid (VOF) method for the dynamics of free boundaries, J. Comp. Phys. 39: 201-225
- Ishii M (1975) Thermo-Fluid Dynamic Theory of Two-Phase Flow. Eyrolles, Paris
- Koebe M, Bothe D, Prüss J, Warnecke H-J (2002) 3D Direct numerical simulation of air bubbles in water at high Reynolds numbers. In: Proc. 2002 ASME Joint U.S.-European Fluids Eng. Conf., Montreal, Canada, FEDSM2002-31143
- Lafaurie B, Nardone C, Scardovelli R, Zaleski S, Zanetti G. (1994) Modelling merging and fragmentation in multiphase flows with SURFER, J. Comp. Phys 113: 134-147
- Mao Z-S, Li T, Chen J (2001) Numerical simulation of steady and transient mass transfer to a single drop dominated by external resistance, Int. J. Heat Mass Trans. 44: 1235-1247
- Paschedag A, Piarah W H, Kraume M (2001) Grenz betrachtungen zum Stofftransport am Einzel tropfen – Validierung numerischer Ergebnisse, Chem. Ing. Tech. 73: 1431-1435
- Pfennig A (2002) Modelling mass transfer and equilibria at liquid-liquid interfaces. In: Fortschritt-Berichte VDI, Reihe 3 Verfahrenstechnik 738 (F.-P. Schindler ed.), VDI 2002, pp. 13-23
- Rieber M, and Frohn A (1999) A numerical study on the mechanism of splashing. Int. J. Heat and Fluid Flow 20: 455-461
- Riethues M, Buchholz R, Onken U, Baumgärtl H, Lübbers D W (1986) Determination of oxygen transfer from single air bubbles to liquids by oxygen microelectrodes, Chem. Eng. Process. 20: 331-337
- Sadhil S S, Ayyaswamy P S, Chung J N (1999) Transport Phenomena with Drops and Bubbles. Springer-Verlag, New York
- Sato T, Jung R-T, Abe S (2000) Direct simulation of droplet flow with mass transfer at interface, Trans. ASME 122: 510-516
- Schlüter M, Bork O, Scheid S, Hövelmann S, Rübiger N (2001) New Aspects of Hydrodynamics and Mass Transfer in Multiphase Flows. In: Proceedings of the ICMF-2001 Tulane University

- Schulze K, Kraume M (2002) Influence of mass transfer on drop rise velocity. In: *Forschritt-Berichte VDI, Reihe 3 Verfahrenstechnik 738* (F.-P. Schindler ed.), VDI 2002, pp. 97-106
- Slattery J C (1999) *Advanced Transport Phenomena*. Cambridge Univ. Press, Cambridge
- Weiss S (1986) *Verfahrenstechnische Berechnungsmethoden, Teil 7: Stoffwerte*, VCH
- Zhang Y, McLaughlin J B, Finch J A (2001) Bubble velocity profile and model of surfactant mass transfer to bubble surface, *Chem. Eng. Sc.* 56: 6605-6616

Analysis of bubble interactions in bidisperse bubble swarms by direct numerical simulation

Manfred F. Göz and Martin Sommerfeld

Institut für Verfahrenstechnik, Fachbereich Ingenieurwissenschaften,
Martin-Luther-Universität Halle-Wittenberg, D-06099 Halle, Germany

Direct numerical simulations of bidisperse bubble swarms have been carried out using a finite difference/front tracking scheme. A number of bubbles were placed into a periodically continued box filled with still liquid. After an initial transient, the system settles towards a statistical quasi-steady state. For this stage, the average bubble motion and pair-wise bubble interaction as well as the liquid pseudo-turbulence have been evaluated. Varied parameters are the bubble size and number ratios, the deformability of the bubble surface, and the volume fraction of the bubbly phase.

It is found that the mean bubble rise and fluctuation velocities as well as the liquid velocity fluctuations follow similar trends as in comparable mono-disperse bubbly flows but that the microstructure of a bubble size and/or shape class can be strongly distorted by the presence of another class. Most bubble pairs prefer a horizontal or near-horizontal alignment at relatively small centroid distance.

Introduction

The most usual modelling approaches for disperse two- and multiphase flows, namely Euler/Euler and Euler/Lagrange, are necessarily affected with assumptions and simplifications. While the multi-fluid approach has to struggle with closure problems and the increasing number of equations with each additional particle fraction, the Euler/Lagrange method must properly account for the interactions between fluid and particles and among many particles themselves. In both cases it is essential, although on somewhat different scales, to represent micro- to mesoscopic effects like the influences of local particle concentrations and configuration, finite particle size as well as size distributions, and the deformation of fluid particles on average on a mesoscale. A further problem is turbulence modelling, via Reynolds averaging or/and source term modification in the framework of these two approaches.

A more basic approach is to use direct numerical simulations (DNS). Solving the three-dimensional time-dependent Navier-Stokes equations directly does not require any such modelling assumptions but allows to simulate the flow almost

without simplifications, i.e., restrictions (on resolution, run time, memory) are set “only” by computing power limitations. This approach enables to take all important physical parameters into account, like inertia, viscosity, surface tension, bubble size and deformation, poly-disperse size distributions. In addition, a detailed view of the flow field is obtainable in this way, also in situations where measurements are hardly possible or do not yield conclusive information. Thus, DNS provides a useful tool to gain insight into bubble interactions and collective motions and to study the dependence of bubble rise velocity and bubble-induced fluid turbulence on volume fraction, number and size, i.e. deformability or shape, of the bubbles. Simultaneously, the calculation of the motion of bubble swarms yields information about the microstructure, i.e. about the interaction and preferred alignment of bubble pairs. Like experimental results, such findings should find their way into practical models.

Of course, DNS has its limits set by the available computer power as already mentioned. To date it is not possible to simulate an entire bubble column in this manner, so one is restricted to the computation of a section of a quasi-homogeneous bubbly flow, as it occurs in the interior of a column. Then wall influences can be neglected and periodic boundary conditions in all three spatial directions can be prescribed. Another drawback is the presence of a large, multi-dimensional parameter space, which can be measured only at a few sampling points, in particular in view of the extremely long simulation times required for the present purposes. In bidisperse bubble systems not only the Galileo and Eötvös numbers (i.e. size, hence rise velocity, and deformability, hence shape) of the two bubble classes can be varied, but also the volume ratio and the number of large and small bubbles and thus their relative volume fractions.

2. Numerical Method

The results described in the sequel have been obtained with a code developed by our cooperation partner Prof. G. Tryggvason (now at Worcester Polytechnic Institute) and his students, notably Dr. B. Bunner (presently with Teragenics), at the University of Michigan. For an extended overview and details of the numerical method see Tryggvason et al. (2001) and for a description regarding the present application see Göz et al. (2002a). The code solves the incompressible time-dependent Navier-Stokes equations for a single fluid field with variable, but locally constant, density and viscosity fields. The equations contain an extra source term accounting for the surface tension forces acting at the gas-liquid interface; here the interface is composed of a finite number of bubble surfaces, simply called fronts. Spatial discretisation is done by second-order centred differencing, time integration is second-order explicit. A projection step utilizes the divergence-freedom of the velocity field and yields Poisson equations for pressure and density, which are solved with a multi-grid solver. The viscosity field is updated by affine transformation of the new density distribution.

The fully deformable surface of each bubble is discretised by an unstructured two-dimensional triangular mesh. The nodes of this mesh serve as marker particles, which are advected with the local flow velocity. This front tracking algorithm requires the interpolation of the velocity field, defined on a fixed, regular, staggered grid, onto the front mesh. After the advection of the marker particles during a time step, each front is restructured by adding or deleting nodes and grid elements to guarantee adequate local resolution of the curved interface. Then surface tension is calculated via local polynomial fitting, interpolated from the flexible front mesh to the fixed grid, and inserted into the discretised momentum balance equation. In addition, the density and viscosity fields are determined according to the new front distribution, also interpolated to the fixed grid, and smeared out over two to three grid cells to avoid discontinuities at the interface.

In order to obtain reliable statistics of bubble motion and interaction, a sufficient number of bubbles need to be tracked for an extended period of time. The thereby required high computational expenditure can be mastered only with modern parallel computers. The parallelized version of the programme uses Cartesian domain decomposition into equally sized sub-domains, which are assigned to different processors. Each processor has its own memory (distributed memory) and boundary data between neighboured sub-domains are exchanged using the Message Passing Interface Protocol (MPI). The front data of a gas bubble extending across two or more sub-domains must also be exchanged. The processor of the sub-domain containing momentarily the largest part of such a bubble gathers all relevant information, performs the necessary front calculations, and distributes the results back to the other involved processors. The parallelization penalty amounts to an increase of about 10 % in computing time and memory. Some data of the simulated systems can be found in Table 1 below.

3. System Characteristics

Two simulation series with void fractions of 2, 6, and 12 % in each case were performed, see Table 1. First, the mono-disperse systems already simulated by Bunner & Tryggvason (2002a,b) were split into an equal number of small and large bubbles, so that the average dimensional parameters remained approximately the same. The idea was to study the influence of a bimodal size distribution on the interaction between the bubbles as well as on the thereby induced turbulence in the liquid phase. The volume ratio between small and large bubbles was chosen as 1:2, and the surface tension was adjusted such that all bubbles could be expected to remain fairly spherical under free rise conditions. The Galileo and Eötvös numbers were $Ga_s = 600$, $Eo_s = 0.63$ and $Ga_l = 1200$, $Eo_l = 1.0$ for the small and large bubbles, respectively. The Morton number had the value $6.945 \cdot 10^{-7}$ in these simulations. (The values of the corresponding mono-disperse simulations were $Ga = 900$, $Eo = 1.0$, $M = 1.2345 \cdot 10^{-6}$.)

Because of resolution and computing time requirements, the number of bubbles had to be rather low in these simulations. For being able to estimate the influence of system size, a test calculation with significantly more bubbles was carried out for a void fraction of 6 %. It turned out that the mean rise velocities and the mean vertical fluctuation velocities of the bubbles depend weakly on the system size, while its effect on the horizontal fluctuation velocities and the liquid turbulence is more pronounced. Although only two 6 % systems were simulated, the results appear to fall in line with those of the mono-disperse systems, where these velocity and pseudo-turbulence values first increase with system size but then level off rather quickly (cf. Göz et al. 2001a).

name	α	$V_s : V_l$	$n_s + n_l$	grid	procs.	T_f [s]	CPU
bd2	2 %	1 : 2	10 + 10	192^3	8	60	87
bd6a	6 %	1 : 2	8 + 8	128^3	8	60	73
bd6b	6 %	1 : 2	29 + 29	192^3	8	54	120
bd12	12 %	1 : 2	9 + 9	104^3	8	60	87
bd2b	2 %	1 : 8	32 + 4	256^3	16	120	213
bd6c	6 %	1 : 8	40 + 5	192^3	18	119	157
bd12a	12 %	1 : 8	64 + 8	192^3	18	121	253

Table 1: List of simulated bidisperse bubble systems. Parameters: void fraction, volume ratio of small to large bubble, number of small and large bubbles, size of the fixed grid, number of processors, end time of the simulation in seconds, computing time in days

In a second simulation series, the effect of the deformability of a part of the bubbles on the system behaviour was investigated. The small bubbles were kept again spherical, while the large bubbles could deform into ellipsoids. Furthermore, the volume ratio was increased to 1:8. Simultaneously, eight times more small than large bubbles were brought into the periodic domain, so that the volume fractions of both size classes were the same this time. The resulting dimensionless parameters were $Ga_s = 900$, $Eo_s = 1.0$; $Ga_l = 7200$, $Eo_l = 4.0$; $M = 1.235 \cdot 10^{-6}$. (Bunner & Tryggvason [2002c] used $Ga = 900$, $Eo = 5.0$, $M = 1.543 \cdot 10^{-4}$ for their mono-disperse simulations of ellipsoidal bubbles.)

4. Bubble Motion and Interactions, Liquid turbulence

Snapshots of the 6 % systems bd6b and bd6c are provided in Figure 1 together with illustrations of the bubble trajectories starting within the respective computational domains. Obviously, the trajectories are not straight lines like for a single spherical bubble, but fluctuate considerably due to frequent bubble interactions (the cross-stream motions appear exaggerated as the horizontal axes have been stretched compared to the vertical axis for better visibility). In addition, the large ellipsoidal bubbles perform zig-zag motions and deform non-uniformly at the lateral turning points. As there are only 5 large bubbles in the bd6c system, they interact rather infrequently with each other and are also relatively unaffected by the presence of the small bubbles. This changes when the system becomes more dense. Since the large ellipsoidal bubbles rise much faster than the small ones, they frequently catch up with a small bubble and push it out of their way. Sometimes a small bubble is briefly drawn into the wake of a large one but is also rather quickly left behind. The evolution of the bubble rise velocities in this system is plotted in Figure 2 (left).

The number of small bubbles is high enough to enable the observation of instantaneous formations of bubble clusters and strands, especially in the bd6c system (fig. 1, bottom right). Such developments can be nicely seen in movies of the bubbles' motion, which have been produced from all simulations. Two sequences with interesting bubble interactions can be found on the web page http://www-mvt.iw.uni-halle.de/mvt-home_e.html (follow the links "Research", then "Research group multiphase flows", scroll down and click on the picture corresponding to that in Figure 1 bottom right).

It turns out that the bidisperse systems with spherical bubbles with volume ratio 2 behave very similarly to the corresponding mono-disperse systems (i.e. essentially spherical bubbles comprising the same total void fraction; for details see Göz et al. 2001a, 2003). Differences occur in the fluctuation velocities (not shown) averaged over all bubbles; they are higher in the bidisperse case because of the difference in the rise velocities of the two bubble size classes. If the fluctuation velocities within only one size class are considered, the difference becomes marginal. Moreover, the mean rise velocity of all bubbles as well as the liquid pseudo-turbulence attain comparable values for corresponding mono- and bidisperse systems (cf. fig. 2/right and fig. 3/left).

The values in the bidisperse systems with deformable large bubbles follow the same trends as in the mono-disperse systems with ellipsoidal bubbles. But since the Galileo number and thus the rise velocity of the large bubbles in the bidisperse systems is substantially larger than in the mono-disperse systems, the average rise Reynolds number and the induced liquid turbulence are accordingly higher for given void fraction (see fig. 2/right and fig. 3/left, respectively). In any case, it is observed that the mean rise Reynolds number of the bubbles decreases with in-

creasing void fraction due to the hindrance effect (fig. 2/right), while the mean fluctuation velocities of the bubbles and the Reynolds stresses of the liquid increase with the void fraction due to more frequent and stronger bubble interactions which also act as a stirring force to the liquid. Interestingly, the mean values of the rise velocities taken within each of the two size classes (only small vs. only large bubbles) converge slightly with increasing void fraction. This is again a result of the increasing bubble interaction, in particular the interaction between small and large bubbles which leads to an acceleration of the small and a deceleration of the large bubbles. This feature is particularly visible in the temporal evolution of the bubble rise velocities of the bd12a system (Göz et al. 2001b).

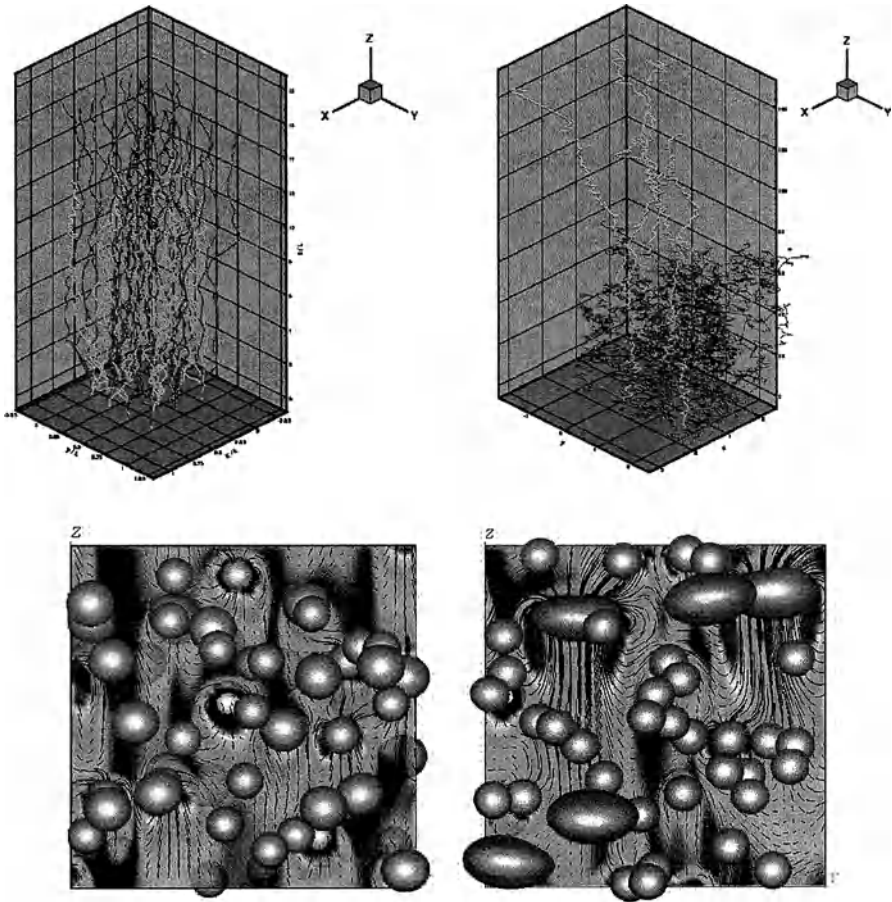


Fig. 1: Bubble trajectories (not to scale) and snapshots (bubble configurations together with a cross section of the velocity field and vorticity contours) of the 6 % systems bd6b (left) and bd6c (right)

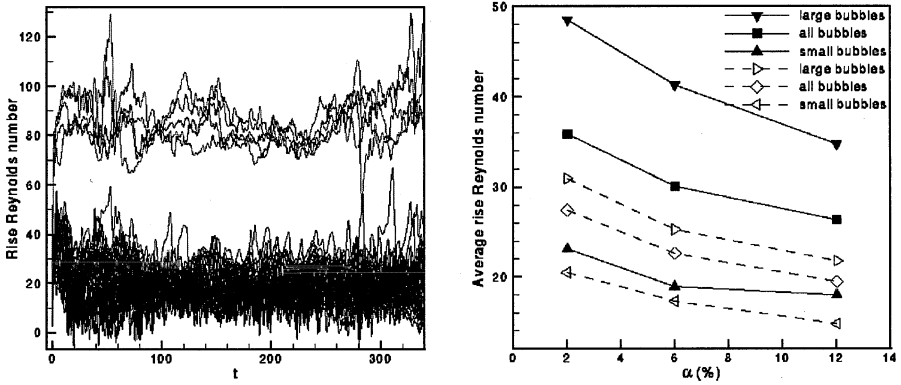


Fig. 2: Left: Individual rise Reynolds numbers versus time of all bubbles in the 6 % system bdc with 5 large deformable (upper band) and 40 small spherical (lower band) bubbles. The velocities have been normalized as Reynolds numbers by using the individual bubble diameters. Right: Average rise Reynolds numbers versus the void fraction for the small, large, and all bubbles of the bidisperse systems; the full symbols and solid lines characterize the systems containing a number of large ellipsoidal bubbles; the open symbols and dashed lines characterize the systems containing almost spherical bubbles. For comparability, all values have been normalized using the same length scale, namely the bubble diameter d_m corresponding to a Galileo number of 900.

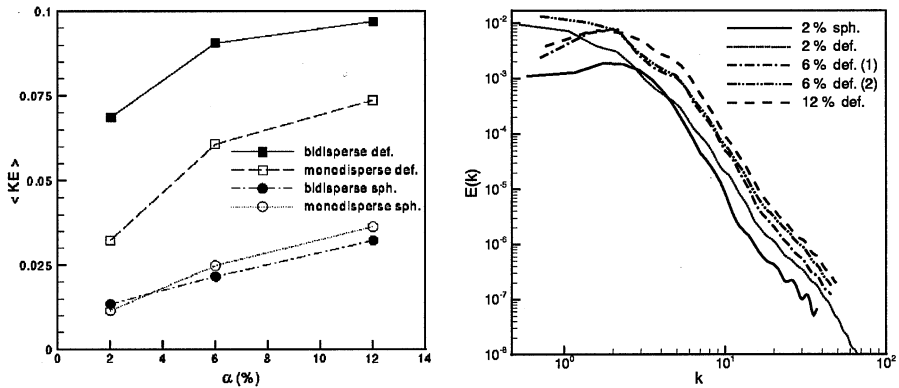


Fig. 3: Left: Turbulent kinetic energy of the liquid versus the void fraction for the mono- and bidisperse systems (normalized by $\rho_1 g d_m$). Right: Spectra of the turbulent kinetic energy for various bidisperse systems (for the 6 % system with deformable bubbles two different time levels are shown, in the initial period of the calculation and at the end). $E(k)$ has been normalized by $\rho_1 g d_m^2$ the wave number k by d_m^{-1} .

The horizontal components of the mean fluctuation velocities and Reynolds stresses increase stronger than the vertical components, so that the anisotropy of the gas-liquid flow diminishes with increasing void fraction (Göz et al. 2003). The effect of void fraction and bubble size and possibly shape on the turbulent kinetic energy of the liquid is shown in the left part of Figure 3 for both mono- and bidisperse simulations. In the right part, a few typical spectra of the kinetic energy in the bidisperse systems are given. Like in the mono-disperse bubbly flows (Bunner & Tryggvason 2002b), they follow approximately a -3.6 power law at large wave numbers. The spectral energy is of course higher for the case of the system with deformable bubbles (shown for 2 % gas volume fraction), especially in the low and high wave number regime. With increasing void fraction a further increase is observed which is consistent with the increase of turbulent kinetic energy of the fluid (Fig. 3/left). The two spectra for the 6 % system with deformable bubbles were obtained at the beginning of the calculation (1) and in the quasi-steady condition (2). The result mainly shows a modification at low and high wave numbers which is associated with the flow development in the system.

5. Microstructure

An important aspect of bubbly flows are the spatial distribution and relative motion of bubbles. The local and instantaneous interactions among two or more bubbles contribute to global and time-averaged flow patterns. The simultaneous presence of multiple bubble populations consisting of differently sized (and thus possibly differently shaped) bubbles adds even more complexity to the flow. In the case of bidisperse bubbly flows, one needs to consider the interaction between small bubbles only, that between large bubbles, and that between small and large bubbles separately.

Preferred bubble configurations can be detected by calculating the pair probability distribution function (ppdf) of relative position, $G(r, \theta)$, which is the probability to find the centroids of two bubbles separated by a distance r and their connecting line oriented at an angle θ with respect to the direction against gravity (Bunner & Tryggvason 2002a). Further insight into the dynamics of bubble interactions can be obtained by analysing the relative motion of bubble pairs. Using a polar coordinate system, the relative velocity of two bubbles is decomposed into its radial and tangential components. A negative radial relative velocity v_r indicates that the two bubbles approach each other and may be interpreted as if the bubbles attract each other; vice versa, a positive v_r may be interpreted as repulsive forces being at work. A positive angular relative velocity, v_θ , occurs, when the connecting line between two bubbles rotates away from the vertical axis towards a horizontal alignment. This may be a true rotation of two close bubbles about each other during a direct encounter like in a collision, or it may simply indicate that a larger and thus faster rising bubble passes a small one at some distance. Since the

main direction of the flow is vertical, the cross-stream directions are equivalent and therefore the third component of the relative motion of bubble pairs representing rotations in the horizontal plane is not considered here.

For reasons of space, we have to focus on the two systems bd6b and bd6c with 6 % void fraction; the influence of the void fraction will be discussed elsewhere (e.g. Göz et al. 2003). The first system contains 29 large and 29 small bubbles with volume ratio 2, all remaining fairly spherical. Due to the high number of bubbles, this is the statistically most reliable system of the first series of simulations. The second system contains 5 large ellipsoidal and 40 small spherical bubbles with volume ratio 8. Unfortunately, the number of large bubbles is somewhat too low so that they do not interact that much with each other. The ppdf's of the relative position and velocity components for the various pair combinations (small, large, mixed) are displayed in the subsequent figures (Figs. 4 to 7) in the form of contour plots. The results were obtained by averaging over 500 evenly spaced time samples. The ppdf's of relative position are normalized by that of a uniform distribution. The relative velocity components are normalized as Reynolds numbers using volumetric-mean bubble diameters (d_m corresponding to $Ga = 900$ for the spherical bubble systems, $1.211 \cdot d_m$ for the systems with ellipsoidal bubbles). The discrete values were interpolated onto a regular grid in polar coordinates.

The angle θ against the vertical axis extends between 0 and π . Because the distribution functions of relative position and relative radial velocity are symmetric, and that of the relative angular velocity is anti-symmetric with respect to $\theta = \pi/2$, it suffices to show only half of this domain. In the case of mixed pairs containing one small and one large bubble, however, it makes more sense to not treat all bubbles equally but to determine biased ppdf's, in which, for instance, the relative position and motion of all small bubbles with respect to all large bubbles is averaged. Clearly, these biased ppdf's cannot be expected to show the same symmetry properties as those obtained by summing over all bubble pairs of a certain size class.

Let us first briefly recap the behaviour of bubble pairs in mono-disperse bubble suspensions with 27 equally sized bubbles (Bunner & Tryggvason 2002a,b, 2003). Except in special situations, where deformable bubbles interact strongly and form a global flow pattern (streaming), the motion of two bubbles at large distances is uncorrelated and the bubbles are uniformly distributed on average. Thus, in general the distance between two bubbles must be small enough for meaningful interaction to occur. The bubbles may interact either by direct collision or through their influence on the flow of the interstitial liquid. Close-range encounters may or may not involve surface deformations depending on parameters like surface tension and approach velocity.

If two bubbles are initially in line, the trailing one accelerates in the wake of the leading one. While two spherical bubbles rotate about each other before they collide, two deformable (ellipsoidal) bubbles remain in line until they collide, then

rotate about each other. According to Legendre & Magnaudet (1998), two spherical bubbles rising side by side attract at large distances but repel when being close, so that there exists an equilibrium distance. Yuan & Prosperetti (1994) found that two in-line spherical bubbles attract due to wake effects and repel due to an adverse pressure gradient. If these forces balance each other, there is also an equilibrium distance, which is however unstable to lateral disturbances.

Overall, in mono-disperse systems, spherical bubbles tend to align themselves horizontally, while deformable bubbles tend to align vertically. In addition, two in-line bubbles rise faster than the average, while two side-by-side bubbles rise slower. This feature can also be observed in the bidisperse systems, no matter which type the two involved bubbles are of. But in the bidisperse systems, the general trend in the relative position of bubble pairs (see the top parts of Figs. 4 and 7 and the left plots of Figs. 5 and 6) is almost always towards horizontal or near-horizontal alignments at small distance ($1 < r/d \leq 2$, where d is the arithmetic mean of the equivalent diameters of the two involved bubbles; i.e., $r/d = 1$ means contact of non-deformed fronts). This is understandable for the small and the large bubbles in the bd6b system (Figs. 4 and 5), as well as for the small bubbles in the bd6c system (Figs. 6 and 7), as all of them are essentially spherical. That no vertically aligned pairs of large ellipsoidal bubbles are found in the bd6c system may be caused by the fact that there are only 5 of them but 40 small bubbles around and between them. The same trend is observed for the other void fractions. Obviously the presence of many small bubbles suppresses direct wake-induced interactions between large bubbles but still allows them rising side by side. Another difference to the behaviour of mono-disperse systems is that the small bubble population is not that much confined to horizontal orientations, see Fig. 4 (top left). Instead the distribution function of the relative position of the small bubbles in the bd6b system has another peak at $\theta = 0$ and $r/d_s = 3.0$ and shows an additional preference for vertical alignments at larger pair separation distances (Fig. 4). Furthermore, while the small bubbles in the bd6c system show a clear preference for horizontal alignment at small distance, this turns into a (weaker) preference for near-vertical alignments as the separation distance increases (Fig. 7, top left). Thus, in the presence of larger bubbles, the small spherical bubbles are pushed into more vertical alignments at intermediate to large distances.

The general trend in the relative radial velocities of pairs of bubbles within the same size class (middle parts of Figs. 4 and 7) points towards strong attraction ($v_r < 0$) at small to intermediate vertical distance and weak horizontal repulsion ($v_r > 0$), like in the mono-disperse systems. The regions of weak repulsion near $\theta = \pi/2$ are often interrupted by regions of weak attraction, especially for the large bubbles in bd6b (Fig. 4, middle right), causing eventually the peaks in the ppdf of relative position (red spots), which apparently represent equilibrium positions. For oblique orientations, the ppdf of v_r is very ragged and no clear trend is visible, as regions of repulsion are interspersed with regions of attraction. It is notable that the regions of strongest attraction as well as strongest repulsion of pairs of large ellip-

soidal bubbles in bd6c (Fig. 7, middle right) occur at close range, the former at $\theta \approx \pi/3$ and the latter at $\theta \approx 5\pi/12$.

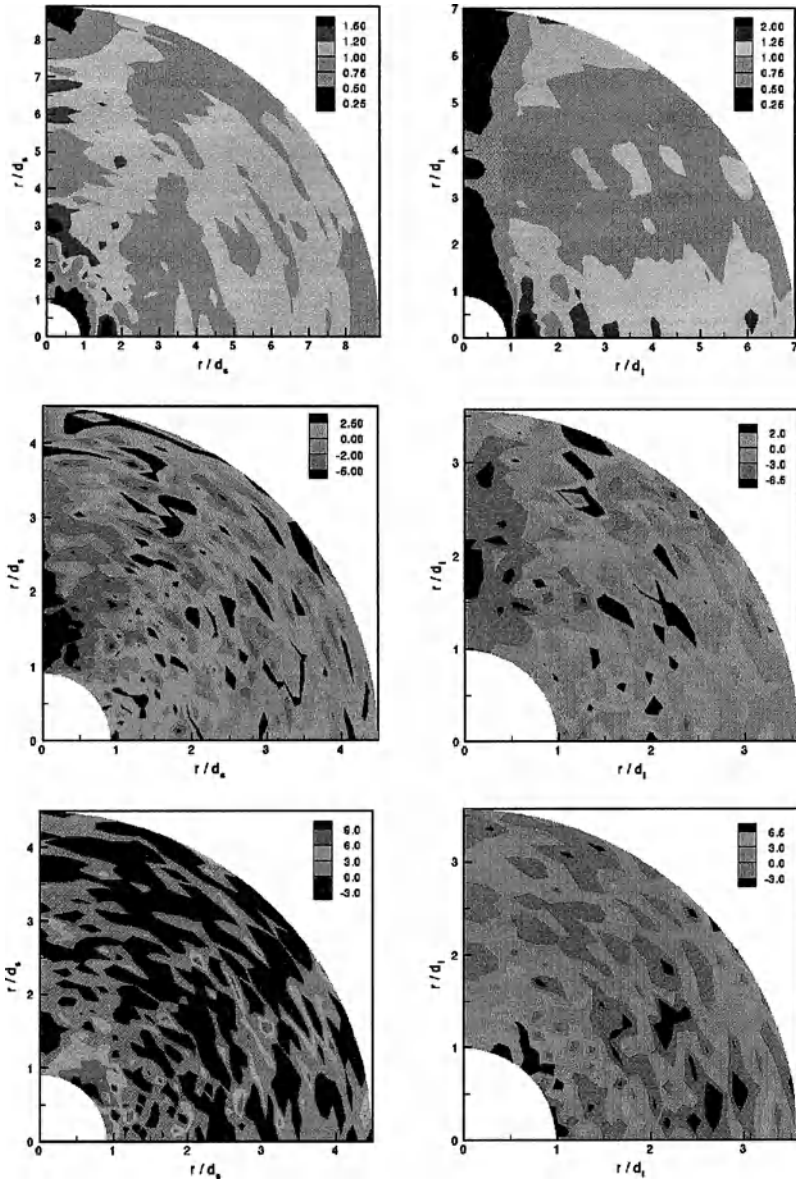


Fig. 4: Pair probability distribution functions of the 29 small spherical (left) and the 29 large almost spherical (right) bubbles for $\alpha = 6\%$ (system bd6b). Top: relative position, middle: relative radial velocity, bottom: relative angular velocity

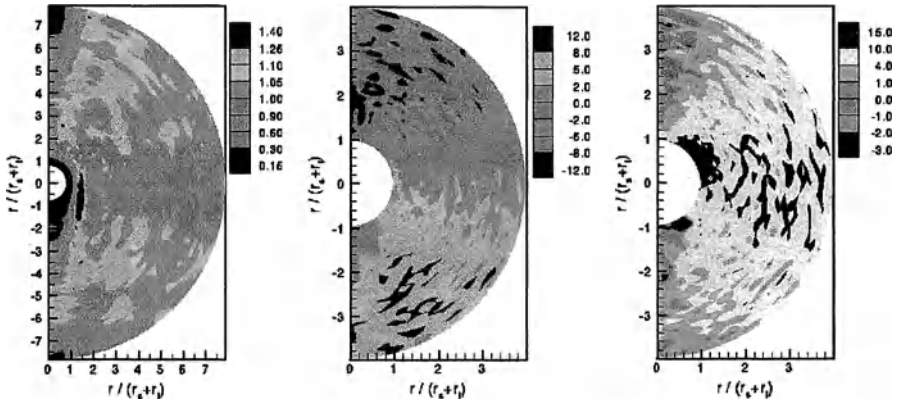


Fig. 5: PDF's of mixed pairs, biased with respect to the large bubbles, for system bd6b. From left to right: relative position, relative radial velocity, relative angular velocity

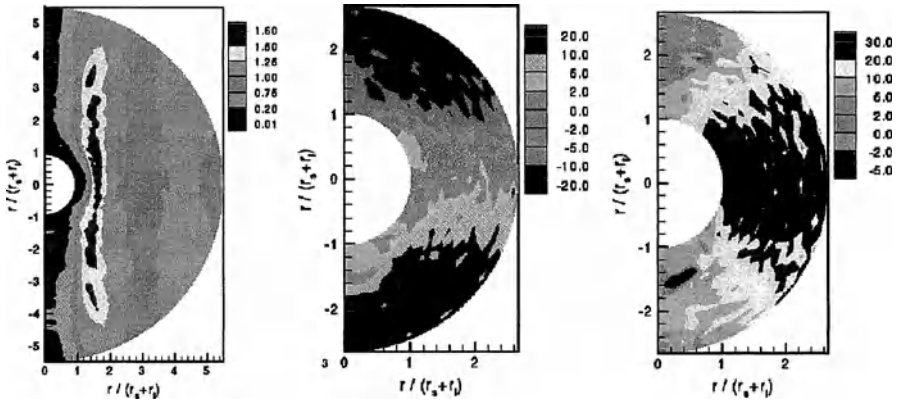


Fig. 6: PDF's of mixed pairs, biased with respect to the large bubbles, for system bd6c. From left to right: relative position, relative radial velocity, relative angular velocity

A similar raggedness is prevailing in the relative angular velocity distributions (bottom parts of Figs. 4 and 7), but there is also a clear tendency for equally sized bubble pairs at close distance to rotate strongly away from the vertical axis toward a more horizontal orientation. This tendency is strongest at near-diagonal orientations ($\theta \approx \pi/4$), in particular for the small bubbles in both 6 % systems (Figs. 4 and 7, bottom left). The maximum in the pdf of v_θ of the large bubbles lies slightly above the diagonal in the bd6b system (Fig. 4, bottom right) and considerably below the diagonal in bd6c (Fig. 7, bottom right); for both distributions, a minimum occurs at close distance near $\theta = \pi/2$ indicating strong rotation of colliding bubble pairs away from the horizontal. However, these interpretations must be treated with some care, as there are very few bubble pairs at touching distance ($r/d \sim 1$); most fronts bounce off each other at a finite distance instead of actually colliding.

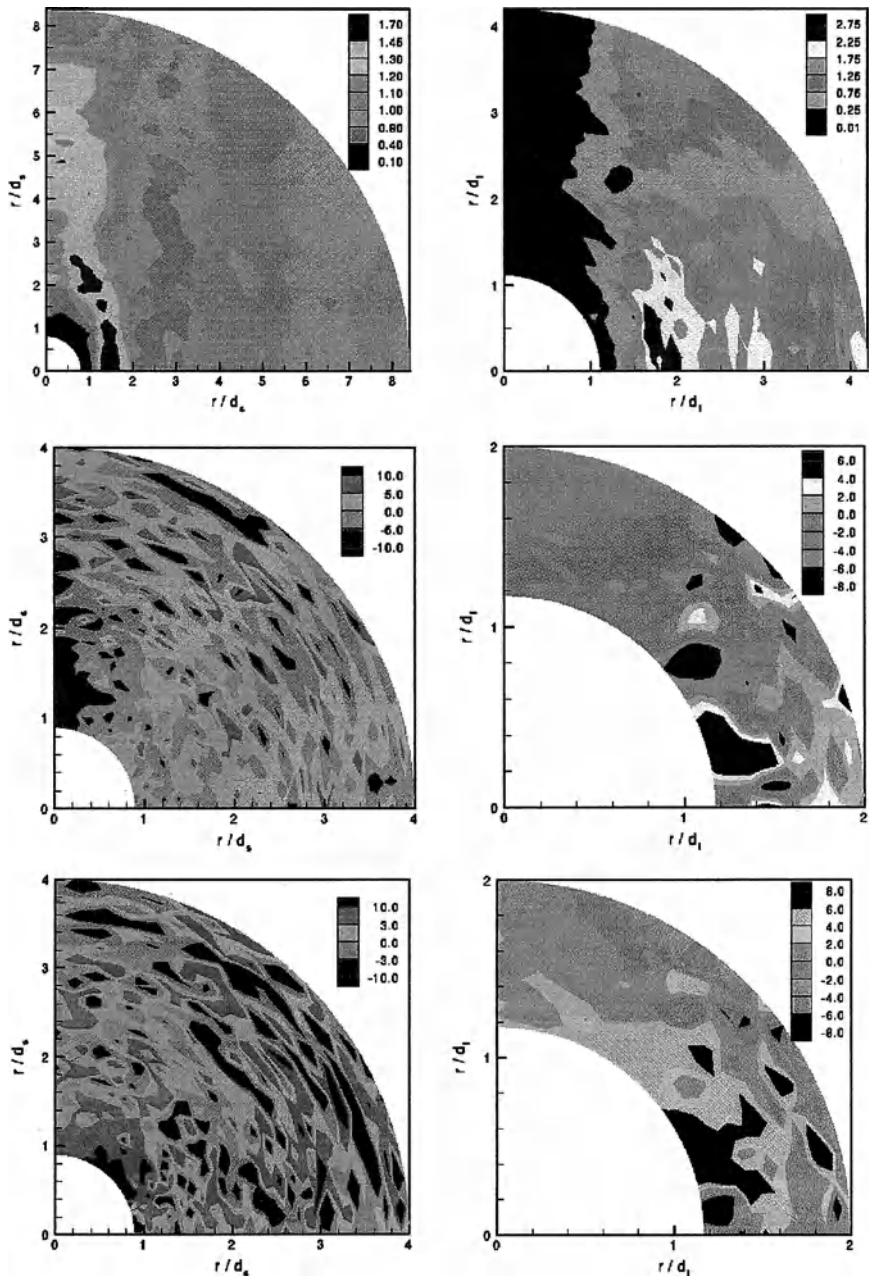


Fig. 7: Pair probability distribution functions of the 40 small spherical (left) and the 5 large ellipsoidal (right) bubbles for $\alpha = 6\%$ (system bd6c). Top: relative position, middle: relative radial velocity, bottom: relative angular velocity

The mixed pairs consisting of a small and a large bubble show also a preference for near-horizontal alignments at small distances (Figs. 5 and 6, left plots). But there are also some new features in the pair probability density functions biased with respect to the large bubbles. In the $bd6b$ system with essentially spherical bubbles (Fig. 5), a small bubble tends to stay sideways to obliquely behind a large bubble at small centroid distances. The probability to find a small bubble side-by-side with a large one at larger distances ($r/d > 2$) is relatively low, and the probability to find a small bubble directly behind a large one is even lower. The relative radial velocity of a small bubble with respect to a large one is negative (approaching), if the small bubble is somewhere ahead the large one and positive if it is behind (Fig. 5, middle). The relative angular velocity is mostly positive except in a small region directly behind large bubbles at an oblique orientation and the maximum velocities occur between the horizontal and the upper diagonal (Fig. 5, right). This indicates that a small bubble to the side and slightly ahead of a large bubble quickly rotates around the large bubble and then slows down; but should it reach the wake region behind the large bubble, it is pushed back and moves out of this region. Rather than interpreting these interaction features in terms of attraction and repulsion, they appear more being simply a result of the different rise velocities of the small and the large bubbles. As a large bubble rises faster than the small ones, it frequently catches up with a small bubble ($v_r < 0$), overtakes it, and leaves it behind ($v_r > 0$). During this process the small bubble appears to rotate about the large one in a spherical coordinate system with the large bubble in the centre ($v_\theta < 0$). This is not too exciting when the small bubble does not lie in the path of the large one, but there are also frequent encounters at close range taking place, during which the large bubble has to push the small one out of its way; here, the former is briefly decelerated while the latter is accelerated (see the movies mentioned above). A similar discussion holds for the alignment of small bubbles with respect to the large ellipsoidal bubbles in the $bd6c$ system (Fig. 6), although the peaks in the relative position do not occur at $\theta = \pi/2$ and small distance but at - non-symmetrical - oblique orientations at somewhat larger distances. In addition, almost no small bubble can be found in line with a large one nor in its wake. There is a small region of repulsion sideways ahead the large bubbles and attraction is found sideways behind, which may be ascribed to the fact that the large bubbles in this system are not spherical as it appears from the plot but actually ellipsoidal.

6. Conclusions

The rise of bimodal bubble distributions through a still liquid were simulated using a parallel finite difference/front tracking scheme. The goal was to elucidate the dependency of the mean rise and fluctuation velocities of the bubble populations and the induced liquid turbulence on the size ratio, deformability, and total volume fraction of small and large bubbles. In the present paper, the emphasis was put on the microstructure of two bubble systems with 6 % void fraction in order to

shed some light on pair-wise bubble interactions. Contour plots of the pair probability density functions of relative position and relative velocity components for pairs of small bubbles, pairs of large bubbles, as well as for mixed pairs were presented and discussed. It was found that the bubbles of a certain size and shape class can behave quite differently in the presence of another class compared to a corresponding mono-disperse system. A general result, on the other hand, is that neither bubble interactions nor liquid Reynolds stresses are isotropic (see Bunner & Tryggvason 2002a,b; Göz et al. 2003). This is not surprising as buoyancy introduces a preferred direction. Furthermore, since the bubble distributions become more uniform with increasing distance indicating that the interaction between two sufficiently distant bubbles is weak, one may concentrate on the influence of nearby bubbles for calculating the effective force on a given bubble, e.g. in an Euler/Lagrange procedure. Because of the anisotropy, however, the meaning of “nearby” varies with the angle θ against the vertical axis.

Acknowledgements

The authors gratefully acknowledge the financial support of the Deutsche Forschungsgemeinschaft (DFG) under grants SO 204/13 and SO 204/19-1 during the course of the Priority Research Programme “Analysis, Modelling and Calculation of Multiphase Flows”. They also want to thank B. Bunner and G. Tryggvason for their continuing collaboration, in particular for the possibility to use their computer code and for their helpful support. Most of the computations were performed on the IBM SP2 parallel computer at the Computing Centre of the University of Karlsruhe. We would like to thank the Computing Centre for the generous grant of computer time and the friendly support.

References

- B. Bunner & G. Tryggvason 2002a: Dynamics of homogeneous bubbly flows. Part I: Rise velocity and microstructure of the bubbles, *J. Fluid Mech.* 466, 17-52.
- B. Bunner & G. Tryggvason 2002b: Dynamics of homogeneous bubbly flows. Part II: Fluctuations of the bubbles and the liquid, *J. Fluid Mech.* 466, 53-84.
- B. Bunner & G. Tryggvason 2003: Effect of bubble deformation on the properties of bubbly flows. *J. Fluid Mech.*, submitted.
- M. F. Göz, B. Bunner, M. Sommerfeld & G. Tryggvason 2001a: Simulation of bubbly gas-liquid flows by a parallel finite-difference/front-tracking method, in: E. Krause & W. Jäger (eds.), *High Performance Computing in Science and Engineering 2000* (Springer 2001), pp. 326-337.
- M. F. Göz, B. Bunner, M. Sommerfeld, G. Tryggvason 2001b: Direct numerical simulation of bidisperse bubble swarms, *Proc. 4th Int. Conf. on Multiphase Flow* (New Orleans, May 2001).

- M. F. Göz, B. Bunner, M. Sommerfeld & G. Tryggvason 2002a: Direct numerical simulation of bubble swarms with a parallel front-tracking method, in: M. Breuer, F. Durst, C. Zenger (eds.), *High Performance Scientific and Engineering Computing*, Erlangen 2001 (Springer 2002), pp. 97-106.
- M. F. Göz, B. Bunner, M. Sommerfeld & G. Tryggvason 2002b: Simulation of bidisperse bubbly gas-liquid flows by a parallel finite-difference/front-tracking method, in: E. Krause & W. Jäger (eds.), *High Performance Computing in Science and Engineering '01* (Springer 2002), pp. 298-308.
- M. F. Göz, M. Sommerfeld, B. Bunner, G. Tryggvason 2002c: Microstructure of a bidisperse swarm of spherical bubbles, *Proc. of the ASME FEDSM'02* (Montreal, July 2002), Paper No. FEDSM2002-31395.
- M. F. Göz, M. Sommerfeld, B. Bunner, G. Tryggvason 2003: Direct numerical simulation of bidispersed bubble suspensions. In preparation for *Physics of Fluids*.
- D. Legendre & J. Magnaudet 1998: Interaction between two spherical bubbles rising side by side, *Proc. 3rd Int. Conf. on Multiphase Flow* (Lyon, France).
- G. Tryggvason, B. Bunner, A. Esmaeeli, D. Juric, N. Al-Rawahi, W. Tauber, J. Han, S. Nas & Y.-J. Jan 2001: A front tracking method for the computations of multiphase flow, *J. Comp. Phys.* 169, 708-759.
- H. Yuan & A. Prosperetti 1994: On the in-line motion of two spherical bubbles in a viscous fluid, *J. Fluid Mech.* 278, 325-349.

Finite Element Discretization Tools for Gas-Liquid Flows

Dmitri Kuzmin and Stefan Turek

Institute of Applied Mathematics, University of Dortmund
Vogelpothsweg 87, D-44227, Dortmund, Germany

A segregated finite element algorithm is proposed for the numerical treatment of gas-liquid flows subject to mass transfer and chemical reaction. The Navier-Stokes equations are solved by an efficient projection-like method. Novel high-resolution finite element schemes of TVD type are introduced for the discretization of unstable convective terms. Iterative solution techniques, operator splitting tools and other relevant algorithmic aspects are discussed.

1 Mathematical Model

It was shown by Sokolichin and Eigenberger [4] that the bubble-induced buoyancy resembles free convection and can be incorporated into an incompressible flow solver using an analog of the Boussinesq approximation. In this paper, we supplement the drift-flux model proposed in [4] by extra transport equations so as to take mass transfer and chemical reactions into account. The resulting PDE system consists of the following subproblems [2]:

- Navier-Stokes/‘Boussinesq’ equations

$$\begin{aligned} \frac{\partial \mathbf{u}_L}{\partial t} + \mathbf{u}_L \cdot \nabla \mathbf{u}_L &= -\nabla p_* + \nu_{\text{eff}} \Delta \mathbf{u}_L - \epsilon \mathbf{g}, \\ \nabla \cdot \mathbf{u}_L &= 0. \end{aligned} \quad (1)$$

- Continuity equations for the gas phase

$$\frac{\partial \tilde{\rho}_G}{\partial t} + \nabla \cdot (\tilde{\rho}_G(\mathbf{u}_L + \mathbf{u}_{\text{slip}}) - d_G \nabla \tilde{\rho}_G) = -m_{\text{int}}, \quad (2)$$

$$\frac{\partial n}{\partial t} + \nabla \cdot (n(\mathbf{u}_L + \mathbf{u}_{\text{slip}}) - d_G \nabla n) = 0. \quad (3)$$

- Transport equations for the liquid phase

$$\frac{\partial \tilde{c}_A}{\partial t} + \nabla \cdot (\tilde{c}_A \mathbf{u}_L - \tilde{d}_A \nabla c_A) = \frac{m_{\text{int}}}{\eta} - \tilde{k}_2 c_A c_B, \quad (4)$$

$$\frac{\partial \tilde{c}_B}{\partial t} + \nabla \cdot (\tilde{c}_B \mathbf{u}_L - \tilde{d}_B \nabla c_B) = -\nu_B \tilde{k}_2 c_A c_B, \quad (5)$$

$$\frac{\partial \tilde{c}_P}{\partial t} + \nabla \cdot (\tilde{c}_P \mathbf{u}_L - \tilde{d}_P \nabla c_P) = \nu_P \tilde{k}_2 c_A c_B. \quad (6)$$

Here \mathbf{u}_L stands for the liquid velocity, \mathbf{u}_{slip} is the laminar slip velocity, ϵ is the local gas holdup, $\tilde{\rho}_G$ is the effective gas density and n is the number density of bubbles. The rate of interphase mass transfer is denoted by m_{int} while the effective concentrations \tilde{c}_A , \tilde{c}_B , \tilde{c}_P refer to the dissolved gas, the liquid component it reacts with and the resulting product, respectively.

The above PDEs are supplemented by the algebraic closure relations

$$\mathbf{u}_{\text{slip}} = -\frac{\nabla p}{C_W}, \quad m_{\text{int}} = Ek_L^0 a_S \left(\frac{p}{H} - c_A \right) \eta, \quad (7)$$

$$\epsilon = \frac{\tilde{\rho}_G RT}{p\eta}, \quad a_S = (4\pi n)^{1/3} (3\epsilon)^{2/3}, \quad \nu_{\text{eff}} = \text{const.} \quad (8)$$

The derivation and analysis of the model is presented elsewhere [1],[2]. The problem statement is to be completed by specifying appropriate initial and boundary conditions which depend on the particular application.

2 Numerical Algorithm

The main features of the numerical algorithm are summarized below. The discretization in space is performed by an unstructured grid finite element method in order to provide an accurate treatment of non-Cartesian geometries with internal obstacles. The incompressible Navier-Stokes equations call for the use of an LBB-stable finite element pair. A suitable candidate is the nonconforming Rannacher-Turek element (rotated multilinear velocity, piecewise-constant pressure). Standard multilinear elements are employed for other variables. The manually generated coarse mesh is successively refined to produce hierarchical data structures for the multigrid solver.

The coupled subproblems are solved one at a time within a block-iterative loop of Gauß-Seidel type. A two-way coupling is currently implemented only for the hydrodynamic part $(\mathbf{u}_L, p, \epsilon)$. We solve the Navier-Stokes equations using the gas holdup from the last outer iteration, then update the gas holdup and repeat this procedure until the residual of the momentum equation or the relative changes of the gas holdup distribution are small enough. The resulting velocity field is substituted into the transport equations (3)–(6) and remains fixed until the end of the time step. The saddle point problem (1) is solved using the Pressure Schur Complement techniques implemented in the software package FEATFLOW (see <http://www.featflow.de>). The mathematical background and implementation aspects are described in [5].

The convection-diffusion and absorption-reaction processes are treated separately using a straightforward operator splitting strategy. First, all scalar quantities are transported without taking the sources/sinks into account. The homogeneous equations (9)–(12) are decoupled and can be processed in parallel. The updated concentration fields serve as initial data for a system of ODEs which describe the accumulation and consumption of species. These

equations are nonlinear and strongly coupled but the nodal ODE systems are independent of one another. The two steps to be performed are:

Step 1: convection-diffusion

$$\frac{\partial \tilde{\rho}_G}{\partial t} + \nabla \cdot (\tilde{\rho}_G \mathbf{u}_G - d_G \nabla \tilde{\rho}_G) = 0, \quad (9)$$

$$\frac{\partial \tilde{c}_A}{\partial t} + \nabla \cdot (\tilde{c}_A \mathbf{u}_L - \tilde{d}_A \nabla c_A) = 0, \quad (10)$$

$$\frac{\partial \tilde{c}_B}{\partial t} + \nabla \cdot (\tilde{c}_B \mathbf{u}_L - \tilde{d}_B \nabla c_B) = 0, \quad (11)$$

$$\frac{\partial \tilde{c}_P}{\partial t} + \nabla \cdot (\tilde{c}_P \mathbf{u}_L - \tilde{d}_P \nabla c_P) = 0. \quad (12)$$

Step 2: absorption-reaction

$$\frac{d \tilde{\rho}_G}{dt} = -m_{\text{int}}, \quad (13)$$

$$\frac{d \tilde{c}_A}{dt} = \frac{m_{\text{int}}}{\eta} - \tilde{k}_2 c_A c_B, \quad (14)$$

$$\frac{d \tilde{c}_B}{dt} = -\nu_B \tilde{k}_2 c_A c_B, \quad (15)$$

$$\frac{d \tilde{c}_P}{dt} = \nu_P \tilde{k}_2 c_A c_B. \quad (16)$$

In equation (9) \mathbf{u}_G stands for $\mathbf{u}_L + \mathbf{u}_{\text{slip}}$. Note that operator splitting is applied locally in time, i.e. within each time step. The solution is integrated in time from t_n to $t_{n+1} = t_n + \Delta t_n$ by the following algorithm:

1. Solve the Navier-Stokes equations (1) for \mathbf{u}_L and p .
2. Recover the pressure gradient ∇p using an L_2 -projection.
3. Calculate the slip velocity as $\mathbf{u}_{\text{slip}} = -\frac{\nabla p}{C_w}$.
4. Advance $\tilde{\rho}_G$ using (9) and recompute $\epsilon = \frac{\tilde{\rho}_G RT}{p \eta}$.
5. Substitute ϵ into (1) and evaluate the residual.
6. If converged then proceed to 7, otherwise go to 1.
7. Update the number density n according to (3).
8. Solve the homogeneous transport equations (10)–(12).
9. Compute the interfacial area $a_S = (4\pi n)^{1/3} (3\epsilon)^{2/3}$.
10. Solve the ODE system (13)–(16) for each node.

Let us briefly discuss the choice of the iterative solver and of the time discretization. In general, explicit schemes are rather inefficient due to severe stability limitations which require taking impractically small time steps. For this reason, we restrict ourselves to the implicit Crank-Nicolson and backward Euler methods which are unconditionally stable and permit large time steps at the expense of solving nonsymmetric linear systems. The local time step can be selected individually for each subproblem so as to maximize accuracy and/or stability. This provides an efficient treatment of physical processes occurring simultaneously but on entirely different time scales. The communication between the subproblems takes place at the end of the common macro time step Δt_n which is chosen adaptively so as to capture the dynamics of the two-phase flow in an efficient way. We adopt a fairly simple PID controller due to Valli *et al.* Specifically, we select the macro time step as follows

1. Monitor the relative changes of the gas holdup distribution

$$e_n = \frac{\|\epsilon^{n+1} - \epsilon^n\|}{\|\epsilon^{n+1}\|}$$

2. If $e_n > \delta$ reject the solution and repeat the time step using

$$\Delta t_* = \frac{\delta}{e_n} \Delta t_n$$

3. Adjust the time step smoothly so as to approach the prescribed tolerance for the relative changes

$$\Delta t_{n+1} = \left(\frac{e_{n-1}}{e_n}\right)^{k_P} \left(\frac{TOL}{e_n}\right)^{k_I} \left(\frac{e_{n-1}^2}{e_n e_{n-2}}\right)^{k_D} \Delta t_n$$

4. Limit the growth and reduction of the time step so that

$$\Delta t_{\min} \leq \Delta t_{n+1} \leq \Delta t_{\max}, \quad m \leq \frac{\Delta t_{n+1}}{\Delta t_n} \leq M$$

Note that the local gas holdup ϵ is a perfect indicator variable because the flows in gas-liquid reactors are driven by the bubble-induced buoyancy.

As far as the iterative solution of linear systems is concerned, we found BiCGSTAB and geometric multigrid to perform very well as long as the parameters are properly tuned and the underlying smoothers/preconditioners are consistent with the size of the time step. If Δt is rather small, standard components like Jacobi, Gauß-Seidel and SOR schemes will suffice. For large time steps, the condition number of the matrix deteriorates and convergence may fail. This can be rectified by resorting to an ILU factorization in conjunction with an appropriate renumbering scheme.

3 Treatment of Convection

As long as our model consists of convection-dominated transport equations, an accurate treatment of convective terms is vitally important. The standard Galerkin method is a ‘centered’ scheme which is known to be unstable. A common remedy is to add streamline diffusion which provides the necessary stabilization without reducing the order of approximation. However, even stabilized high-order methods tend to produce nonphysical undershoots and overshoots in the vicinity of steep gradients. As a result, negative gas holdups or concentrations may arise, which is clearly unacceptable. It is possible to get rid of oscillations by adding adaptive artificial diffusion depending on the local solution behavior. The high-order scheme can be used in smooth regions but near discontinuities it should be replaced by a low-order scheme like ‘upwind’ which is diffusive enough to prevent the formation of wiggles.

Below we illustrate how this can be accomplished in the framework of high-resolution schemes based on a new generalization of TVD concepts.

3.1 Galerkin discretization

As a model problem, we consider the scalar conservation law

$$\frac{\partial u}{\partial t} + \nabla \cdot (\mathbf{f} - d\nabla u) = 0 \quad \text{in } \Omega, \quad (17)$$

where $\mathbf{f} = \mathbf{v}u$ stands for the convective flux and d denotes the diffusion coefficient. All of our homogeneous transport equations (3), (9)–(12) can be written in this form. The concomitant flux boundary conditions are

$$-\mathbf{n} \cdot (\mathbf{f} - d\nabla u) = g \quad \text{on } \Gamma_1, \quad \mathbf{n} \cdot (\mathbf{f} - d\nabla u) = 0 \quad \text{on } \Gamma_2, \quad \mathbf{n} \cdot \nabla u = 0 \quad \text{on } \Gamma_3$$

where \mathbf{n} denotes the outward unit normal. On the feed boundary Γ_1 the incoming flux is determined by the operating conditions. In particular, the total gas throughput divided by the aerated area yields the value of g for the continuity equation (9). Obviously, there is no flux through the solid wall Γ_2 . On the outflow boundary Γ_3 the diffusive flux is canceled while the convective one is left free as required by the hyperbolic limit of pure convection ($d = 0$). It is implied that $\mathbf{v} \cdot \mathbf{n} < 0$ on Γ_1 while $\mathbf{v} \cdot \mathbf{n} > 0$ on Γ_3 . Using the divergence theorem to integrate the spatial derivatives in the weak form of (17) by parts and inserting the natural boundary conditions, we obtain

$$\int_{\Omega} w \frac{\partial u}{\partial t} d\mathbf{x} - \int_{\Omega} \nabla w \cdot (\mathbf{f} - d\nabla u) d\mathbf{x} + \int_{\Gamma_3} w \mathbf{f} \cdot \mathbf{n} ds = \int_{\Gamma_1} w g ds. \quad (18)$$

A common practice in finite element methods for conservation laws is to interpolate the fluxes in the same way as the approximate solution:

$$u_h = \sum_j u_j \varphi_j, \quad \mathbf{f}_h = \sum_j \mathbf{f}_j \varphi_j = \sum_j (\mathbf{v}_j u_j) \varphi_j, \quad (19)$$

where φ_i are the basis functions spanning the finite-dimensional subspace. The resulting Galerkin discretization of equation (17) reads

$$\begin{aligned} \sum_j \left[\int_{\Omega} \varphi_i \varphi_j d\mathbf{x} \right] \frac{du_j}{dt} - \sum_j \left[\int_{\Omega} \nabla \varphi_i \cdot (\mathbf{v}_j \varphi_j - d\nabla \varphi_j) d\mathbf{x} \right] u_j \\ + \sum_j \left[\int_{\Gamma_3} \varphi_i \varphi_j \mathbf{v}_j \cdot \mathbf{n} ds \right] u_j = \int_{\Gamma_1} \varphi_i g ds. \end{aligned} \quad (20)$$

This ODE system can be written in compact matrix form as follows

$$M_C \frac{du}{dt} = (K - B)u + q, \quad (21)$$

where M_C is the consistent mass matrix, K is the discrete transport operator, B is the contribution of the surface integral over the Neumann boundary and q is the source term due to incoming fluxes. The matrix entries are given by

$$m_{ij} = \int_{\Omega} \varphi_i \varphi_j \, d\mathbf{x}, \quad k_{ij} = \mathbf{v}_j \cdot \mathbf{c}_{ij} - d s_{ij}, \quad (22)$$

where \mathbf{c}_{ij} and s_{ij} stand for the constant coefficients

$$\mathbf{c}_{ij} = \int_{\Omega} \nabla \varphi_i \varphi_j \, d\mathbf{x}, \quad s_{ij} = \int_{\Omega} \nabla \varphi_i \cdot \nabla \varphi_j \, d\mathbf{x} \quad (23)$$

corresponding to the first- and second-order derivatives, respectively. For customary finite elements, the sum of basis functions is identically one so that the sum of their derivatives vanishes. Hence, the above coefficient matrices have zero column sums and so does the discrete transport operator: $\sum_i k_{ij} = \mathbf{v}_j \cdot \sum_i \mathbf{c}_{ij} - d \sum_i s_{ij} = 0$. Note that the differential operators defined by equation (23) do not change and need to be assembled just once. As long as they are available, the matrix K can be updated in an efficient way by computing the off-diagonal entries k_{ij} from the formula (22) without resorting to costly numerical integration. Due to the zero column sum property, the diagonal matrix entries can be recovered as $k_{jj} = -\sum_{i \neq j} k_{ij}$.

The boundary terms are assembled separately. It is expedient to calculate the surface integrals approximately using a one-point quadrature rule. For each boundary edge/face ∂E_k we evaluate the normal flux at the midpoint, multiply it by the respective area $|\partial E_k|$ and distribute between the nodes. This leads to a diagonal matrix B with entries

$$b_i = \frac{1}{m} \sum_{k \in \mathcal{J}_1^i} \mathbf{v}_i \cdot \mathbf{n}_k |\partial E_k|, \quad \mathcal{J}_1^i = \{j : \mathbf{x}_i \in \partial E_j \cap \Gamma_1\}, \quad (24)$$

where m denotes the number of local degrees of freedom and \mathbf{n}_k is the (unique) normal to ∂E_k . The source term is assembled in a similar way:

$$q_i = \frac{1}{m} \sum_{k \in \mathcal{J}_3^i} g_k |\partial E_k|, \quad \mathcal{J}_3^i = \{j : \mathbf{x}_i \in \partial E_j \cap \Gamma_3\}. \quad (25)$$

An important advantage of using piecewise-constant normal fluxes is that the disjoint boundary components $\Gamma_1, \Gamma_2, \Gamma_3$ are unambiguously defined and the boundary conditions are allowed to have a jump at the interface.

3.2 Construction of a linear LED scheme

Let us perform mass lumping and cast the semi-discrete problem in the form

$$M_L \frac{du}{dt} = (K - B)u + q \quad \Leftrightarrow \quad m_i \frac{du_i}{dt} = \sum_{j \neq i} k_{ij} (u_j - u_i) + r_i u_i + q_i,$$

where $m_i = \sum_j m_{ij}$ and $r_i = \sum_j k_{ij} - b_i$. The term $r_i u_i$ is a discrete counterpart of $u \nabla \cdot \mathbf{v}$ which vanishes for incompressible flows. It is instructive to consider the special case $r_i = q_i = 0$ in which the discrete transport operator K has zero row sum. Such a discretization would be *local extremum diminishing* if all off-diagonal coefficients k_{ij} were nonnegative. Indeed, if u_i is a maximum, then $k_{ij}(u_j - u_i) \leq 0$, so that $\frac{du_i}{dt} \leq 0$. Hence, a maximum cannot increase, and similarly a minimum cannot decrease. In one dimension, a LED scheme is total variation diminishing and monotonicity preserving.

The transport operator K can be rendered LED by adding artificial diffusion D designed so as to eliminate negative off-diagonal entries [3]

$$L = K + D, \quad d_{ii} = - \sum_{k \neq i} d_{ik}, \quad d_{ij} = d_{ji} = \max\{0, -k_{ij}, -k_{ji}\}. \quad (26)$$

The diffusion coefficients d_{ij} are associated with the edges of the graph representing the connectivity of the matrix. For each pair of neighboring nodes i and j , a negative off-diagonal coefficient (say, k_{ij}) is set to zero, while its mirror image k_{ji} is incremented by $-k_{ij}$ and the diagonal entries k_{ii} , k_{jj} are updated so as to maintain zero column sums. This yields the least diffusive linear LED scheme which reduces to the standard upwind approximation for scalar convection problems in one dimension [3]. The row number of the nullified off-diagonal entry determines which of the two nodes is located ‘upwind’. Without loss of generality, we will assume that i is the upwind node for the numerical edge ij , so that $l_{ij} = 0$ whereas $l_{ji} = |k_{ji} - k_{ij}|$. The diffusive flux $d_{ij}(u_j - u_i)$ reduces the difference between the nodal values so as to enforce the positivity constraint.

Note that the artificial diffusion coefficients d_{ij} as defined in (26) are independent of the diagonal part r_i which allows for the physical growth and decay of extrema due to compressibility. The boundary terms q_i are assumed to be nonnegative and may only increase the value of u in the interior. Physical diffusion (if any) built into the coefficients k_{ij} is automatically detected and the amount of artificial diffusion is reduced accordingly. Alternatively, discrete upwinding can be performed only for the convective part of K .

3.3 Defect correction

According to the well-known Godunov theorem, linear monotonicity preserving schemes can be at most first order accurate. To obtain a nonlinear high-resolution scheme, we combine the Galerkin discretization and the associated low-order method within an iterative defect correction loop for the fully discretized problem:

$$\mathbf{u}^{(l+1)} = \mathbf{u}^{(l)} + \omega^{(l)} [C(\mathbf{u}^{(l)})]^{-1} R(\mathbf{u}^{(l)}), \quad l = 0, 1, 2, \dots \quad (27)$$

In a practical implementation one solves a linear subproblem for the solution increment and applies the weighted correction to the last iterate:

$$C(u^{(l)})\Delta u^{(l)} = R(u^{(l)}), \quad u^{(l+1)} = u^{(l)} + \omega^{(l)}\Delta u^{(l)}, \quad u^{(0)} = u^n. \quad (28)$$

Specifically, we take the ‘preconditioner’ to be the low-order operator

$$C(u^{(l)}) = M_L - \theta\Delta t L(u^{(l)}), \quad 0 \leq \theta \leq 1,$$

where θ is the implicitness parameter. By construction, C is an M-matrix which makes it amenable to iterative solution. The residual is given by

$$R(u^{(l)}) = M_L(u^n - u^{(l)}) + \theta\Delta t[L - A]u^{(l)} + (1 - \theta)\Delta t[L - A]u^n + q^{n+\theta},$$

where A is a nonlinear antidiffusion operator to be defined below.

The difference between $K^* = L - A = K + D - A$ and the original transport operator K is a matrix with zero row and column sums. Hence, the diffusive-antidiffusive terms can be decomposed into skew-symmetric internodal fluxes:

$$(K^*u)_i = \sum_j k_{ij}u_j + \sum_{j \neq i} (f_{ij}^d + f_{ij}^a), \quad f_{ij}^d = d_{ij}(u_j - u_i) = -f_{ji}^d. \quad (29)$$

The antidiffusive flux f_{ij}^a from node j into node i is supposed to comply with the LED principle for the discrete scheme. The flux limiters presented below determine how much antidiffusion can be added without generating wiggles.

3.4 TVD flux limiter

For the discrete scheme to be LED, the antidiffusive flux f_{ij}^a must be interpretable as a diffusive flux from some other node(s). To provide this property, we may consider

$$f_{ij}^a = a_{ij}\mathcal{L}(1, \theta_i)(u_i - u_j) = a_{ij}\mathcal{L}(u_i - u_j, \Delta u_{ij}), \quad f_{ji}^a = -f_{ij}^a. \quad (30)$$

Let us leave a_{ij} and $\Delta u_{ij} = \theta_i(u_i - u_j)$ unspecified for the time being. The flux limiter \mathcal{L} represents a limited average operator satisfying certain properties which guarantee the positivity of coefficients. In particular, $\mathcal{L}(a, b) = 0$ if a and b have opposite sign. Some popular TVD limiters are:

- $\mathcal{L}(a, b) = \mathcal{S}(a, b) \cdot \min\{|a|, |b|\}$ minmod
- $\mathcal{L}(a, b) = \mathcal{S}(a, b) \cdot \frac{2ab}{|a+b|}$ Van Leer
- $\mathcal{L}(a, b) = \mathcal{S}(a, b) \cdot \min\left\{\frac{|a+b|}{2}, 2|a|, 2|b|\right\}$ 2-mean
- $\mathcal{L}(a, b) = \mathcal{S}(a, b) \cdot \max\{\min\{2|a|, |b|\}, \min\{|a|, 2|b|\}\}$ superbee

where $\mathcal{S}(a, b) = (\text{sign}(a) + \text{sign}(b))/2$. Recall that the edge ij connects an upwind node i and a downwind node j . Its contributions to the modified convective term can be written as

$$\begin{aligned} \text{node } i : \quad & k_{ij}^*(u_j - u_i) = a_{ij}\mathcal{L}(1, \theta_i)(u_i - u_j) = a_{ij}\mathcal{L}(1, 1/\theta_i)\Delta u_{ij}, \\ \text{node } j : \quad & k_{ji}^*(u_i - u_j) = (|k_{ji} - k_{ij}| - a_{ij}\mathcal{L}(1, \theta_i))(u_i - u_j). \end{aligned}$$

The increment to node j exhibits a LED structure provided that the coefficient k_{ji}^* is nonnegative. All of the flux limiters presented above satisfy the inequality $0 \leq \mathcal{L}(1, \theta) \leq 2$. Hence, the antidiffusion coefficient is taken to be

$$a_{ij} = \min\{d_{ij}, |k_{ji} - k_{ij}|/2\}. \quad (31)$$

The increment to node i will also be local extremum diminishing as long as the upwind difference Δu_{ij} can be cast in the form $\Delta u_{ij} = \sum_{k \neq i} c_{ik}(u_k - u_i)$ with $c_{ik} \geq 0$.

In one-dimensional TVD schemes, θ_i represents the slope ratio at the upwind node, so that $\Delta u_{ij} = u_k - u_i$, where $k \neq j$ refers to the second neighbor of node i . However, the choice of Δu_{ij} for unstructured meshes is nontrivial. A geometric approach commonly employed in the literature is to reconstruct a local one-dimensional stencil by introducing two dummy nodes on the continuation of the edge ij . The difference Δu_{ij} is defined as in the 1D case using the interpolated or extrapolated solution value at the dummy node k adjacent to the upwind node.

A detailed comparison of various techniques for the recovery of u_k shows that the numerical results strongly depend on the employed procedure. Among the least successful methods is the use of gradient reconstruction

$$\Delta u_{ij} = (\mathbf{x}_i - \mathbf{x}_j) \cdot \nabla_h u_i, \quad \nabla_h u_i = \frac{1}{m_i} \sum_{k \neq i} \mathbf{c}_{ki}(u_k - u_i). \quad (32)$$

It is quite clear why this choice of the upwind difference may fail to produce non-oscillatory results. The L_2 -projection of the discrete gradient using Galerkin differential operators is not monotone. Some of the coefficients in the formula for Δu_{ij} may be negative, so that it will not possess the desired form. To rectify this, we employ a low-order projection operator designed by resorting to discrete upwinding as proposed above. Note that $\mathbf{c}_{ki} = -\mathbf{c}_{ik}$ (for internal nodes), so that the elimination of negative off-diagonal coefficients leads to the following LED-type expression:

$$\Delta u_{ij} = \frac{2}{m_i} \sum_{k \neq i} \max\{0, \mathbf{c}_{ki} \cdot (\mathbf{x}_i - \mathbf{x}_j)\}(u_k - u_i).$$

For uniform meshes in one dimension, this kind of extrapolation corresponds to using the upwind gradient and yields the standard value $\Delta u_{ij} = u_k - u_i$.

To illustrate the performance of the algorithm, we apply it to a test problem proposed by LeVeque. A slotted cylinder, a cone and a smooth hump rotate about the origin. The numerical solution after one complete revolution is shown in Fig. 1. It was computed on a uniform mesh of 128×128 bilinear elements. The discontinuities are resolved very well, and the smooth

part of the solution also looks quite reasonable even though the employed superbee limiter is known to be slightly underdiffusive. For an alternative limiting strategy based on the concepts of flux-corrected transport (FCT), the reader is referred to [2],[3].

4 Conclusions

The drift-flux model for buoyancy-driven gas-liquid flows was coupled with scalar transport equations describing the absorption of gas followed (and enhanced) by chemical reactions in the liquid phase. An unstructured grid FEM was proposed for the numerical solution. The discretization of the troublesome convective terms was performed by a novel high-resolution scheme. Numerical results for reactive bubbly flows in 2D and 3D geometries have been published elsewhere [1],[2]. Work is under way to provide a stonger coupling of equations and combine them with a $k - \epsilon$ turbulence model.

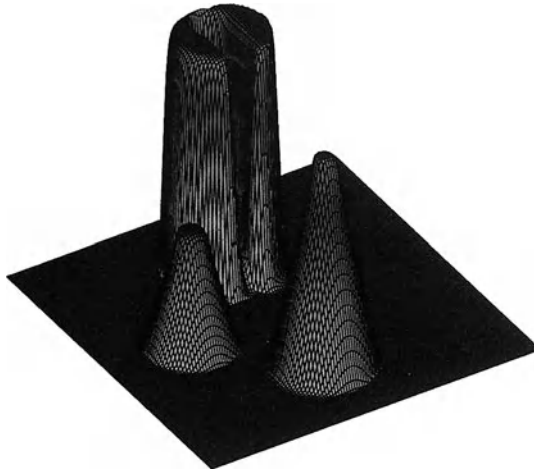


Figure 1: Solid body rotation. Numerical solution at $t = 2\pi$.

References

1. Kuzmin D., Turek S.: Efficient numerical techniques for flow simulation in bubble column reactors. In: *Preprints of the 5th German-Japanese Symposium on Bubble Columns*, VDI/GVC, pp 99–104 (2000)
2. Kuzmin D., Turek S.: Finite element discretization and iterative solution techniques for multiphase flows in gas-liquid reactors. Technical report, University of Dortmund (2002)

3. Kuzmin D., Turek S.: Flux correction tools for finite elements. *J. Comput. Phys.* **175**, pp 525–558 (2002)
4. Sokolichin A., Eigenberger G.: Modellierung und effiziente numerische Simulation von Gas-Flüssigkeits-Reaktoren mit Blasenströmungen nach dem Euler-Euler-Konzept. DFG report, University of Stuttgart (1997). Available at <http://pcvt12.verfahrenstechnik.uni-stuttgart.de/alex/icvt2.html>
5. Turek S.: *Efficient Solvers for Incompressible Flow Problems: An Algorithmic and Computational Approach*, LNCSE **6**, (Springer, Berlin Heidelberg 1999)

A transport equation for the interfacial area in bubble columns using a population balance approach

F. Lehr, D. Mewes

Institute of Process Engineering, University of Hannover, Callinstr. 36, D-30167 Hannover, Germany

Abstract

A transport equation for the interfacial area density in bubbly flow is derived using a population balance approach. Therefore the population balance equation is simplified and reduced to a transport equation for the arithmetic bubble volume. The kernel functions for the bubble coalescence and bubble break-up processes are modelled using a physical approach. For high superficial gas velocities the formation of large bubbles is considered thus the model predicts the interfacial area density for the homogeneous and the heterogeneous flow regime.

1 Introduction

The momentum, energy and mass transport processes in multiphase flows occur through the interface between the phases. Therefore the interfacial area is one of the key parameters for the design of multiphase reactors. Two basic approaches are common for the calculation of the interfacial area: a global and a local one. The global approach describes the interfacial area density in the whole column with empirical or semi-empirical correlations. The local approach describes the interfacial area density in dependence of the bubble size distribution and models for the bubble break-up and coalescence processes are developed. The interfacial area in bubbly flow has been investigated by Hibiki and Ishii (1999, 2001). Assuming spherical bubbles the population balance approach is used to describe the probability density of the bubbles.

The population balance equation is a transport equation for the number probability of the bubbles. The amount of bubbles is divided into classes containing

bubbles with a volume between v_n and v_n+dv . The probability density of bubbles in a certain class is defined as

$$f(v) = \frac{N(v)}{\Delta v \Delta V}. \quad (1)$$

The total amount of bubbles in the volume V is calculated by integrating f over all bubble classes. The application of population balance equations for modeling disperse flows is discussed by Ramkrishna and Mahoney (2002). A derivation of the population balance equation is given by several authors (Valentas and Amundsen, 1966; Kocamustafaogullari and Ishii, 1995; Millies and Mewes, 1999). For this work the population balance equation is used as given in Table 1.

Table 1. Population Balance Equation (Millies and Mewes, 1999)

Temporal change and convective transport	$\frac{\partial f}{\partial t} + \nabla(\bar{u}_g) =$
Changes in the gas density	$+\frac{1}{\rho_g} \frac{D\rho_g}{Dt} \frac{\partial}{\partial v}(vf)$
Mass transfer	$-\frac{\partial}{\partial v} \left(\dot{n} A_p \frac{\mu_g}{\rho_g} f \right)$
Break-up of larger bubbles	$+\int_v^\infty r_1(v, v') f(v') dv'$
Break-up of bubbles with volume v	$-\int_0^v v r_1(v, v') dv' \frac{f(v)}{v}$
Coalescence of smaller bubbles	$+\frac{1}{2} \int_0^v r_2(v', v-v') f(v') f(v', v-v') dv'$
Coalescence of bubbles with volume v	$-\int_0^\infty r_2(v, v') f(v') dv' f(v)$

The population balance equation considers the convective transport of bubbles, the changes in the gas phase density, mass transfer and bubble break-up and coalescence processes. The volume of a bubble in the considered fraction is v , the volume of bubbles which do not belong to this fraction is v' . The break-up of bubbles influences the bubble-size in two ways. The break-up of bubbles which belong to the fraction reduces the probability density, whereas the break-up of bubbles with larger volume increases the probability density. For modeling the break-up process the probability of breakage is modeled. The probability for the break-up of a bubble with volume v into fragments of volumes between v' and $v'+dv'$ is described by the break-up kernel function

$$r_1(v, v') = \frac{df(v, v')}{f(v) dv dt}. \quad (2)$$

Thus $r_1(v, v')$ is the number of fragments with a volume between v' and $v'+dv'$ that is formed per unit time and volume by the break-up of bubbles with volumes between v and $v+dv$.

Bubble coalescence has two consequences for the probability function, too. First the probability density of a bubble class with a certain volume v decreases with the coalescence of its bubbles. Second the coalescence of bubbles with a volume smaller than the regarded one increases the probability density. The probability for the coalescence of bubbles with the volume v and v' is described by the coalescence kernel-function

$$r_2(v, v') = \frac{df(v+v')d(v+v')}{f(v')f(v)dv dv' dt} \quad (3)$$

The coalescence kernel function describes the number of bubbles with volume $v+v'$ which are formed by the coalescence of a bubble with volume v' and v per unit volume and time. In this work only binary coalescence is considered. The coalescence of more than two bubbles is described as a series of binary coalescence processes.

The numerical effort for solving the population balance equation is high. A partial solution can be derived following the proposal of Millies and Mewes (1999). For this purpose the kernel functions $r_1(v, v')$ and $r_2(v, v')$ are assumed to be independent from the volume v' . Thus they can be taken out of the integral terms in Table 1. The solution

$$f(v) = \frac{\alpha_g}{\bar{v}^2} \exp\left(-\frac{v}{\bar{v}}\right) \quad (4)$$

with the arithmetic bubble volume \bar{v} is obtained. This solution is valid for the steady state between coalescence and break-up processes. Equation (4) is used to evaluate the population balance equation given in Table 1. The resulting equation only consists of terms with zero or first power of the bubble volume v . From this equation two ones were formed containing either the terms without or with the bubble volume. From the first one the continuity equation of the gas phase can be derived. The second equation which contains the terms with the bubble volume is rearranged to the equation

$$\begin{aligned} \frac{\partial \bar{v}}{\partial t} + \bar{u}_g \nabla \bar{v} = \\ - \frac{1}{\rho_g} \frac{D\rho_g}{Dt} \bar{v} - \frac{\dot{n}a_p}{\alpha_g \rho_g / \mu_g} \bar{v} - \frac{1}{2} r_1 \bar{v}^2 + \frac{1}{2} r_2 \alpha_g \end{aligned} \quad (5)$$

The Lagrangian derivative of the average bubble volume on the left side of Eq. (5) is balanced by changes in the gas phase density, mass transfer phenomena, bubble break-up, and coalescence. Thus this partial differential equation can be interpreted as a transport equation for the arithmetic bubble volume \bar{v} .

2 Modelling the break-up kernel function

The break-up of bubbles is investigated by several authors (Walter and Blanch, 1986; Hesketh et al., 1991; Wilkinson et al.; 1993). The authors are in agreement about the mechanism of bubble break-up. The bubble break-up is caused by a strong deformation of a bubble in the flow-field due to the turbulent velocity fluctuations in the liquid phase. This deformation leads to a constriction of the bubble and may result in breakage. For modelling the break-up kernel function four assumptions are made:

1. The break-up of bubbles occurs due to the collision of the bubble with eddies of different length-scales (Walter and Blanch, 1986; Lee et al., 1987; Luo and Svendsen, 1996).
2. In this work only the binary break-up is considered, thus two daughter bubbles are formed by the break-up of a bubble (Walter and Blanch 1986; Hesketh et al.; 1991).
3. The force equilibrium between the interfacial force of the bubble and the inertial force of the eddy rules the bubble break-up (Levich, 1962). Breakage occurs, if the inertial force of the eddy is higher than the superficial force of the bubble. Assuming a cylindrical constriction the force equilibrium at the smaller daughter bubble is

$$\frac{1}{2} \rho_1 u_\lambda^2 = 2 \frac{\sigma}{d'} \quad (6)$$

with the turbulent velocity of the eddy u_λ .

4. The length-scale of the eddy λ must be smaller than the bubble to induce breakage. Greater eddies only transport the bubble (Lee et al., 1987; Luo and Svendsen, 1996; Prince and Blanch, 1990). Also the diameter of the smaller daughter bubble must be smaller than the eddy, thus

$$d' \leq \lambda \leq d. \quad (7)$$

The break-up kernel function is modelled by integrating the product of the collision frequency $P(v, \lambda)$ between a bubble of volume v and an eddy with the length-scale λ and the probability $P_B(\lambda, v, v')$ that this collision leads to breakage as proposed by Luo and Svendsen (1996):

$$r_1(v, v') = \int_0^d \omega(v, \lambda) P_B(\lambda, v, v') d\lambda \quad (8)$$

The initial diameter of the bubble is d , the diameter of the smaller daughter bubble is d' . The arriving frequency of the eddies is modelled analogous to the kinetic gas theory. Therefore it is assumed that the turbulence is isotropic at least on the length scale of the bubbles. The frequency of collisions between a bubble with volume v and an eddy with length scale λ is then calculated by

$$\omega(v, \lambda) = \frac{\Pi}{4} (\lambda + d) \bar{u}_\lambda n_\lambda, \quad (9)$$

where n_λ denotes the number of eddies per unit volume and \bar{u}_λ denotes the mean eddy velocity. The velocities are normal distributed around this mean value. In the inertial subrange of turbulence the mean eddy velocity can be calculated following Hinze (1975):

$$\bar{u}_\lambda = \sqrt{2}(\varepsilon\lambda)^{1/3}. \quad (10)$$

The number density of eddies with length scales between λ and $\lambda+d\lambda$ is obtained from the inertial subrange of turbulence by

$$n_1 = \frac{C}{\lambda^4}, \text{ with } C = \frac{9}{2} \frac{2^{1/3}}{\Pi^{5/3}} = 0.8413. \quad (11)$$

Equation (10) is only valid in the inertial subrange of isotropic turbulence. The applicability for modelling the bubble break-up process is not restricted because smaller eddies do not have enough energy to overcome the interfacial forces. The applicability of Eq. (10) is supported by the experimental investigation from Mudde et al. (1997). The turbulence spectrum in bubbly flow has been investigated using a LDA technique. For high wave numbers the turbulent energy decreases proportional to $k^{-5/3}$ as it is known for isotropic turbulence.

The probability that a collision between an eddy and a bubble leads to breakage is calculated from the force balance between the inertial force of the eddy and the surface tension. Considering the normal distribution of the eddy velocity around the mean value \bar{u}_λ the resulting breakage probability is described by

$$P_B(\lambda, v', v) = \frac{4}{\Pi} \frac{\sigma}{\rho_f} \frac{1}{(\varepsilon\lambda)^{2/3}} \frac{1}{d'^4} \exp\left[\frac{-2\sigma}{\rho_f} \frac{1}{(\varepsilon\lambda)^{2/3}} \frac{1}{d'}\right] \quad (12)$$

This equation is valid for the smaller daughter bubble since the force balance is based on the smaller diameter d' . The breakage probability for the larger daughter bubble is then obtained by the equation

$$P_B(\lambda, v, v') = P_B(\lambda, v-v', v') \quad (13)$$

since it is assumed that two bubble fragments are formed by breakage. The break-up kernel function is then derived using eq. (8) thus

$$r_1(v, v') = \int_{d'}^d \sqrt{2} C \frac{\sigma}{\rho_1 \varepsilon^{2/3} d'^4} \frac{(\lambda + d)^2}{\lambda^{13/3}} \exp\left(-\frac{2\sigma}{\rho_1 \varepsilon^{2/3} d'} \frac{1}{\lambda^{2/3}}\right) d\lambda \quad (14)$$

with $C=0.8413$ for $0 \leq v' \leq v/2$. The break-up frequency for a bubble with volume v is then calculated by integrating the break-up kernel function from $v=0$ to $v=v/2$. Equation (14) is valid for bubbles larger than the maximum stable bubble diameter, which results from Eqs. (6) and (7)

$$d_{\max} = 2^{1/5} \frac{\sigma^{3/5}}{\rho_1^{3/5} \varepsilon^{2/5}} \quad (15)$$

3 Modelling the coalescence kernel function

The coalescence process is divided into three steps following (Chesters, 1991). In the first step the bubble collide and a small amount of liquid is captured between them. This liquid film drains off and finally the bubbles coalesce after the film ruptured. Otherwise the bubbles bounce back without coalescing.

Not every collision leads to coalescence, thus the probability that coalescence occurs after a collision has to be determined. This probability, which is called coalescence efficiency, is mainly influenced by the liquid phase properties, e.g. the composition or the viscosity. The coalescence kernel function is modeled as proposed by Prince and Blanch (1990):

$$r_2 = P_C A u' \quad (16)$$

where P_C denotes the probability for coalescence, A is the cross-sectional area for collision and u' is a characteristic velocity for the coalescence process. The cross-sectional area is calculated from the diameters d_1 and d_2 of the colliding bubbles, yielding

$$A = \frac{\Pi}{4} (d_1 + d_2). \quad (17)$$

The collisions of bubbles are considered due to the turbulent fluctuations in the liquid phase and differences of the rise velocities for different sized bubbles. The characteristic velocity is assumed to be the velocity of a turbulent eddy of the bubbles length scale, since smaller eddies do not affect the bubble motion and larger eddies transport groups of bubbles. The characteristic velocity is therefore calculated as

$$u' = \max(\sqrt{2\varepsilon}^{1/3} \sqrt{(d_1^{2/3} + d_2^{2/3})}, |\bar{u}_1 - \bar{u}_2|). \quad (18)$$

Coalescence occurs if the relative velocity of approach perpendicular to the surface of contact is lower than a certain critical velocity. It is assumed that the prob-

ability for a collision is equal for all steradians. The coalescence efficiency is therefore calculated as

$$P_C = \max\left(\frac{u_{\text{crit}}}{u'}, 1\right). \quad (19)$$

Considering the limited range of the turbulent fluctuations the coalescence kernel function is written as

$$r_2(v_1, v_2) = \frac{\Pi}{4} (d_1 + d_2)^2 \min(u', u_{\text{crit}}) \exp\left(-\left(\frac{0.6}{\alpha^{1/3}} - 1\right)^2\right). \quad (20)$$

The last term accounts for the limitation in the range of the turbulent fluctuations. These fluctuations are assumed to be distributed normally around the mean value $\lambda=d$. The maximum packing density is 0.6 (Millies and Mewes, 1999). In Eq. (20) the only parameter is the critical velocity.

3.1 Measurement of the critical velocity

The coalescence process is investigated experimentally to obtain the critical velocity for coalescence. The experimental setup is shown in Fig. 1. The liquid flows vertically downwards inside of a channel. The conic shape of this measurement section leads to a decrease of the liquid velocity in the flow direction. The bubbles are injected by a capillary at the lower end of the measurement section. The injected bubbles rise up until the relative velocity to the surrounding liquid is equal to their terminal rising velocity. When the first bubble reached its fixed position the second one is injected. The collision between the two bubbles is investigated by high speed images. Therefore two perpendicular views are recorded simultaneously.

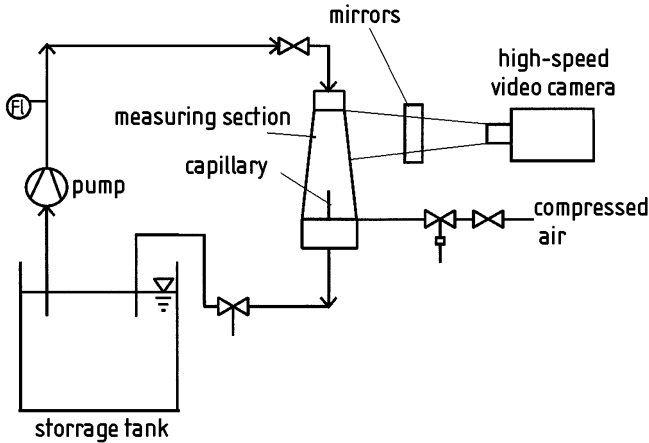


Fig. 1. Experimental setup

The images are then analyzed automatically and the relative velocity of approach and the occurrence of coalescence can be determined. The relative velocity perpendicular to the bubble surface is shown in Fig. 2 in dependence of the equivalent bubble diameter, which is calculated in accordance to Chesters (1991)

$$d_{eq} = 2 \left(\frac{1}{d_1} + \frac{1}{d_2} \right)^{-1} \quad (21)$$

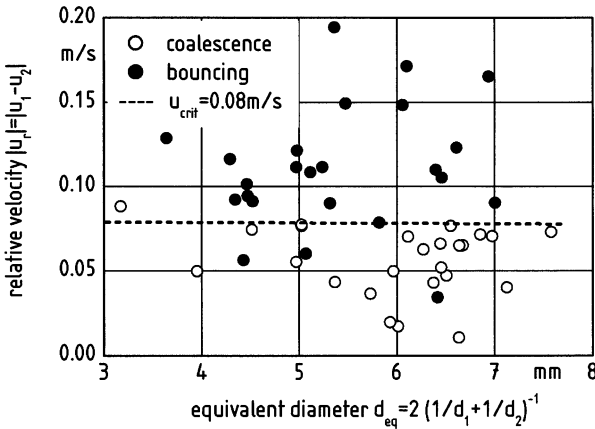


Fig. 2. Coalescence in dependence of the velocity of approach

The coalescence of bubbles occurs in dependence of the velocity of approach. From the experimental investigations the critical velocity is determined to $u_{crit} = 0.08$ m/s. The critical velocity is independent of the bubble diameter.

4 Transport equation for the mean bubble volume

The population balance equation is simplified to a transport equation for the mean average bubble diameter. Therefore the developed models for bubble break-up and coalescence are used to evaluate the population balance equation numerically.

The population balance equation is an integro-differential equation. It is solved numerically applying an algorithm proposed by Kumar and Ramkrishna (1996), which uses variable class widths. The calculations are performed for various constant values of the volume fraction of gas, the turbulent dissipation rate and a liquid velocity of zero.

For high superficial gas velocities, corresponding to high volume fractions of gas, the bubble size distribution becomes bimodal. Thus one fraction of small and a second fraction of large bubbles appear. The time dependent accumulated volume fraction of gas is shown in Fig. 3 for a total volume fraction of 0.25.

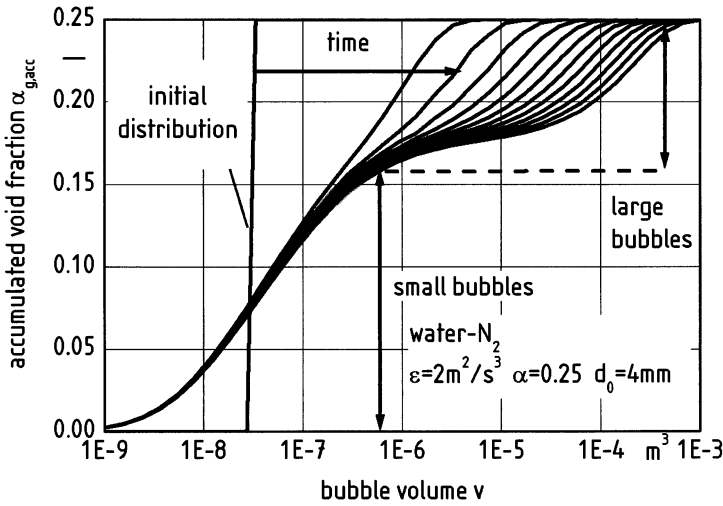


Fig. 3. Time-dependant bubble size distribution

The bubble size distribution of the small bubble fraction is almost constant after a short time. For the larger bubble fraction a constant value is calculated after considerably long times, thus a constant bimodal bubble size distribution appears.

The calculated number density distributions for the large and the small bubble fraction are self-similar. The dimensionless number density is defined as

$$f_i^* = \frac{\bar{v}_i}{\alpha_i} f_i, \quad i = 1, 2. \quad (22)$$

The index 1 denotes the small bubble fraction, the index 2 the large bubble fraction. The number density distribution for the small bubble fraction is approximated as

$$f_1^* = \sqrt{\frac{2}{\pi}} \frac{\bar{v}_1}{3v_1} \exp \left[-\frac{2}{9} \left(\ln \left(e^{8/9} \frac{v_1}{\bar{v}_1} \right) \right)^2 \right]. \quad (23)$$

For the large bubble fraction the following approximation is made

$$f_2^* = \exp \left(-\frac{v_2}{\bar{v}_2} \right). \quad (24)$$

The population balance equation is evaluated using Eqs. (23) and (24). Integrating the population balance equation considering all bubble volumes the transport equations for the mean bubble volume and the volume fraction of the small and large bubble fraction are obtained (Lehr, 2002).

The bubble size distribution can be calculated independent of CFD simulations if the equilibrium between break-up and coalescence is reached.

The break-up frequency is calculated by integrating Eq. (20)

$$f_z = \int_0^{v/2} r_1(v', v) dv' \quad (25)$$

The dimensionless break-up frequency is defined by

$$f_z^* = f_z \left(\frac{\sigma}{\rho_l} \right)^{2/5} \varepsilon^{-3/5} \quad (26)$$

In Fig. 4 the dimensionless break-up frequency is shown in dependence of the dimensionless bubble diameter. In addition to the calculated values the experimental results from Lasheras (1999) and Wilkinson (1991) are shown.

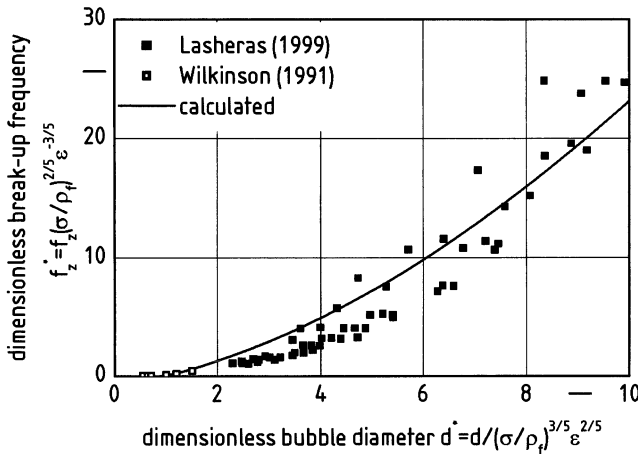


Fig. 4. Dimensionless bubble break-up frequency

The calculated break-up frequency increases with the bubble diameter and the turbulent dissipation rate in accordance with the experimental results.

The calculated bubble size distributions are shown in Fig. 5 together with the experimental results from Grienberger and Hofmann (1992) and Schrag (1976). The calculated and measured values are in agreement thus it is concluded that the coalescence kernel function can be calculated using Eq. (20).

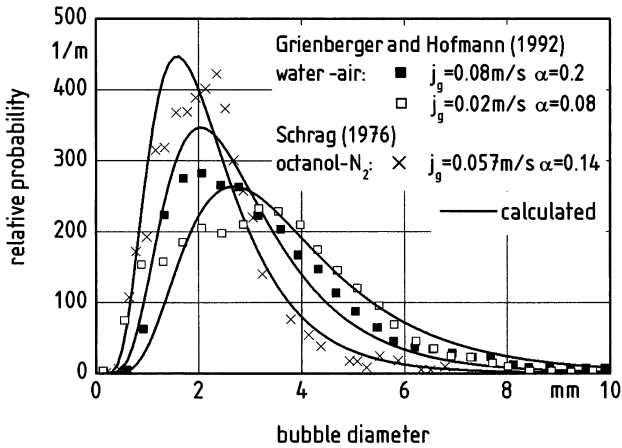


Fig. 5. Bubble-size distribution for the equilibrium of break-up and coalescence

Conclusion

A transport equation for the mean bubble diameter in bubbly flow is derived from a population balance equation for the bubble number density. The kernel functions describing bubble break-up and coalescence are modeled based on a physical approach. The population balance is solved numerically for certain cases. For higher volume fractions of gas the bubble size distribution is bimodal due to the enhanced coalescence. Thus two bubble fractions are formed. The first bubble fraction contains the small bubble, the second one the large bubbles. The calculated bubble-size distributions for the small and the large bubble fraction are self-similar. Therefore both distributions are approximated by an analytical solution. The calculated bubble size distributions are in agreement with experimental results from several authors.

Acknowledgement

The authors gratefully acknowledge the financial support of the German Research Foundation (DFG).

Notation

symbol	unit	meaning
a_p	$[m^{-1}]$	interfacial area density
C_D	$[-]$	drag coefficient
D	$[m]$	bubble column diameter
d	$[m]$	bubble diameter
d_{eq}	$[m]$	equivalent bubble diameter
d_s	$[m]$	sauter mean diameter
f	$[m^{-6}]$	number density distribution
H	$[m]$	bubble column height
j	$[ms^{-1}]$	superficial velocity
k	$[m^2s^{-2}]$	turbulent kinetic energy
L	$[m]$	characteristic length scale
N	$[-]$	number
n	$[m^{-3}]$	number density
n_λ	$[m^{-4}]$	number density of eddies with length scale λ
\dot{n}	$[kmol\ m^2s^{-1}]$	molar flux
P_B	$[m^{-3}]$	break-up probability
P_C	$[-]$	coalescence efficiency
r	$[m]$	radius
r_1	$[m^{-3}s^{-1}]$	break-up kernel function
r_2	$[m^3s^{-1}]$	coalescence kernel function
T	$[s]$	characteristic time scale
\vec{u}	$[ms^{-1}]$	velocity
u_{crit}	$[ms^{-1}]$	critical velocity for coalescence
u'	$[ms^{-1}]$	turbulent fluctuating velocity
v_b	$[m^3]$	bubble volume
\bar{v}_b	$[m^3]$	average bubble volume
V	$[m^3]$	volume
f_z	$[s^{-1}]$	break-up frequency

Greek symbols

α	$[-]$	volume fraction
β	$[m^{-3}]$	daughter size distribution
ε	$[m^2s^{-3}]$	dissipation rate
λ	$[m]$	length scale of an eddy
μ	$[kg\ kmol^{-1}]$	molar mass
σ	$[kgs^{-2}]$	surface tension
ρ	$[kgm^{-3}]$	density
τ	$[kgm^{-1}s^{-2}]$	shear stress
ω	$[m^{-1}s^{-1}]$	collision frequency
Δ	$[-]$	difference

Indices

0	initial value
1	small bubbles
2	large bubbles
l	Liquid
g	Gas
t	turbulent
,	daughter bubble
*	dimensionless variable

References

- Chesters AK (1991) The modelling of coalescence processes in fluid-liquid dispersions: A review of current understanding. *Inst Chem Engrs* 69: 259-270
- de Bertodano ML, Lahey RT, Jones OC Development of a k- ϵ -Model for bubbly two-phase flow. *J Fluids Eng* 116: 128-134
- Grienberger J, Hofmann H (1992) Investigation and modelling of bubble columns. *Chem Eng Sci* 47: 2215- 2220
- Hesketh RP, Etechells AW, Russell TWF (1991) Bubble breakage in pipeline flow. *Chem Eng Sci* 46: 1-9
- Hibiki T, Ishii M (1999) Experimental study on interfacial area transport in bubbly two-phase flows. *Int J Heat and Mass Trans.* 42: 3019- 3035
- Hibiki T, Ishii M (2001) Interfacial area concentration in steady fully-developed bubbly flow. *Int J Heat and Mass Trans.* 44: 3443- 3461
- Hinze JO (1975) *Turbulence*. McGraw Hill series in mechanical engineering
- Jacobsen HA, Sannaes BH, Grevskott S, Svendsen HF (1997) Modeling of vertical bubble driven flows. *Ind Eng Chem Res* 36: 4052-4074
- Kocamustafaogullari G, Ishii M (1995) Foundation of the interfacial area transport equation and its closure relations. *Int J Heat and Mass Transfer* 38: 481- 493
- Kumar S, Ramkrishna D (1996) On the solution of population balance equations by discretization- I and II. *Chem Eng Sci* 59: 1311- 1342
- Lasheras JC, Martinez-Bazan C, Montanes JL(1999) On the break-up of an air bubble injected into a fully developed turbulent flow. Part 1: Break-up frequency. *J Fluid Mechanics* 401: 157 -182
- Lee CH, Erickson LE, Glasgow LA (1987) Bubble break-up and coalescence in turbulent gas-liquid dispersions. *Chem Eng Com* 59: 65-84
- Lehr F (2002) Berechnen von Blasengrößenverteilungen und Strömungsfeldern in Blasen-säulen, VDI Fortschritt Berichte Reihe 3 Nr 726, VDI Verlag
- Levich VG (1962) *Physicochemical Hydrodynamics*. Prentice-Hall, N.J.
- Luo H, Svendsen, HF (1996) Theoretical model for drop and bubble breakup in turbulent dispersions. *AIChE J* 42: 1225-1233
- Millies M, Mewes D (1999) Interfacial area density in bubbly flow. *Chem Engng Processing* 38: 307-319

- Mudde RF, Simonin O (1999) Two- and three dimensional simulations of a bubble plume using a two-fluid model. *Chem Eng Sci* 54: 5061-5069
- Prince MJ, Blanch HW (1990) Bubble coalescence and break-up in air-sparged bubble columns. *AIChE J* 36: 1485-1499
- Ramkrishna D, Mahoney AW (2002) Population balance modelling. Promise for the future. *Chem Eng Sci* 57: 595-606
- Schrag HJ (1976) Blasengrößen-Häufigkeitsverteilungen bei der Begasung von Gemischen organisch-chemischer Flüssigkeiten mit Stickstoff in Blasensäulen-Reaktoren. Ph.D. thesis, University of Aachen, Germany
- Valentas KJ, Amundson NR (1966) Breakage and coalescence in dispersed phase systems. *I and EC Fundamentals* 5: 533- 542
- Walter JF, Blanch HW (1986) Bubble break-up in gas-liquid bioreactors: Break-up in turbulent flows. *The Chem Eng J* 32: B7-B17
- Wilkinson PM (1991) Physical aspects and scale-up of high pressure bubble columns. Ph.D. thesis, University of Groningen, The Netherlands
- Wilkinson PM, van Schayk A, Spronken JPM, van Dierendonk LL (1993) The influence of gas density and liquid properties on bubble breakup. *Chem Eng Sci* 48: 1213-1226

Publications

- Lehr F, Mewes D (1999) Numerical Simulation of the Hydrodynamics and the Bubble Size Distribution in Bubble Columns. 4th Workshop on Transport Phenomena in Two-Phase Flow, September 11-16, 1999, Sozopol, Bulgaria
- Lehr F, Mewes D (1999) A Transport Equation for the Interfacial Area Density in Two-Phase Flow; 2nd European Congress of Chemical Engineering, October 5-7, 1999, Montpellier, France
- Lehr F, Mewes D (2000) A transport equation for the interfacial area density applied to bubble columns; ASME Fluids Engineering Conference, June 11-15, 2000, Boston, USA
- Lehr F, Mewes D (2000) A transport equation for the interfacial area density applied to bubble columns; 16th International Symposium on Chemical Reactor Engineering, ISCRE 16, Sept. 10-13, Cracow, Poland
- Lehr F, Mewes D (2001) A transport equation for the interfacial area density applied to bubble columns. *Chem Eng Sci* 56: 1159-1166

Flow fields in bubble columns with mass transfer

D. Wiemann, F. Lehr, D. Mewes

Institute of Process Engineering, University of Hannover, Callinstr. 36, D-30167 Hannover, Germany

Abstract

In this work a transport equation for the interfacial area density based on a population balance equation approach is applied to calculate the flow field in bubble columns numerically. The resulting transport equation for the arithmetic bubble volume is coupled with the balance equations for mass and momentum. The calculations are performed for three dimensional, instationary flow fields in cylindrical bubble columns using the Euler-Euler approach. The calculations consider the homogeneous and the heterogenous flow regimes. In addition the mass transfer between the phases is considered. For the calculation the commercial code CFX-4 is used.

1 Introduction

For the numerical calculation of the flow field in bubble columns the Euler-Euler or the Euler-Lagrange approach are common. The Euler-Lagrange approach calculates the motion of individual bubbles. Therefore the numerical effort is considerably high. The Euler-Euler approach describes the disperse phase as a continuous fluid. The interactions between the phases are considered by interphasial exchange terms. A comparison of both methods is given by Sokolichin et al. (1997).

For axisymmetric and stationary flow fields numerical and analytical calculations have been presented by several authors (Torvik and Svendsen 1990, Jacobsen et al., 1997; Sayanal et al., 1999; Thakre and Joshi, 1999). The highly transient and three-dimensional flow fields which are observed in experiments cannot be calculated with these models. The first simulations for the time-

dependent flow field in bubble columns are presented by Webb et al. (1992). They used the Euler-Lagrange approach to calculate the rise of a bubble swarm in a two dimensional flat bubble column assuming laminar flow. Calculations for the transient and three dimensional flow field in a cylindrical bubble column are presented by Lapin and Lübbert (1995, 1996). They also employ the Euler-Lagrange method. The authors obtain a chaotic behavior of the two phase flow. They do not use a turbulence model but consider the flow to be laminar.

Sokolichin and Eigenberger (1999) perform transient three-dimensional calculations for the flow field in a flat bubble column using a simplified Euler-Euler method. For laminar flow the calculations do not result in grid independent results. A stable solution is only obtained by using a turbulence model. The turbulence is calculated with a $k-\epsilon$ turbulence model. The predicted time-averaged and time-dependent flow fields are in good agreement with their experimental results.

Similar calculations for the flow fields in locally sparged, flat rectangular bubble columns are performed by several groups. Delnoij et al. (1999) use the Euler-Lagrange method assuming laminar flow. Lain et al. (1999) also work with the Euler-Lagrange method but they use a $k-\epsilon$ turbulence model. Results from calculations using the Euler-Euler method are presented by Mudde and Simonin (1999), Pflieger et al. (1999) and Pan et al. (1999, 2000).

For the calculation of flow fields in cylindrical bubble columns Krishna et al. (1999, 2000) applied the Euler-Euler method considering a turbulence model. For high superficial gas velocities they consider large bubbles as a third eulerian phase in their calculations. They neglect bubble coalescence and break-up and assume a constant superficial velocity for the large and small bubbles as well as a constant bubble size.

The local bubble size distribution is considered in none of these works. In addition most of the simulations are performed for low superficial gas velocities. Only Krishna et al. (2000) present results for higher superficial gas velocities which are relevant in practice. With none of the existing methods the interfacial area available for heat and mass transfer can be calculated.

This paper deals with the numerical calculation of bubbly flow considering the local bubble size distribution. In particular for cylindrical bubble columns the flow field is calculated using an Euler-Euler approach with an additional transport equation for the mean bubble volume and the volume fraction of the small and large bubble fraction. Therefore the transport equations are used as proposed by Lehr et al. (2002). The equations are summarized in Table 1. The index 1 refers to the small bubble fraction, the index 2 denotes the large bubble fraction.

Table 1. Transport equations for the mean bubble volume and the volume fraction

\bar{v}_1	$\frac{\partial \bar{v}_1}{\partial t} + \bar{u}_{g1} \nabla(\bar{v}_1) = Z_1 \bar{v}_1 - 0,3463 r_2(\bar{v}_1, \bar{v}_1) \alpha_1 - \frac{1}{\rho_g} \frac{D\rho_g}{Dt} \bar{v}_1 + \dot{n}_{a,p1} \frac{\mu_g}{\rho_g} \frac{\bar{v}_1}{\alpha_1}$
\bar{v}_2	$\frac{\partial \bar{v}_2}{\partial t} + \bar{u}_{g2} \nabla(\bar{v}_2) = Z_2 \bar{v}_2 - 0,4250 r_2(\bar{v}_2, \bar{v}_2) \alpha_2 + 0,9024 r_2(\bar{v}_2, 5\bar{v}_1) \alpha_1 - \frac{1}{\rho_g} \frac{D\rho_g}{Dt} \bar{v}_2 + \dot{n}_{a,p2} \frac{\mu_g}{\rho_g} \frac{\bar{v}_2}{\alpha_2}$
α_1	$\frac{\partial \alpha_1 \rho_g}{\partial t} + \nabla(\alpha_1 \rho_g \bar{u}_{g1}) = Z_2 \rho_g \alpha_2 - 0,9024 r_2(\bar{v}_2, 5\bar{v}_1) \rho_g \frac{\alpha_2 \alpha_1}{\bar{v}_2} - 3,1043 r_2(\bar{v}_1, \bar{v}_1) \rho_g \frac{\alpha_1^2}{\bar{v}_2} + \dot{n}_{a,p1} \mu_g$
α_2	$\frac{\partial \alpha_2 \rho_g}{\partial t} + \nabla(\alpha_2 \rho_g \bar{u}_{g2}) = -Z_2 \rho_g \alpha_2 + 0,9024 r_2(\bar{v}_2, 5\bar{v}_1) \rho_g \frac{\alpha_2 \alpha_1}{\bar{v}_2} + 3,1043 r_2(\bar{v}_1, \bar{v}_1) \rho_g \frac{\alpha_1^2}{\bar{v}_2} + \dot{n}_{a,p2} \mu_g$
	$Z_1 = 0,6082 \left(\frac{\rho_f}{\sigma} \right)^{7/5} \varepsilon^{19/15} \bar{v}_1^{5/9} \exp \left(-\frac{0,8565}{\sqrt{\bar{v}_1}} \left(\frac{\sigma}{\rho_f} \right)^{9/10} \frac{1}{\varepsilon^{3/5}} \right)$ $Z_2 = 0,2545 \left(\frac{\sigma}{\rho_f} \right)^{2/5} \varepsilon^{1/15} \frac{1}{\bar{v}_2^{4/9}}$ $r_2(v_i, v_j) = \frac{\pi}{4} \left(\left(\frac{6}{\pi} v_i \right)^{1/3} + \left(\frac{6}{\pi} v_j \right)^{1/3} \right)^2 \min(u', u_{crit}) \exp \left(-\left(\frac{\alpha_{max}^{1/3}}{\alpha^{1/3}} - 1 \right)^2 \right)$

In case of low superficial gas velocities corresponding to the homogeneous flow regime only the transport equation for the mean bubble volume of the small bubble fraction has to be considered.

2 Numerical calculation

The numerical calculation is based on the two-fluid approach. Both phases are therefore assumed as continuous fluids. The interactions are taken into account by interphase exchange terms. The momentum balance equation is

$$\frac{\partial(\alpha_i \rho_i \bar{u}_i)}{\partial t} + \nabla(\alpha_i [\rho_i \bar{u}_i \bar{u}_i - \eta_i (\nabla \bar{u}_i + \nabla \bar{u}_i^T)]) = -\alpha_i \nabla p + \bar{F}_d + \alpha_i \rho_i \bar{g} \begin{cases} + \dot{M}_{g,l} \bar{u}_g, i=1 \\ - \dot{M}_{g,l} \bar{u}_g, i=g \end{cases} \quad (1)$$

The second term on the right side considers the interphase drag force per unit volume which is calculated as

$$\bar{F}_d = \frac{3}{4} \rho_l \frac{\alpha_g}{d_s} C_D |\bar{u}_g - \bar{u}_l| (\bar{u}_j - \bar{u}_i) \quad (2)$$

where $j=g, l \neq i$. The drag coefficient is calculated as

$$C_D = \max \left[\frac{24}{Re} (1 + 0.1 Re^{0.75}); \min \left\{ \max(0.44, \frac{2}{3} Eo^{1/2}), \frac{8}{3} \right\} \right] \quad (3)$$

(Clift et al., 1978). The Reynolds-number and the Eotvos-number are defined as

$$Re = \frac{|\bar{u}_g - \bar{u}_l| d_s}{\nu_l} \quad (4)$$

$$Eo = \frac{g(\rho_l - \rho_g) d_s}{\sigma}, \quad (5)$$

where σ is the surface tension. The lift and the virtual mass forces are not considered. The sauter mean diameter for the small and large bubble fraction is calculated as

$$d_{S1} = 1.613 \bar{v}_1^{1/3}; d_{S2} = 1.374 \bar{v}_2^{1/3}. \quad (6)$$

The mass balance equation for both phases is

$$\frac{\partial(\alpha_i \rho_i)}{\partial t} + \nabla(\alpha_i \rho_i \bar{u}_i) = \begin{cases} + \dot{M}_{g,l}, i=1 \\ - \dot{M}_{g,l}, i=g \end{cases} \quad (7)$$

The mass transfer rate of component A from the gas into the liquid phase is $\dot{M}_{g,l}$.

The mass balance for the component A is

$$\frac{\partial(\xi_{Ai} \alpha_i \rho_i)}{\partial t} + \nabla(\xi_{Ai} \alpha_i \rho_i \bar{u}_i) = \begin{cases} + \dot{M}_{g,l}, i=1 \\ - \dot{M}_{g,l}, i=g \end{cases} \quad (8)$$

The turbulence in the flow field is considered using a k-ε model. The application of a k-ε turbulence model for the numerical calculation of bubbly flow at low volume fractions of gas has been reported by Sokolichin and Eigenberger (1999). The turbulent viscosity in the liquid phase is modeled as

$$\mu_t = 0.09\rho_1 \frac{k_1^2}{\varepsilon_1} \quad (9)$$

The gas phase is treated as laminar. The turbulent kinetic energy and the dissipation rate are calculated as

$$\begin{aligned} \frac{\partial \alpha_1 \rho_1 k_1}{\partial t} + \nabla(\alpha_1 \rho_1 \bar{u}_1 k_1 - (\mu_1 + \mu_t) \nabla k_1) &= \alpha_1 (P_1 - \rho_1 \varepsilon_1) \\ \frac{\partial \alpha_1 \rho_1 \varepsilon_1}{\partial t} + \nabla(\alpha_1 \rho_1 \bar{u}_1 \varepsilon_1 - (\mu_1 + \mu_t) \nabla \varepsilon_1) &= \alpha_1 \frac{\varepsilon_1}{k_1} (1.44 P_1 - 1.92 \rho_1 \varepsilon_1) \end{aligned} \quad (10)$$

$$\text{with } P_1 = (\mu_1 + \mu_t) \nabla \bar{u}_1 \cdot (\nabla \bar{u}_1 + \nabla \bar{u}_1^T) - \frac{2}{3} \nabla \cdot \bar{u}_1 ((\mu_1 + \mu_t) \nabla \cdot \bar{u}_1 + \rho_1 k_1)$$

In addition the bubble induced turbulence is taken into account. Therefore the model proposed by de Bertodano et al. (1994) is used. Following this model the resulting turbulent kinetic energy and dissipation rate are calculated from the shear and the bubble induced turbulence

$$\begin{aligned} k_{\text{res}} &= k_1 + k_b = k_1 + \frac{1}{4} \alpha_{g1} |\bar{u}_{g1}|^2 + \frac{1}{4} \alpha_{g2} |\bar{u}_{g2}|^2 \\ \varepsilon_{\text{res}} &= \varepsilon_1 + \varepsilon_b = \varepsilon_1 + \frac{\bar{F}_{d,g1,l}}{\rho_1} |\bar{u}_{g1}| + \frac{\bar{F}_{d,g2,l}}{\rho_1} |\bar{u}_{g2}| \end{aligned} \quad (11)$$

The change in the liquid viscosity due to the bubble induced turbulence is neglected since the shear induced viscosity is much higher.

Equations (1) to (11) are implemented into the commercial code CFX. In addition the transport equations for the mean bubble volume and the volume fraction of gas as shown in Table 1 are coupled with the balance equations for mass and momentum. The geometric model consists of a cylindrical domain. The gas phase enters the column at the bottom through a sparger. The cross section at the top is modeled as a semi-permeable wall without shear stress, thus the gas phase can leave the domain whereas the liquid phase remains inside. The liquid leaves the domain at the top through an overflow at the outer wall of the column. The domain is discretized with a block structured grid. The edge length of the cells is in the range of $\Delta l = 0.01 - 0.02$ m. The time steps are in the range of $\Delta t = 0.01 - 0.05$ s. For the discretization of convective terms a TVD scheme is used.

Mass transfer

The mass transfer is directed from the dispersed gas phase into the continuous liquid phase. The gas phase consists of a pure substance. Therefore the mass transfer

resistance occurs only in the liquid phase. For small variations of the bubble diameter the mass transfer process is assumed to be stationary. The mass transfer rate per unit interfacial area is calculated as

$$\dot{m}_{g,l} = \beta_1 (\rho_{A,pl} - \rho_{A,l}) \quad (12)$$

The mass transfer coefficient is β_1 , the partial density of component A at the liquid side interface is $\rho_{A,pl}$ and the bulk density is $\rho_{A,l}$. The interfacial density is assumed to be in equilibrium with the gas phase following Henry's law. The partial density at the liquid side interface is calculated as

$$\rho_{A,pl} = p_{A,g} \rho_1 / \left(\frac{\mu_1}{\mu_g} H \right), \quad (13)$$

where the molecular weight of the liquid and the gas phase are μ_1 and μ_g , the Henry constant is H. For spherical bubbles the mass transfer coefficient is calculated following Brauer (1981)

$$Sh = Sh_\infty \left[\left(1 + 0.433 Re^2 \right)^{-1} + 4.23 \right]^{-0.055} \quad (14)$$

where

$$Sh_\infty = 2 + \frac{0.651(Re Sc)^{1.72}}{1 + (Re Sc)^{1.22}} \quad (15)$$

The Sherwood-number and the Schmidt-number are

$$Sh = \beta d / D \quad \text{and} \quad Sc = \nu / D, \quad (16)$$

where D is the diffusion coefficient. Equation (14) is only valid if the Bubble-Reynolds-number does not exceed a critical value which is determined as

$$Re_{crit} = 3.73 \left(\frac{\rho_1 \sigma^3}{g \eta^4} \right)^{0.209} \quad (17)$$

For $Re > Re_{crit}$ the bubbles loose their spherical shape. The stochastic deformations of the interface induce turbulent motions in the surrounding fluid. The mass transfer coefficient for non-spherical bubbles considering the influence of deformation turbulence is calculated following Brauer (1981)

$$Sh = 2 + 0.015 Re^{0.89} Sc^{0.7} \quad (18)$$

In this article the physical absorption of CO₂ into water is used to consider mass transfer. For a non-spherical bubble with a diameter of $d = 3$ mm using Eq. (14) the mass transfer coefficient is $\beta = 2.3 \cdot 10^{-4}$ m/s. The mass transfer coefficient for the physical absorption of CO₂ into water is investigated experimentally by Hallensle-

ben (1980). For bubbles with diameters in the range of $d_b=2.0$ up to 6.0 mm an almost constant value for the mass transfer coefficient of $\beta_l=2.8 \cdot 10^{-4}$ m/s is reported.

3 Results and discussion

3.1 Low superficial gas velocities

The calculations are performed for three-dimensional, instationary flow fields in cylindrical bubble columns. First the results for the system air-water are shown.

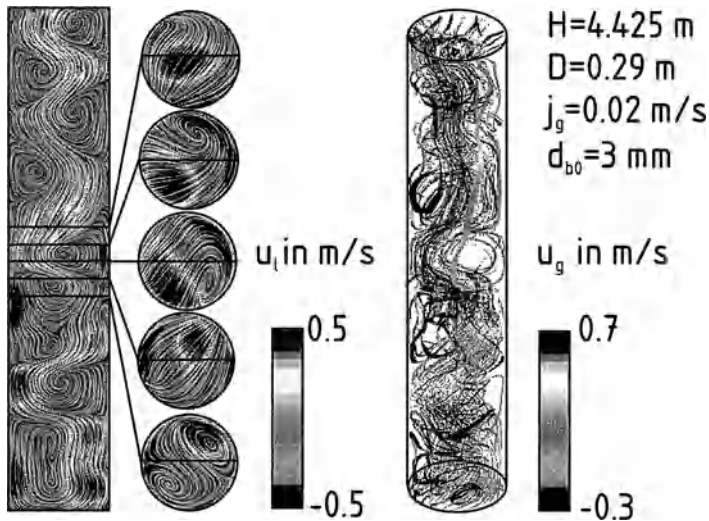


Fig. 1. Flow field for a low superficial gas velocity

The calculated flow field for a column with a height of $H=4.425$ m and a diameter of $D=0.29$ m is shown in Fig. 1. The superficial gas velocity is $j_g=0.02$ m/s and the initial bubble size at the inlet is $d_{b0}=3$ mm. The streamlines of the liquid are visualized with a texture. The flow field of the liquid is characterized by vortices thus the liquid rises up in a spiral manner. The magnitude of the vortices is in the order of the column diameter. In the right part the streamlines of bubbles are shown. The gas bubbles rise up in particular in the center part of the column. In the wall region some bubbles are transported downwards with the liquid.

The time dependent motion of the bubble swarm is shown in Fig. 2 for the same column. The time between the snapshots is 1s. The bubble swarm rises up in a spiral manner and rotate over the cross sectional area. The axial and radial movement of the liquid vortices cause the deformations of the bubble swarm.

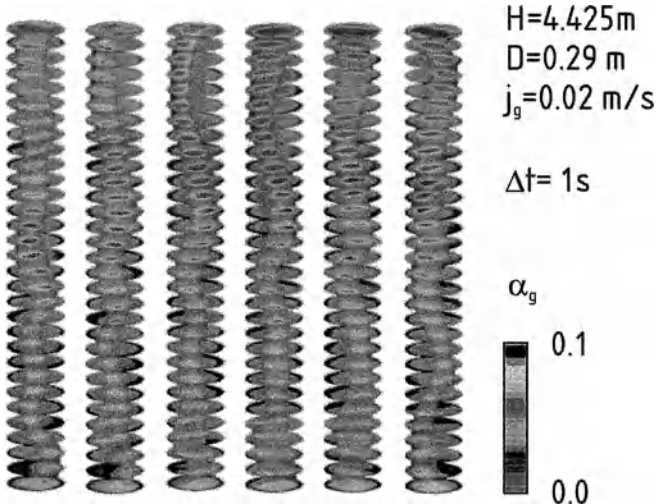


Fig. 2. Time dependent motion of the bubble swarm

The time-averaged volume fraction of gas is shown in Fig.3. In addition to the calculated results the experiments from Grienberger (1992) are given.

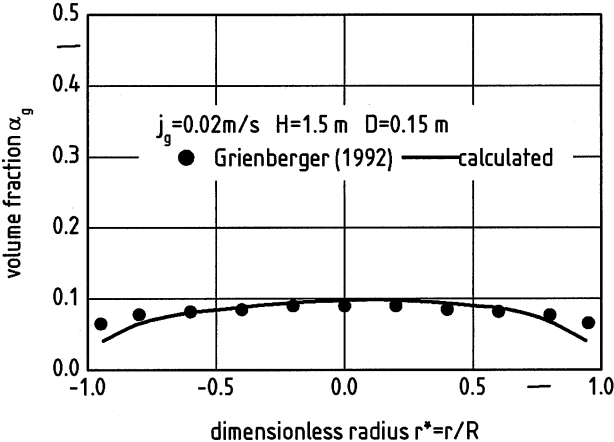


Fig. 3. Time-averaged volume fraction of gas

The time-averaged volume fraction is axisymmetric and almost constant over the cross section. Only in the near wall region a decrease of the volume fraction occurs.

The influence of mass transfer from the gaseous into the liquid phase is shown in Fig. 4. The gas phase is air and the liquid phase is water. A constant amount of gas per unit interfacial area is transferred into the liquid phase. In addition to the liquid velocity the streamlines of the liquid phase are given.

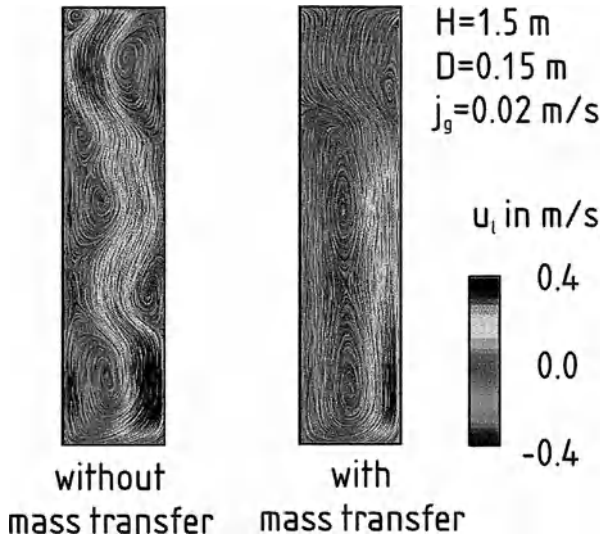


Fig. 4. Influence of mass transfer

The absorption of the gas phase leads to a decrease in the momentum transfer from the gas into the liquid phase. Therefore the amount and the size of the vortices decrease with the column height. This change in the flow pattern enhances the backflow of liquid.

The following calculations are performed for the physical absorption of CO_2 into water. The column has a diameter of $D=0.19$ m and a height of $H=2.80$ m. The superficial gas velocity is $j_g=0.02$ m/s and the superficial liquid velocity is of $j_l=0.05$ m/s. A constant mass transfer coefficient of $\beta=2.8 \cdot 10^{-4}$ m/s is used. In Fig. 5 the calculated partial density of CO_2 , the volume fraction of gas and the liquid velocity are shown for $t=100$ s. In addition the streamlines of liquid are visualized with a texture. The partial density of CO_2 in the liquid increases with the column height. According to the increasing concentration of CO_2 in the liquid phase the volume fraction of gas decreases significantly. At the top of the column the volume fraction is reduced to $\alpha_g=0.02$. The flow pattern is changed according to the reduced momentum transfer. In the lower part of the column the liquid velocity

field is strongly influenced by vortices. With decreasing volume fraction of gas the momentum transfer from the gaseous to the liquid phase is reduced and therefore the flow pattern in the upper part of the column is almost stratified.

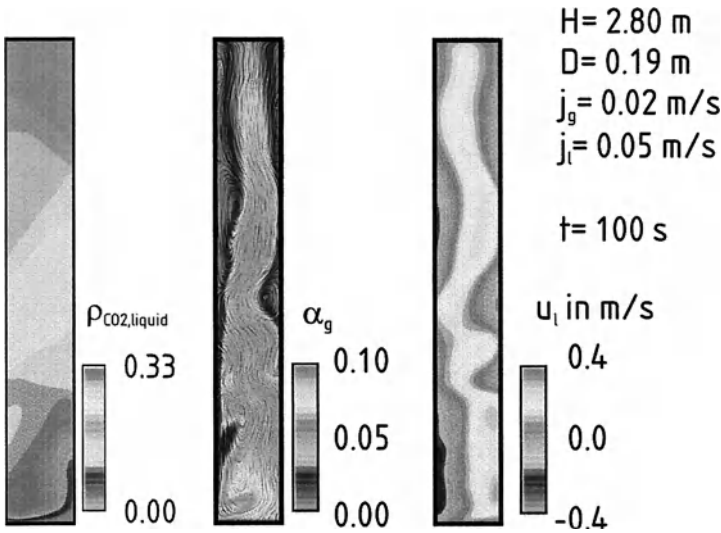


Fig. 5. Instantaneous flow field considering mass transfer

3.2 High superficial gas velocities

For higher superficial gas velocities the gas phase is described by two phases: one gaseous phase containing the small bubbles and a second one which accounts for the large bubbles.

The calculated fields for the volume fraction and the mean bubble diameter are shown in Fig. 6. The column has a height of $H=1.5\text{m}$ and a diameter of $D=0.15 \text{ m}$. The superficial gas velocity is $j_g=0.10 \text{ m/s}$. The initial bubble diameter of the small bubbles at the inlet is 2 mm and for the large bubbles the initial diameter is set to 20 mm. The diameter of the large bubbles increase to 50 mm at the top of the column whereas the small bubbles diameter decreases. The enhanced coalescence rate increases the volume fraction of the large bubble fraction significantly with the column height. The time-averaged volume fraction of gas is shown in Fig. 7. In addition to the calculated results the experiments from Hills (1974) are given. The time-averaged volume fraction of gas is axisymmetric with the maximum in the middle of the column. The volume fraction of small bubbles is almost constant except of the near wall region. The volume fraction of the large bubbles

has a parabolic profile. Thus the large bubbles rise up in particular in the center of the column.

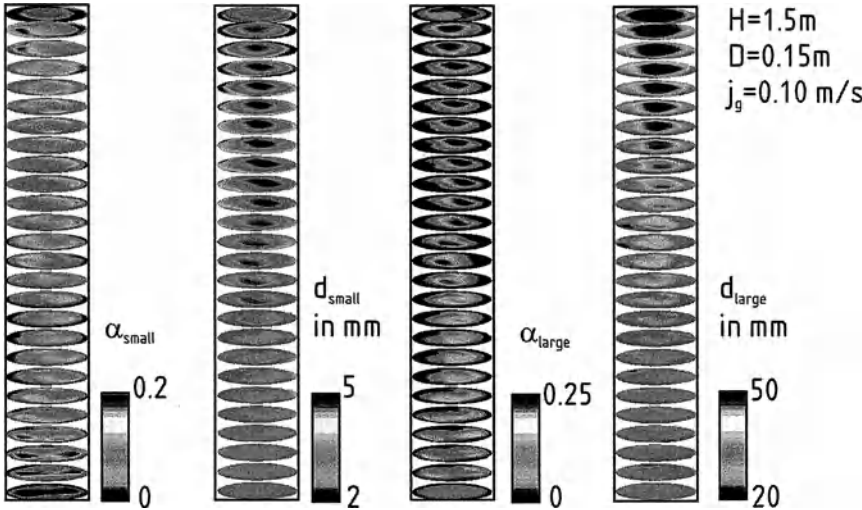


Fig. 6. Flow field for high superficial gas velocities

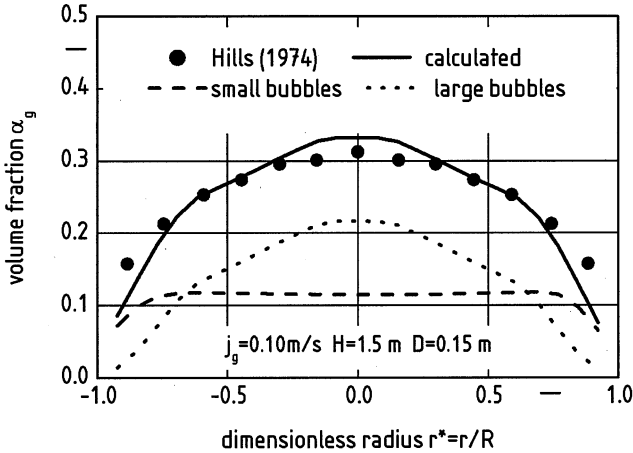


Fig. 7. Time averaged volume fraction for $j_g=0.10\text{ m/s}$

4 Conclusion

The flow fields in bubble columns are numerically calculated using a two-fluid approach. The calculations are performed for three dimensional, instationary flow fields in cylindrical bubble columns. A simplified form of the population balance equation is used to calculate the local bubble size distribution in dependence of the local flow field. For high superficial gas velocities the formation of large bubbles is considered using two gaseous phases: one phase containing the small bubble fraction and a second one accounting for the large bubbles. The calculated flow fields for the liquid and the gas phase are three-dimensional and instationary. The time-averaged flow fields are axisymmetric. In addition to the system air-water the influence of mass transfer is considered modelling the physical absorption of CO₂ into water. The numerical results are compared with experimental results for bubble columns up to a diameter of 0.3 m and a height of 4.5 m.

Acknowledgement

The authors gratefully acknowledge the financial support of the German Research Foundation (DFG).

Notation

a_p	[m ⁻¹]	interfacial area density
C_D	[-]	drag coefficient
D	[m]	bubble column diameter
d	[m]	bubble diameter
d_{eq}	[m]	equivalent bubble diameter
d_s	[m]	sauter mean diameter
f	[m ⁻⁶]	number density distribution
H	[m]	bubble column height
j	[ms ⁻¹]	superficial velocity
k	[m ² s ⁻²]	turbulent kinetic energy
n	[m ⁻³]	number density
n_λ	[m ⁻⁴]	number density of eddies with length scale λ
\dot{n}	[kmol m ² s ⁻¹]	molar flux
r	[m]	radius
r_1	[m ³ s ⁻¹]	break-up kernel function
r_2	[m ³ s ⁻¹]	coalescence kernel function
\vec{u}	[ms ⁻¹]	velocity
u_{crit}	[ms ⁻¹]	critical velocity for coalescence
u'	[ms ⁻¹]	turbulent fluctuating velocity
v_b	[m ³]	bubble volume

Greek symbols

α	[-]	volume fraction
β	[m ⁻³]	daughter size distribution
ε	[m ² s ⁻³]	dissipation rate
λ	[m]	length scale of an eddy
μ	[kg kmol ⁻¹]	molar mass
ξ	[-]	mass fraction
ρ	[kgm ⁻³]	density
σ	[kgs ⁻²]	surface tension

Indices

0	initial value
1	small bubbles
2	large bubbles
l	Liquid
g	Gas
t	turbulent
'	daughter bubble
*	dimensionless variable

References

- Brauer H (1981) Particle/fluid transport processes. *Progress in Chem Eng* 19: 81-111
- Clift R, Grace JR, Weber ME (1978) *Bubbles, Drops and Particles*. Academic Press, New York, San Francisco, London
- de Bertodano ML, Lahey RT, Jones OC (1994) Development of a k- ε turbulence model for bubbly two-phase flow. *J Fluids Eng* 116: 128- 134
- Delnoij E, Kuipers JAM, van Swaaij WPM (1999) A three dimensional CFD model for gas-liquid bubble columns; *Chem Eng Sci* 54: 2217-2226
- Drew DA (1983) *Mathematical Modelling of Two-Phase Flow*. *Ann Rev Fluid Mech* 15:261-291
- Grienberger J (1992) *Untersuchung und Modellierung von Blasensäulen*. Ph.D. thesis, Universität Erlangen-Nürnberg, Germany
- Hallensleben J (1980) *Simultaner Stoffaustausch von CO₂ und Sauerstoff an Einzelblasen und in Blasenschwärmen*. Ph.D. thesis, Universität Hannover, Germany
- Hills JH (1974) Radial Non-Uniformity of Velocity and Voidage in a Bubble Column. *Trans. Instn Chem Engrs* 52:1-9
- Jacobsen HA, Sannaes BH, Grevskott S, Svendsen HF (1997) Modeling of vertical bubble driven flows. *Ind Eng Chem Res* 36:4052-4074
- Krishna R, Urseanu MI, van Baten JM, Ellenberger L (1999) Influence of scale on the hydrodynamics of bubble columns operating in the churn-turbulent regime: Experiments vs. eulerian simulations. *Chem Eng Sci* 54: 4903-4911

- Krishna R, van Baten JM, Urseanu MI (2000) Three phase eulerian simulations of bubble column reactors operating in the churn-turbulent regime: A scale up strategy. *Chem Eng Sci* 55: 3725-3286
- Lain S, Bröder D, Sommerfeld M (1999) Experimental and numerical studies of the hydrodynamics in a bubble column. *Chem Eng Sci* 54: 4913-4920
- Lapin A, Lübbert A (1995) Chaotic flow in bubble column reactors; *Chem Eng Sci* 50: 2661-2667
- Lapin A, Lübbert A (1996) Fluid dynamics in bubble column bioreactors: Experiments and numerical simulation. *Biotechnology and Bioengineering* 52: 248-258
- Lehr F, Millies M, Mewes D (2002) Bubble-Size Distribution and Flow Fields in Bubble Columns, *AIChE J* October 2002
- Mudde, RF, Simonin, O (1999) Two- and three dimensional simulations of a bubble plume using a two-fluid model. *Chem Eng Sci* 54: 5061-5069
- Pan Y, Dudukovic MP, Chang, M (1999) Dynamic simulation of bubbly flow in bubble columns. *Chem Eng Sci* 54: 2481-2489
- Pan Y, Dudukovic MP, Chang M (2000) Numerical investigation of gas-driven flow in 2-D bubble columns; *AIChE J* 46: 434-449
- Pfleger D, Gomes S, Gilbert N, Wagner HG (1999) Hydrodynamic simulations of laboratory scale bubble columns fundamental studies of the eulerian-eulerian modelling approach. *Chem Eng Sci* 54: 5091-5099
- Saynaya J, Vasquez S, Roy S, Dudukovic MP (1999) Numerical simulation of gas-liquid dynamics in cylindrical bubble column reactors. *Chem Eng Sci* 54: 5071-5083
- Sokolichin A, Eigenberger G, Lapin A, Lübbert A (1997) Dynamic numerical simulation of gas-liquid two-phase flows. *Chem Eng Sci* 52: 661-626
- Sokolichin A, Eigenberger G (1999) Applicability of the standard k- ϵ turbulence model to the dynamic simulation of bubble columns. Part I: Detailed numerical simulations. *Chem Eng Sci* 54: 2273-2284
- Sokolichin A, Eigenberger G, Borchers O, Busch C (1999) Applicability of the standard k- ϵ turbulence model to the dynamic simulation of bubble columns. Part II: Comparison of detailed experiments and flow simulations. *Chem Eng Sci* 54: 5927-5935
- Thakre SS, Joshi JB (1999) CFD simulation of bubble column reactors: Importance of drag force formulation. *Chem Eng Sci* 54: 5055-5060
- Torvik R, Svendsen HF (1990) Modeling of slurry reactors, a fundamental approach. *Chem Eng Sci* 45: 2325-2332
- Webb C, Que F, Senior PR (1992) Dynamic simulation of gas-liquid dispersion behavior in a 2-D bubble column. *Chem Eng Sci* 47: 3305-3312

Publications

- Lehr F, Mewes D (2000) Berechnen des Strömungsfeldes in Blasensäulen unter Berücksichtigung der lokalen Blasengrößenverteilung; GVC-Jahrestreffen, 20.-22. Sept. 2000, Karlsruhe, Chemie Ingenieur Technik 72: 1046
- Lehr F, Mewes D (2001) Gekoppeltes Berechnen von Blasengrößenverteilungen und Strömungsfeldern in Blasensäulen. *Chemie Ingenieur Technik* 73: 1245-1259

- Lehr F (2002) Berechnen von Blasengrößenverteilungen und Strömungsfeldern in Blasen-säulen. VDI Fortschritt Berichte Reihe 3 Nr 726, VDI Verlag
- Lehr F, Millies M, Mewes D (2002) Numerical simulation of bubble size distributions and flow fields in bubble columns. *AIChE J* October 2002
- Wiemann D, Lehr F, Mewes D (2002) Numerical calculation of the flow field in bubble columns using a simplified form of the population balance equation. In: *Proceedings of ASME FEDSM 2002*, Montreal
- Wiemann D, Lehr F, Mewes D (2002) Numerical calculation of the flow field in a bubble column considering the absorption of the gas phase. *Int. Conf. on Distillation and Absorption*, Sept. 30 –Oct.2, 2002, Baden-Baden

X-ray computational tomography measurement of 3-phase flow in bubble columns

M. Behling, D. Mewes

Institute of Process Engineering, University of Hannover, Callinstrasse 36, 30167 Hannover, Germany

Abstract

A pilot plant scale 3-phase bubble column is examined experimentally. The liquid phase is water, the gas phase is air, the solid phase are PVC-particles. Local phase holdups of all 3 phases are measured by X-ray tomography. An extended form of X-ray tomography is used, the dual energy technique. The proper operation of this technique is ensured by the choice of the examined materials and applied X-ray photon energies. The high data resolution of the X-ray detector ensures high resolution of the measured phase fractions.

1 Introduction

3-phase bubble columns are often used for technical catalytic reactions or as bioreactors. Additionally to the continuous liquid phase and the disperse gas phase, in a 3-phase bubble column solid particles are suspended. These can be a catalyst or the biomass, for instance. The efficiency of a bubble column depends on the available phase boundaries, the phase distributions and the flow field. To know and be able to predict these properties enables both an optimized operation of existing bubble columns and a better design of future bubble columns.

For 2-phase bubble columns, mathematical models exist that allow, for instance, to calculate the flow field in consideration of breakup and coalescence of bubbles (cp. Lehr 2001). The development of mathematical models for 3-phase bubble columns is still in progress (cp. Michele and Hempel 2002). For the validation of such models experimental data are required. Several experimental investigations to measure local parameters in 3-phase bubble columns are carried out. Warsito et al. (1997) and Michele and Hempel (2002) use intrusive probes to measure local phase holdups and velocities in a 3-phase bubble column. Grevskott et al. (1996) and Dudukovic et al. (1997) use radioactive particle tracking to measure velocities in bubble columns. George et al. (2001) use a combination of gamma-densitometry tomography and electrical tomography to measure phase distributions in 3-phase bubble column. This measuring technique is non-intrusive,

but limited by the assumption of an axisymmetric phase distribution for the reconstruction. Non-intrusive high-resolution measurements of the local phase fractions for whole cross sections are still required.

Therefore the aim of his work is to non-intrusively measure time-averaged local phase fractions of liquid, solid and gas in a 3-phase bubble column. The influence of superficial gas velocity, solid loading and sparger geometry are to be examined. The applied measuring technique is X-ray computational tomography. X-ray tomography is a non-intrusive measuring technique with high spatial resolution. It can be used to penetrate objects that are inaccessible to optical measuring techniques. The measurement results are material distributions in cross sections through the measured object. To measure the local phase fractions of all 3 phases, an extended form of X-ray tomography is used, the so-called dual-energy technique. The applicability of the dual-energy technique for measuring 3-phase bubble columns has been shown in principle by Grassler and Wirth (2001) and Strabel and Wirth (2002).

2 Test facility

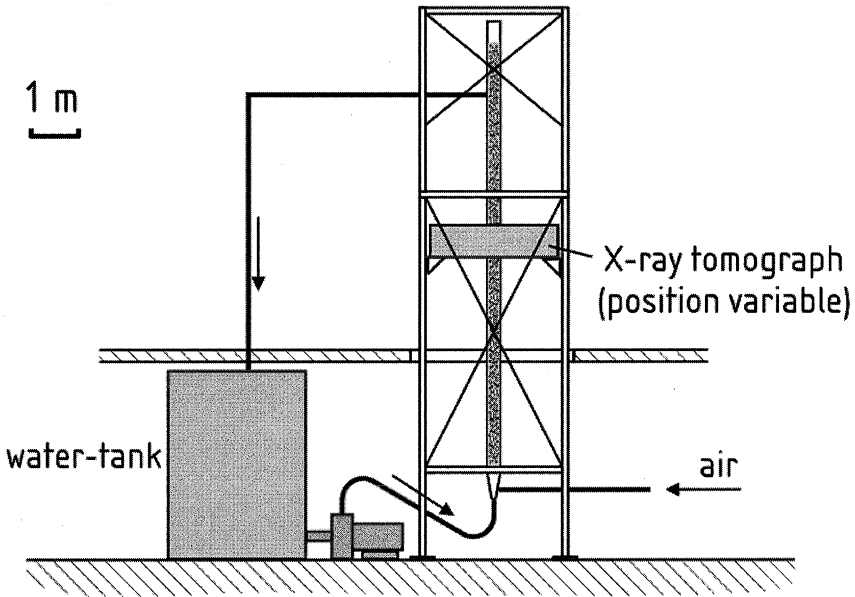


Fig. 1. Test facility

A pilot plant scale bubble column is examined. A drawing of the test facility is shown in **Fig. 1**. The inner diameter of the column is 244 mm, the height is 7.5 m.

The liquid phase is water, the gas phase is air. The water in the column can either be operated in batch mode or flowing upward. Both water and air inlet are through a sieve plate at the bottom of the column. The solid phase is PVC resin. Particle sizes are in the range of 2 - 3.5 mm. Several PVC compounds with densities in the range of 1.2 to 1.5 g/cm³ are examined. The solid particles in the column are operated in batch mode. The X-ray tomograph can be mounted in various vertical positions to measure various cross sections through the bubble column.

3 X-ray tomography

3.1 Measuring principle

X-ray tomography has been developed in the early 1970s, initially for medical diagnosis (cp. Morneburg et al. 1995, Kalender 2000). Later it was adopted to technical applications like material and workpiece testing. In recent years, X-ray tomography has been used in the process industry to measure multiphase flows (cp. Mewes and Schmitz 2000). The measurement principle of X-ray tomography is shown in Fig. 2.

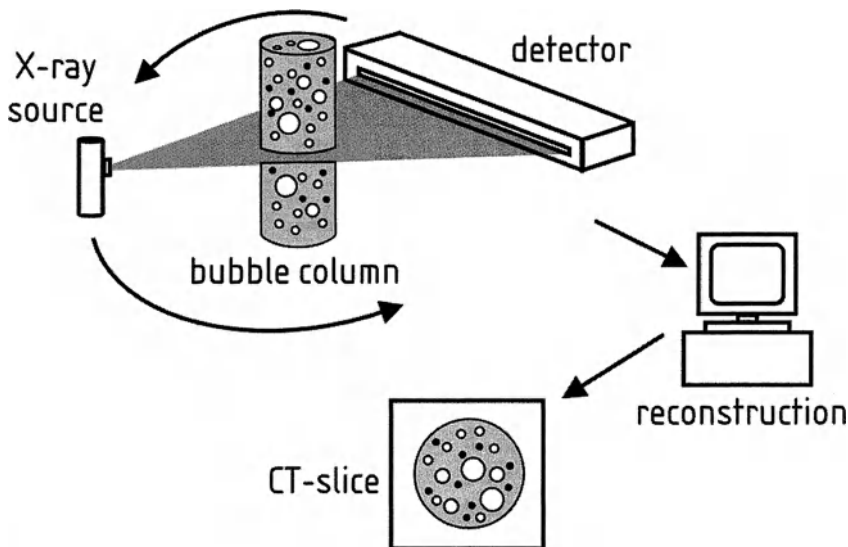


Fig. 2. X-ray tomography measurement principle

The measured object, in this case the bubble column, is irradiated by an X-ray fan beam. The X-rays penetrate and are attenuated by the measured object. A linear detector is used to measure the intensity of the attenuated X-rays. The attenua-

tion along each X-ray path is a measure for the penetrated material. From only one projection it is impossible to determine where along this X-ray path the attenuation has taken place. Therefore the X-ray source and detector are rotated around the bubble column. Projections are measured in multiple directions and stored. After measuring the projections, in a second step the local phase holdups in a slice through the bubble column are reconstructed. Since the projections are not measured at the same time, the reconstructed slice is time averaged. X-ray tomography is completely non-intrusive, it has no influence on the measured object.

The intensity of the attenuated X-rays can be calculated by the Lambert-Beer law as

$$I = I_0 e^{-\mu_{\text{water}} d_{\text{water}}} \quad (3.1)$$

for the 2-phase case with only air and water in the column. I is the intensity of the attenuated X-rays, I_0 the intensity of the X-rays without attenuation. d_{water} is the total penetrated length of water along the path of the X-rays, and μ_{water} is the attenuation coefficient of water, a material property. Apart from the material, the attenuation coefficient μ depends on the X-ray “hardness”, i.e. the photon energy. The penetrated air does not attenuate the X-rays and therefore does not appear in Eq.(3.1). The bubble column wall also attenuates the X-rays. This effect is the same for all measurements. It is eliminated by calibration and thus is neglected here.

For the simple 2-phase case, the penetrated length of air d_{air} along each X-ray path can be calculated from

$$d_{\text{water}} + d_{\text{air}} = d_{\text{column}} \cdot \quad (3.2)$$

d_{column} is the total way of the X-ray through the column. With Eq.(3.1) and Eq.(3.2) 2 equations are available for the 2 unknowns d_{water} and d_{air} . This system of equations can easily be solved, and the penetrated amounts of water and air can be determined for each X-ray intensity measurement.

For the 3-phase case with the the PVC particles as the additional solid phase, Eq.(3.1) and Eq.(3.2) are extended to

$$I = I_0 e^{-(\mu_{\text{water}} d_{\text{water}} + \mu_{\text{PVC}} d_{\text{PVC}})} \quad (3.3)$$

and

$$d_{\text{water}} + d_{\text{air}} + d_{\text{PVC}} = d_{\text{column}} \cdot \quad (3.4)$$

In this case there are 3 unknowns: d_{water} , d_{air} and d_{PVC} , the penetrated length of PVC. The 2 equations Eq.(3.3) and Eq.(3.4) are not sufficient to determine these 3 unknowns. This problem is overcome by the dual energy technique.

3.2 Dual energy technique

The X-ray attenuation coefficient μ of each material depends on the X-ray photon energy. This effect is used for the dual energy technique in X-ray tomography. The measured object is successively irradiated with X-rays with 2 different X-ray photon energies, giving 2 separate intensity measurements for the attenuated X-rays. These 2 attenuated intensities can be calculated by 2 separate attenuation equations as

$$I_1 = I_{0,1} e^{-(\mu_{\text{water},1}d_{\text{water}} + \mu_{\text{PVC},1}d_{\text{PVC}})} \quad (3.5)$$

and

$$I_2 = I_{0,2} e^{-(\mu_{\text{water},2}d_{\text{water}} + \mu_{\text{PVC},2}d_{\text{PVC}})} \quad (3.6)$$

The indices “1” and “2” indicate the 2 different X-ray photon energies. Solving the system of Eqs.(3.4 - 3.6), the 3 unknowns d_{water} , d_{air} and d_{PVC} can be determined.

The attenuation coefficients of the examined materials must differ from each other. Otherwise the materials can not be distinguished by X-ray tomography. This is ensured by the choice of the examined materials. In this work water is used as the liquid phase, PVC particles as the solid phase.

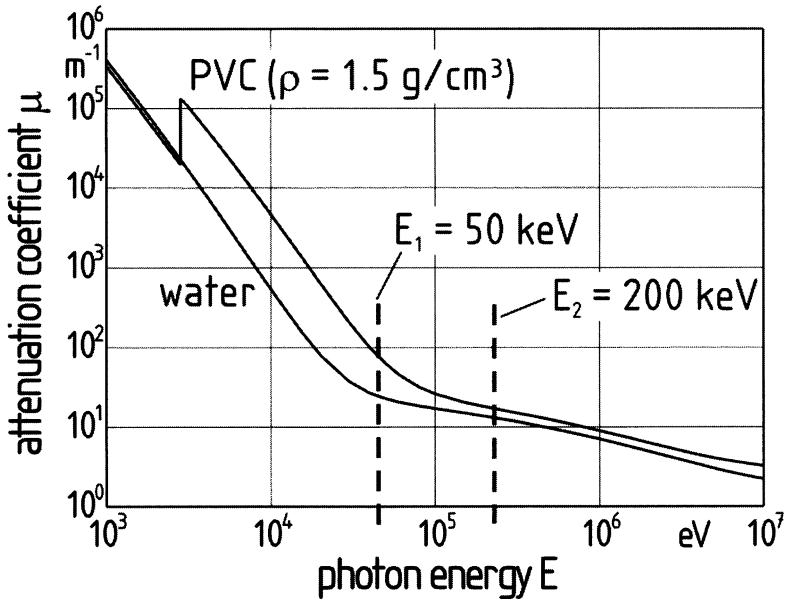


Fig. 3. Attenuation coefficients of PVC and water

In Fig. 3 the attenuation coefficients of water and PVC (density 1.5 g/cm^3) are plotted as a function of the X-ray photon energy. It is obvious that over a broad range of photon energies the attenuation coefficients differ significantly. The dual energy technique can only work when Eq.(3.5) and Eq.(3.6) are linearly independent. This is ensured by the proper choice of the 2 applied X-ray photon energies. In Fig. 3 the 2 photon energies used in this work are indicated, 50 and 200 keV.

3.3 X-ray tomograph setup

The setup of the X-ray tomograph is shown in Fig. 4. The X-ray source and linear detector are mounted on a rotating frame on opposite sides of the bubble column. The X-ray source produces a cone-shaped beam. For the measurements only a flat fan beam of X-rays is required. To reduce scattered radiation, the unused part of the cone beam is screened by a lead collimator, obtaining the required flat fan beam. Another collimator in front of the detector also prevents remaining scattered radiation from outside the measurement plane from getting into the detector.

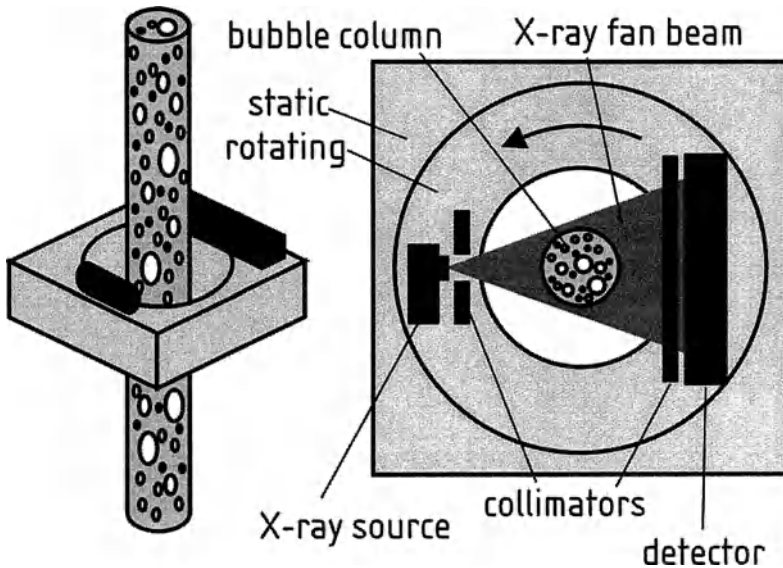


Fig. 4. Setup of X-ray tomograph

The linear X-ray detector consists of 384 pixels. The pixel size is 1.6 mm. The minimum integration time is $10 \mu\text{s}$. The detector offers a 16bit data resolution, i.e. more than 65 000 levels of X-ray intensity can be distinguished. This high intensity resolution allows to measure all possible volume fractions of water, air and PVC-particles from 0 to 100 %. As an example, in the bubble column filled with water, 0.1 mm PVC can be detected. This corresponds to 0.04 % of PVC in 99.96% of water along an X-ray path through the column center.

The rotation of X-ray source and detector is implemented by using the mechanical unit of a medical X-ray tomograph. A photograph of this gantry is shown in Fig. 5. It consists of a static frame and the rotating inner, on which the X-ray equipment is mounted (which on the photograph is not yet in place). The rotation can achieve a maximum speed of 45 rpm. Due to the short measurement time of the detector, projections can be measured throughout the rotation without the need to stop at the required positions.

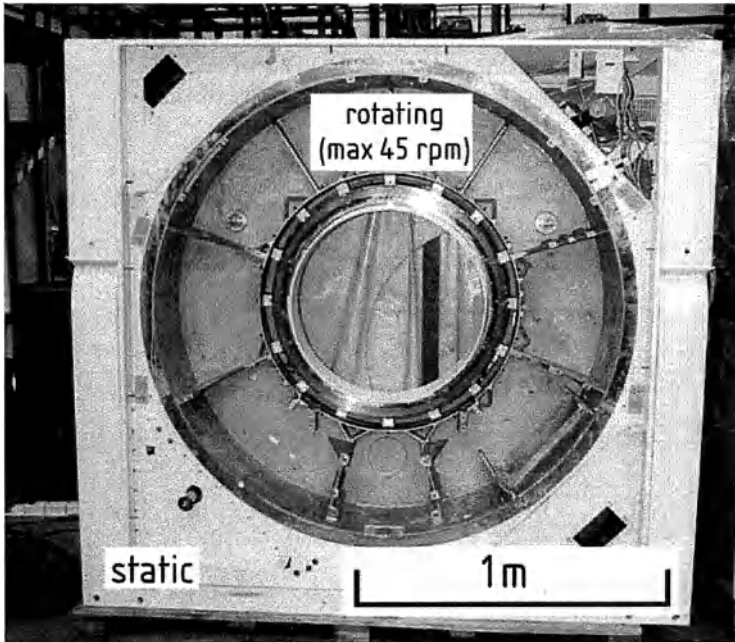


Fig. 5. Tomograph gantry

Electrical power is supplied to the rotating equipment via sliprings. For the data connection to the X-ray detector and the X-ray source control a wireless computer connection is established.

4 Conclusion and outlook

A 3-phase bubbler column with 244 mm inner diameter is examined. Dual-energy computational X-ray tomography is used to measure time-averaged local phase holdups of all 3 phases (liquid, gas, and solid). At the editorial deadline of this report, the assembly of the X-ray tomograph is nearly complete. First X-ray measurements will start in late 2002.

Acknowledgement

The authors gratefully acknowledge the financial support of the German Research Foundation (DFG).

Notation

d	[m]	distance / penetrated length of material
E	[keV]	X-ray photon energy
I	[Gy/s]	X-ray intensity

Greek symbols

μ	[cm ⁻¹]	X-ray attenuation coefficient
-------	---------------------	-------------------------------

Indices

0	initial value
1	X-ray photon energy 1
2	X-ray photon energy 2
air	air
column	bubble column
water	water

References

- George DL et al. (2001) Three-phase material distribution measurements in a vertical flow using gamma-densitometry tomography and electrical-impedance tomography. *Int. Journal of Multiphase Flow* 27: 1903 - 1930
- Grassler T, Wirth KE (2001) Dual-Energy x-ray tomography in process engineering - a non-intrusive technique to characterise vertical multiphase flows. In: 2nd world congress on industrial process tomography, Hannover, Germany
- Grevskott S et al. (1996) Liquid circulation, bubble size distributions, and solid movement in two- and three-phase bubble columns. *Chemical Engineering Science* 51: 1703 - 1713
- Kalender WA (2000) *Computed Tomography: Fundamentals, System Technology, Image Quality, Applications*. Publicis MCD, München, Germany
- Lehr F (2001) Berechnen von Blasengrößenverteilungen und Strömungsfeldern in Blasensäulen (in German). Ph.D. thesis, University of Hannover, Germany
- Mewes D, Schmitz D (2000) Analysis of the flow patterns in pipes and packings using tomographic methods. In: ASME 2000 Fluids engineering division Summer Meeting, Boston, Massachusetts
- Michele V, Hempel DC (2002) Liquid flow and phase holdup - measurement and CFD modeling for two- and three-phase bubble columns. *Chem. Eng. Sci.* 57: 1899 - 1908

- Morneburg H et al. (1995) Bildgebende Systeme für die medizinische Diagnostik (in German). Publicis MCD, Erlangen, Germany
- Strabel M, Wirth KE (2002) Dual-Energy X-ray Tomography in Process Engineering (in German). *Technisches Messen* 69: 333 - 339
- Warsito et al. (1997) Flow structure and phase distributions in a slurry bubble column. *Chemical Engineering Science* 52: 3941 - 3947

Euler/Lagrange Calculations of Gas-Liquid-Solid-Flows in Bubble Columns with Phase Interaction

E. Bourloutski and M. Sommerfeld

Mechanische Verfahrenstechnik, Fachbereich Ingenieurwissenschaften, Martin-Luther-Universität Halle-Wittenberg, D-06099 Halle (Saale), Germany

Abstract. This paper presents a mathematical model based on Euler/Lagrange approach for time-dependent calculations of two- (gas-liquid) and three- (gas-liquid-solid) phase flows in a bubble column. The fluid phase flow was calculated based on the Euler approach by solving the three-dimensional Reynolds-averaged conservation equations in a time dependent way. The set of equations was closed using the standard $k-\epsilon$ turbulence model. Two-way coupling was accounted for by adding dispersed phase source terms in all conservation equations of the continuous phase and additionally considering wake-induced turbulence. Bubble motion was calculated by solving the equation of motion taking into account drag force, pressure, added mass force, transverse lift force, buoyancy and gravity. The tracking of solid particles was based on considering drag force, pressure, added mass force, Saffman force, Magnus force and gravity. The introduction of the effective density in the continuous phase conservation equations permitted to perform the calculations up to relatively high volume fractions of the dispersed phase. The interaction between bubbles and particles was considered by adding simple correction terms to the drag coefficient of both bubbles and particles. Alternatively, the interaction was described by collisions between bubbles and particles using a stochastic collision model. The comparison of the predicted results with experimental data from the literature showed reasonable good agreement for the cases of two-phase and three-phase flows.

1. Introduction

Traditionally the design and/or scale-up of three phase flow processes is based on experimental studies and empirical correlation's resulting there from. As a consequence, also numerous experimental studies are available. Relevant for the design of three phase bubble columns are mainly the flow regime, the solid concentration distribution and the gas hold-up along column. These operational conditions depend for a situation without net liquid flow mainly on the gas flow rate and the solid concentration (e.g. Smith & Ruether 1985, Chen et. al. 1995, Ohkawa et. al. 1997). In order to predict for example solids concentration in a bubble column, rather simple semi-empirical models have been used so far, such as for example a

sedimentation-dispersion models (Smith et. al. 1986). A more sophisticated approach for predicting the solids concentration profiles is the wake shedding model which accounts for more details of bubble-particle interaction (Tsutsumi et. al. 1992).

In recent years also computational fluid dynamics (CFD) has considerably advanced and was extended for the numerical calculation of multiphase flows in process engineering (see for example Birtigh et. al. 2000). For the numerical calculation of flows in two- or three-phase bubble columns mainly the two- or multi-fluid model is preferred due to the generally high volume fractions of both phases (typically around 20 %). This method is based on the assumption of interacting continua, which implies that also the dispersed phases are treated as continua (Simonin 2000). However, a detailed modeling of the involved relevant physical mechanisms and interaction processes is rather sophisticated with this approach. More detailed reviews on the state-of-the-art on numerical calculations of bubble columns (two-phase flow) may be found in Lain et. al. (2002) and Bourloutski & Sommerfeld (2002). Regarding the prediction of three-phase bubble columns (i.e. gas-liquid-solids flows) the work of Mitra-Majumdar et. al. (1997) should be mentioned. Here a multi-fluid approach in connection with a $k-\epsilon$ turbulence model supplemented by an extended eddy-viscosity approach to account for bubble induced turbulence was adopted. The interaction between both dispersed phases (i.e. bubbles and solids) was considered by a simple modification to the drag forces by empirical terms depending on the volume fraction of the other phase. These terms describe the dragging of the solids by the bubbles and the hindering of bubble rise by the particles. The comparison of the predicted solids volume fraction along the column with experimental data was found to be reasonably good with these simple interaction terms. However, this model uses empirical constants which are not universal and will strongly depend on the size ratio of bubbles and particles.

In the present study the Euler/Lagrange approach was extended and applied to three-phase bubble columns. Bubble and particle motion was described in detail by accounting for all relevant forces. Moreover, the momentum transfer from the dispersed phases to the liquid was considered including a model of turbulence modification. The momentum transfer between bubbles and particles was described by simple interaction terms and alternatively by accounting for collisions.

2. Euler/Lagrange approach

2.1 Flow calculation and bubble/particle tracking

For the present studies the Euler/Lagrange approach was solved in a time-dependent way in order to resolve the inherent unsteady nature of the flow in a bubble column. The fluid flow was calculated based on Euler approach by solv-

ing the unsteady Reynolds-averaged conservation equations including the source terms of the dispersed phases. These equations were closed using the standard $k-\varepsilon$ turbulence model (Launder & Spalding 1974) which was extended by accounting for the effects of the dispersed phase and especially wake induced turbulence. The conservation equations for a three-dimensional flow may be written in a generalized form with the different terms give in Table 1 in the following way:

$$\begin{aligned} & \frac{\partial(\sigma_F \phi)}{\partial t} + \frac{\partial}{\partial x}(\sigma_F U \phi) + \frac{\partial}{\partial y}(\sigma_F V \phi) + \frac{\partial}{\partial z}(\sigma_F W \phi) = \\ & \frac{\partial}{\partial x}\left(\Gamma \frac{\partial \phi}{\partial x}\right) + \frac{\partial}{\partial y}\left(\Gamma \frac{\partial \phi}{\partial y}\right) + \frac{\partial}{\partial z}\left(\Gamma \frac{\partial \phi}{\partial z}\right) + S_\phi + S_{\phi D} \end{aligned} \quad (1)$$

ϕ	Γ	S_ϕ	$S_{\phi D}$
1	-	-	$S_{\sigma_F D} = 0$
U	$\mu + \mu_t$	$\frac{\partial}{\partial x}\left(\Gamma \frac{\partial U}{\partial x}\right) + \frac{\partial}{\partial y}\left(\Gamma \frac{\partial V}{\partial x}\right) + \frac{\partial}{\partial z}\left(\Gamma \frac{\partial W}{\partial x}\right) - \frac{\partial p}{\partial x} + \sigma_F g_i$	S_{UD}
V	$\mu + \mu_t$	$\frac{\partial}{\partial x}\left(\Gamma \frac{\partial U}{\partial y}\right) + \frac{\partial}{\partial y}\left(\Gamma \frac{\partial V}{\partial y}\right) + \frac{\partial}{\partial z}\left(\Gamma \frac{\partial W}{\partial y}\right) - \frac{\partial p}{\partial y} + \sigma_F g_i$	S_{VD}
W	$\mu + \mu_t$	$\frac{\partial}{\partial x}\left(\Gamma \frac{\partial U}{\partial z}\right) + \frac{\partial}{\partial y}\left(\Gamma \frac{\partial V}{\partial z}\right) + \frac{\partial}{\partial z}\left(\Gamma \frac{\partial W}{\partial z}\right) - \frac{\partial p}{\partial z} + \sigma_F g_i$	S_{WD}
k	$\mu + \frac{\mu_t}{\sigma_k}$	$P_k - \sigma_F \varepsilon$	S_{kD}
ε	$\mu + \frac{\mu_t}{\sigma_\varepsilon}$	$\frac{\varepsilon}{k}(C_{\varepsilon 1} P_k - C_{\varepsilon 2} \sigma_F \varepsilon)$	$S_{\varepsilon D}$
$P_k = \mu_t \left[2 \left\{ \left(\frac{\partial U}{\partial x} \right)^2 + \left(\frac{\partial V}{\partial y} \right)^2 + \left(\frac{\partial W}{\partial z} \right)^2 \right\} + \left(\frac{\partial U}{\partial y} + \frac{\partial V}{\partial x} \right)^2 + \left(\frac{\partial U}{\partial z} + \frac{\partial W}{\partial x} \right)^2 + \left(\frac{\partial W}{\partial y} + \frac{\partial V}{\partial z} \right)^2 \right]$ $\mu_t = C_\mu \rho \frac{k^2}{\varepsilon}, \quad \sigma_F = \rho(1 - \alpha_B - \alpha_P), \quad C_\mu = 0.09, \quad C_1 = 1.44, \quad C_2 = 1.92$ $\sigma_k = 1.0, \quad \sigma_\varepsilon = 1.3$			

Table 1: Source term expressions of fluid phase for the different variables ϕ and constants of turbulence model.

Here, ρ is the liquid density, α_B is the bubble phase volume fraction, α_P is the solid phase volume fraction, σ_F is the effective fluid density, U, V, W are the Reynolds-averaged velocity components. The resulting set of conservation equations was solved by using a finite-volume discretization scheme with collocated grid arrangement, which implies the solution of the integral form of the conservation equations. The diffusive terms are discretized by central differences,

while an upwind scheme is used for the convective terms. The fluid flow was solved with the code FASTEST 3D, which is based on non-orthogonal block-structured grids with block-wise free topology. Pressure-velocity coupling was realized by the SIMPLE algorithm.

The dispersed phases (bubbles and solid particles) are simulated in a Lagrangian way, where a large number of disperse elements are tracked simultaneously through the flow field. Depending on bubble and particle size and volume fraction typically between 50,000 and 100,000 computational particles of both phases were simultaneously present in the flow field. In the equation of motion for bubble tracking the drag, pressure, added mass, transverse lift forces, buoyancy and gravity are considered. This results in the following set of ordinary differential equations for the bubble phase:

$$\frac{d x_{Bi}}{d t} = u_{Bi} \quad (2)$$

$$\begin{aligned} m_B \frac{d u_{Bi}}{d t} = & \frac{3}{4} \frac{\rho}{\rho_B D_B} m_B C_D (u_i - u_{Bi}) |\bar{u} - \bar{u}_B| + m_B \frac{\rho}{\rho_B} \frac{d u_i}{d t} \\ & + \frac{1}{2} m_B \frac{\rho}{\rho_B} \left(\frac{d u_i}{d t} - \frac{d u_{Bi}}{d t} \right) + \frac{1}{2} m_B \frac{\rho}{\rho_B} [(\bar{u} - \bar{u}_B) \times (\nabla \times \bar{u})]_k + m_B g_i \left(1 - \frac{\rho}{\rho_B} \right) \end{aligned} \quad (3)$$

Here, x_{Bi} are the co-ordinates of the bubble position, u_{Bi} the velocity components, D_B is the bubble diameter, and ρ_B is the bubble density. The Basset history term was neglected in the present study. It should be noted that the pressure term is already split into the fluid acceleration and the buoyancy (Crowe et al. 1996).

For tracking the solid particles the forces, such as drag, fluid acceleration, added mass, Saffman force, Magnus force and gravity/buoyancy are considered in the equation of motion (Sommerfeld 2000). Hence, the particle motion is calculated by solving the following set of ordinary differential equations:

$$\frac{d x_{Pi}}{d t} = u_{Pi} \quad (4)$$

$$\begin{aligned} m_P \frac{d u_{Pi}}{d t} = & \frac{3}{4} \frac{\rho}{\rho_P D_P} m_P C_D (u_i - u_{Pi}) |\bar{u} - \bar{u}_P| + \\ & m_P \frac{\rho}{\rho_P} \frac{d u_i}{d t} + \frac{1}{2} m_P \frac{\rho}{\rho_P} \left(\frac{d u_i}{d t} - \frac{d u_{Pi}}{d t} \right) + m_P g_i \left(1 - \frac{\rho}{\rho_P} \right) + \\ & 1.615 D_P^2 \left(\frac{\rho \mu}{|\bar{\omega}_F|} \right)^{0.5} \{ \bar{\omega}_F \times (\bar{u} - \bar{u}_P) \} f(\text{Re}_P, \text{Re}_S) + \\ & \frac{\pi D_P^3}{6} \frac{\rho}{2 \text{Re}_R} \text{Re}_P C_{LR} \left[\left(\frac{1}{2} \nabla \times \bar{u} - \bar{\omega}_P \right) \times (\bar{u} - \bar{u}_P) \right] \end{aligned} \quad (5)$$

Here, x_{p_i} are the co-ordinates of the solid particle position, u_{p_i} are the velocity components, D_p is the solid particle diameter, and ρ_p is the solid particle density, $\vec{\omega}_F$ is the fluid rotation vector, $\vec{\omega}_p$ is the angular velocity vector, $f(Re_p, Re_s)$ is the ratio of the extended lift force to the Saffman force, Re_p is the particle Reynolds number, Re_s is the particle Reynolds number of the shear flow, Re_r is the Reynolds number of particle rotation and $C_{L,R}$ is the lift coefficient (for details see Sommerfeld 2000). The fluid acceleration terms are calculated as the derivative following the disperse element trajectory. The drag coefficient $C_{D,B}$ for the bubbles was calculated using the empirical correlation's for a fluid sphere, namely:

$$C_{D,B} = \begin{cases} 16 Re_B^{-1} & Re_B < 1.5 \\ 14.9 Re_B^{-0.78} & 1.5 < Re_B < 80 \\ 49.9 Re_B^{-1} (1 - 2.21 Re_B^{-0.5}) + 1.17 \cdot 10^{-8} Re_B^{2.615} & 80 < Re_B < 1530 \\ 2.61 & Re_B > 1530 \end{cases} \quad (6)$$

where $Re_B = \rho D_B |\vec{u} - \vec{u}_B| / \mu$ is the bubble Reynolds number. The drag coefficient for the solid particles is obtained from the following correlation's:

$$C_{D,p} = \begin{cases} 24 Re_p^{-1} (1 + 0.15 Re_p^{0.687}) & Re_p < 1000 \\ 0.44 & Re_p > 1000 \end{cases} \quad (7)$$

where $Re_p = \rho D_p |\vec{u} - \vec{u}_p| / \mu$ is the particle Reynolds number.

The instantaneous fluid velocity components at the disperse element location occurring in the equation of motion (Eqs. 3 and 5), are determined from the local mean fluid velocity interpolated from the neighboring grid points and a fluctuating component generated by the Langevin model (Sommerfeld et. al. 1993). In this model the fluctuation velocity is composed of a correlated part from the previous time step and a random component sampled from a Gaussian distribution function. The correlated part is calculated using the appropriate time and length scales of the turbulence from k- ϵ turbulence model. Additionally, a drift correction is imposed in order to avoid the spurious accumulation of bubbles in the regions of low turbulence.

The equations of motion for bubbles and particles are analytically integrated by assuming that all forces are constant during the Lagrangian time step Δt_L . The resulting equations are discretized and solved using a first order Euler method. The Lagrangian time step Δt_L is automatically adjusted during the trajectory calculation and must be smaller than 25% of the relevant time scales, such as, particle/bubble relaxation time integral time scale of turbulence obtained through

the Langevin model and collision time scale. As a solver for the disperse phases flow the code LAG 3D was used.

2.2 Interaction models

In three-phase upward flows bubbles are moving with much higher velocity than the particles, whereby the slip between bubbles and solid particles is relatively large. The difference in the density and the resulting buoyancy force is the main cause of such behavior. Hence, there will be a strong interaction and momentum transfer between the dispersed phases. The bubbles will drag the particles and the bubble rise will be hindered by the solid. In a first stage, this interaction was modeled by simply multiplying the drag coefficients by empirical correlations which depend on the volume fraction of the other phase, as done by Mitra-Majumdar et. al. (1997) in the frame of the continuum approach. Hence, the modified drag coefficient for bubble can be written as:

$$C'_{D,B} = \frac{C_{D,B}}{1 - \alpha_p^{0.3}} \quad (8)$$

This correction factor implies an increase of the bubble drag due to interactions with solid particles. In the same manner the drag coefficient for solid particles has been modified, which provides a reduction of particle drag since they are dragged by the bubbles:

$$C'_{D,P} = C_{D,P} (1 - \alpha_B^{0.06}) \quad (9)$$

Complementary, a direct interaction between bubbles and particles was modeled also by accounting for collisions, however initially only between bubbles and particles. For this purpose, the stochastic collision model proposed by Sommerfeld (2001) was applied. During the tracking of the bubbles, a fictitious solid particle was generated each time step with a velocity sampled from local distribution functions. The occurrence of a collision was determined from the collision probability according to kinetic theory of gases. The rebound velocity of the considered bubble was determined by accounting for a momentum loss expressed by a normal restitution coefficient e . Friction and rotation effects were neglected at this stage. When tracking the solid particles the fictitious collision partner was always a bubble. The collision calculation is identical as described above.

It should be emphasized, that both approaches most probably cannot capture the complete physics involved in the interaction between bubbles and particles. This interaction process should strongly depend on the size ratio of bubbles and particles. In practical situations particles are smaller than the bubbles, hence, there will be first an interaction through collisions with a certain impact probability. This implies that not all particle approaching the bubble will collide, rather they partly will move around the bubble with the relative flow. Additionally, particles smaller than the bubbles will accumulate in the wake of the bubbles and consequently will increase the added mass if their density is larger than that of the

liquid. The studies of Chen & Fan (1989) also demonstrated that a collision between particles and bubbles might result in bubble breakage. All the above describe effects could however not modeled in detail, due to the lack of basic experiments or direct numerical simulations. As a consequence, the proposed interaction modeling can only be regarded as a first attempt to calculate three-phase flows in bubble columns on the basis of the Euler/Lagrange approach.

2.3 Coupling between phases

Both the continuous and the dispersed phases were calculated in a time-dependent way in order to resolve temporal changes of the flow structure. The Eulerian time step was selected to be 0.4 s in the present cases and determines the temporal resolution of the flow field. The Lagrangian time step is usually much smaller (i.e. typically in the range 10^{-4} sec.) whereby a temporal and spatial averaging of the source terms is realized for each control volume. The computational procedure is summarized as follows:

- 1) The calculation starts with the solution of the fluid flow by not accounting for the source terms of the dispersed phase and assuming a very small upward liquid velocity. When a certain degree of convergence is reached this calculation is terminated.
- 2) The bubble and particle trajectories are calculated simultaneously up to a time level corresponding to that of the Eulerian part. During each Eulerian time step about 2000 bubbles and 500 particles are injected at the bottom. The bubble phase and solids phase source terms and properties (i.e. volume fraction and velocities) are evaluated for each control volume.
- 3) Further, the continuous phase is calculated (Eulerian calculation) for the next time level by accounting for the bubble phase source terms until a certain degree of convergence is reached. All of the present computations were of course performed with 100 % of coupling (i.e. under-relaxation should be not considered).
- 4) The bubble and solids tracking (Lagrangian part) is continued starting with the previously obtained bubble and solid locations and velocities. Each Lagrangian time step additional bubbles and solids are injected at the bottom of the column and bubbles reaching the top of the column are removed from the computations. The particle injection is of course terminated when the desired solids volume fraction is reached. The bubble phase and particulate phase source terms and properties are evaluated for each control volume.

The computational steps 3 and 4 are successively repeated until a desired time level in the quasi-steady regime is reached. Usually, a quasi-steady solution is reached after 50 to 70 seconds. The instantaneous properties of both phases are averaged only within an Eulerian time step. The time averaged properties are determined in accumulative way starting after the initial transient and terminating at the end of the computation.

Since the liquid flow in the bubble column is driven by the bubble rise and hindered by particles, the source terms due to the disperse phase are therefore extremely important. The influence of the bubbles and particles on the liquid is taken into account by appropriate source terms in the momentum and the k - and ε -equations. The source terms for both phases in the momentum equations are obtained for each control volume in the following way:

$$\overline{S_{U_i,D}} = -\frac{1}{V_{cv} \Delta t_E} \sum_k m_k N_k \sum_n \left\{ \left([u_{D_i}]_k^{n+1} - [u_{D_i}]_k^n \right) - g_i \left(1 - \frac{\rho}{\rho_D} \right) \Delta t_L \right\} \quad (10)$$

where the sum over n indicates averaging along the particle/bubble trajectory (time averaging) and the sum over k is related to the number of computational particle (i.e. bubbles or solids) passing the considered control volume with the volume V_{cv} , the index D means the disperse element (i.e. bubbles or solids). The mass of individual particle/bubbles is m_k and N_k is the number of real particles/bubbles in the computational particle. These terms are calculated from the change of the particle/bubble velocity along their trajectory within the considered control volume by subtracting the external field forces. Hence, the influence of all hydrodynamic forces acting on the particles/bubbles is accounted for.

The modification of the turbulence by bubbles and particles is additionally considered by appropriate source terms in the k - and ε -equation. In order to account for the turbulence generated by the wakes of the dispersed phase elements a Lagrangian Consistent Term was proposed recently which takes into account all forces acting on the particles (Lain et. al. 2002). For the individual dispersed phases this term is written as:

$$S_{kD,1} = \sum_{i=1}^3 \overline{u_{D_i} S_{U_i,D}} - U_i \overline{S_{U_i,D}} \quad (11)$$

A further term in the k -equation, which was proposed by Varaksin and Zaichik (2000) based on theoretical considerations, reflects the additional dissipation effect in case the dispersed phase elements are smaller than the integral scale of turbulence:

$$S_{kD,2} = -\frac{2 \alpha_D \rho_D k}{T_L (1 + \tau_p / T_L)} \quad (12)$$

Here α_D and ρ_D are the volume fraction and density of the respective dispersed phase, τ_D is the response time of particles or bubbles and T_L represents the Lagrangian integral time scale. In the case of large particles or bubbles ($\tau_D / T_L \gg 1$, $d_D / D_C \gg 1\%$, where D_C is the bubble column diameter) this term will be negligibly small.

The modeling of the analogous term in the ε -equation is performed in the standard manner, which assumes that it is proportional to S_{kD} and the Lagrangian turbulent characteristic time scale:

$$S_{\varepsilon D} = C_{\varepsilon 3} \frac{\varepsilon}{k} S_{kD} \quad (13)$$

where the value of the parameter $C_{\varepsilon 3}$ can depend on the size of dispersed phase elements and their volume fraction. Since this information is not available, all calculations presented in this paper have been performed with $C_{\varepsilon 3} = 1.87$.

3. Results of two- and three- phase flow calculations

The numerical calculations were performed according to experiments in a large-scale bubble column (Michele et. al. 2000). The bubble column diameter was 630 mm and the height 4400 mm (water level in the column). Measurements were performed for two- and three-phase flows with different volume fractions. The bubble size was about 8 mm and as solids PMMA-particles with a diameter of 3 mm and a density of 1190 kg/m^3 were used. Both were assumed to be mono-disperse in the computations. Unfortunately, only limited measurement data were available. The bubble column was discretized by a grid with 5 blocks and $10 \times 10 \times 70$ cells in both radial and the axial direction, respectively. Hence, the entire computational domain had about 35,000 control volumes. The boundary conditions employed for the continuous phase are:

- wall boundary conditions at the bottom and side wall,
- the free surface of the bubble column was specified as a symmetry condition.

The bubbles were injected just above the bottom of the bubble column over a cross-section with a diameter of 300 mm according to the experiments and the gas phase mass flux was assumed to be constant across the aerator. Several experimental conditions with different bubble and solids volume fraction were considered in the calculations.

The flow structure for a gas-liquid flow with a gas hold-up of 16 % is illustrated in Fig. 1 for two instants of time. The distribution of the gas volume fraction in the center plane of the column shows that the bubbles are mainly concentrated in the core of the column (Fig. 1a). This produces a flow pattern typically found in bubble columns with a strong upward motion of the liquid in the core and a downward flow near the wall (Fig. 1b). The temporal fluctuation of the gas volume fraction is clearly visible, while the liquid phase velocity field seems to have a less pronounced unsteadiness.

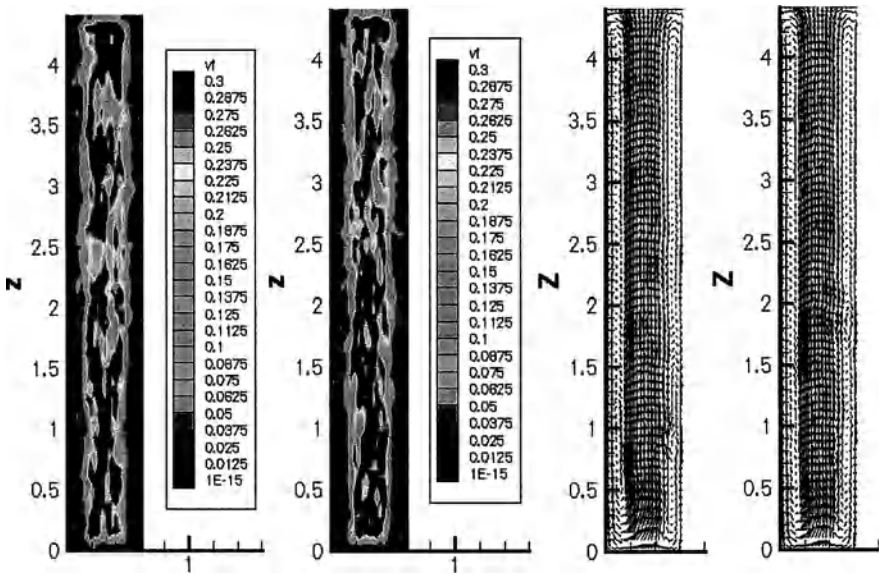


Fig. 1: Gas and liquid parameters from two-phase flow calculations (gas hold-up 16%, solids volume fraction 0%), (a) time series for bubble hold-up distribution (40 sec., 60 sec.), (b) vectors of instantaneous vertical velocity of fluid phase (40 sec., 60 sec.)

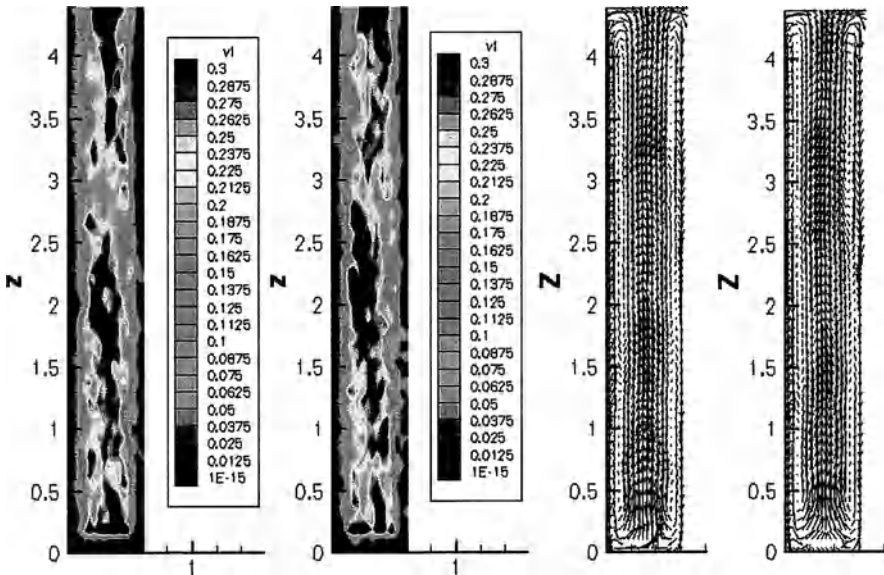


Fig. 2: Gas and liquid parameters from three-phase flow calculations (gas hold-up 16%, solids volume fraction 10%), (a) time series for bubble hold-up distribution (40 sec., 60 sec.), (b) vectors of instantaneous vertical velocity of fluid phase (40 sec., 60 sec.)

The temporal evolution of the flow structure for a three-phase flow (gas hold-up 16 % and overall solids volume fraction 10 %) shows somewhat stronger fluctuations as compared to the gas-liquid flow without solids (Fig. 2). These calculations were performed with the simple interaction terms described above. It is obvious that the bubbles are dispersed much better in the three-phase situation and the liquid velocity field shows lower upward and downward velocities compared to the two-phase flow. The temporal fluctuations are however similar in both cases.

An essential property for the performance of a three-phase bubble column is the distribution of the solids concentration. Due to the gravity acting on the solids they tend to settle, however are transported upward in the core of the column by the liquid flow. Moreover, the interaction of the particles with the bubbles causes an additional upward transport. This effect is illustrated by comparing the instantaneous solids concentration field without and with simple interaction terms, as well as by accounting for collisions between bubbles and particles (Fig. 3) at a time where a quasi-steady situation was reached. Without interaction modeling, the upward liquid flow cannot fully disperse the particles and they are concentrated in the lower half of the bubble column (Fig. 3 a). This is also obvious from the time-averaged solids volume fraction along the center line of the column (Fig. 4). In the upper half of the column the solids concentration is almost zero, whereas near the bottom a volume fraction up to about 35 % is reached. Please note that this high volume fraction of solids is not resolved in the contour plots (Fig. 3). These values are located within the area with $\alpha_s > 0.1$.

When the simple interaction terms or particle-bubble collisions are considered in the calculations, the particles are much better dispersed throughout the column (Fig. 3b and c). The vertical profiles of the time-averaged solids volume fraction however still show high values near the bottom. Between 0.5 and 2.0 m the solids volume fraction is almost constant and then gradually decrease towards the top of the column for both model calculations (Fig. 4). The measurements show an almost constant solids volume fraction along the column. In view of the gravitational settling of the solid particles this however seems not to be realistic and does not agree with other experimental studies (Chen et al. 1995) where a pronounced decrease of the solids volume fraction along the column was reported. As a result, the calculations with simple interaction terms or particle-bubble collisions compare fairly well with the measurements in the lower half of the column, whereas in the upper half the measured values are considerably above the calculated ones.

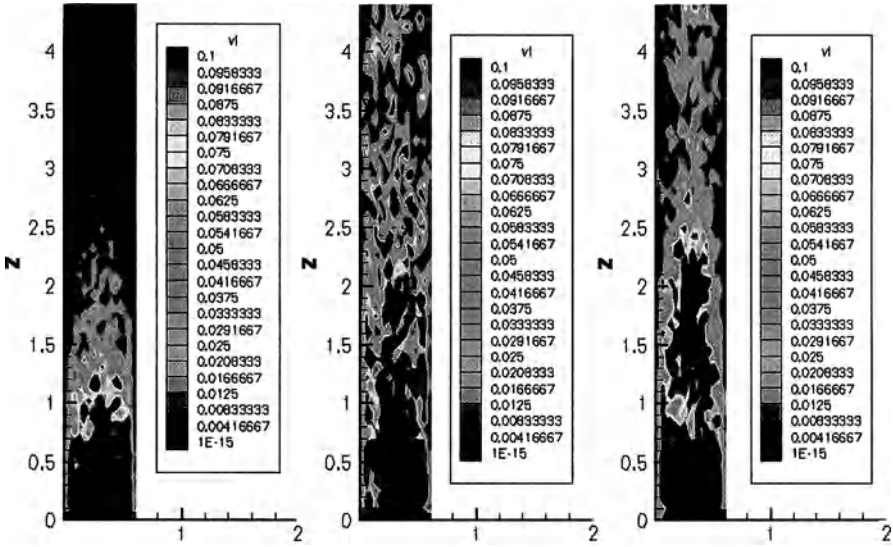


Fig. 3. Instantaneous distribution of the particulate phase volume fraction in the centre plane of the column after 60 sec. real time (gas hold-up 16%, solids volume fraction 10%), (a) without interaction between bubbles and solid, (b) with simple interaction between bubbles and solid, (c) with collisions between particles and bubbles with the coefficient of restitution $e=1.0$.

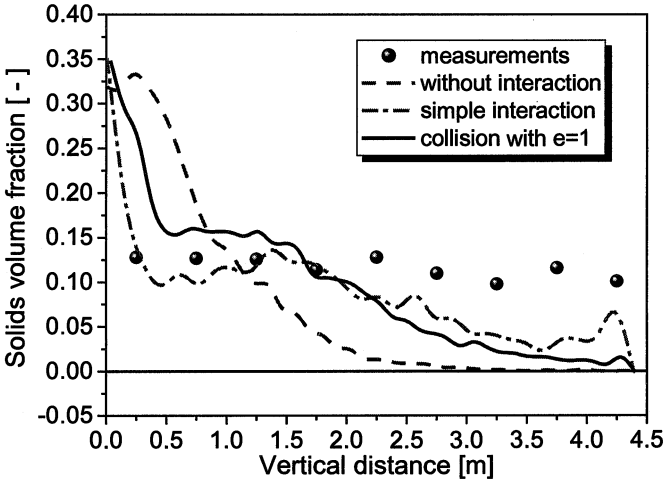


Fig. 4. Comparison between measured and predicted time-averaged solids volume fraction along the center-line of the column without and with interaction between bubbles and solids (gas hold-up 16%, solids volume fraction 10%)

The liquid phase velocity profiles of the vertical component measured 2.35 m above the aerator for a two- and three-phase flow are compared with the calculations in Fig. 5. In the bubbly flow without solids the calculations yield the highest upward and downward velocities similar to the experiments. The calculated liquid velocities for the three-phase flow without interaction terms show a drastic reduction in the core of the column compared to the two-phase flow. Also the magnitude of the downward velocity is reduced. This is caused by the momentum transfer between liquid and solid particles which are in this case only transported by the liquid phase. Accounting for a simple interaction between bubbles and particles, provides a dragging of the solids by the bubble rise. Hence, the solids are more homogeneously dispersed in the column, their upward velocity is increased, and the coupling with the liquid phase is reduced. Thereby, the liquid velocity in the core becomes again slightly higher than without interaction and the agreement with the velocity measurements is improved. The consideration of collisions between bubbles and particles with different restitution ratio ($e = 0.5$ and 1.0) yields similar profiles of the liquid velocity. Similar results were also obtained for the case with an averaged gas hold-up of 6 % and a solids volume fraction of 10 %.

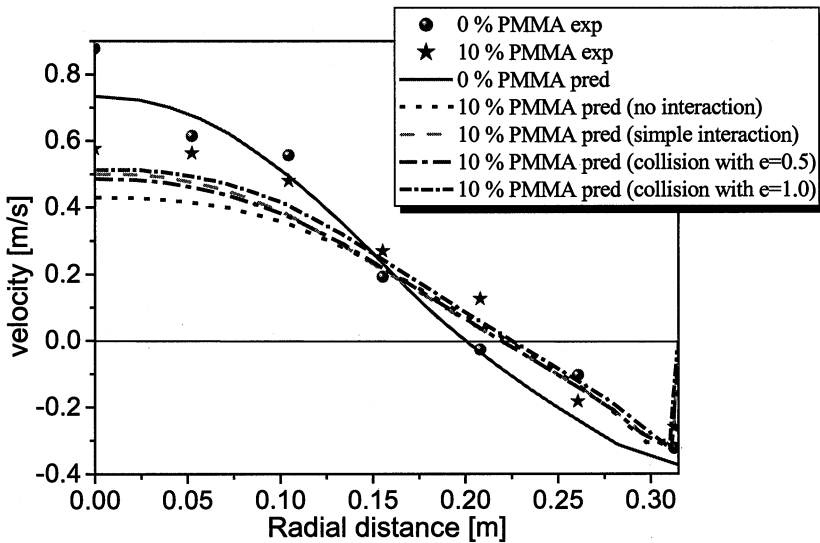


Fig. 5: Comparison of the time-averaged liquid velocity profiles at a height of 2.35 m above the aerator resulting from measurements and numerical calculations (gas hold-up 16%, solids volume fraction 10%).

In order to demonstrate eventually also the interaction between bubbles and particles, Fig. 6 shows profiles of the vertical mean velocity component of both dispersed phases for different model assumptions. The bubble velocity shows a strong upward motion in the core of the column and a downward motion near the walls, which has of course a lower magnitude than the liquid velocity (see Fig.

5). Similarly the particles are carried upward in the core of the column and move downward near the wall, of course with a higher velocity than the liquid when no interaction is taken into account in the calculations. Accounting for the interaction between particles and bubbles (i.e. simple interaction and collisions) causes only a slight reduction of the bubble velocities (Fig. 6 a).

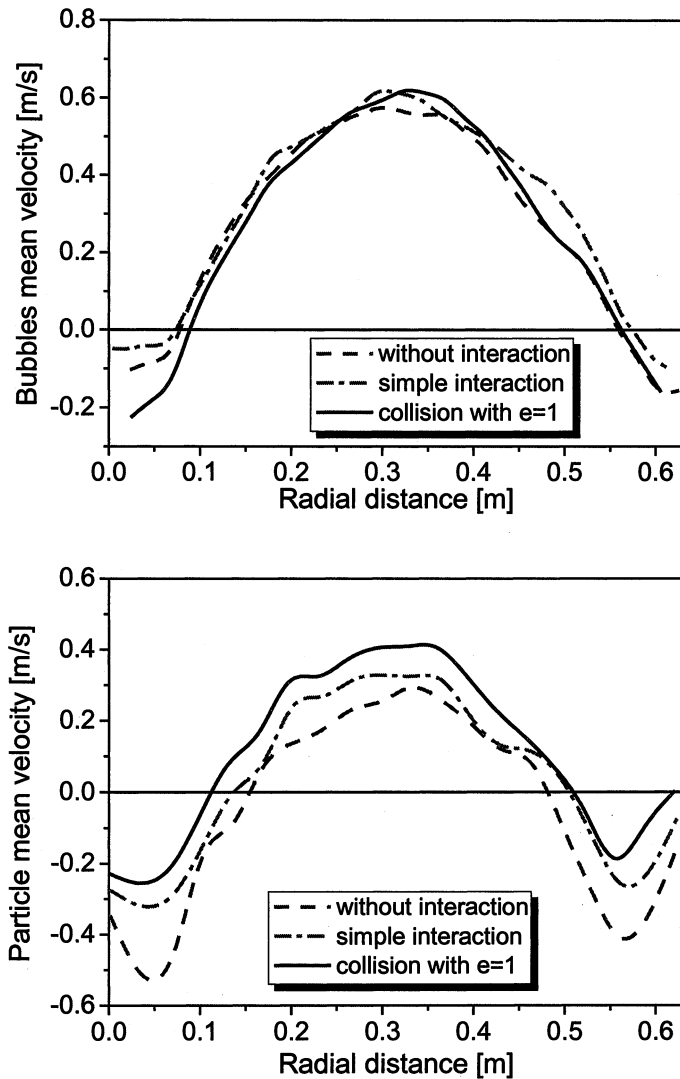


Fig. 6: Time-averaged profiles of bubble (a) and particle (b) velocities at a height of 2.35 m above the aerator, comparison of calculations without interaction, simple interaction and collisions between particles and bubbles (gas hold-up 16%, solids volume fraction 10%).

The dragging of the particles by the bubbles is very pronounced for both interaction models, yielding an increased particle velocity in the core and a reduction of the magnitude of the downward velocity (Fig. 6 b). The collision model with $e = 1.0$ results in the strongest modification compared to a calculation without interaction. Moreover, it can be observed that the region of particle downward motion is decreased when accounting for particle-bubble interaction.

CONCLUSIONS

The Euler/Lagrange approach was extended to allow time-dependent numerical calculations of three-phase flows (i.e. gas-liquid-solid) in a pilot-scale bubble column. Calculations for realistic dispersed phase volume fractions was possible by incorporating the effective fluid density in the continuous phase conservation equations and solving the flow in a time-dependent way. Moreover, source terms due to the dispersed phase were included in the momentum equations and the conservation equations for the turbulence properties, also accounting for wake induced turbulence modulation. Bubble and particle motion was calculated by considering all relevant forces. Results were presented for up to 16% gas hold-up and 10% solids volume fraction.

The calculated liquid velocity was found to be in a good agreement with measurements in the two-phase flow (i.e. gas hold-up 16%). When introducing the third phase however, the liquid phase velocity was considerably under-predicted due to the effect of gravity and the resulting low solids velocity. This introduces a strong reduction of liquid velocity due to two-way coupling and as a result the particles were concentrated in the lower half of the column. Therefore, simplified modified drag coefficients were incorporated for describing an interaction between bubbles and particles. By this, the particles were dragged by the bubbles and hence were somewhat better dispersed throughout the column. Since the solids upward velocity is increased the two-way coupling reduces, whereby the liquid upward velocity again increases. Hence, the applied simple interaction model already gave a better agreement with measured liquid velocities in the three-phase flow. The description of the interaction by collisions between bubbles and particles provided a similar concentration distribution along the column. The measured constant solids concentration along the center-line of the column was not predicted and seems to be unphysical, since it does not show the effect of gravitational settling. The liquid velocity profile obtained with the collision model was similar to that obtained with the simple interaction terms. Finally, the comparison of the velocity profiles of bubbles and particles showed clearly the dragging effect of the particles by the bubbles. This was most pronounced for the calculations with bubble-particle collisions.

For further improving the modeling of three-phase flows, a combined hydrodynamic interaction and collision model should be considered, since this will describe the physics more realistic. However, such model development requires

also detailed experiments on the interaction of bubbles and particles, preferably using imaging techniques.

ACKNOWLEDGEMENTS

The research project is financially supported by the Deutsche Forschungsgemeinschaft. This support under contract number So 204/20-1 is gratefully acknowledged.

REFERENCES

Birtigh A., Lauschke G., Schierholz W.F., Beck D., Maul Ch., Gilbert N, Wagner H.G. and Werninger C.Y. CFD in der chemischen Verfahrenstechnik aus industrieller Sicht. *Chemie Ingenieur Technik*, 72, 175-193 (2000).

Bourloutski E. and Sommerfeld M. Parameter studies on the effect of boundary conditions in the three-dimensional calculations of bubble columns. Proc. of ASME FEDSM'02, Montreal (Canada), July 14-18 2002.

Chen, Y.-M. and Fan, L.-S. Bubble breakage mechanisms due to collision with a particle in a liquid medium. *Chem. Eng. Sci.* 44, 117-132 (1989)

Chen Z., Zheng C., Feng Y. and Hoffmann H. Distributions of flow regimes and phase hold-ups in three-phase fluidized beds. *Chem. Eng. Science*, 50, 2153-2159 (1995).

Crowe C.T. On models for turbulence modulation in fluid- particle flows. *Int. J. Multiphase Flow*, 26, 719-727 (2000).

Lain S., Bröder D. and Sommerfeld M. Numerical simulation of the hydrodynamics in a bubble column: quantitative comparisons with experiments. Proc. of 4th Int. Conf. On Multiphase Flow, New Orleans (USA), May 27- June 1 2001.

Lain S., Bröder D., Sommerfeld M. and M.F. Göz. Modelling hydrodynamics and turbulence in a bubble column using the Euler-Lagrange procedure. Accepted for publication in: *Int. J. Multiphase Flow* (2002).

Lauder B.E., and Spalding D.B. The numerical computation of turbulent flows. *Comp. Meth. Appl. Mech. and Eng.*, 3, 269-289 (1974).

Michele V., Dziallas H., Hempel D.C. Measurement and modelling of local phase hold-up and flow structure in three phase bubble columns. Proc. of the ICHMT Int. Symp. on Multiphase Flow and Transport Phenomena, Antalya (Turkey), November 5 - 10, 2000.

Mitra-Majumdar D, Farouk B. and Shah Y.T. Hydrodynamic modelling of three phase flows through a vertical column. *Chem. Eng. Science*, 52, 4485-4497 (1997).

Ohkawa W. M., Maezawa A. and Uchida S. Flow structure and phase distributions in a slurry bubble column. *Chem. Eng. Science*, 52, 21-22 (1997).

Smith D.N. and Ruether J.A. Dispersed solid dynamics in a slurry bubble column. *Chem. Eng. Science*, 40, 741-754 (1985).

Smith D.N. and Ruether J.A., Shah Y.T. and Badgajar M.N. Modified sedimentation- dispersion model for solids in a three-phase slurry column. *AIChE Journal*, 32, 426-436 (1986).

Sommerfeld M., Kohnen G. and Rüger M. Some open questions and inconsistencies of Lagrangian particle dispersion models. 9th Symp. on Turbulent Shear Flows, Kyoto, Aug. 1993, Paper 15.1.

Sommerfeld M. Theoretical and experimental modelling of particulate flow: Overview and fundamentals. Von Karman Institute for Fluid Mechanics, Rhode Saint Genese, Belgium, Lecture Series No. 2000-6, 1-62 (2000).

Sommerfeld M. Validation of a Lagrangian modelling approach for inter-particle collisions in homogeneous isotropic turbulence. *Int. J. of Multiphase Flows*, 27, 1828-1858 (2001).

Tsutsumi A., Charinpanitkul T and Yoshida K. Prediction of solid concentration profiles in three-phase reactors by wake shedding model. *Chem. Eng. Science*, 47, 13-14 (1992).

Varaksin A.Y., Zaichik L.I. Effect of particles on the carrier flow turbulence. *Thermophysics and Aeromechanics*, 7, 237-248 (2000).

Local Parameters of Three-Phase Flow in Column Reactors with High Disperse Phase Hold-Up

Jan H. Enß, Jörg Schallenberg, Volker Michele, Holger Dziallas,
Dietmar C. Hempel

Institute of Biochemical Engineering
Technical University of Braunschweig

Introduction

Multiphase flows are widely-used in various applications in the chemical and biochemical industry. Bubble columns offer a simple design for all tasks where an intensive contact between a liquid and a gas phase is needed, but they are also able to fluidize particles and operate with a comparatively low energy input. Despite these advantages little is known about local parameters of three-phase bubble columns in pilot plant or industrial scale with high disperse phase hold-ups. So scale-up of these reactors is still based on empirical correlations.

Due to the incapability of optical non-invasive measurement systems, like laser- or phase-doppler-anemometry (LDA / PDA), to penetrate flows with high disperse phase hold-ups deep enough to provide reasonable results from the inner parts of pilot size plants, invasive measurement probes were used for this work. Differential pressure measurement (DPM), electrical conductivity measurement (ECM) and time domain reflectometry (TDR) were used for measuring local phase hold-ups in two- and three phase flows in a pilot plant bubble column (Dziallas et al. 2000). The electro diffusion measurement (EDM) delivers insight into the liquid flow field (Michele and Hempel 2002).

All data acquired by these methods were used to verify and improve a CFD-simulation of the flow structure in the bubble column. With the commercial CFD-program CFX calculations has been carried the Eulerian-Eulerian-approach. The turbulence in the liquid phase is described using the k - ϵ -model. An additional momentum exchange term between the gas and the liquid phase has been added to achieve a good agreement between the measured and the computed dispersed phase distribution (Michele and Hempel 2002).

Experiments and calculations show a worse fluidization of the solid phase containing PMMA-particles with increasing superficial gas velocity. The measured gas distribution and the values for the axial liquid velocity and the fluctuational liquid velocity can explain this surprising behaviour (Enss et al. 2002).

Experimental Setup

Bubble Column

The measurements of the phase distributions and liquid velocity were carried out at an aspect ratio of water level to diameter of $H_l/d_i = 7$ in a Plexiglass bubble column, with an inner diameter of $d_i = 630$ mm and a total height of $H = 6$ m that is shown in **fig. 1**. The measuring ports have an axial distance of 500 mm starting 350 mm over the sparger. There are seven radial measuring points beginning at the column axis with a distance of 50 mm. The superficial gas velocities were between 0.02 m s^{-1} and 0.09 m s^{-1} . As gas spargers a perforated plate with 335 holes with a diameter of 1 mm, a ring with 12 nozzles with a diameter of 4 mm on a circle with the radius of 225 mm and a central nozzle with a diameter of 22 mm is used.

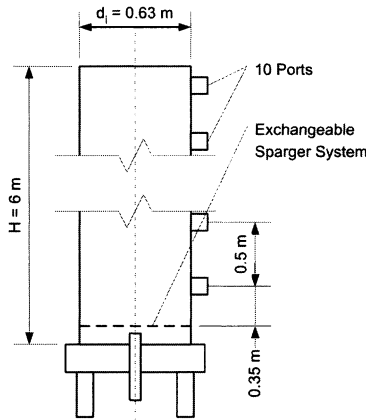


Fig. 1. Pilot plant size bubble column with exchangeable sparger system and probe ports for invasive measurement devices

As liquid phase a 0.01-molar solution of K_2SO_4 in deionized water is used, the gas phase is compressed air and as solid phase plastics granules of polymethylmethacrylate (PMMA) and polyoxymethylene (POM) are used. The PMMA-particles have a cubic shape and a density of $\rho_{\text{PMMA}} = 1200 \text{ kg m}^{-3}$, the POM-particles have an ellipsoidal shape and a density of $\rho_{\text{POM}} = 1400 \text{ kg m}^{-3}$. Both plastics granules particles have an equivalent volume diameter of 3.1 mm.

Measurement Techniques

For measuring the local disperse phase hold-up in three-phase flows two independent measuring principles has to be applied. Two different kinds of probes that allow the application in multiphase flow with high disperse phase content had to be combined in one device. A probe was designed that combines differential pressure measurement (DPM) with time domain reflectometry (TDR) and electrical conductivity measurement (ECM) respectively (fig. 2).

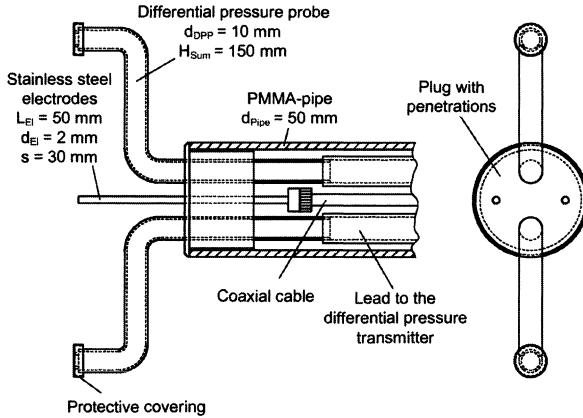


Fig. 2. Schematically view of phase hold-up measurement device

Between the two probes the differential pressure is defined by the density of the medium in between, according to the equation for the hydrostatic pressure difference

$$\Delta p_{meas} = (\rho_s \cdot \varepsilon_s + \rho_g \cdot \varepsilon_g + \rho_l \cdot \varepsilon_l) \cdot g \cdot H_{Sum} \quad (1)$$

For TDR-measurement a high-frequency electromagnetic pulse is sent into the examined system and the reflected energy is measured depending on the running time of the pulse. The electromagnetic pulse induces a circular electromagnetic field around the stainless steel bar electrodes that are used with a distance of $s = 30$ mm in the sensing probe (fig. 2). The running time of the pulse that is reflected at the end of the electrodes is depending on the dielectric surrounding the electrodes. A linear relationship between the relative changes of the running time caused by a disperse phase

$$\varphi = \frac{\Delta t_{0,l} - \Delta t}{\Delta t_{0,l}} \quad (2)$$

and the volumetric phase hold-up of the disperse gas or solid phase was found. A calibration of the electrodes in the two-phase systems water-gas and water-solid leads to the linear relationships:

$$\begin{aligned}\varepsilon_g &= a_{TDR,g} \cdot \varphi_g \\ \varepsilon_s &= a_{TDR,s} \cdot \varphi_s\end{aligned}\tag{3}$$

Using the ECM works in analogy to the TDR instead of the relative change of the impulse running time the relative change of the electrical conductivity depending on the disperse phase hold-up is measured. A calibration of the ECM in the two-phase systems water-gas and water-solid is also needed resulting in equations similar to Eqs. (2) and (3). Combining the Eqs. (1) and (3) yield a system of equations that allow to determine the phase hold-up of both disperse phases in a three-phase flow (Dziallas et al. 2000).

Measurements of the liquid flow field have been carried out with the electro diffusion measurement (EDM). The measurement principle is based on oxygen and hydroxide mass transfer at the probe surface being influenced by the liquid velocity close to the surface. Increasing velocities yields a decreasing boundary layer thickness at the electrode surface, leading to an increased mass transfer and subsequently increased electric current at constant voltage. After a calibration it is possible to determine the value and direction of the liquid flow velocity in a layer perpendicular to the probe (Onken and Hainke 1999, John et al. 2000). The used EDM probes were provided by the Institute of Environmental Process Engineering in Bremen.

CFD Modelling

In multiphase CFD two general approaches have gained large importance and practical relevance in the past years. The Eulerian-Lagrangian approach assumes the dispersed phase to consist of representative particles transported with the continuous phase. A set of Navier-Stokes equations is solved only for the continuous phase. The Eulerian-Eulerian approach assumes the dispersed and the continuous phases to be interpenetrating continua, for both of which a complete set of Navier-Stokes equations has to be solved. Coupling between the motion of the dispersed and the continuous phase is achieved by implementing momentum exchange terms into the respective phases momentum balance equations.

For the CFD calculations performed as part of this project, the Eulerian-Eulerian approach has been chosen because of its obvious computational advantages at high dispersed phase contents: While in Eulerian-Lagrangian computations the computational effort grows with increasing dispersed phase hold-up, since more particles have to be tracked, it remains constant in Eulerian-Eulerian multi-fluid calculations. With the high solid (up to 10 vol.-%) and gas (up to 20 vol.-%) hold-ups encountered in the context of this project, an Eulerian-Lagrangian calculation would yield to high computational demand.

For each of the phases the volume-averaged mass and momentum conservation equations in the Eulerian framework are given by:

$$\frac{\partial}{\partial t}(\rho_\alpha \varepsilon_\alpha) + \nabla \cdot (\rho_\alpha \varepsilon_\alpha \mathbf{u}_\alpha) = 0 \quad (4)$$

$$\begin{aligned} \frac{\partial}{\partial t}(\rho_\alpha \varepsilon_\alpha \mathbf{u}_\alpha) + \nabla \bullet (\varepsilon_\alpha (\rho_\alpha \mathbf{u}_\alpha \mathbf{u}_\alpha)) \\ = \varepsilon_\alpha \nabla p_\alpha + \nabla \bullet (\varepsilon_\alpha \mu_\alpha (\nabla \mathbf{u}_\alpha + (\nabla \mathbf{u}_\alpha)^T)) + \rho_\alpha \mathbf{g} + \mathbf{M}_{\alpha,\beta} \end{aligned} \quad (5)$$

Gas and liquid viscosity in the above equations are given by their actual values for the local temperature and pressure or (in the liquid case) are modified to account for turbulence effects using the standard k - ε model. Solid viscosity is basically a fitting parameter and has been set constant to the value of water (10^{-3} Pa s⁻¹).

Transient calculations have been performed on a three-dimensional grid since two-dimensional and steady-state calculations did not yield reasonable results; this observation is in agreement with experiences reported by other workgroups (Pfleger et al. 1999). Gravity terms have to be included into the momentum balances as well as compressibility effects for the gas phase to obtain correct local phase distributions. Compressibility has been implemented by means of the ideal gas law.

Liquid phase turbulence has been included using the standard k - ε model with standard single phase parameters. As a two-equation turbulence model, the k - ε model introduces two additional variables into the calculations, namely the turbulent kinetic energy k and the turbulent dissipation rate ε . The applicability of the k - ε model for bubble columns has been considered (Sokolichin and Eigenberger 1999). The k - ε model as implemented here does not account for bubble- or particle-induced turbulence. The dispersed gas and solid phases themselves are computed as laminar.

Interaction of dispersed and continuous phases is implemented by introducing momentum exchange terms into the respective balance equations. For the interaction of the continuous liquid phase and the dispersed gas and solid phases respectively, drag law considerations give the momentum exchange terms in Eq. (5) the following appearance:

$$\mathbf{M}_{\alpha,\beta} = \frac{3}{4} \frac{C_D}{d_p} \varepsilon_\beta \rho_\alpha |\mathbf{u}_\beta - \mathbf{u}_\alpha| (\mathbf{u}_\beta - \mathbf{u}_\alpha) \quad (6)$$

For the determination of the drag coefficient C_D in Eq. (6), correlations are available for the flow regime corresponding to the particle Reynolds number; for a survey of correlations see Clift et al. 1978. For the PMMA particles as used in this project, the viscous flow regime correlation is valid (assuming particles are spherical):

$$C_D = \frac{24}{\text{Re}} (1 + 0.1 \text{Re}^{0.75}) \quad (7)$$

In all calculations presented here, the bubbles are assumed as rigid and spherical having a constant diameter of 8 mm. Effects like bubble size distribution, swarm behaviour or bubble deformability are not under consideration in this project. Due to their higher Reynolds numbers, the bubbles fall into the range of the Newtonian flow regime where the drag coefficient becomes constant:

$$C_D = \text{constant} = 0.44 \quad (8)$$

In order to correctly model solid fluidization, direct interactions between the dispersed gas and solid phases have to be considered as well. As part of this project, several approaches for direct gas-solid momentum transfer have been tested; best results were obtained by implementing a modified drag law model (Padiál et al. 2000). In this model, the momentum balances eq. (5) for the gas and the solid phase are extended by the following momentum exchange term (Michele and Hempel 2002):

$$\mathbf{M}_{g,s} = \frac{3}{4} \frac{c_{g,s}}{d_p} \varepsilon_s \rho_g \underbrace{\left| \mathbf{u}_s - \mathbf{u}_g \right|}_{u_{slip,g,s}} \left(\mathbf{u}_s - \mathbf{u}_g \right) \quad (9)$$

Particle diameter d_p was set to a fixed value of 3 mm, gas density ρ_g for technical reasons had to be set constant to 1.22 kg m^{-3} . The combination of $c_{g,s} u_{slip,g,s}$ was used as fitting parameter; its value was determined by fitting modelling results to measured local solid hold-up distributions (Dziallas 2000, Dziallas et al. 2000) and was set constant to 118 m s^{-1} during all calculations carried out with this model. This value may not be considered as a real physical settling velocity but is merely a fitting parameter.

In order to numerically solve the system of partial and ordinary differential equations presented above, discretization of the equations has been carried out using a finite volume scheme with an algebraic multigrid solver (AMG) as implemented in the CFD code CFX. Due to the large dimensions of the flow domain under consideration (bubble column height 5.0 m, diameter 0.63 m), the need for transient and three-dimensional calculations and due to limited computational resources, a very coarse numerical grid had to be implemented with an average grid cell edge length of 0.059 m corresponding to a total number of 13,600 cells. Time step width was chosen as 0.4 s. Calculations always assumed fully-fluidized state as an initial condition.

Parameter variations for the computations were similar to those with the measurements, i.e. superficial gas velocity was varied between 0.02 and 0.09 m s^{-1} , solid loading ranged between 0 and 10 vol.-% (solid density was 1200 kg m^{-3}).

Results and Discussion

Gas Hold-Up

Fig. 3 shows the measured local gas hold-up in the bubble column with the plate sparger for five superficial gas velocities at an integral solid loading of 10 vol.-% PMMA particles. At $u_g = 0.02 \text{ m s}^{-1}$ homogeneous flow regime can be found, there is almost no dependency of gas hold-up from the radial position only a slight increase with a rising axial position can be observed. With higher superficial gas velocities this axial gradient of gas hold-up becomes stronger and a partly very steep radial gradient with a maximum of gas in the reactor centre appears. The flow regime is heterogeneous ($u_g \geq 0.04 \text{ m s}^{-1}$).

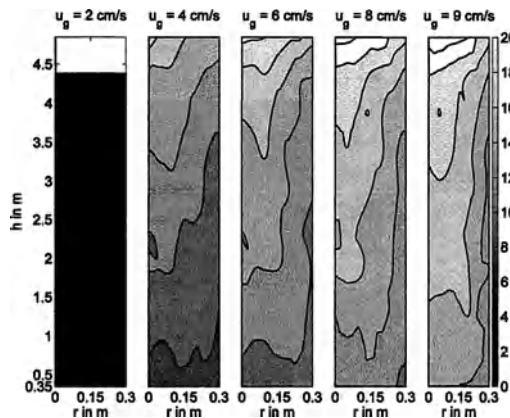


Fig. 3. Measured local gas hold-up at different superficial gas velocities (10 vol.-% PMMA, plate sparger), displayed is always a half cross-section

Measurements with the other spargers show that in the lower part of the column the gas profiles are different up to $H/d_i \approx 4$ depending on the sparger geometry whereas a similar radial gas profile can be found above this height for all sparger systems. While an increasing solid hold-up causes a decreasing gas hold-up the form of the profiles stays constant.

Solid Hold-Up

For $u_g = 0.02 \text{ m s}^{-1}$ and the usage of the particles with the lower density ($\rho_{PMMA} = 1200 \text{ kg m}^{-3}$) and a plate sparger a homogeneous fluidisation can be observed (see fig. 4). This can be explained by the low density difference between water and the particles. With increasing superficial gas velocity ($u_g \geq 0.04 \text{ m s}^{-1}$) the solid distri-

bution becomes more heterogeneously. At first an axial gradient with an accumulation of particles near the reactor bottom can be found for even higher superficial gas velocities ($u_g \geq 0.06 \text{ m s}^{-1}$). An additional radial gradient appears showing deterioration of particles at the wall regions. At a superficial gas velocity of $u_g = 0.09 \text{ m s}^{-1}$ there are almost solid free regions at the upper outer parts of the reactor.

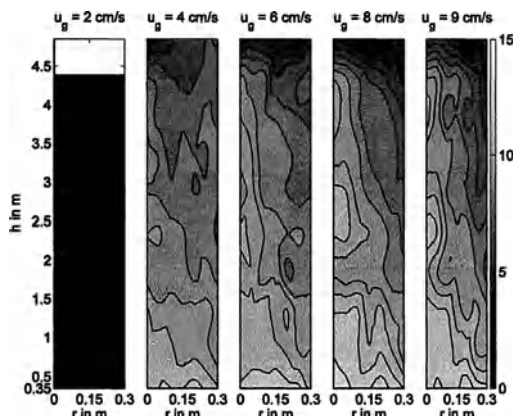


Fig. 4. Measured local solid hold-up at different superficial gas velocities (10 vol.-% PMMA, plate sparger), displayed is always a half cross-section

The same effects can be found for lower concentrations of the same particles or when using the ring sparger, but a central jet nozzle as sparger is unsuitable for solid fluidisation. If the particles with higher density ($\rho_{POM} = 1400 \text{ kg m}^{-3}$) are used the result is completely different. For low superficial gas velocity no solid fluidisation occurs at all, only for high superficial gas velocities ($u_g \geq 0.08 \text{ m s}^{-1}$) very few particles are dispersed; a homogenous distribution is not reached within the examined superficial gas velocities.

CFD Results

Experience in modelling three-phase flows in bubble columns shows that an implementation of the interaction between the dispersed gas and solid phases is of vital importance in order to obtain reasonable agreement between measured and computed solid fluidisation. **Fig. 5** shows the local solid hold-ups for superficial gas velocities between 0.02 and 0.09 m s^{-1} computed for a bubble column equipped with a plate sparger and operated at a solid loading of 10 vol.-% (solid density 1200 kg m^{-3} , like PMMA).

In **fig. 5** it can be seen that the computed fluidisation is like the measured (**fig. 4**). The solid distribution inside the reactor is almost homogenous, even at the

lowest superficial gas velocity of 0.02 m s^{-1} . Also in good agreement with the experimental results is the fact that with increasing superficial gas velocity, the solid distribution homogeneity deteriorates significant. Solid are transported to the reactor bottom and a large region is developing at the upper reactor edge without solids. Asymmetry in the hold-up images is due to the insufficient averaging time during calculations.

The large bubbles occurring with increasing superficial gas velocity are accounted for a higher liquid centre line velocity and accumulation of the solid in the reactor centre. Due to the direct interaction between the gas and the solid phase the large bubbles in the middle of the reactor carry along the particles with them. This yields to a higher concentration of the solid phase in the centre of the bubble column up to a height of 4 m above the sparger. In the higher regions of the reactor the fluidisation of the particles deteriorates due to the high gas hold-ups. So the particles tend towards the wall and are slumped due to the increasing downwards vectored liquid flow.

Still, the fact that the complex interactions leading to the fluidisation effects observed during the measurements can be captured by the rather simple momentum exchange model as given in Eq. (9) is a good confirmation for the validity of this general modelling approach.

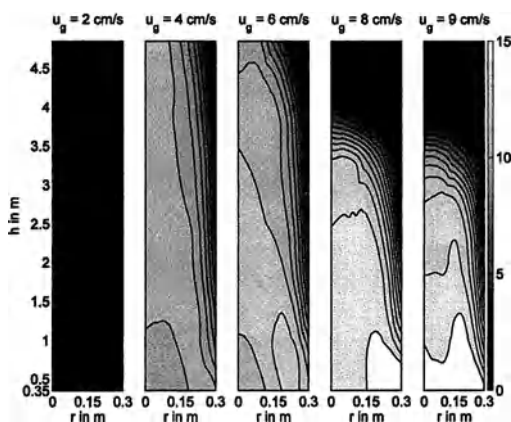


Fig. 5. Computed local solid hold-up at different superficial gas velocities (10 vol.-% PMMA, plate sparger), displayed is always a half cross-section

Liquid Velocities

In **fig. 6** the measured axial liquid velocities are shown for the two-phase flow compared with the three-phase flow with 10 vol.-% PMMA particles. The radial profile over the reactor radius is clearly visible. According to the gas hold-up profiles the axial liquid velocity profiles are defined by the sparger geometry in the

lower part of the reactor. In the upper regions of the column always radial profiles like the ones in fig. 6 can be observed. The values of the velocities are depending on the sparger geometry.

In the three-phase flow the profiles are somewhat flatter than in the two-phase flow. Big bubbles rising in the centre of the reactor causing these very high centre-line velocities in two-phase flows are suppressed in three-phase flows, which yield in flatter velocity profiles in three-phase flows. Generally the velocities in two-phase flows reach about twice the values than in three-phase flows with 10 vol.-% solid loading, which can be explained with additional energy that is needed for fluidisation of the particles.

In two-phase flows at superficial gas velocities of $u_g \geq 0.06 \text{ m s}^{-1}$ and in three-phase flows at $u_g \geq 0.04 \text{ m s}^{-1}$ additional energy input does not yield in further increase of the mean axial liquid velocity but only in higher turbulence intensity.

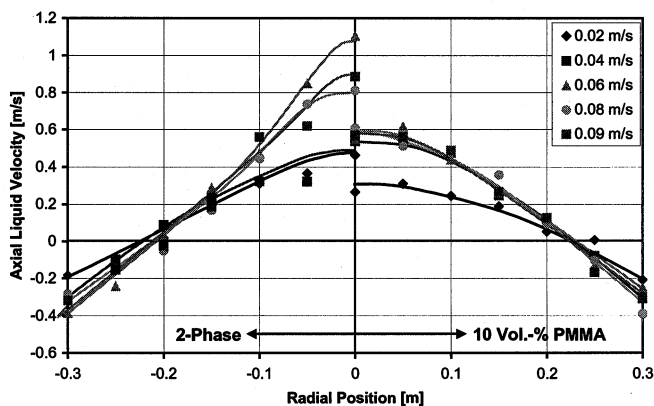


Fig. 6. Axial liquid velocity measured 2.35 m above plate sparger and five different superficial gas velocities for 0 and 10 vol.-% solid loading (PMMA)

Conclusions

A new constructed invasive phase hold-up probe allows determining the local phase hold-ups in three-phase flows with industrial used high disperse phase contents even in pilot plant size reactors. Together with so also invasive liquid velocity probe valuable measurement data has been gained that help understanding the highly turbulent and transient flow structure in bubble columns.

Adding a solid phase shows a lot of interesting effects on the flow structure in bubble column like the decreasing liquid velocities but first of all the tendency of worse particle fluidisation at higher energy input. The influence of the sparger geometry on liquid velocities and local phase hold-ups are restricted to the lower region of the bubble column. But there is still plenty unknown like the unenlightened interactions between a solid phase and both of the other phases. There also

many parameters of solid particles whose influence on the flow are yet unknown, like particle density, size, or form.

Adding an additional interaction term between the gas and the solid phase into the momentum exchange in the CFD model enhanced the computational result a lot. Even with low computing power qualitative and quantitative good agreement between measured and computed local phase distribution has been reached. The effects of the still not fully clarified direct interactions between a solid phase and the gas phase are reproduced by the model.

Notation

$a_{TDR,g}$	-	time domain reflectometry calibration coefficient for the system liquid-gas
$a_{TDR,s}$	-	time domain reflectometry calibration coefficient for the system liquid-solid
$c_{g,s}$	-	constant for direct dispersed phase interaction model
C_D	-	drag coefficient
ECM	-	electrical conductivity measurement
EDM	-	electro diffusion measurement
DPM	-	differential pressure measurement
D_{DPM}	m	diameter of the differential pressure probe
d_{El}	m	diameter of the steel electrodes
d_i	m	inner diameter of the bubble column
d_P	m	particle diameter
d_{Pipe}	m	diameter of the phase hold-up measurement device
\mathbf{g}	m s^{-2}	gravitational acceleration (as a vector)
H	m	height of the bubble column
H_l	m	liquid height
H_{Sum}	m	axial difference between the differential pressure measurement orifices
L_{El}	m	length of the steel electrodes
$\mathbf{M}_{\alpha,\beta}$	N m^{-3}	momentum interphase transfer term (as a vector)
p	Pa	pressure
Δp_{meas}	Pa	measured hydrostatic pressure difference
Re	-	Reynolds number
s	m	distance between the steel electrodes
TDR	-	time domain reflectometry
Δt	s	running time of the electromagnetic pulse in the multi-phase system
$\Delta t_{0,l}$	s	running time of the electromagnetic pulse in the liquid phase
\mathbf{u}_α	m s^{-1}	velocity of phase α (as a vector)
u_g	m s^{-1}	superficial gas velocity

$u_{slip,g,s}$	m s^{-1}	slip velocity between gas and solid phase
ε_α	-	volume fraction of phase α
ε_g	-	local gas hold-up
ε_l	-	local liquid volume fraction
ε_s	-	local solid hold-up
μ_α	Pa s	effective dynamic viscosity of phase α
φ	-	relative change of the running time of the electromagnetic pulse
φ_g	-	relative change of the running time of the electromagnetic pulse caused by the gas phase
φ_s	-	relative change of the running time of the electromagnetic pulse caused by the solid phase
ρ_α	kg m^{-3}	density of phase α
ρ_g	kg m^{-3}	density of gas phase
ρ_l	kg m^{-3}	density of liquid phase
ρ_{PMMA}	kg m^{-3}	density of polymethylmethacrylate
ρ_{POM}	kg m^{-3}	density of polyoxymethylene
ρ_s	kg m^{-3}	density of solid phase

References

- Clift R, Grace JR, Weber ME (1978) Bubbles, Drops and Particles. Academic Press, New York
- Dziallas H (2000) Lokale Phasengehalte in zwei- und dreiphasig betriebenen Blasensäulenreaktoren Ph.D. thesis, Technical University of Braunschweig, in Hempel DC (Ed.): *ibvt-Schriftenreihe*, Vol. 10, FIT-Verlag, Paderborn 2000
- Dziallas H, Michele V, Hemperl DC (2000) Measurement of Local Phase Holdups in a Two- and Three-Phase Bubble Column. *Chem. Eng. Technol.* 23:877-884
- Enss JH, Schallenberg J, Michele V, Hempel DC (2002) Messung und Modellierung von Strömungsstrukturen und Phasengehalten bei dreiphasigen Strömungen in Blasensäulenreaktoren. *Chem. Ing. Tech.* 74: 1326-1331
- John S, Parchmann H, Rübiger N (2000) Messung hydrodynamischer Parameter in Mehrphasenströmungen bei hohen Dispersphasengehalten mit Hilfe der Elektrodiffraktionsmesstechnik (EDM). Tagungsband der AICHEM 2000, 22.-27.05.00 Frankfurt a.M.
- Michele V (2002) CFD Modeling and Measurement of Liquid Flow Structure and Phase Holdup in Two- and Three-Phase Bubble Columns. Ph.D. thesis, Technical University of Braunschweig, in Hempel DC (Ed.): *ibvt-Schriftenreihe*, Vol. 13, FIT-Verlag, Paderborn 2002
- Michele V, Hempel DC (2002) Liquid Flow and Phase Holdup—Measurement and CFD Modeling for Two- and Three-Phase Bubble Columns. *Chem. Eng. Sci.* 57:1899-1908
- Onken U, Hainke M (1999) Measurement of Hydrodynamics and Dissolved Oxygen with a Polarographic Microelectrode. *Chem. Eng. Technol.* 22:767-772

- Padial NT, VanderHeyden WB, Rauenzahn RM, Yarbrow SL (2000) Three-Dimensional Simulation of a Three-Phase Draft-Tube Bubble Column. *Chem. Eng. Sci.* 55:3261-3273
- Pfleger D, Gomes S, Gilbert N, Wagner HG (1999) Hydrodynamic Simulations of Laboratory Scale Bubble Columns Fundamental Studies of the Eulerian-Eulerian Modeling Approach. *Chem. Eng. Sci.* 54:5091-5099
- Sokolichin A, Eigenberger G (1999) Applicability of the standard-turbulence model to the dynamic Simulation of Bubble columns: Part I. Detailed numerical Simulations. *Chem. Eng. Sci.* 54:2273-2284

Model fundamentals for the design of three-phase loop reactors

S. John, S. Scheid, H. Parchmann, O. Bork, M. Schlüter, N. Rübiger

Institute of Environmental Process Engineering, University of Bremen

Introduction

Loop reactors under multiphase operation are distinguished by low-maintenance and usually economically and ecologically advantageous operating conditions and thus have a broad spectrum of applications in chemical as well as biotechnological industries. Nevertheless, the design of these reactors is currently based on inaccurate physical and mathematical models. The interactions found in three-phase flows, which can result, e.g., in both an increase and a decrease in gas-void fraction due to an increase in solids-void fraction, have been explained phenomenologically in recent experiments and are schematically shown in fig. 1.

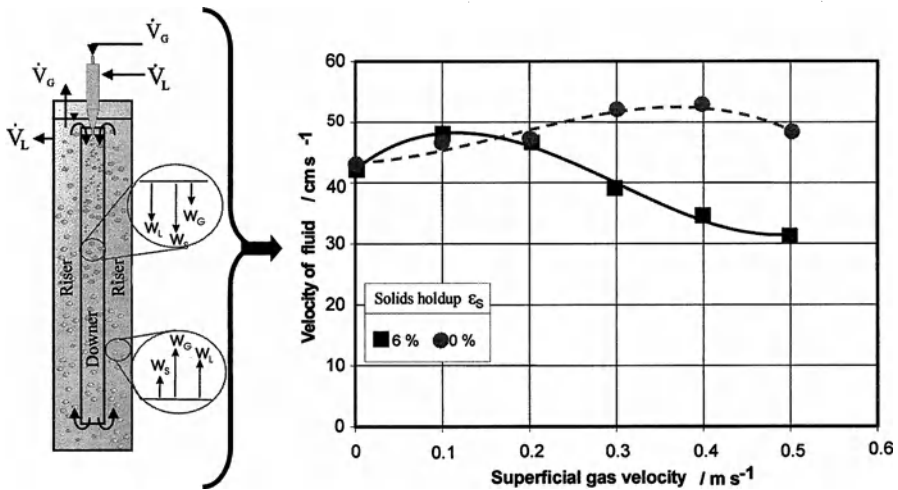


Fig. 1. Hydrodynamics of a three-phase flow affected by phase interaction

In these experiments two major effects were found to be of paramount importance for future physical models:

- A change of the drag coefficient of the three-phase flow due to increased solids loading.
- A change in pressure difference between downcomer and riser due to variations of the dispersed phase fractions.

Corresponding experiments were conducted at the Institute of Environmental Process Engineering regarding three-phase flows in a jet-driven loop reactor. It becomes clear that the most important basis for modeling full scale reactors is the exact calculation of the differences in dispersed phase fractions between downcomer and riser. This cannot be done based on integral measurements alone.

Discussion of the theoretical background

In many cases, loop-reactors under multiphase conditions are designed and calculated based on momentum balances with a number of simplifications. A comparison between a calculation from Tebel and Zehner (Tebel and Zehner 1989) which is based on momentum balance and the assumption of a constant slip velocity and experimental data recently recorded in a loop reactor, shows that already for a two-phase flow significant differences occur (fig.2).

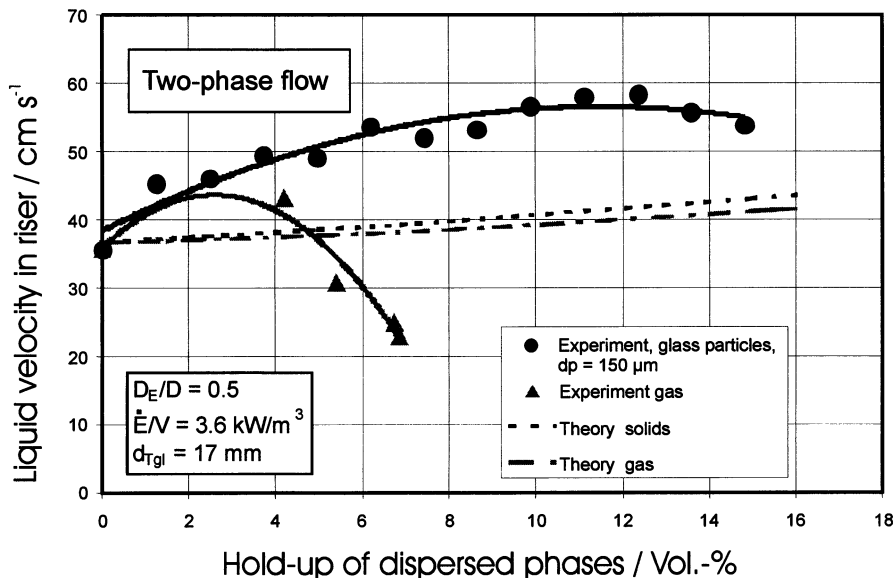


Fig. 2. Comparison of theoretically and experimentally generated data of a two-phase flow

These suppositions were acceptable in the past due to a lack of appropriate measurement techniques, whereas Zehner (Zehner 1980) already showed in a comparison between calculated and measured data that smaller solid particles behave less according to theoretically calculated data than larger particles. And as these simplifications often lead to significant errors, resulting in faulty data from the calculations of momentum balance, a new investigation and reconsideration of modeling is advisable:

- Layer model / no interaction

Although many authors dealt with the subject of interaction of phases and/or bubbles and developed models to enable a physical and/or mathematical description, the layer model does not take into account any interaction. In this model, the three phases are considered to exist simultaneously but without any influence on each other or any interaction (like the two-fluid-model in two-phase flow). As a matter of fact especially in three-phase flows, the probability of phase interaction is relatively high. Direct interactions (Lee et al. 1974, Henriksen and Østergaard 1974) such as bubble-particle collisions or bubble-bubble collisions as well as indirect interactions, e.g. the influence of turbulence on bubble size (Räbiger 1985) or the enrichment of small solid particles in bubble wakes (Fan 1989) may occur (Guder 1997).

- Constant slip velocity of the gas phase

In addition to the simplifications of the layer model, the (single-) bubble rise velocity was usually supposed to be constant (generally assumed to lie between 23-25 cm/s) and independent of flow direction, superficial liquid velocity or phase hold-up. Recent investigations of Schlüter in two-phase flows (Schlüter 2002) pointed out, that the slip velocity in bubble swarms can increase by more than 40 % compared to freely rising single bubbles and is strongly related to liquid velocity and gas void fraction. This should be of relevance for three-phase flows as well. Furthermore, it is expected that the enrichment of solid particles in the wake of a rising bubble (Fan 1989) decreases the slip velocity (as it is shown in fig. 3).

- Pressure drop / drag-coefficients of single phases are summable

In many cases, an additive superposition of drag coefficients for each phase is postulated in order to calculate the pressure drop or momentum balance of the fluid flow (Tebel and Zehner 1989). This implies that the different mechanisms of pressure drop do not affect each other. This assumption corresponds to the already mentioned simplifications, but cannot be upheld for real systems, in which a superposition of direct and in-

direct phase interaction, as well as special phenomena like solids-enrichment in bubble wakes may occur.

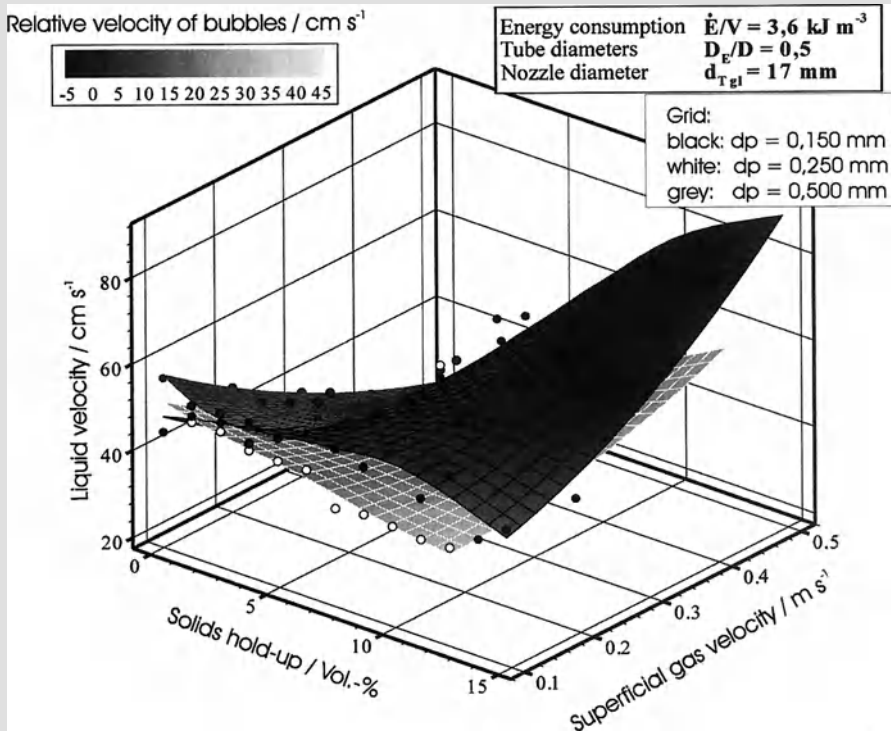


Fig.3. Hydrodynamic parameters in a three-phase flow

Obviously, the physical processes of hydrodynamics in three-phase flows must be taken into account for a more precise calculation and reactor design.

Experimental set-up

For all experiments, we used a jet-driven loop reactor with an effective height of 2 m and a reactor tube diameter of 290 mm (fig. 4). Four settling tanks at the top of the reactor ensure the constancy of solids hold-up in the reactor volume. We made the following variations for the diameter of the inner tube D_E (downer zone) in relation to the reactor size: $D_E/D = 0.3, 0.4, 0.5$. The liquid as well as the gas was injected at the top of the reactor by means of a special nozzle (injector), whereas the liquid flow rate determines the total energy input.

The main measuring point for phase velocities and hold-ups was situated at a height of 1 m in the middle of riser (or downer) zone. According to investigations of Guder (1997), this measurement point is representative for the flow.

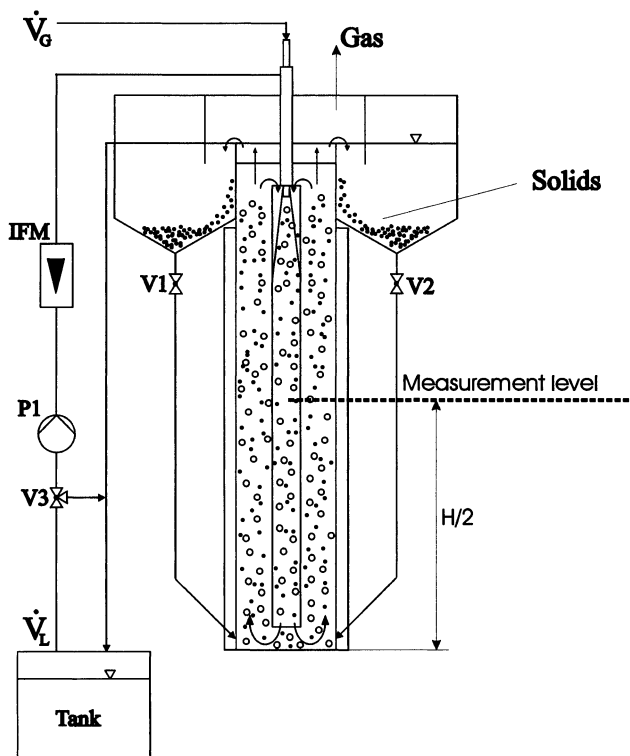


Fig. 4. Loop Reactor

For measurements of liquid velocity we used a three-segment electrodiffusion probe (Hainke et al. 1998, John et al. 1999, Pauli 1991, Pannek 1997) and a conductivity probe to measure the bubble velocity and other parameters of the gaseous phase (e.g. Pannek 1997). The pressure differences were detected with a differential pressure transducer.

Extended modeling of hydrodynamics in three-phase flows

In order to consider phase interaction as well as local phenomena (e.g. particle enrichment in bubble wakes) in momentum balance, a replacement of some of the above mentioned simplifications by a physically correct model is necessary.

A central hydrodynamic parameter is the mean circulation velocity of the loop flow, in general formulated as

$$w_{cir} = w_{jet} \sqrt{\frac{2 \cdot \rho_{jet}}{\zeta_{ov.} \cdot \rho_{riser}}} \cdot \frac{d_{jet}}{D}, \quad (1)$$

wherein the overall drag coefficient of the loop flow is supposed to be able to be summed up by superposition (Tebel and Zehner 1989)

$$\zeta_{ov.} = \zeta_I + \zeta_{II} + \zeta_{III}. \quad (2)$$

As the drag coefficient is a direct function of the pressure drop, both the gas hold-up and /or the solids hold-up affect the drag coefficient,

$$\Delta p = \Delta \rho \cdot g \cdot H \cdot \Delta \varepsilon = \zeta_{ov.} \cdot \frac{\rho_{cir.} \cdot w_{cir}^2}{2} \quad (3)$$

and any process which influences the local phase hold-up is a significant parameter for hydrodynamic interactions (Tebel and Zehner 1989). It becomes obvious now, that a sound estimation of phase hold-ups leads to a more exact description of the pressure drop.

In general, the gas hold-up

$$\varepsilon_G = \frac{w_0^G}{w_{swarm}^G} \quad (4)$$

is formulated as a function of bubble swarm velocity and superficial gas velocity. Thus, the swarm velocity postulated e.g. by Richardson and Zaki (1954)

$$w_{swarm}^G = w_{sl}^G \cdot (1 - \varepsilon_G)^n \quad (5)$$

represents the central parameter required to calculate the pressure difference (downer - riser). This points out that the correct assumption of slip velocity, which can be estimated in loop reactors with a homogenous cross-sectional distribution of gas bubbles by

$$w_{sl}^G = w_{rel}^G = w_{bubble}^G - w_{abs}^L, \quad (6)$$

is of great importance. In fig. 5, some experimental data of the mean relative velocity between gas and liquid phase in the riser of the loop reactor is shown and makes clear, that the slip velocity is not constant but a function not only of gas and

solids hold-up, but also of size and density of solid particles. The reason is assumed to be the enrichment of small particles in bubble wakes (Fan 1989), depending on their inertia and size.

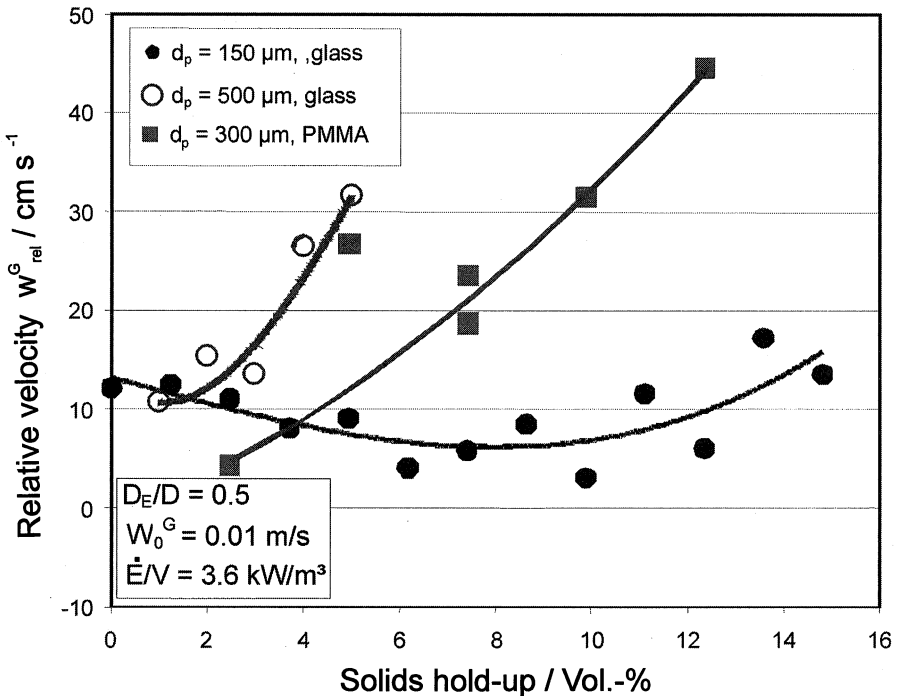


Fig. 5. Relative velocity between bubbles and liquid, depending on solids hold-up and inertia

In case of small particles (glass particles with a diameter of $150 \mu\text{m}$), they are transported into bubble wakes and remain there over a longer period due to their low inertia. This can lead to an decrease of the bubble rise velocity, as the overall density of the bubble and its wake increases. At a critical solids concentration, no increase of solid particles in the wake region is possible, the concentration in the wake region becomes equal to the concentration in the bulk flow, so that the density difference between bulk and bubble with bubble wake increases again. Thus, the relative velocity increases as well. Particles with higher inertia and/or size (glass particles with $500 \mu\text{m}$ diameter, PMMA particles) do influence the relative velocity in a different way, which leads to the conclusion that these particles are not as a rule enriched in bubble wakes or that the enrichment does not lead to mechanisms as described above. As far as the glass particles with a diameter of $500 \mu\text{m}$ are concerned, we assume that high inertia prevents the enrichment preferably in bubble wakes, thus the density difference between bulk and bubble in-

creases with increasing solids hold-up. We suppose that the PMMA particles do enrich in bubble wakes – due to their low inertia. But as their density to volume ratio is rather low, the enrichment does not lead to such obvious effects compared to small glass particles. Additionally, the volume of the single particle is relatively high, so the above mentioned critical concentration of solids in the wake region will be reached much earlier in contrast to small glass particles.

As the local distribution of solid particles, and the rising velocity of the gas phase affect the overall difference of pressure between downer and riser of the reactor (fig. 6), the enrichment of solids in wakes should be taken into account for calculation of bubble rise velocities. This can be explained by the preferred position of the solid particles: In case of relatively large particles with high inertia, they do not tend to enrich in bubbles wakes, so that the bubbles and the particles behave more in accordance with the layer-theory. This implies a higher gas-hold-up in the downer-region of the reactor, than in the riser region, due to its lower density compared to the liquid, whereas the solids concentration is higher in the riser region than in the downer region. In case of relatively small particles with lower inertia, they tend to enrich in bubbles wakes, so that the bubbles seem to have a higher density. For this reason, the difference of phase hold-ups between downer and riser decreases compared with larger solid particles, which affects directly the pressure difference (fig. 6). In case of the PMMA particles, the inertia seems not to be the only parameter to describe the mechanism of particle enrichment sufficiently. We are now validating an already existing theory in a new research program, which takes into account that the particle size and the density can affect the hydrodynamics independently and in different manners.

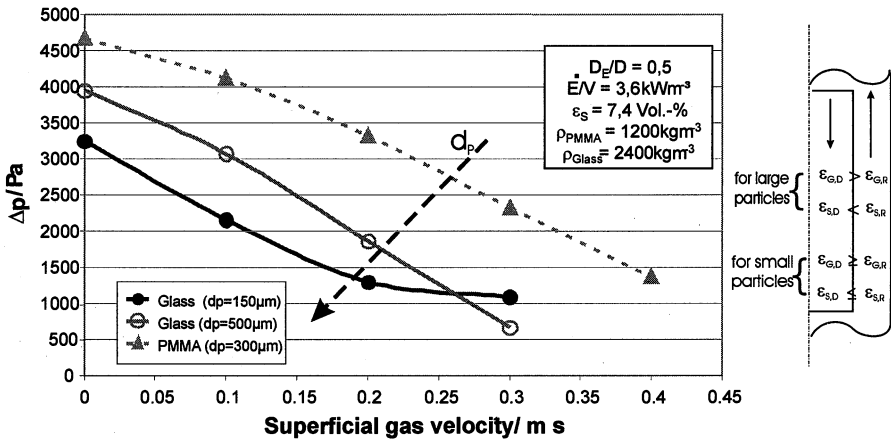


Fig. 6. Pressure difference between downer and riser in three-phase flows

Discussion and results

The driving force of loop reactors, i.e. the overall pressure difference between downer and riser, depends directly on phase-hold-ups and drag coefficients (see eq. 2 and 3). In order to calculate minimal energy demand of loop reactors for example, any phenomenon which influences the pressure difference should be taken into account. By calculating the liquid velocity in the riser in a three-phase flow with experimental data for the gas hold-up and swarm velocity, we found that the absolute velocity is still too low but there is a slight change in quality of the curves as a function of gas hold-up (fig. 7). Evidently, local phenomena have to be taken into account to reach a better reproduction of the reality.

The consequence of neglecting phase interactions, especially solids enrichment in bubble wakes, may cause significant mistakes in reactor design, as can be seen in fig. 8, which shows a comparison between small and large reactors (height of 1 m and 10 m).

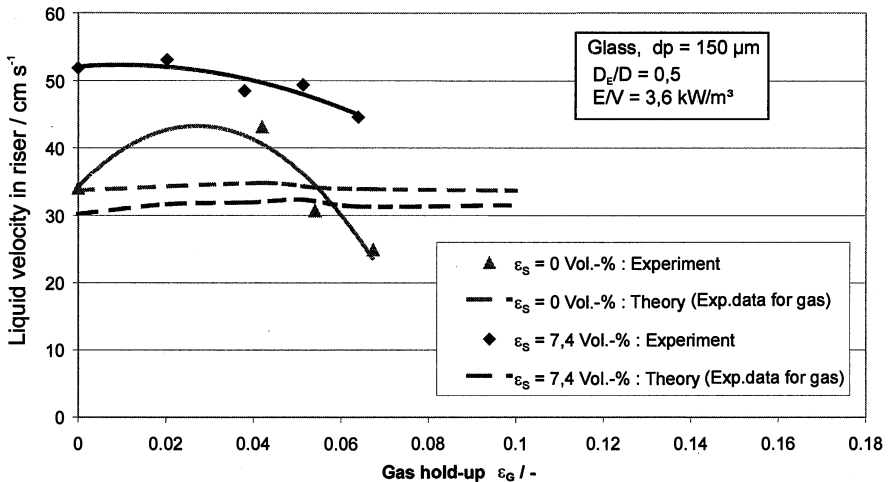


Fig. 7. Comparison of theoretical and experimental data

In case of small reactors, the pressure difference between riser and downer is dominated by the drag due to the change of flow-direction at the bottom (baffle location). To make this clear, we calculated the pressure difference for small reactors caused by the fraction of the dispersed phases only, neglecting the drag due to the one-phase flow at the baffle location and compared it to the experimental data. The difference is relatively high in comparison with the pressure difference due to a rising gas hold-up.

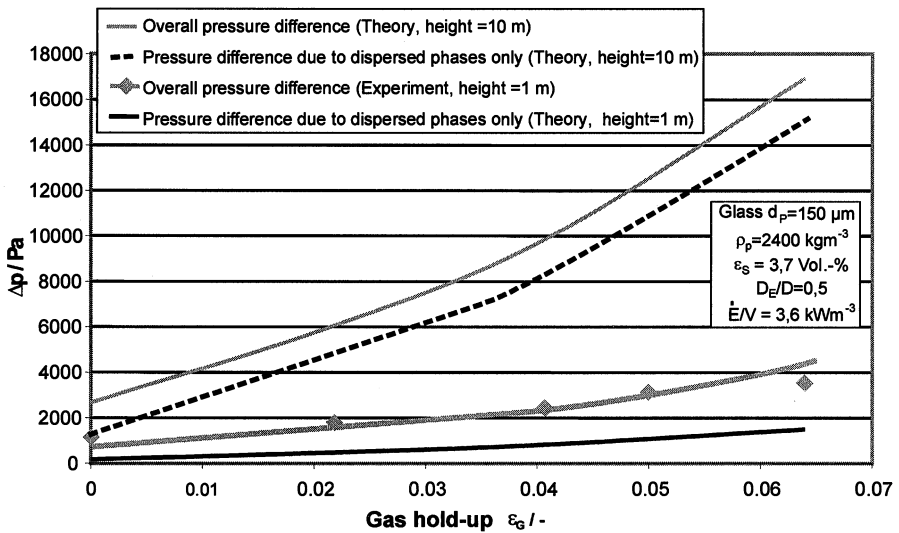


Fig. 8. Effect of gas hold-up on pressure difference for small and large reactors

Conclusion

The calculation of pressure difference between downer and riser for larger reactors, as commonly used in industrial applications, clearly shows that the difference due to the drag at the baffle location becomes less important than the pressure difference between downer and riser region. Instead, the difference of phase hold-ups now becomes dominant and affects the pressure difference.

So it is obvious, that an increase in reactor size requires a proper modeling of phase hold-ups, which has to take into account the effect of solids enrichment in bubble wakes on the rise velocity of the bubble swarm, and the gas hold-up in riser and downer.

References

- Fan L-S (1989) Gas-liquid solid fluidization engineering. Butterworth Publishers, Stoneham
- Guder R (1997) Fluidodynamik von Dreiphasenströmungen in Treibstrahlschlaufenreaktoren. Fortschrittberichte VDI Reihe 3 Nr. 461, VDI-Verlag, Düsseldorf
- Hainke M, Ammon K, Onken U (1998) Simultane Messung von Gelöstsauerstoffkonzentration und Hydrodynamik in aeroben Submersfermentationen. Chem Ing Tech 70: 299-301
- Henriksen HK, Østergaard K (1974) On the mechanism of break-up of large bubbles in liquids and three-phase fluidized beds. Chem Eng Sci 29: 626-629

- John S, Wilfer R, Rübiger N (1999) Messung hydrodynamischer Parameter in Mehrphasenströmungen bei hohen Dispersphasengehalten mit Hilfe der Elektrodiffrusionsmesstechnik. In: Prasser HM (eds) Wissenschaftlich-Technische Berichte FZR-281, FZ Rossendorf
- Lee JC, Sherrad, AJ, Buckley PS (1974) Optimum particle size in three phase fluidized bed reactors. Comptes rendus du congrès international La Fluidisation et ses applications, pp. 407-4016
- Pannek S (1997) Untersuchung der Elektrodiffrusionsmesstechnik mit Sauerstoff als Depolarisator für den Einsatz in Mehrphasenströmungen. Dissertation, Universität Dortmund
- Pauli J (1991) Einsatz der Elektrodiffrusionsmesstechnik in Gas-Flüssigkeitströmungen mit Sauerstoff als Depolarisator. Dissertation, Universität Dortmund
- Rübiger N (1985) Die Auswirkungen von Feststoffpartikeln auf den Gasgehalt in einem von oben begasten Schlaufenreaktor. Chem Ing Tech 57 3: 248-249
- Richardson JF, Zaki WN (1954) Sedimentation and fluidization, Trans Inst Chem Eng 32: 35-53
- Schlüter M (2002) Blasenbewegung in praxisrelevanten Zweiphasenströmungen. Fortschrittberichte VDI Reihe 7 Nr. 432, VDI-Verlag, Düsseldorf
- Tebel KH, Zehner P (1989) Fluid dynamik description of jet-loop reactors in multiphase operation. Chem Eng Techn 12: 274-280
- Zehner P (1980) Suspendieren von Feststoffen im Strahlschlaufenreaktor. Chem.-Ing.-Tech. 59: 910-911

Symbols:

D	Diameter of reactor	m
d_{jet}	Diameter of jet tube	m
g	gravitation	m/s ²
H	High of reactor tube	m
w_{cir}	Circulation velocity	m/s
w_{jet}	Jet velocity	m/s
w_0^G	Superficial gas velocity	m/s
w_{abs}^L	Absolute liquid velocity	m/s
w_{bubble}^G	Rising velocity of a bubble	m/s
w_{rel}^G	Relative velocity of a bubble	m/s
w_{sl}^G	Slip velocity of a bubble	m/s

w_{swarm}^G	Swarm velocity of a bubble	m/s
ε_G	Gas hold-up	
ε_s	Solids hold-up	
$\Delta\varepsilon$	Difference of phase hold-ups	
Δp	Difference of pressure	Pa
$\Delta\rho$	Difference of density	kg/m ³
ρ_{jet}	Density of jet	kg/m ³
ρ_{riser}	Density of flow in riser	kg/m ³
$\zeta_{ov.}$	Overall drag coefficient	
ζ_I	Drag coefficient of liquid flow	
ζ_{II}	Drag coefficient of two-phase flow	
ζ_{III}	Drag coefficient of three-phase flow	

Simultaneous measurement of the local liquid and the local solid velocities

Kertzscher, U., Seeger, A., Affeld, K., Wellnhofer, E.

Biofluidmechanics Laboratory, Charité, Spandauer Damm 130, D-14050 Berlin, Germany

German Heart Institute Berlin DHZB, Augustenburger Platz 1, 13353 Berlin, Germany

1 Introduction

Many biomedical and chemical processes are based on multi-phase reactors (Dudukovic, Larachi, F., & Mills, 1999). To design these reactors, many investigators have tried to simulate the fluid mechanics common in multi-phase flow (Jakobsen et al., 1997). However, the complexity of the system requires that the numerical results achieved with computational fluid dynamics (CFD) have to be validated with experiments (Dudukovic, Larachi, F., & Mills, 1999).

The fluid mechanics of the fluid and solid phases in three-phase reactors (three phases: gas/liquid/solid) can be investigated by optical techniques (Dudukovic, Larachi, F., & Mills, 1999, Seeger et al., 2001, Chen, Reese, & Fan, 1994). As demonstrated by Seeger (Seeger et al., 2001), all these methods (Laser Doppler Velocimetry, Particle Image Velocimetry, Particle Tracking Velocimetry) face the problem of reflection and refraction of the visible light at the gas-liquid boundaries. This therefore limits the application of these methods to cases when no bubbles obscure the path of light. However, solids obscure the path of light too, and, in the case of opaque particles, do not allow the light to pass. This means that these methods are only applicable for small void fraction and small solid hold-up.

A measurement method without these limitations is the Computer Aided Radioactive Particle Tracking (CARPT, solid phase: Larachi, Chaouki, & Kennedy, 1995, liquid phase: Chen et al., 1999), where the motion of just one radioactive particle is recorded by different sensors around a bubble column. This method works independently from solid hold-up and/or void fraction. However, this method is a single point measurement method and it can take up to 24 hours to assess a velocity field (Chen et al., 1999).

Only X-ray based Particle Tracking Velocimetry (XPTV) works independently from the void fraction and solid hold-up and is, in addition, a multi-point measurement method. The main advantage of this over methods based on visible light

is that X-rays penetrate a multi-phase flow in straight lines. This is a 3D-3C (three-dimensional / three component) method and enables us to obtain a mean velocity field of the investigated area within 20 seconds. This method was applied in the measurement of the liquid velocity in a bubble column (Seeger et al., 2001) as well as in the measurement of the solid velocity in a three-phase flow (Seeger et al., 2002b). However, the potential of this method is even greater: it gives us the possibility to measure the solid velocity and the liquid velocity simultaneously in a three-phase flow. Results obtained by this method are subject of this paper. Other X-ray based methods applicable to multi-phase flows are described in (Seeger et al., 2002a).

With the application of this X-ray based measurement technique, it is possible to gain sufficient information about the flow phenomena in multi-phase-flows to validate numerical methods.

2 Method

The aim of this work was to measure the liquid and the solid velocity in a three-phase flow (three phases: gas/liquid/solid) simultaneously.

2.1 Measurement principle

The measurement principle is closely related to the technique described in (Seeger et al., 2001) for a gas-fluid flow. The multi-phase flow is seeded with X-ray absorbing tracer particles. However, now two kinds of particle are used. One kind has the same density and size as the solid phase. It is assumed that these particles represent the solid phase, in other words, move as a solid. Therefore, using our knowledge of the tracer particle motion, the solid velocity is measured. The other kind of particle has the same density as the fluid phase. From the movement of these particles it is possible to measure the fluid velocity. In other words, if the motion of the two different tracer particles can be recorded separately, one can measure both velocities simultaneously.

As mentioned before, X-rays penetrate a gas-liquid interface and solid particles in straight lines. Thus the problems described above - those of the observation using visible light with refraction and reflection on phase boundaries and absorption by particles - do not occur.

The basic experimental set-up is shown in figure 1. X-rays, generated by two sources S1 and S2, penetrate the multi-phase reactor, and are received by two image intensifiers I1 and I2. The image intensifiers convert X-rays into visible light and amplify it. Two digital cameras behind the image intensifiers record the images. An X-ray absorbing particle P inside the reactor is mapped on the two image intensifiers I1 and I2. This creates two particle images P1 and P2. The three dimensional position of the particle P can be reconstructed from P1 and P2. This is possible because the three dimensional positions of both X-ray sources and P1 and P2 are known. By recording the image series, the motion of a particle can be ob-

served. Additionally the velocity of a particle can be calculated by its displacement divided by the time difference between the images. By the observation of a large number of tracer particles, a three dimensional vector field in an Eulerian coordinate mesh can be assessed. This method is closely related to 3D optical PTV, but can however be used for opaque fluids and solids.

In the first step of this development, the method was used to track particles that represented the liquid flow (Seeger et al., 2001). A second developmental step allowed us to track particles that represent the solid phase (Seeger et al., 2002b).

Our new technique tracks both - particles that represent the solid phase and particles that represent the liquid phase - simultaneously.

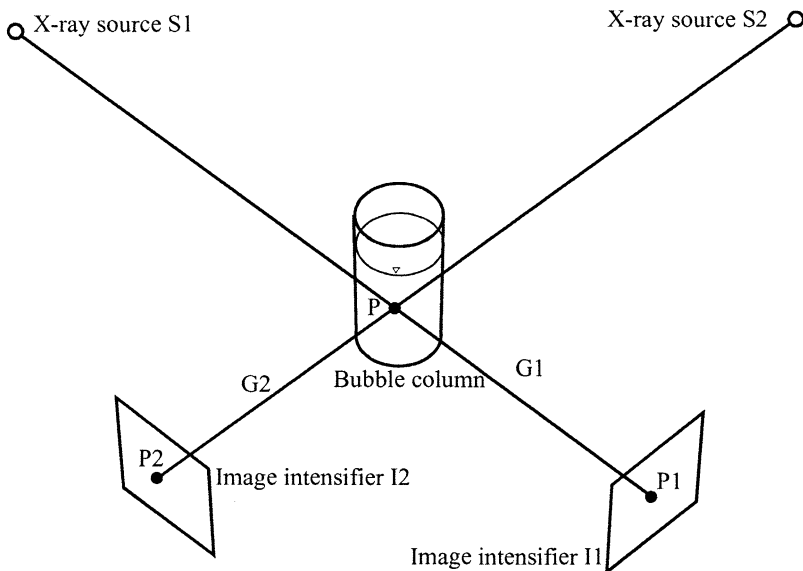


Fig. 1: Experimental set-up.

2.2 Measurement device

A biplane angiography device (Philips Integris BH 3000) was used for the measurements. This system is a medical device used by cardiologists to get a three dimensional view of the geometry of human coronary blood flow. The German Heart Institute (DHZB) in Berlin generously provided access to this device when it was not needed for clinical investigations. The parameters of the system are:

Size of input screen of the image intensifier	23 cm x 23 cm.
Resolution of image intensifier	1024x1024 Pixel

Digital image	8 bit grayscale
Resolution of CCD-camera	512x512 Pixel
Maximal investigation area	104mm x 104mm x 104mm

It was possible to obtain an image series of up to 1000 images (500 image pairs).

2.3 Particles

Two kinds of particles were used, one with the same density as the fluid phase (glycerin), and one with a different size and density. The latter is the solid phase. The particles for the liquid phase are cubic with a side length of 2 mm. They are made out of polyurethane foam and a cylindrical insert of a tin alloy (see: Seeger et al.: “X-ray Based Particle Tracking Velocimetry for Bubble Columns with High Void Fraction” in this book). The solid particles are also cubic but with a side length of 3 mm and a radio opaque layer of $3 \times 3 \text{ mm}^2$. Therefore, it is possible to discriminate between the two kind of particles with image processing. The density of the solid particles is 2 g/cm^3 .

Thirty particles of each kind of were used.

2.4 Software

The software algorithms enabled us to do the following (see figure 1):

1. Particle recognition and distinction between the two phases: The particle recognition algorithm detects in a first step if a pixel is much darker than its surroundings. Then areas with darker pixels are detected. If this size is within a certain limit, this area is also considered to be a particle. The X-ray absorbing portion of the particle which represents the solid phase is larger than that which represents the liquid phase. The distinction between the two phases uses this fact.
2. Distortion correction: Distortion correction is necessary because the image intensifier works with a curved input screen, which leads to a pincushion distortion. This distortion is corrected in this step.
3. Separate Particle Tracking for the two phases: The particles are tracked two-dimensionally with a standard next neighborhood-algorithm (resembling that of Guezennec et al. (1994)). This is done for both phases separately.
4. Isocenter correction (see: Seeger et al.: “X-ray Based Particle Tracking Velocimetry for Bubble Columns with High Void Fraction” in this book)
5. Reconstruction of the three-dimensional trajectories separately for the two phases: The two-dimensional trajectories are reconstructed in the three-dimensional space.
6. Calculation of a velocity field separately for the two phases: The velocity field is calculated assuming that the flow during the measurement time is stationary (see: Seeger et al.: “X-ray Based Particle Tracking Velocimetry for Bubble Columns with High Void Fraction” in this book).

The software is described in detail in Seeger et al. (2001).

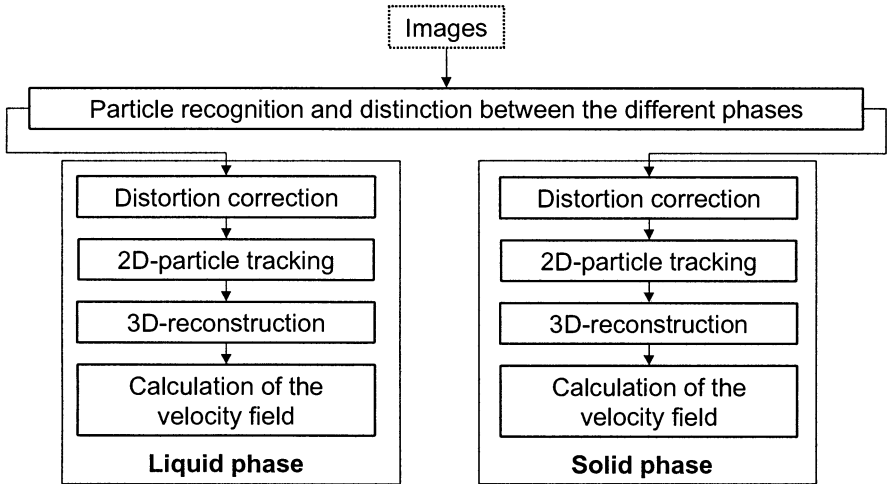


Fig. 2: Flow chart of the algorithm

3 Results

The method was applied to a cylindrical bubble column. The cylindrical bubble column had an inner diameter of 104 mm and a filling height of 93 mm. 91 hypodermic needles with an inner diameter of 0.34 mm were used as gas dispersers. Glycerin with a viscosity of $8.5 \cdot 10^{-4} \text{ m}^2/\text{s}$ was used as a liquid.

The solid phase consisted of the radio opaque particles with a side length of 3 mm, as described above.

The measurements in the cylindrical bubble column were taken under different conditions. One example is shown here. The superficial gas velocity was set to 1 mm/s. The void fraction was about 1 %.

A velocity field for the liquid and the solid phase was calculated separately from the trajectories obtained. Figure 2 shows the velocity field of the liquid phase and figure 3 shows the results for the solid phase. Both are mean values of 100 seconds recording time. This long measurement time was necessary because of the small number of particles used.

The difference between the velocity of the two phases was calculated, and is shown in figure 4. As expected, the slip velocity between the two phases correlates with the acceleration of the fluid phase: a small acceleration causes low slip velocities, a high acceleration high values of the slip velocity. The reason is the higher density of the solid phase compared to the density of the fluid phase.

The visualization was performed with AMIRA (Indeed - Visual Concepts GmbH, Berlin), a software package for the visualization of three-dimensional data.

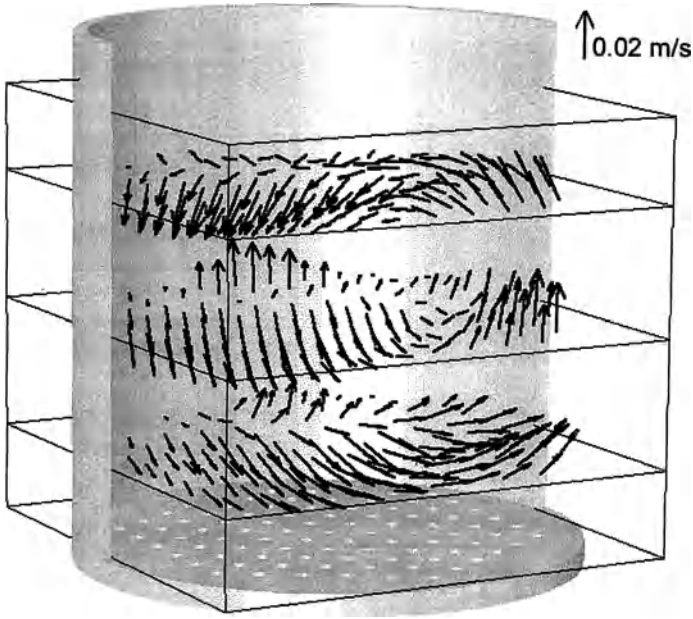


Fig. 3: The local liquid velocity.

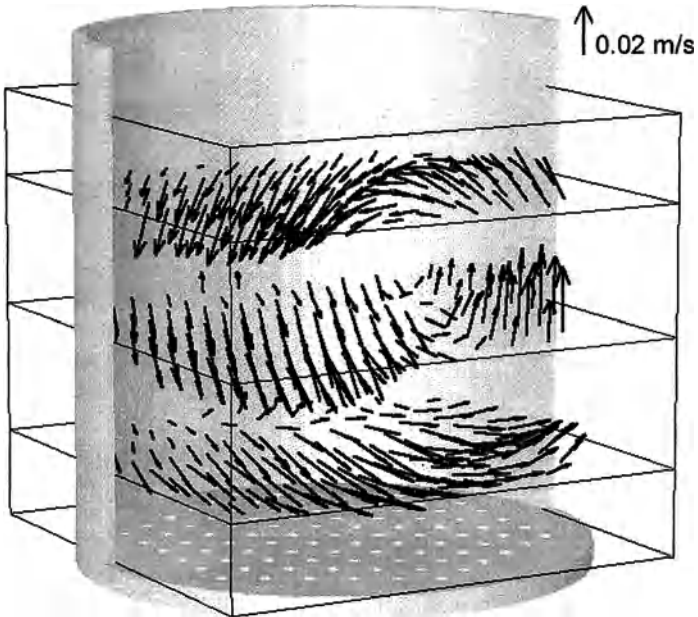


Fig. 4: The local solid velocity.

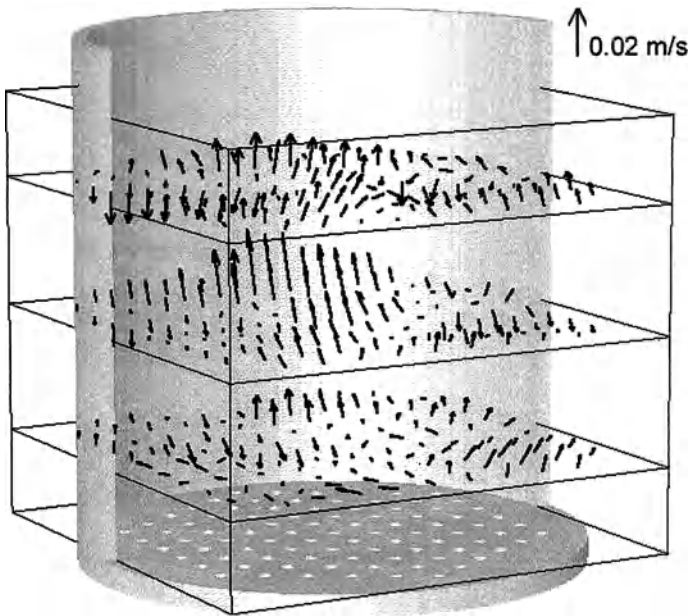


Fig. 5: The local liquid velocity subtracted by the local solid velocity.

4 Discussion

In this paper, results of the simultaneous measurement of the fluid and solid velocity are presented. The measurement method applied is an adaptation of the X-ray based Particle Tracking Velocimetry, as described by Seeger (Seeger et al., 2001 and Seeger et al., 2002b). These results show the feasibility and the potential of the method. Until now, the method has been limited to steady and slow flows, if the acquisition of a whole velocity field is the aim. But it is possible to detect instationary effects by tracking single particles.

Future work is intended to extend the present limitations. The next steps are:

- Use of smaller particles representing the fluid phase
- Use of more radio opaque particles in order to shorten the measurement time
- Introduction of a solid phase, which is not radio opaque. This phase will be represented by the particles used in the present work.
- Validation of the method in a known flow model
- Calculation of the time and space resolved solid hold-up. The basic idea is that the solid hold up can be assessed from the distribution of the radio opaque particles (Seeger et al., 2002b).

With a specialized X-ray device with enhanced parameters, the assessment of liquid velocity, solid velocity and other parameters could be much faster and with a better resolution. Such an optimized device is described in Seeger et al.: “X-ray Based Particle Tracking Velocimetry for Bubble Columns with High Void Fraction” in this book.

5 References

- Chen RC, Reese J, Fan LS (1994) Flow structures in a three-dimensional bubble column and three-phase fluidized bed. *AIChE Journal* 40: 1093-1104
- Chen JAK, Al-Dahhan MH, Dudukovic MP, Lee DJ, Fan LS (1999) Comparative hydrodynamics study in a bubble column using computer-automated radioactive particle tracking (CARPT), computed tomography (CT), and particle image velocimetry (PIV). *Chem Eng Sci* 54: 2199-2207
- Dudukovic MP, Larachi F, Mills PL (1999) Multiphase reactors - revisited. *ChemEngSci* 54: 1975-1995
- Guezennec YG, Brodkey RS, Trigui N, Kent JC (1994) Algorithms for fully automated three-dimensional particle tracking velocimetry. *Exp Fluids* 17: 209-219
- Jakobsen HA, Sannæs BH, Grevskott S, Svendsen HF (1997) Modeling of Vertical Bubble-Driven Flows. *Ind Eng Chem Res* 36: 4052-4074
- Larachi F, Chaouki J, Kennedy G (1995) 3D-Mapping of solids flow fields in multiphase reactors with RPT. *AIChE Journal* 41: 439-443
- Seeger A, Affeld K, Goubergrits L, Kertzscher U, Wellenhofer E (2001) X-ray-based assessment of the three-dimensional velocity of the liquid phase in a bubble column. *Exp Fluids* 31: 193-201
- Seeger A, Affeld K, Goubergrits L, Kertzscher U, Wellenhofer E, Delfos R (2002a) X-ray based flow visualization and measurement: Application in multi-phase flows. *Ann NY Acad Sci* 972: in press
- Seeger A, Kertzscher U, Affeld K, Wellenhofer E (2002b) Measurement of the local velocity of the solid phase and the local solid hold-up in a three-phase flow by X-ray based Particle Tracking Velocimetry (XPTV). *Chem Eng Sci*: in press

A Numerical Model of Dispersed Two Phase Flow in Aerated Stirred Vessels based on Presumed Shape Number Density Functions

Emad Gharaibah, Wolfgang Polifke

Lehrstuhl für Thermodynamik, Technische Universität München

Abstract

Based on the two fluid model and the population balance equation for bubble size, a novel approach is proposed for the numerical simulation of dispersed two phase flow, e.g. in aerated stirred vessels. The bubble size distribution is represented with a number density function of presumed shape, which makes possible the partial solution of the population balance equation in a pre-processing step. The pre-processing is not computationally expensive, so the number of bubble size groups may be chosen sufficiently large to represent the evolution of the size distribution due to break-up and coalescence of bubbles very accurately. In the subsequent CFD simulation, it is not necessary to solve a set of transport equations for each size group. Instead, the size distribution of the dispersed phase is represented by its first two moments, i.e. the mean and variance of bubble diameter. Transport equations for mean and variance are solved by the CFD code, with source terms depending on local flow parameters and bubble size distribution. These source terms are taken from a look-up table, which has been generated in the pre-processing step.

In the present paper, the overall formulation and solution algorithm of the proposed model is outlined. For a spatially homogeneous system, it is demonstrated that number density functions of presumed shape can indeed represent accurately the evolution of a bubble size distribution under the action of bubble break-up and coalescence with realistic kernel functions. Furthermore, it is shown that a rather large number of bubble size groups is required to reach discretization independence for the population balance equation. The proposed model has been implemented in a multi-dimensional CFD code, and employed in the simulation of turbulent two-phase (gas-liquid) dispersed flow in an aerated stirred vessel.

Introduction

In multiphase flows, for example in an aerated stirred vessel, the transfer of momentum, mass, and energy across the phase interface is of crucial importance. In general, the transfer processes depend in a sensitive manner on the available inter-

face area, which can only be computed if the bubble (or particle) size distribution is known. The transient evolution of the bubble size distribution resulting from the break-up and coalescence can be reproduced by means of a population balance, formulated in terms of a number density function.

Within the last few years, a variety of models for the numerical simulation of two phase flows including the dispersion and coalescence of gas bubbles have been proposed. The discussion here is limited to Euler-Euler multi-fluid models, where one set of transport equations has to be solved for each phase.

In the simplest mono-disperse models, it is assumed that the bubble diameter is locally single-valued. Of course, this is for many applications an inadmissible over-simplification. More advanced models represent the bubble size distribution by several size groups. Each size group represents particles from a certain range of diameters and is treated as a separate phase in the flow calculation. This formulation requires the solution of $5N+1$ equations for N size groups. In practice, the number of the size groups is limited to low values, say $N=4$, due to the extensive numerical effort resulting from the (non-linear) coupling between the equations due to the transfer processes mentioned above. Therefore, the evolution of the bubble size distribution can be represented only in a rudimentary manner.

The MUSIG (MUltiple-SIze-Group) model (Lo 1999) represents a further development of this type of model. Again a continuity equation for each size group is solved, but it is assumed that all bubble velocities can be related to the average value in an algebraic manner, so that only one set of momentum equations for the gas phase has to be solved. With this simplification, it is claimed that up to 20 size classes can be taken into account (Lo 2000). An alternative approach (Millies and Mewes 1996) is to assume a certain (self-similar) shape for the number density function, which is determined completely by the mean bubble diameter. This self-similar shape is expected for disperse flows where bubble coalescence and dispersion exhibit certain special properties.

We propose a novel approach to simulate disperse two phase flow (gas bubbles – fluid). This model is based on the two fluid model (Ishii 1975) and a number density function (NDF) of *presumed functional shape* for the bubble size. With the proposed formulation, it is not necessary to solve a set of transport equations for each size group in the CFD model. Instead, the size distribution is represented by its first two moments (therefore “moments model”), i.e. the mean and variance of bubble diameter. Besides one set of transport equations for both the liquid and gaseous phase, only two additional transport equations for mean and variance of the bubble size distribution are solved by the CFD code. Changes in the size distribution due to coalescence and dispersion are represented by source terms in the transport equations for the moments. The source terms depend on local size distribution as well as flow parameters (e.g. turbulent dissipation or gas volume fraction). With a presumed shape NDF, the source terms can be computed in a pre-processing step for later transfer to the CFD solver via a look-up table. The pre-processing is not computationally expensive, so the number of bubble size groups may be chosen sufficiently large to represent the evolution of the size distribution due to break-up and coalescence of bubbles very accurately.

This novel formulation offers several advantages: a) the bubble size distribution can be represented in great detail due to the possibility to consider a large number of bubble size groups efficiently, b) numerical stability problems are reduced significantly, as it is not necessary to solve strongly coupled transport equations for numerous size groups, c) arbitrary break-up and coalescence kernel functions can be implemented, appropriate for the respective disperse flow regimes in turbulent or laminar, stirred vessel or bubble column two phase flow, d) significant computing time reduction can be expected from the tabulation of the population balance dynamics in a pre-processing step.

In this paper, the formulation of the moments model is outlined and the possibility to replace the NDF by a function of presumed shape, which is the basis of this model, is demonstrated. The proposed model has been implemented in a multi-dimensional CFD code, and employed in the simulation of the two-phase (gas-liquid) dispersed flow in an aerated stirred vessel.

The Moments Model

The population balance

The population balance equation (PBE) for the temporal evolution of the bubble number density n due to break-up and coalescence can be formulated as follows (Hulburt and Katz 1964):

$$\frac{\partial n}{\partial t} = B_B - D_c + B_c - D_c \quad (1)$$

where the bubble number density $n = N/\Delta DV$ is the number N of bubbles in the control volume V with the size $D \pm \Delta D/2$ at time t . ΔD is the bubble size class width. B_B and B_c are birth rates in a certain bubble size class due to a break-up of bigger bubbles and coalescence of smaller bubbles. D_B and D_c are death rates in this class resulting from break-up into smaller bubbles and coalescence with other bubbles, respectively. The rate functions are referred to as *kernel functions* and formed with the break-up frequency, the number and size distribution of daughter bubbles in the break-up case as well as collision frequency and efficiency for the determination of the coalescence rate. More detailed descriptions of the PBE, including changes in local bubble diameter due to mass transfer and in bubble number due to convective transport as well as the kernel functions employed in this work can be found in the literature (e.g. Millies and Mewes 1996; Gharaibah and Polifke 2002).

Flow chart of the moments model

In CFD simulation of multiphase flow, the computational domain is usually divided into tens or hundreds of thousands of control volumes. A complete CFD model with PBEs calculated in each cell, with a number of size groups sufficient to obtain a realistic particle size distribution, will typically exceed presently available computational resources. In the moments model suggested here, the size distribution of the bubbles is represented by a number density function of presumed shape – i.e. presumed functional form – per which the size distribution is determined by the first two moments of the bubble diameter, i.e. mean μ and variance σ^2 . Possible functional distributions f must satisfy a normalization condition, e.g. $\int_0^1 f(D; \mu, \sigma^2) dD = 1$; then the distribution can be scaled according to the gas volume fraction to yield the actual bubble number density n_f .

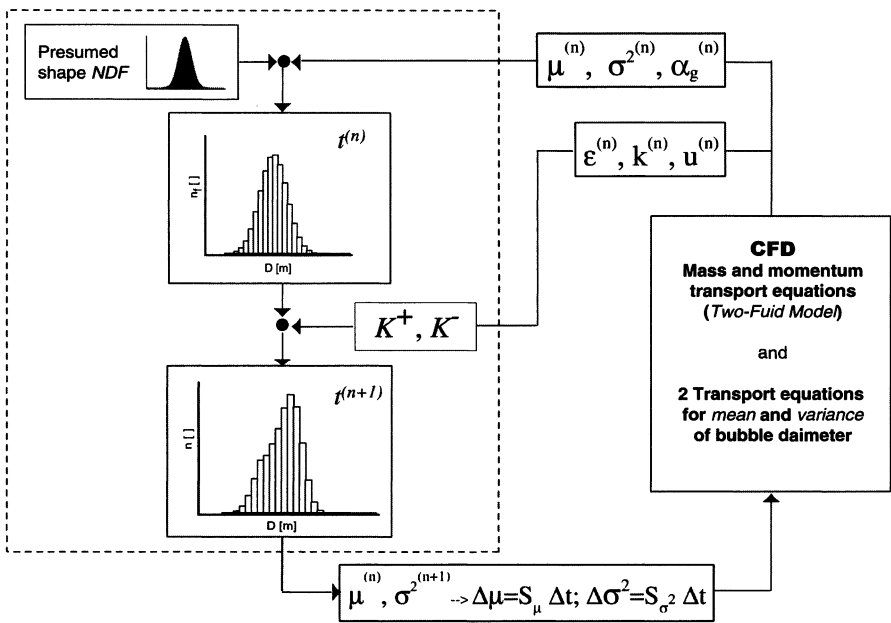


Fig. 1. The functionality of the proposed moments model and the links to the CFD.

The evolution of the population balance over a short time interval dt – a time step in the numerical simulation – proceeds then as follows: Given certain values for the mean and variance, the kernel functions for bubble break-up and coalescence act in the usual manner on the presumed shape NDF to generate new values for mean and variance. Fig. 1 illustrates the principle of the proposed model in a flow chart.

In the CFD model, the usual equations of mass and momentum transport for the gaseous and the liquid phase are solved. Additionally, two transport equations are solved for the first two moments of the bubble diameter. These equations contain source terms accounting for bubble break-up and coalescence, which depend on the local values of mean and variance of bubble diameter as well as gas volume fraction and flow parameters (dissipation rate, velocity gradients, etc.). It is advantageous to generate a lookup-table with source terms S_μ and S_σ^2 in a pre-processing step, which is then accessed during the CFD computation. As mentioned above, arbitrary kernels can be implemented in the moments model in principle. Different formulations for the kernel functions may depend on different flow parameters and fluid properties, thus a tabulation system with a locally adaptive algorithm and arbitrary dimensioning has been implemented. A detailed description of the tabulation system may be found in (Gharaibah et al. 2002).

Representation of the size distribution by a presumed shape number density function

The computational scheme outlined in the previous section is very flexible in the choice of kernel functions for dispersion and coalescence, and it may be expected that it is computationally robust and effective. However, it is in general not possible to prove a priori that a number density function of a certain shape will adequately represent the bubble size distribution for a given multiphase flow. Therefore, solutions of the population balance equations with presumed shape NDF have been validated against a reference solution obtained by direct solution of the PBE. For this validation study, a spatially homogeneous system has been chosen, starting from an initially nearly mono-disperse bubble distribution with large mean bubble size and relaxing with time towards an asymptotic state with much smaller mean diameter, where coalescence and dispersion are in dynamic equilibrium.

In this context it is of course important that the reference solution be *discretization independent*, i.e. the number of size classes nc should be chosen so large, that a further increase in nc brings no discernible change in the evolution of the bubble population. The influence of the size group number nc has been investigated in a preliminary study by direct numerical solution of the PBE with varying numbers of size groups and several initial bubble distributions. A detailed description of

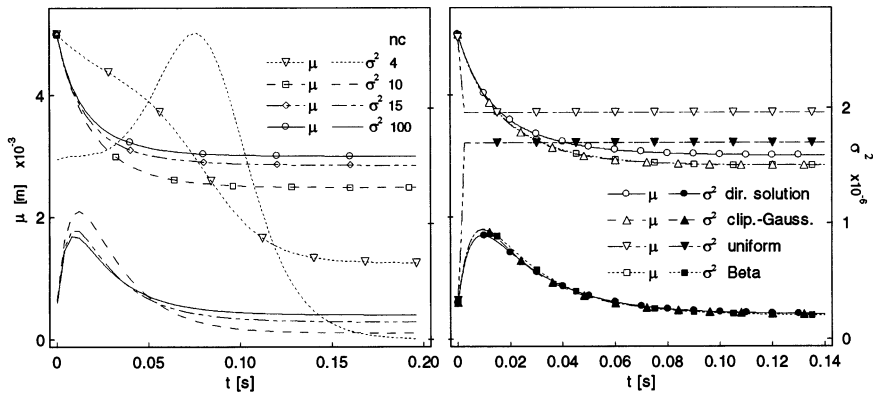


Fig. 2. The mean and variance of the bubble diameter resulting from the direct solution of the PBE in its general form with different bubble size groups number (left) and the comparison of this direct solution – with 100 classes – to the PBE solution, in which the bubble size distribution is represented by a presumed shape of NDF – clipped-Gaussian, beta, and the uniform distribution – (right).

these conditions as well as the assumed flow parameters and rate functions – turbulent dissipation, collision frequency, collision efficiency, droplet break-up frequency, size distribution of daughter droplets – are given in (Gharaibah and Polifke 2002). Figure 2 (left) shows the temporal evolution of bubble diameter means and variances computed with various bubble size group numbers $nc = 4, 10, 15, 100$. The solution with $nc = 100$ agrees very well with a case $nc = 200$ (not shown) and may therefore be considered to be discretization independent. With only 4 size classes – which is often the maximum permissible number of classes in CFD simulations with a discretized PBE – the solution very severely underpredicts the mean bubble diameter obtained in quasi-steady state. Even with 10 or 15 size classes agreement with the reference solution is barely acceptable.

Results obtained with a presumed shape number density function are compared with the direct solution of the PBE – all with $nc=100$ – in Fig. 2 (right). Three different functional forms were used in this comparison, i.e. the so-called *uniform* or *top-hat*, the *clipped-Gaussian* and the β -function. All three distribution functions are unambiguously related to their means and variances, and satisfy the normalization condition mentioned above. Note that the clipped-Gaussian as well as the β -function may assume a bi-modal shape for large variances. Further details on the functional forms are discussed in (Gharaibah and Polifke 2002).

Good agreement between the direct solution and the solutions with the β - as well as the clipped-Gaussian- function is found. The solution with the uniform function is unacceptable and shall not be discussed further. Comparing with the left side of Fig. 2 , we note that the direct solution obtained with 10 size classes shows a larger discrepancy with the reference case than solutions obtained with the β or clipped-Gaussian distributions.

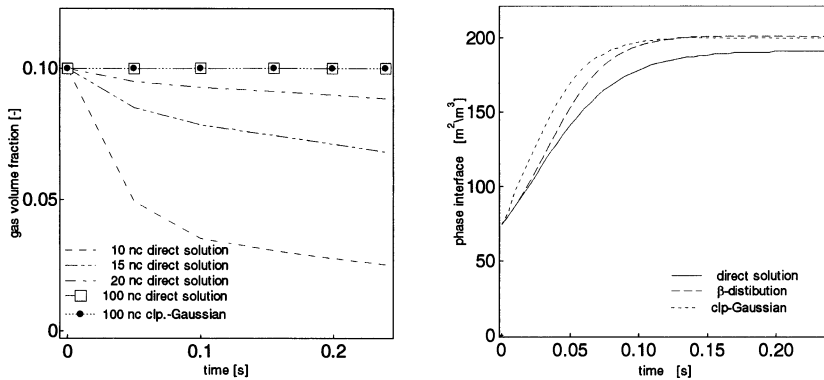


Fig. 3. The gas volume fraction conservation resulting by solving the PBE with different number bubble size groups and with presumed shapes of the number density function (left) and the specific phase interface area resulting by direct solving of PBE and with presumed shapes of the number density function.

Note that we have chosen to discretize the size classes in terms of bubble diameter rather than volume. This has the advantage that a wider range of bubble sizes can be represented with a given number of size classes. However, in this formulation, total gas volume fraction will not be conserved adequately if an insufficient number of size classes is chosen. Figure 3 (left) shows the degree of gas volume fraction conservation achieved by solving the PBE. The volume is conserved very well by the $nc = 100$ reference solution. Figure 3 (left) also shows that the gas volume is *fully* conserved by the solution of the PBE with the clipped Gaussian function. This is also true for the β -function (not shown).

One important objective of the simulation of dispersed two phase flows is the determination of the phase interface area, over which mass, heat or chemical species are exchanged between the phases. Figure 3 (right) shows the specific phase interface area obtained via direct solution of PBE and with presumed shape number density functions. The phase interface area increases due to the dispersion of bubbles until it reaches a constant value once the bubble population approaches the steady state with equilibrium between dispersion and coalescence. Both simulations with presumed shapes NDF reproduce this behavior with acceptable quantitative agreement.

It is concluded that for the spatially homogeneous disperse two phase flow considered in this validation study, the evolution of bubble size distribution due to break-up and coalescence can be well represented with the β - as well as the clipped-Gaussian functions for the number density. Whether this holds true also for flow in an aerated stirred vessel can only be determined by comparison with experiment, because obviously it is not possible to generate a reference solution by means of a direct, discretization independent solution of the PBE with present computational means. Validation of the moments model against experimental data is the subject of ongoing work.

It should also be pointed out that the choice of presumed shape functions is not limited to the forms considered in this study. Although both the β - as well as the clipped-Gaussian functions are quite flexible and can indeed assume bi-modal shapes, one can imagine flow configurations where an extended moments ansatz is required, depending e.g. on more than just two parameters or more than just one set of transport equations to describe the size distribution of the disperse phase.

CFD Implementation and Simulation Results

Two main techniques are in use to model the flow in a stirred vessel with a rotating impeller: the fully time-dependent *sliding mesh* (*SM*) approach (Luo et al 1994) and an approximate steady-state approach known as the method of *multiple reference frames* (*MRF*) (Luo et al. 1993). Also, the flow in stirred vessels is usually turbulent, and due to the significant streamline curvature found, the use of the Reynolds-Stress (RSM) turbulence model rather than the standard k - ϵ might be called for.

As a preliminary to the implementation of the moments model in a three-dimensional, finite-volume based CFD code, a validation study has been carried out for *single-phase* flow in a stirred vessel, with the goal of identifying the flow modeling approach most suitable for our purposes. Simulations of flow in a stirred tank with a 6-blade Rushton turbine and four baffles have been carried out with both impeller modeling methods as well as k - ϵ and RSM for the turbulence modeling. Also, the dependence of results on grid resolution has been explored. The results were compared to LDA data measured at the Lehrstuhl für Strömungsmechanik at Erlangen University. Due to lack of space, only a very brief synopsis of these results can be given here: 1) the results obtained with steady state MRF agree well with the more time consuming sliding mesh-results for the vessel geometry investigated. 2) Both simulation results with the k - ϵ model agree well with the velocity fields and turbulent kinetic energy (k) measured by LDA. Discrepancies are observed in the immediate vicinity of the impeller; Fig. 4 shows the k -values in a mid-plane between two baffles in the height of the impeller. Neither the LDA measurements nor the simulation with the k - ϵ model achieve the desired accuracy in the vicinity of the impeller, presumably due to the complex instationary and anisotropic flow pattern in this region. 3) Grids with 110000 cells represent a reasonable compromise between CPU requirements and accuracy.

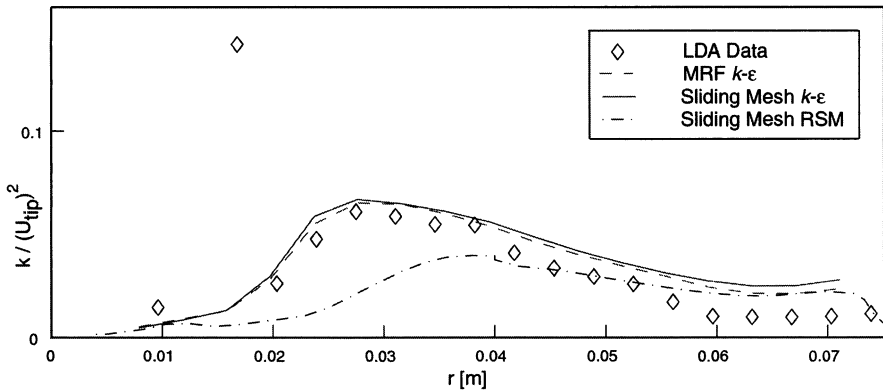


Fig. 4. The turbulent kinetic energy in a mid-plane between two baffles in the height of the impeller. LDA data vs. simulation results with SM-, MRF-techniques, $k-\epsilon$ and RSM.

The moments model with full momentum coupling and source terms for bubble diameter mean and variance as described above has been implemented in the CFD code CFX-5.5.1. First exploratory simulations with the MRF approach and the $k-\epsilon$ turbulence model have been carried out for a disperse gas-liquid flow in an aerated stirred vessel with a downward pumping turbine. Fig. 5 shows the distributions of bubble size diameter (right) and the velocity field of the fluid phase (left) in the lower part of the vessel. These results must be considered preliminary, nevertheless they exhibit physically reasonable behaviour: near the injection nozzle, the mean diameter is close to the initial value of 6 mm. As the bubbles are transported down- and outwards by the flow, the bubble size decreases quickly due to the intense turbulent shearing. Above the turbine, a nearly constant bubble diameter of the order of 3.5 mm is established. Bubbles of this radius have sufficient surface energy to withstand the low local shear stresses in this region.

At the time of writing, it is not clear whether the decrease in bubble diameter found below the injection nozzle towards the center of the vessel is physically correct or an artefact of the numerical model. In future work, the moments model will be validated comprehensively against experimental data on bubble size distribution in a stirred vessel (Ilchenko et al. 2002).

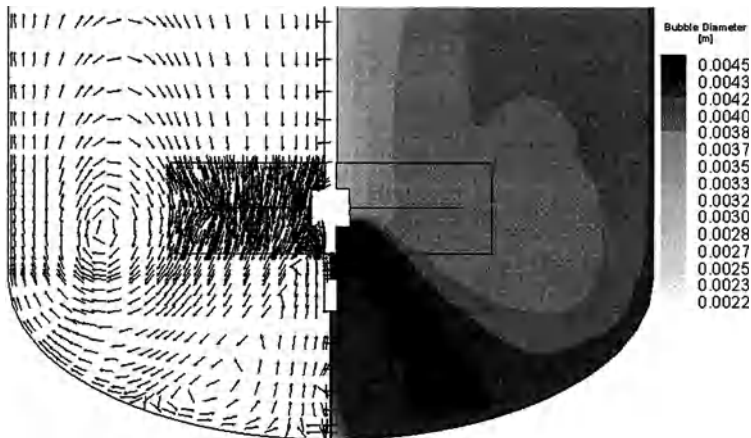


Fig. 5. The distribution of the bubble size diameter (right) and the vector plot of the velocity field of the fluid phase (left) in the stirred vessel.

Conclusions and Outlook

The population balance equation is in principle a suitable method to represent the size distribution of the disperse phase in two phase flows (gas bubbles – fluid). A complete CFD model with PBE calculated explicitly in each cell for a number of particle size groups sufficient to obtain a reasonable particle size distribution is, however, not affordable with present computational means. In the last few years, several multiphase models have been developed to describe the transient evolution of the bubble size distribution resulting from the break-up and coalescence processes with the help of a simplified PBE or with only a few bubble size groups. However, these methods are limited in accuracy or in their range of applicability.

In this paper, we propose a novel approach to simulate disperse two phase flow by solving the PBE for bubble size distribution by a number density function of presumed shape. First, the dependence of the PBE solution on the number n_c of particle size classes has been explored. For a spatially homogeneous disperse system, it has been found that significantly more than 10 size classes are needed to approach a solution independent of discretization. Secondly, a direct solution of the full PBE with well-established break-up and coalescence kernels from the literature was compared against a solution of the PBE, in which the size distribution of the bubbles was represented by a NDF of presumed shape. Good agreement has been achieved with the β - and clipped-Gaussian distributions. Arbitrary break-up and coalescence kernels can be implemented in the model and during pre-processing a great number of bubble size groups may be used to achieve discreti-

zation independence for the PBE. First simulations of a gas-liquid disperse flow in a stirred vessel with the proposed model show physically reasonable results, a very satisfactory numerical stability and a significant reduction in computation time.

Acknowledgments

This project was supported by the Deutsche Forschungsgemeinschaft as part of the Schwerpunktprogramm 1018 "Analyse, Modellierung und Berechnung mehrphasiger Strömungen". Generous support by M. Brandt (TU München), A. Maltsev and J. Janicka (TU Darmstadt) in adapting the look-up table generation algorithm to the special requirements of a PBE is greatly appreciated. B. Genenger, A. Nassar and F. Durst (Univ. Erlangen) have provided experimental validation data and helpful comments on the nature of the flow field in a stirred vessel.

References

- Ilchenko V, Maurus R, Sattelmayer T (2002) Influence of the Operating Conditions on the Bubble Characteristics in an Aerated Stirred Vessel. In this proceeding.
- Ishii M. (1975) Thermo-fluid dynamic theory of two-phase flow. Eyrolles, Paris.
- Luo J Y, Gosman A D, Issa J C, Fitzgerald M. K. (1993) Full flows Field computation of mixing in based stirred vessels. *Trans IChemE* 71A: 342—344.
- Luo J Y, Issa R I, Gosman A D (1994): Prediction of impeller-induced flows in mixing vessels using multiple frames of reference. *IChemE Symp.* 136: 549—556.
- Millies M, Mewes D (1996) Phasengrenzflaechen in Blasenstroemungen -- Teil 1: Blasen-saeulen. *Chem. Ing. Tech.* 68: 660-669.
- Gharaibah E, Polifke W (2002) A Numerical Model for the Simultion of Dispersed Two Phase Flows based on Presumed Shape Number Density Functions. 10th Workshop on Two-Phase Flow Predictions, Merseburg, Germany, April 2002. ERCOFTAC.
- Gharaibah E, Brandt M, Polifke W (2002) A Numerical Model of Dispersed Two Phase Flow in Aerated Stirred Vessels based on Presumed Shape Number Density Functions. German-Japan Workshop on Multi-Phase Flow. Karlsruhe, Germany, August 2002.
- Lo S (1999) Application of Population Balance to CFD Modelling of Bubbly Flows via the MUSIG Model. 4th Int. Conf. on Gas-Liquid and Gas-Liquid-Solid Reactor Engineering, Delft 1999.
- Lo S (2000) Some Recent Developments and Applications of CFD to Multiphase Flows in Stirred Reactors. AMIF-ESF Workshop: Computing Methods for Two-Phase Flow, Aussois, France, 12-14 January 2000.
- Randolph A (1964) A Population Balance for Countable Entities. *Can. J. Chem. Eng.* 42: 208-281.
- Valentas K J, Amundson N R (1996) Breakage and coalescence in dispersed phase system. *Industrial and Engineering Chemistry Fundamentals* 5: 533—542.

Influence of the Operating Conditions on the Bubble Characteristics in an Aerated Stirred Vessel

Volodymyr Ilchenko, Reinhold Maurus, Thomas Sattelmayer

Lehrstuhl für Thermodynamik, Technische Universität München, 85747 Garching, Germany, phone: + 49-89-28916238, fax: +49-89-28916218, e-mail: ilchenko@td.mw.tum.de

1. Introduction and Goal of the Study

Aerated stirred vessels are widely used in the chemical and process industry. In these vessels the interfacial area between the two phases and the gas hold-up characterize the efficiency of the gas-liquid contact. Whereas the interfacial area determines the heat and mass transfer rate, the gas hold-up determines the residence time. For these reasons, improving the knowledge concerning the bubble characteristics, namely their sizes, spatial coordinates and number is of primary importance. These parameters depend on the operating conditions, such as the volumetric flow rate of the gas, the type and speed of the impeller, the injector type and its geometry and the physical properties of the liquid phase. From the viewpoint of the technical application the development of empirical correlations is of major interest (Bouaifi at al. 2001; Paglianti at al. 2000; Rewatkar at al. 1993; Yawalkar at al. 2002; Zhengming at al. 1996). Most often, these equations show good agreement when they are compared with the database which they are based on, but they often fail to predict the gas hold-up for the other operating conditions (Yawalkar at al. 2002). In particular, difficulties have been reported for extremely low gas hold-up and low gas flow rate, which are of major interest for the validation of numerical two-phase codes.

In order to provide a wider range of experimental results, the entire volume of a stirred aerated vessel has been recorded by means of the non-intrusive short time holography (Mayinger 1994). The optically reconstructed distribution of the interfaces between both phases from the hologram is saved as a series of 2D images representing slices of the entire vessel at different depth positions. These slices are generated by an intensified CCD camera with a small depth of focus moving in the depth direction with respect to the hologram during the reconstruction. For the fully automated processing of the images, for the determination of the bubble characteristics and the numerical reconstruction of the 3D phase distribution in the vessel, powerful imaging routines have been developed, which do no longer re-

quire manual control of the data-handling. In additional, post-processing steps, the gas hold-up, the interfacial area and the bubble size distribution are calculated.

Since the novel analysis method for the holographic images allows processing of a wide database, the holographic technique could be applied for the first time for the analysis of many configurations, fluids and operating points. The gas flow rate, the impeller type and speed, the type and the geometry of the injector and the liquid viscosity have been investigated in detail. The most important results from this study are presented in the second part of the paper after the experimental technique and the data evaluation procedures have been presented.

2. Measurement Technique

The short time holography allows to record non-intrusively the whole optical information about the light scattered or reflected at the phase interfaces of two phase flows. All objects with sizes above approximately ten times the wavelength of the used laser light are detected. Furthermore, moving objects are imaged sharply due to the short exposure time. For the recording of the holograms an optical set-up, proposed by Feldmann and Mayinger (1998), is applied (Fig. 1a). In order to avoid refraction of the laser light on the cylindrical surface of the aerated vessel, the last one is placed into a cubic enclosure. The space between the two vessels is filled with glycerin, which has the same refractive index than the glass. After appropriate chemical processing the recorded hologram is placed in the reconstruction set-up (Fig. 1b). By illumination of the hologram with a continuous laser beam the original test volume is optically reconstructed.

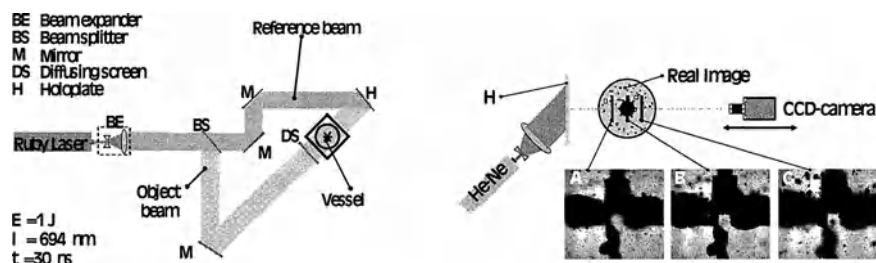


Fig. 1. Recording (a) and reconstruction (b) set-ups

During the reconstruction, a CCD camera (Hamamatsu C2400-07, 512x512 pixels, 8 bit) is shifted in depth direction in order to isolate 2D planes from the 3D image. The volume is recorded slice by slice and digitally stored in terms of a series of 2D images. For a sufficient resolution, the field of view of the employed camera had to be restricted to 40x40 mm² and the entire volume of the vessel was split into smaller subvolumes during the reconstruction in order to retain the full resolution of the hologram and to evaluate the entire vessel volume.

Although the CCD camera has a small depth of focus, this depth is nevertheless finite. As a consequence, bubbles usually appear in more than 1 slice and the true depth position must be defined using a suitable postprocessing algorithm. This problem can be overcome if a second hologram perpendicular to the first is recorded, as proposed by Feldmann and Mayinger (1998), at the expense of a higher complexity of the set-up and the data processing. After reconstruction of the two perpendicular views of the test volume a stereomatching algorithm can be applied in order to detect the depth coordinates of the bubbles. The advantage of the advanced data processing method described below is the simplicity of the set-up for recording and reconstruction of the holograms. The phase distribution in the vessel is recorded only from one side and the depth coordinate of the bubbles is determined by means of novel image processing routines. Due to the improved software evaluation of the 2D images the hardware requirement for holographic method is considerably reduced and the optical reconstruction procedure is simplified.

3. Image Processing

As the first step of the evaluation, the series of 2D images representing the 3D test volume is converted into a 3D matrix, which serves as the base for the subsequent image processing steps. In order to remove high frequency noise in the images, they are filtered by a 3x3 finite impulse response (FIR) filter. Then, several morphological operators are applied one after the other (Crespo et al. 1995; Serra and Soille 1994; Vincent 1993). The first one removes white dots in the bubble images, which appear due to reflection of the light on the spherical surfaces of the bubbles and the second improves the uniformity of the image background. In the next step the generation of the binary image is performed with the threshold level adjusted on the basis of the statistic information of the grayscale image (Fig. 2).

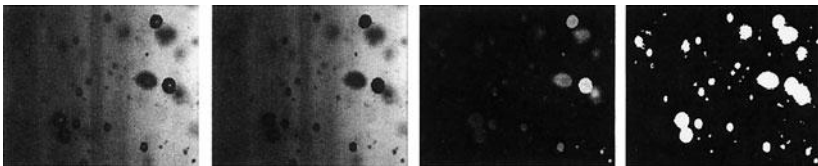


Fig. 2. Original image (a), white dots removing (b), equalization of the background (c), binary image generation (d)

Since for low contrast between the bubbles and the background a suitable threshold is difficult to select, the binary images of such bubbles do not represent their contours accurately. Therefore, an additional algorithm, based on the active contour model, also known as “snakes”, is applied for precise contour detection (Fig. 3). The applied model uses a gradient vector flow (GVF) as the external force (Xu and Prince 1998). For the computation of the GVF, the gradient map of the grayscale image is calculated. The “snake” with initial circular shape is placed

around the bubble of interest, with the radius and the position calculated from the binary image of the bubble. During the iterations of the “snake”, the maximum distance between two iterations is calculated. As soon as this value drops below a properly preset value, the snake has approximated the true bubble shape as precise as possible and a new binary array with the improved bubble contours is finally generated.

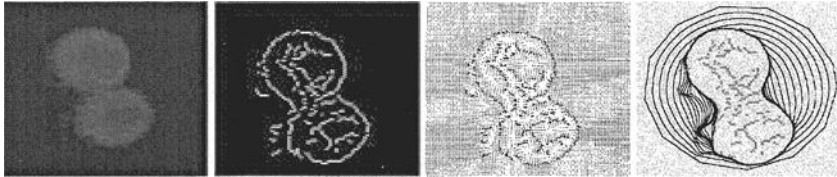


Fig. 3. Cropped gray-scale bubble image (a), gradient map (b), GVF computation (c), iterations of the snake (d)

The next routine solves the problem of the overlapping bubbles (Fig. 4). This procedure starts from the detection of a marker for each bubble by dilating the regional maximums of the distance transform. The result of the distance transform is illustrated as topographic surface and the detected markers as light dots above the bubbles. The watershed algorithm is now applied (Beucher 1992). The detected watershed lines are shown as dark lines.

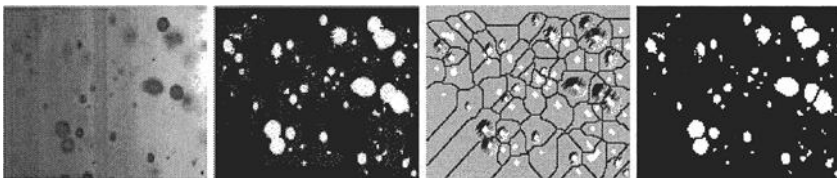


Fig. 4. Gray-scale image (a), binary image (b), dilated regional maximums of the distance transform and watershed lines detection (c), bubble separation (d)

An additional algorithm had to be developed for the detection of the bubble depth position, since, as already mentioned, the bubbles are found in more than one slice of the investigated volume. Fortunately, only one slice contains a sharp image of each bubble. The bubble image sharpness is numerically expressed in terms of a sharpness value, which is defined as the sum of the gradient intensity values on the bubble contour, normalized with the contour length in order to make it independent from the bubble size. This sharpness value unfortunately depends on the contrast of the bubble image and the background. Therefore, simply choosing a preset value of the sharpness for the determination of the bubble position leads to errors. To overcome this problem, a tracking algorithm was developed, which follows each bubble in all slices where it is visible and generates a vector of the sharpness values (Fig. 5a). The peak value corresponds to the focus position of the bubble being tracked. Finally, only the bubbles in the focus positions are saved in the binary array and all unsharp images of the bubbles are deleted from the

dataset. The volume of each bubble is calculated subsequently assuming a spherical bubble shape. Since the information concerning the spatial position of all bubbles is now available, the phase distribution in the test volume can be numerically reconstructed (Fig. 5b).

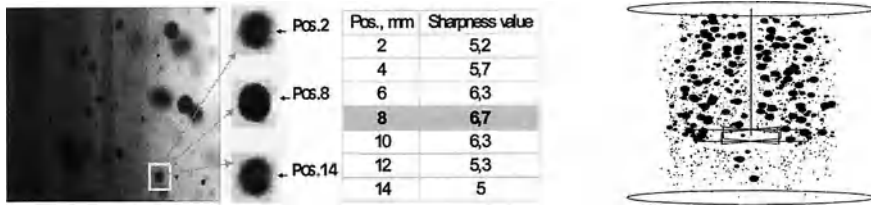


Fig. 5. Bubble image in different slices and sharpness values (a), numerically reconstructed test volume (b)

4 Results

The experiments were carried out in a plexiglas vessel with $T = 0.124$ m. The vessel was equipped with four baffles (0.0124 m depth) and a standard Rushton turbine (RT) with 6 blades. A six blade pitched turbine with a pitch angle of 45° (PTD) was used additionally in the study (flow direction downwards). Both turbines had a diameter ratio of $D/T = 1/3$. The liquid height to vessel diameter ratio was $H/T = 1$ throughout the study. The clearance of the impellers to the vessel base was $T/3$. The fluid used in most experiments was Dimethyl sulfoxide (DMSO) with a viscosity of $\mu = 2.48$ mPas, a density of $\rho = 1100$ kg/m³ and a surface tension of $\sigma = 43$ mN/m.

4.1 Influence of the gas flow rate and the impeller speed

The gas flow rate and the impeller speed are the factors that influence the gas dispersion and hold-up most (Lin and Lee 1997). Higher impeller speeds lead to increasing turbulence of the flow, to an augmentation of bubble break up in the shear zone near the impeller and to smaller bubbles (Fig. 6a). Since the fluid employed has a low surface tension of $\sigma = 43$ mN/m and, as a consequence, bubble coalescence is weak, this effect is stronger than for water. The expected higher mean bubble diameter for the higher gas flow rate due to the bubble coalescence (Dhainaut 2002) is not observed for the regime of low gas hold-ups investigated. Both, the presence of smaller bubbles, which have lower drift velocity and a larger residence time as well as the increase of flow intensity result in larger bubble numbers, gas hold-ups and interfacial areas in the vessel at higher impeller speeds (Figs. 6b, 7). The larger gas flow rate results in larger bubble numbers, gas hold-ups and interfacial areas over the entire covered range of impeller speeds investigated.

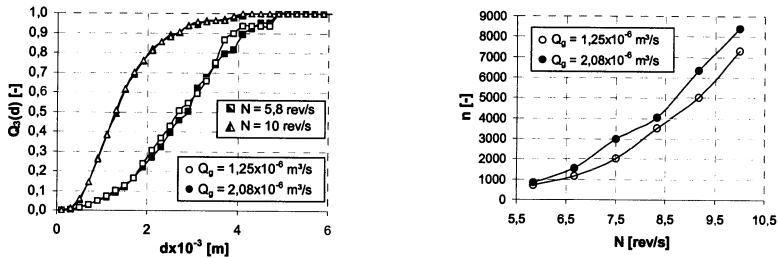


Fig. 6. Cumulative volume distributions $Q_3(d)$ (a) and bubble number n (b) for gas flow rates $Q_g=1.25 \times 10^{-6} \text{ m}^3/\text{s}$ and $Q_g=2.08 \times 10^{-6} \text{ m}^3/\text{s}$ vs. impeller speed N

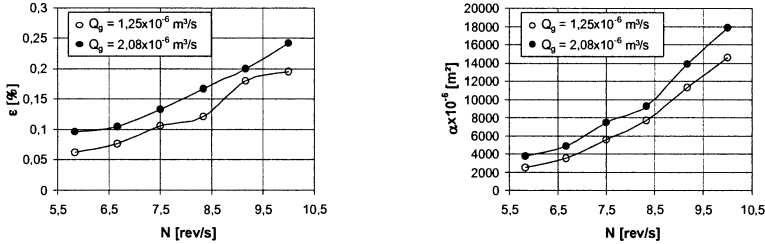


Fig. 7. Gas hold-up ϵ (a) and interfacial area α (b) for gas flow rates $Q_g=1.25 \times 10^{-6} \text{ m}^3/\text{s}$ and $Q_g=2.08 \times 10^{-6} \text{ m}^3/\text{s}$ vs. impeller speed N

4.2 Influence of nozzle diameter

In addition to the reference nozzle with 0.5 mm orifice a nozzle with 0.2 mm diameter has been investigated. The bubble characteristics was compared for the different impeller speeds and for a fixed gas volume rate $Q_g=2.08 \times 10^{-6} \text{ m}^3/\text{s}$. In the vessel equipped with the smaller diameter nozzle the bubble number is considerably bigger for low stirrer speeds (Fig. 8b). Surprisingly, the cumulative volume distributions in the vessel are nearly identical for the two nozzles (Fig. 8a). A smaller injector orifice and consequently a high injection momentum does obviously not lead to a finer average bubble size distribution in the vessel.

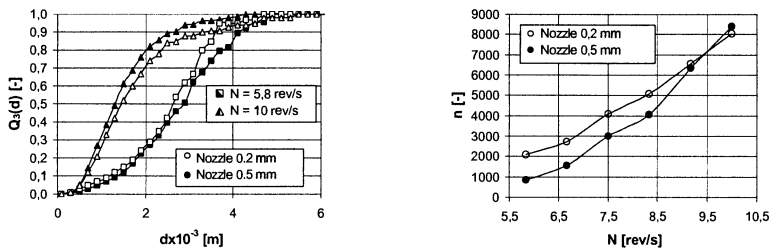


Fig. 8. Cumulative volume distributions (a) and bubble number (b) for nozzles with 0.2 mm and 0.5 mm diameter vs. impeller speed N

The higher total number of bubbles in the vessel for the nozzle with 0.2 mm diameter results in higher gas hold-ups and interfacial areas (Fig. 9). It is worth to note, that both injectors behave differently only for low impeller speeds, whereas at the higher impeller speeds the higher flow velocity and turbulence as well as the increased shear dominates the process of bubble formation.

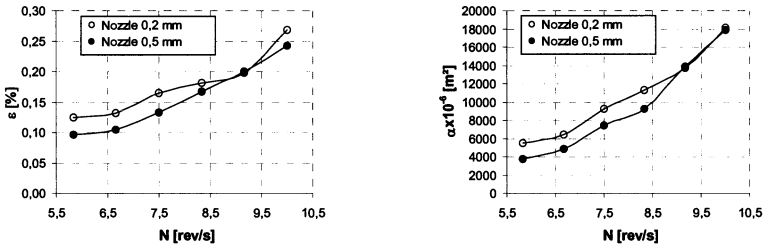


Fig. 9. Gas hold-up ϵ (a) and interfacial area α (b) for nozzles with 0.2 mm and 0.5 mm diameter vs. impeller speed N

4.3 Influence of the liquid viscosity

The influence of the liquid viscosity was investigated using mixtures of DMSO and Glycerin ($\mu = 1490$ mPas, $\rho = 1260$ kg/m³, $\sigma = 72.9$ mN/m). Both fluids have almost the same density and refractive index and can be mixed in any ratio. Thus, the viscosity can be adjusted in a wide range from 2.5 mPas (pure DMSO) up to 1490 mPas (pure Glycerin). In the experiments the range from 2.5 up to 50 mPas was covered ($7097 > Re > 352$).

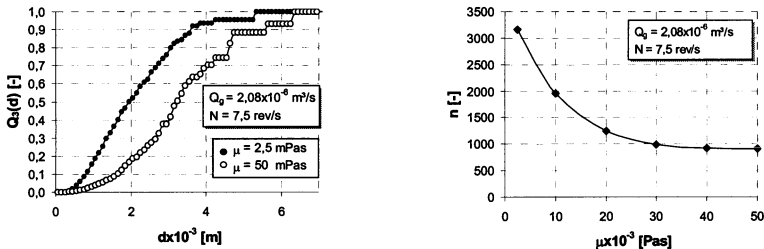


Fig. 10. Cumulative volumetric distributions $Q_3(d)$ (a) and bubble number n (b) vs. viscosity μ

With increasing liquid viscosity the bubble mean diameter is growing considerably due to the decrease of the flow turbulence and the lower intensity of bubble break-up (Fig. 10a). This effect is also noted by Dhainaut (2002). Due to the lower bubble break-up rate lower total bubble numbers in the vessel are observed (Fig. 10b). The gas hold-up does not change considerably, although the bubble mean diameter is increasing with viscosity (Fig. 11). As the direct result of the mentioned effect, the interfacial area drops when the viscosity is increased up to 30mPas, but it remains almost unchanged above this upper limit.

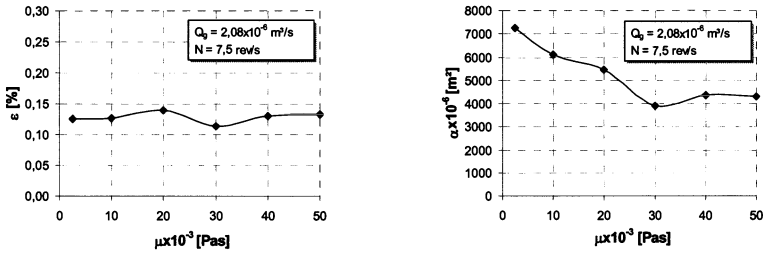


Fig. 11. Gas hold-up ε (a) and interfacial area α (b) vs. viscosity μ

4.4 Influence of the impeller type

In addition to the Rushton turbine (RT), the performance of a pitched blade turbine (downward flow, PTD) has been investigated, as both turbines are commonly employed in practice (Joshi at al. 1982). The experiments for PTD were carried out for the same impeller speeds than for the RT. The performance of both impeller types has been investigated as a function of the power consumption per liquid mass in the vessel. This comparison reveals, that the PTD produces much bigger mean diameters than the RT (Fig. 12a). At the same time the number of bubbles is bigger in the vessel with the RT and this difference is increasing with impeller power (Fig. 12b).

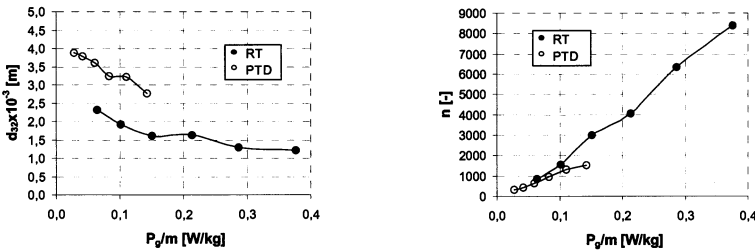


Fig. 12. Bubble Sauter mean diameter d_{32} (a) and bubble number n (b) for the RT and the PTD vs. power consumption per liquid mass P_g/m

The reason for this behavior can be explained examining the flows generated by both turbines. The Rushton turbine produces high shear and low pumping, whereas the pitched blade turbine is a high pumping and low shear impeller (Yawalkar at al. 2002). Therefore, the Rushton turbine exhibits strong bubble break-up although the pumping capacity is insufficient for inducing a circulating motion of the bigger bubbles. In contrast, the pitched blade turbine has enough pumping power for the generation of this circular motion, but this is not equivalent to a high bubble break-up capability. The mentioned effects result in higher gas hold-ups for the pitched blade turbine with increasing agitation power (Fig. 13a). This effect is in good agreement with results presented by Rewatkar at al. (1993). Inter-

Interestingly, it was found, that the interfacial area generated by both turbines is almost the same (Fig. 13b).

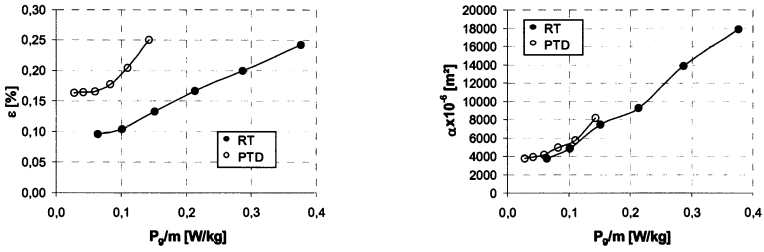


Fig. 13. Gas hold-up ϵ (a) and interfacial area α (b) for the RT and the PTD vs. power consumption P_g/m

4.5 Influence of the gas disperser type

In order to investigate the influence of the position and number of the gas injection holes a ring injector was additionally tested. It has four holes, which are symmetrically positioned on a radius of 15 mm. A diameter of 0.25 mm was selected having in mind to keep the pressure drop identical to the reference nozzle with one orifice of 0.5 mm diameter. The gas flow rate was kept constant at $Q_g = 2.08 \times 10^{-6}$ m³/s.

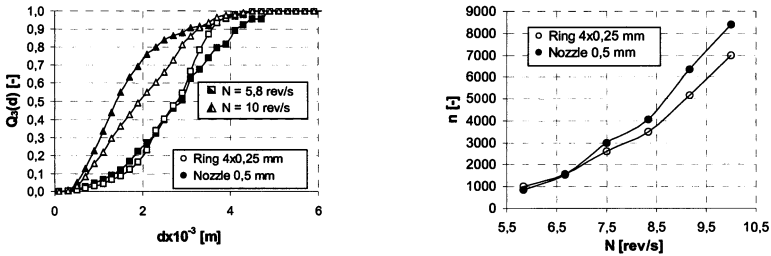


Fig. 14. Cumulative volumetric distributions $Q_3(d)$ (a) and bubble number n (b) for ring injector (4x0.25 mm) and nozzle (0.5 mm) vs. impeller speed N

The comparison of the cumulative volume distributions for both injectors reveals a more uniform bubble size distribution for the ring injector at low rotation speed. Interestingly, much larger bubble mean diameters were found at the high rotation speed (Fig. 14a), although the gas distribution is better for the ring injector. According to Fig. 14b the total bubble number is slightly lower for the ring injector at high speeds.

Above mentioned effects lead to a considerable increase of the gas hold-up and the interfacial area in the case of the ring injector (Fig. 15). This can be explained considering the location of the injector orifices in both cases. At the low rotation speed, when the circulation in the lower part of the vessel is weak, the bubbles

dispersed by the ring injector are more uniformly introduced into the impeller region. This results in a more uniform bubble size distribution after bubble break-up. For higher impeller speeds the increased circulation transports a big share of the produced bubbles directly into the upward circulating zone. As a consequence, the desired intense contact of all bubbles with impeller cannot be realized.

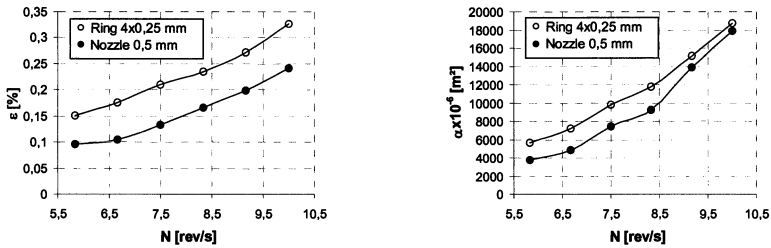


Fig. 15. Gas hold-up ϵ (a) and interfacial area α (b) for the ring injector (4x0.25 mm) and the nozzle (0.5 mm) vs. impeller speed N

5. Conclusions

Holography is a highly efficient non-intrusive optical measurement technique for the investigation of bubbly flows. The novel image processing technique developed in the study allows for the first time the fully automatic analysis of a wide database and releases the full potential of the holographic method, since the application to the investigation of two-phase flows becomes less cumbersome than in the past. This is demonstrated studying the influence of the operating conditions on the bubble characteristics in a stirred aerated vessel. A comprehensive database could be developed with limited effort and several interesting and so far unknown features of the bubbly flow were discovered which are useful for the improvement of stirrers for aerated vessels.

Nomenclature

d	bubble diameter, (m)
d_{32}	Sauter mean diameter, (m)
D	impeller diameter, (m)
H	height of clear liquid in vessel, (m)
m	mass of liquid, (kg)
n	number of bubbles in vessel, (-)
N	impeller rotational speed, (rev/s)
P_g	power input in presence of gas, (W)
$Q_3(d)$	cumulative volume distributions, (-)
Q_g	volumetric gas flow rate, (m ³ /s)
Re	Reynolds number based on impeller speed, ($ND^2\rho/\mu$)
T	inside diameter of vessel, (m)

Greek symbols

α	interfacial area, (m ²)
ε	gas hold-up, (%)
μ	liquid viscosity, (Pas)
ρ	liquid density, (kg/m ³)
σ	liquid surface tension, (N/m)

References

1. Beucher S (1992) The watershed transformation applied to image segmentation. *Scanning Microscopy* 6: 299-314
2. Bouaifi M, Hebrard G, Bastoul D, Roustan M (2001) A comparative study of gas hold-up, bubble size, interfacial area and mass transfer coefficients in stirred gas-liquid reactors and bubble columns. *Chemical Engineering and Processing* 40: 97-111
3. Crespo J, Serra J, Schafer RW (1995) Theoretical aspects of morphological filters by reconstruction. *Signal Processing* 47(2): 201-225
4. Dhainaut M (2002) Literature study on observations and experiments on coalescence and break-up of bubbles and drops. SINTEF report for NTNU-Department of Chemical Engineering
5. Feldmann O, Mayinger F (1998) Short-time holography applied to the three dimensional two-phase flow in an aerated, stirred vessel. 8th International Symposium on flow visualization. In Carlomagno GM, Grant I (eds) CD Rom Proc. of the 8th Intern. Symp. on Flow Visualization
6. Joshi JB, Pandit AB, Sharma MM (1982) Mechanically agitated gas-liquid reactors. *Chemical Engineering Science* 37(6): 813-844
7. Lin WW, Lee DJ (1997) Micromixing effects in aerated stirred tank. *J Chemical Engineering Science* 52: 3837-3842
8. Mayinger F (1994) *Optical measurements, techniques and application*, 1st edition, Springer Verlag, Berlin
9. Paglianti A, Takenaka K, Bujalski W, Takahashi K (2000) Estimation of gas hold-up in aerated vessels. *The Canadian J of Chemical Engineering* 78: 386-392
10. Rewatkar V, Deshpande A, Pandit A, Joshi J (1993) Gas hold-up behavior of mechanically agitated gas-liquid reactors using pitched blade downflow turbines. *The Canadian J Of Chemical Engineering* 71: 226-237
11. Serra J, Soille P (1994) *Mathematical morphology and its applications to signal processing*, Kluwer Academic Publishers, Dordrecht
12. Vincent L (1993) Morphological area openings and closings for grey-scale images. In O Y.-L, Toet A, Foster D, Heijmans HJAM, Meer P (eds) *Shape in Picture: Mathematical Description of Shape in Grey-level Images*, Springer Verlag, Berlin, pp 197-208
13. Xu C, Prince JL (1998) Generalized gradient vector flow external forces for active contours. *Signal Processing* 71(2): 131-139
14. Xu C, Prince JL (1998) Snakes, shapes, and gradient vector flow. *IEEE Transactions on Image Processing* 7(3): 359-369

15. Yawalkar A, Pangarkar V, Beenackers A (2002) Gas hold-up in stirred tank reactor. *The Canadian J of Chemical Engineering* 80: 158-166
16. Zhengming G, Yingchen W, Litian S, Jufu F (1996) Theoretical and experimental studies on bubble diameter and gas hold-up in aerated stirred tanks. *Chinese J of Chemical Engineering* 4(4): 283-289

Bubble dispersion in aerated stirred vessels

F. Mayinger, O. Feldmann

Lehrstuhl A für Thermodynamik, Technische Universität München
85747 Garching, Germany

Introduction

An important application of stirred vessels is to disperse a gaseous phase in a liquid phase in order to enhance mass transfer between the two phases. This is achieved by both enlarging the phase interface and prolonging the period of dwell of the gaseous phase in the vessel [22]. The optimum design of an aerated, stirred vessel depends on the requirements in terms of parameters such as generated phase interface, period of dwell of the gaseous phase, hold-up, and other quantities. These parameters may be linked. Design requirements are met by the correct choice of stirrer, rotational speed, and type and location of the gas injector. Therefore, a detailed knowledge is required of the number and size of bubbles generated as a function of the different operating points [22,23].

Though aerated stirred vessels are widely used, their design is based on empirical models. Common to each model is the assumption, that the mean diameter of the bubbles is proportional to their maximum stable diameter at the given operating point [1,2,3,12,14,18,19,20,21,24].

In the literature, the Rushton turbine is the standard dispersing stirrer [e.g.: 2,18,21,22]. However, since the experimental determination of bubble sizes in stirred vessels is very difficult, only few experimental data are available. These data are often gained with invasive measurement techniques that disturb the flow inside the vessel and therefore influence the measured quantities.

In this study, the investigations were performed by applying modern optical measurement techniques. These non-invasive measurement techniques do not influence the conditions in the test section during the measurements. The short-time holography was applied to determine the number and the size of the bubbles in the entire vessel at the different operating points. The high-speed cinematography was applied to analyze the dispersion process itself.

The dispersion characteristics of an aerated stirred vessel agitated by a Rushton turbine were analyzed. The different operating points were adjusted by varying the nozzle diameter, gas flow rate, and agitator speed. The results indicate, that neither the Rushton turbine is an appropriate stirrer to disperse bubbles, nor the mean bubble diameter is a measure for efficient bubble dispersion, when a Rushton turbine is applied.

Experimental Setup

A condition to apply optical measurement techniques is a complete optical access to the test section. The accrued design of the test section and the short-time holography is explained in the following [5,6,7].

Test Section

The cylindrical stirrer tank was located inside a rectangular vessel (see Fig. 1). Both vessels were made of glass. The clearance between the two vessels was filled with glycerin. As test fluid, Dimethylsulfoxide (DMSO) was chosen. Both fluids have the refractive index of the glass the vessels were made of. This setup ensured optical access to the entire test section without any distortion at the cylindrical surface of the stirrer tank [5].

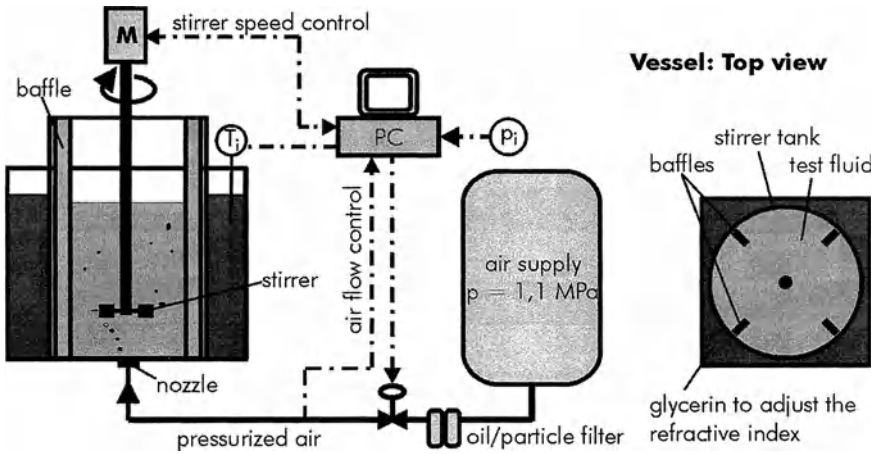


Fig. 1. Design of the test section.

The standard stirrer tank ($D = 124 \text{ mm}$) was equipped with four baffles to impede the formation of waterspouts. The filling level corresponded to the tank diameter ($H = D$). The diameter of the Rushton turbine was chosen to be $d/D = 1/3$. Its clearance from the bottom was set to be $h = d$. The air was supplied from a nozzle that was centrally located in the flat bottom of the stirrer tank (see Fig. 1).

The stirrer speed and the air flow during the experiments were adjusted, controlled, and measured by a PC [5].

Optical Measurement Technique: Short time holography

The test section was located in a stereoscopic holographic setup as it is shown schematically in Fig. 2. With this optical setup, two holograms were simultaneously recorded from two different perspectives at each operating point in order to correctly determine the size of non-spherical bubbles [5,6,7].

Recording the holograms

A pulsed ruby laser generates light pulses with a wavelength of $\lambda = 694 \text{ nm}$ and an energy of up to $E = 1 \text{ J}$ for the exposure time of $t = 30 \text{ ns}$. The emitted laser beam is collimated by passing through two lenses (CL) and is then split into two object beams and two reference beams by a bank of beamsplitters (BS). The object beams are diverted at the mirrors (M), are diffused by a ground glass plate (GG), then cross the test section perpendicular to one another. Upon exiting the test section, the object beams fall perpendicularly onto the holographic plates (H1, H2).

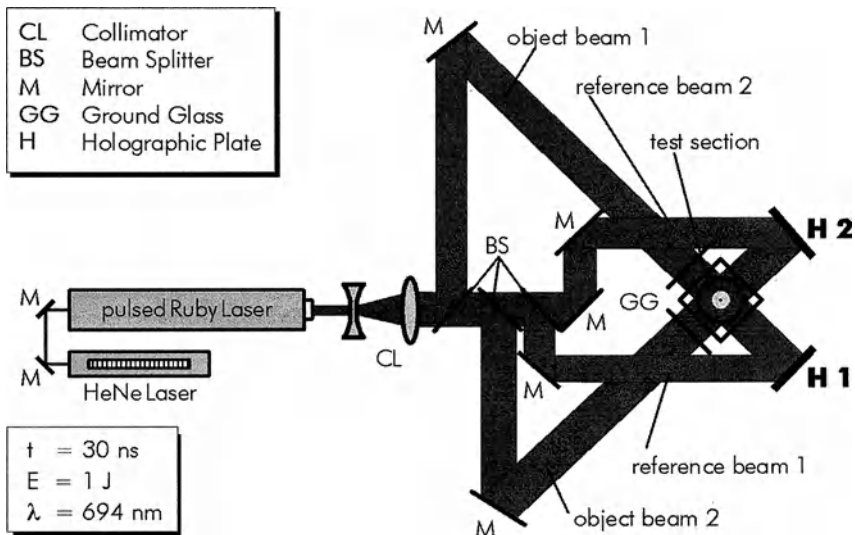


Fig. 2. Stereoscopic holographic setup for hologram recording

The object beams contain the entire optical information of the test section. The reference beams are diverted directly to the holographic (see Fig. 2). The superposition of an object beam and a reference beam results in an interference figure which is stored on the coating of the holographic plates. The situation inside the vessel is stored three-dimensionally and distortionless [4,6,7,9,17,18]

Both holograms contain both macroscopic information about the location of the bubbles and microscopic information, such as the number, size, and shape of the bubbles in the vessel [4,6,9].

Reconstruction and evaluation of the holograms

The exposed holographic plates of coated glass are developed similarly to black and white photographs. The developed plates - now called holograms - are reconstructed by illumination with a continuous HeNe laser beam. This laser beam simulates the reference beam during the exposure of the hologram with respect to its geometry and to its angle of incidence. The HeNe laser beam is diffracted by the stored interference figure. As a result, the object beam containing the entire optical information of the test section is reconstructed. In front of each holographic plate a stationary image, the real image of the recorded scene, is formed three-dimensionally and distortionless, as shown schematically in Fig. 3.

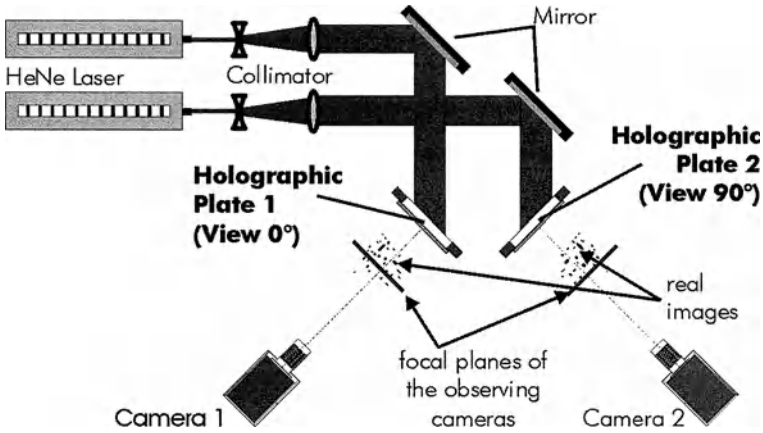


Fig. 3. Stereoscopic holographic setup for hologram reconstruction

The spatial information of the entire measuring volume is furnished in three dimensions with a width of approximately $d = 130$ mm and an infinite depth of field. This 3D image is recorded by means of a CCD-camera. The camera lens has a large focal length and a small depth of field, so that only a small fraction of a reconstruction is in focus, as indicated by the gray bars in Fig. 3 [4,6,9].

By moving the camera step by step along its depth coordinate, the entire 3D information contained in the holographic reconstruction is scanned and transformed into a series of 2D digital images (see Fig. 4). The depth of field determines the step size and thus the resolution in the depth dimension. The images depicted in Fig. 4 reveal how the field of view of the camera changes with its position. Bubbles that are depicted sharply in one image are out of focus at a different camera position [6,7].

Both holograms taken in one experiment are reconstructed and scanned as described above. They represent two 3D images corresponding to one situation in the test section, so that the entire 3D-information of the test section seen from two different views is provided in the form of digital images [4,6,9].

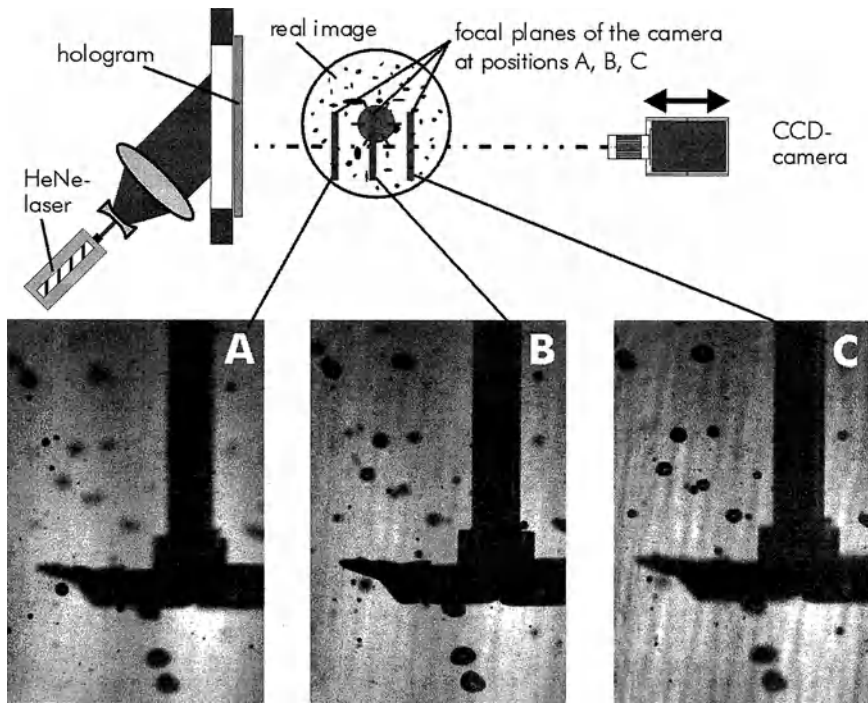


Fig. 4. Scanning of a reconstructed hologram

Image processing

The objective of image processing is to obtain an image with exclusively sharply depicted bubbles which are clearly separated from the background. The information about the shape, size, and location of the bubbles is subsequently derived from these images.

The obtained images show distinctive properties (see Fig. 4). Especially for high bubble densities and a small depth of field of the observing camera, only a small fraction of the bubbles visible in such an image is depicted sharply. The edges of these bubbles can be blurred by other bubbles reconstructed in different planes. In addition, the gray value of the background varies significantly due to the Gaussian profile of the laser beam intensity and defects inherent in the optical parts, such as the irregularity of the mirrors. Due to these peculiarities, commercially available image processing systems could not be applied. Therefore, evaluation software was developed in this study, to overcome these difficulties. Its algorithms are described in detail in [6,7].

Stereo matching of the two holograms

After both holograms taken at one operating point have been completely scanned into the series of 2D images and evaluated, the images are numerically reconstructed based on the obtained results. This results in two 3D reconstructions of the flow field in the vessel, displaying the same scenario from two perpendicular viewing directions. These two 3D images are correlated with one another by applying a stereo matching algorithm. The vertical and the lateral coordinates of each bubble are derived from one evaluated holographic reconstruction. The depth coordinate is derived from the position of the camera, but it can only be determined within the accuracy of the depth of field. Since the two holograms were recorded perpendicularly, the depth coordinate of a bubble in one holographic reconstruction is its lateral coordinate in the second.

Thus, by considering the vertical coordinate in both views, the position of each bubble can be determined exactly. The depth of field of the cameras is adjusted in such a way that this correlation is definite. The model upon which this algorithm is based is given schematically in Fig. 5.

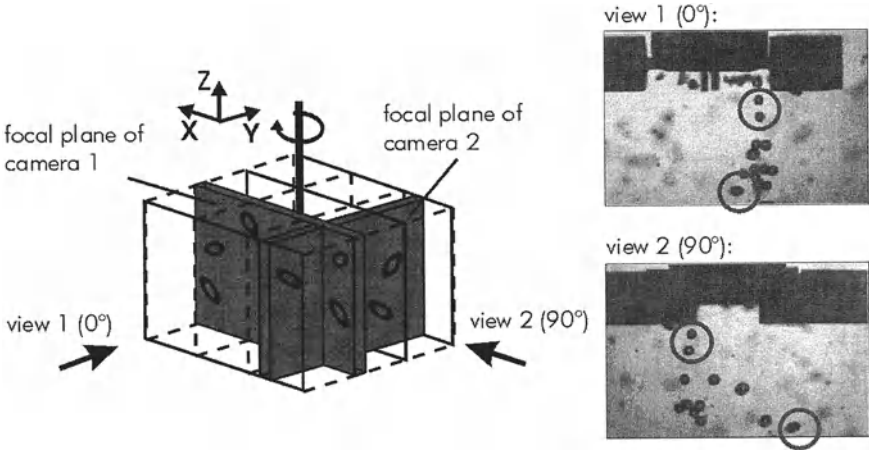


Fig. 5. Physical model for the stereo matching algorithm

The correlation of the bubbles in both views is performed without considering any feature-based criterion. This is important, since the shape and size of a bubble can vary significantly between the two views. After the two views are correlated, the determination of the sizes and the spatial locations is performed. Since especially the bubbles with a diameter of more than one millimeter are not spherical, determination of bubble diameter can be made more accurately by assuming ellipsoid bubbles and correlating the two holographically obtained images of each bubble [5,6,7].

Accuracy

Due to the high quality of the lenses utilized no distortion correction has to be performed. The cameras conduct only translatoric movements. The parallelism of the axis is ensured by alignment of the traversing slide and horizontal justification of the camera by means of a pitch plane regulating screw. A simplified calibration process can thus be applied. The projection equation is simplified and the number of unknown projection parameters is reduced.

The main source of uncertainty in this measuring technique was found to be the pixel representation of circular objects (bubbles), especially if these objects are represented by less than 10 pixels (independent of the absolute pixel size). The resolution of the area measurement tool in the developed code was set to 5 pixels, resulting in a maximum error of $\pm 3\%$ for areas with sizes between 6 and 40 pixels. In this work, the sizes of the bubbles' images ranged between 14 pixels ($d = 0.3$ mm) and 200 pixels ($d = 1$ mm). The error in imaging larger objects or structures was found to be less than 1% [4,6,8,9].

Application example

The results obtained when the two holograms taken in one experiment were recorded and evaluated as explained above are exemplarily shown in **Fig. 6**. The number of bubbles in one size interval and the cumulative volumetric frequency is plotted against the bubble diameter interval. At this operating point, a nozzle diameter of $d_N = 0,5$ mm and a stirrer speed of $n = 500$ rpm were chosen.

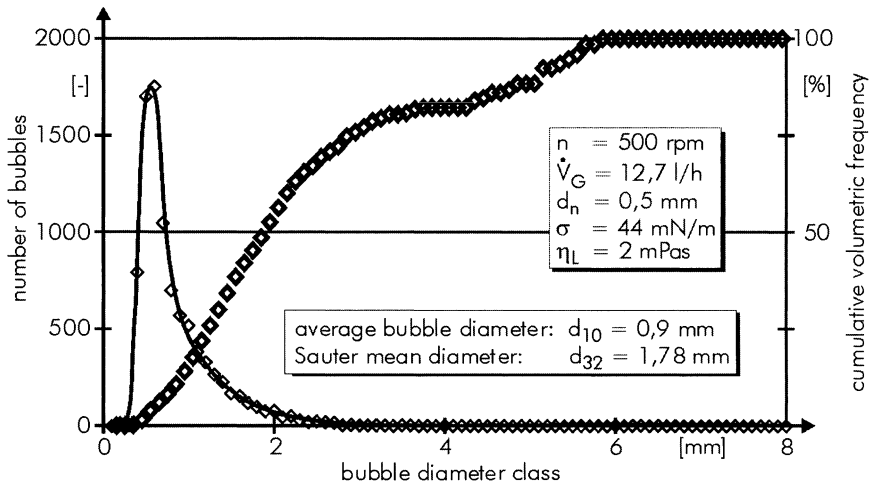


Fig. 6. diameter distribution and cumulative volumetric frequency of the bubbles

Every bubble in the vessel was taken into account to generate the bubble size distribution. Therefore, the average bubble diameter, the Sauter mean diameter, as well as the hold-up and phase interface can be calculated highly accurately [5].

Results

With the described procedure the influence of the stirrer speed, the nozzle diameter and the gas flow rate on the bubble size distribution was analyzed. The measured Sauter mean diameters were compared to calculated mean diameters from equations taken from the literature.

Influence of the stirrer speed on the bubble size distribution

The influence of different stirrer speeds on the resulting size distribution of the bubble diameters can be derived from Fig. 7. An increasing stirrer speed results in a decrease in average bubble size and a significant narrowing of the bubble size distribution.

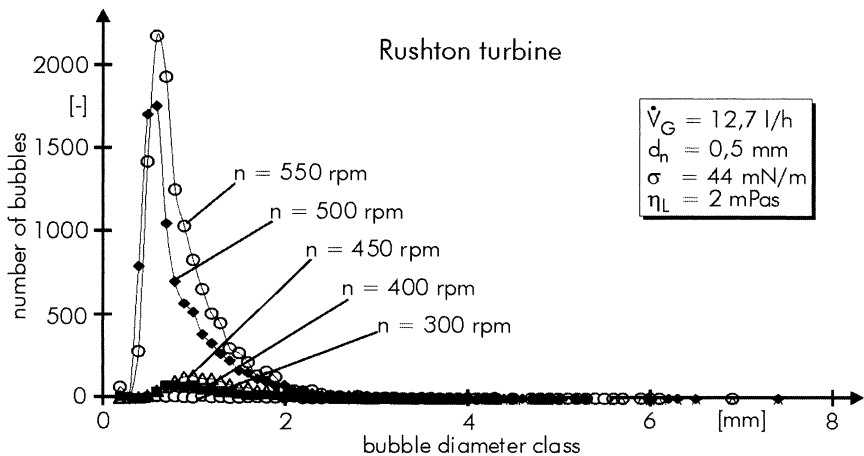


Fig. 7. Diameter distribution of the bubbles dependent on the stirrer speed

At impeller speeds below a value n_1 , the shear field in the liquid induced by the stirring process is not yet strong enough to significantly split up the bubbles. The bubbles are merely deflected in the radial flow field towards the vessel wall as they pass the agitator and rise up to the liquid surface.

When the impeller speed is increased above n_1 , smaller bubbles are dragged into the area below the stirrer again. The formation of a bubble vortex below the stirrer is initiated. This results from the stronger liquid eddy below the stirrer with increasing stirrer speed and from the reduced buoyancy of the smaller bubbles.

This eddy becomes more distinctive with further increases in impeller speed. As the eddy becomes stronger it begins to capture larger bubbles. However, the bubbles which have passed the agitator leave the vessel directly, since the liquid eddy above the stirrer is not strong enough to force the rising bubbles back downwards again.

At a certain impeller speed (n_2), bubbles above the agitator begin to be dragged by the upper liquid eddy back to the agitator. A further increase in speed enhances formation of both the eddy and the vortex. The number of the bubbles in the vessel volume rises significantly.

An increase in air flow rate or the variation of the nozzle diameter, however, did not have a remarkable impact on these specific speeds, unless bubbles of such a small size are generated at the nozzle that these are already entrained at lower speeds than n_1 [6].

Determination of the Sauter mean diameter

From the bubble size distributions depicted in **Fig. 7**, the Sauter mean diameter of the bubbles d_{32} were calculated by applying Eq.1:

$$d_{32} = \sum_i \frac{n_i d_i^3}{n_i d_i^2} \quad (1)$$

The experimentally derived Sauter mean diameters calculated from Eq. 1 were then compared to those predicted by the most common correlation taken from the literature [e.g. 1,2,19-25]:

$$\frac{d_{32}}{d} = C_{We} \cdot \left(\frac{\sigma}{\rho_L n^2 d^3} \right)^{0,6} = C_{We} \cdot We^{-0,6} \quad (2)$$

Eq. 2 is based on two main assumptions: firstly, the shear field induced by the stirring process induces turbulent shear forces, which in turn define the maximum stable bubble diameter [9], and secondly, the Sauter mean diameter is proportional to this maximum stable bubble diameter [3]. With these assumptions, the Sauter mean diameter – made dimensionless with the diameter d of the stirrer – was expressed by the Weber-Number We . The constant coefficient C_{We} in Eq. 2 was fit to experimental data by those authors, who investigated Sauter mean diameters in aerated stirred vessels [13,19, 20,21,22].

A condition for the application of Eq.2 is a turbulent operating point. An indicator for a turbulent operating point is the Reynolds-Number of $Re > 5 \cdot 10^3$, that is calculated from Eq. 3:

$$Re = \frac{\rho_L n d^2}{\eta_L} \quad (3)$$

When comparing Eq.1 with Eq. 2, the expected dependence of the Sauter mean diameter from the stirrer speed is: $d_{32} \sim n^{-1,2} \sim Re^{-1,2}$.

The influence of the Reynolds-Number, i.e. of the stirrer speed, on the measured Sauter mean diameter is plotted in **Fig. 8**. Also included in **Fig. 8** is the expected dependence of the Sauter mean diameter on the Reynolds-Number (solid line). The constant coefficient was fit to the experimental data plotted in **Fig. 7**.

As it can be derived from **Fig. 8**, the experimental data met well the theoretically predicted dependence on the stirrer speed. However, when a nozzle with a larger diameter is mounted in the vessel, larger Sauter mean diameters are measured, as it is indicated by the squared symbols in **Fig. 8** [6].

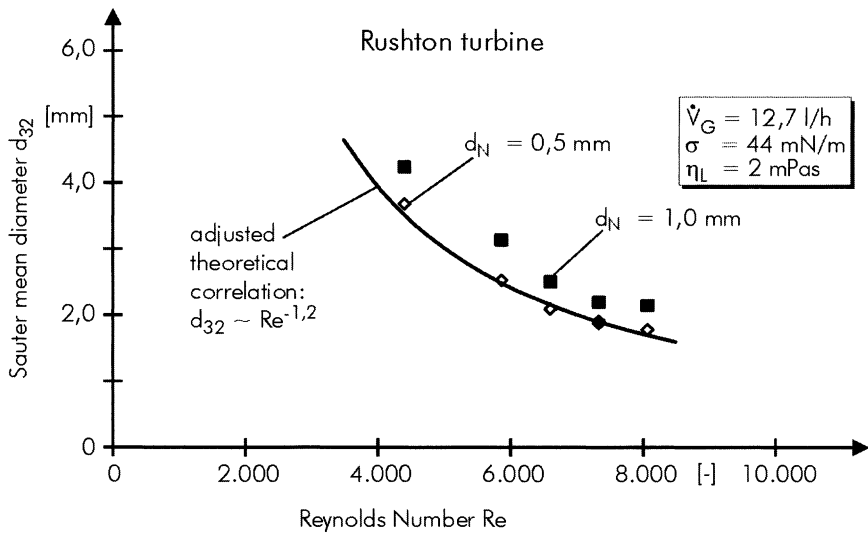


Fig. 8. Sauter mean diameter as a function of the Reynolds Number

A larger nozzle diameter resulted in larger primary bubbles generated at the nozzle. Larger primary bubbles in turn yield to larger Sauter mean diameters. This influence is not taken into account, when Eq. 2 is applied. The constant coefficient adjusted to series 1 does not fit the experimental data measured in series 2.

An increase in air flow rate also yielded larger primary bubbles at the nozzle and larger Sauter mean diameters in the vessel [6].

The effect of varying both the nozzle diameter and the air flow rate on the Sauter mean diameter is plotted in **Fig. 9**. Also included are correlations calculated from Eq. 2 with constant coefficients taken from the literature [13,19,20,22].

As it can be derived from **Fig. 9**, in every experimental series a different Sauter mean diameter was measured at constant Weber-Numbers. Both the variation of the nozzle diameter and the air flow rate resulted in different primary bubble diameters and in different Sauter mean diameters. This can not be described by Eq. 2 and may be the explanation for the significant spread of the constant coefficient C_{We} in the literature.

This leads to the conclusion that the influence of the different diameters of the primary bubbles on the bubble dispersion, and the bubble dispersion itself has to be investigated to correctly predict the bubble size distribution at a given operating point.

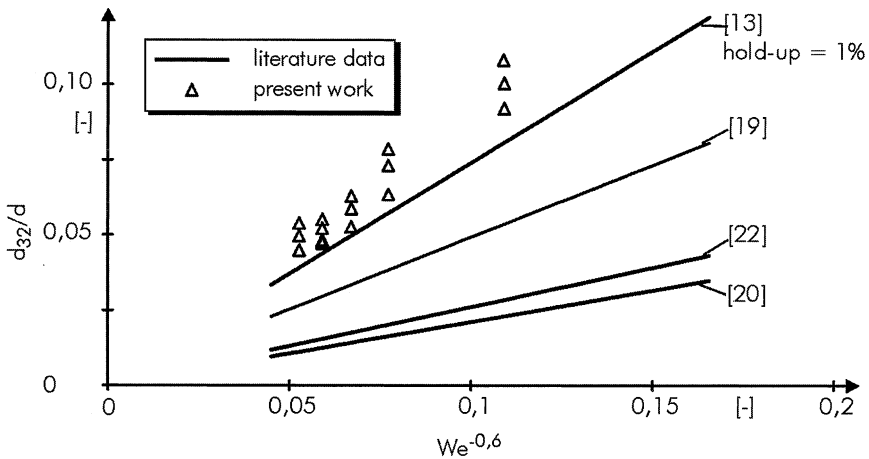


Fig. 9. Influence of both the nozzle diameter and the air flow rate on the Sauter mean diameter. Comparison between experimental data and correlations taken from the literature

Bubble dispersion and flow field of the bubbles

The bubble dispersion process and the flow field of the bubbles was analyzed by means of the high-speed cinematography. Time series of the stirrer region were recorded. As an example, a time series is given in **Fig. 10**, recorded at the operating point the bubble size distribution depicted in **Fig. 7** was derived from.

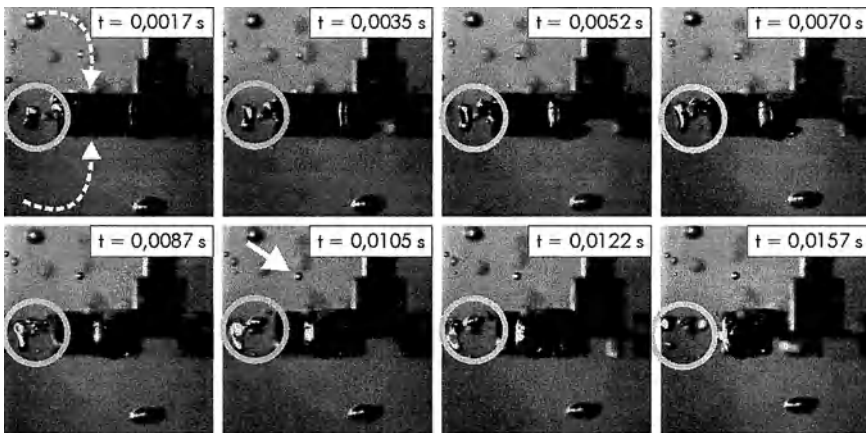


Fig. 10. High speed recording of the stirrer region (recording rate: 560 Hz)

As it can be derived from **Fig. 10**, the primary bubble rising from the nozzle enters the stirrer region and is then – following the liquid flow – radially accelerated towards the vessel wall (gray circle). The bubble is strongly deformed due to the high shear stresses acting on it and finally split up in two bubbles (gray circle, last

image), a larger and a smaller fraction. The larger bubble ('rest'-bubble) may be split up a second time, the smaller bubble ('daughter' bubble) is stable.

The number of bubble breakages was observed to be a function of the bubble size and the intensity of the turbulent shear stress (i.e. stirrer speed). However, it was not observed in this study that one bubble was broken up more often than five times [6].

It can also be derived from **Fig. 10** that the liquid flow (white dashed arrows) is not strong enough to force relatively small rising bubbles back downwards to the stirrer region (white arrow). This indicates, that only the small 'daughter' bubbles can be kept in the bubble vortices. The bigger 'rest' bubbles rise and leave the vessel directly [6].

Discussion of the experimental results

On the one hand, the holographic analysis yielded that the number of 'daughter' bubbles is significantly higher than the number of 'rest' bubbles. This can be explained by the fact that the bubble vortices consist of only the 'daughter' bubbles, as it was confirmed by the high speed analysis. On the other hand only up to five daughter bubbles are disintegrated from one primary bubble, as the high speed recordings demonstrated.

A 'daughter' bubble is the smaller fraction generated when one primary bubble is disintegrated. Its maximum volume is then half the volume of the primary bubble. At the operating point, the bubble size distribution plotted in **Fig. 7** was measured, primary bubbles with a diameter of 5,24 mm were generated at the nozzle. The maximum diameter of a 'daughter' bubble is then 4,16 mm. With the knowledge of this diameter it can be concluded, that approximately 20 % of the hold-up consists of 'rest' bubbles having a short residence time, whereas the daughter bubbles (80% of the hold-up) must have a significantly higher residence time in the vessel [6].

The cumulative volumetric frequency of every bubble plotted in **Fig. 7** is plotted in **Fig. 11** as the cumulative volumetric frequency of the 'daughter' bubbles and that of the 'rest' bubbles. In order to correctly predict the bubble size distribution in the vessel, both the size of the primary bubbles generated at the nozzle and the size distribution of the daughter bubbles generated by dispersing the primary bubbles has to be known.

In this work, the model introduced by Lehr [14] was modified and applied to determine the size distribution of the 'daughter' bubbles. In this model, the bubble diameter is compared to the diameter of the maximum stable bubble. The latter is defined by the intensity of the shear field (i. e. stirrer speed) [10,11,14,25]. The ratio of these two diameters defines the instability of the bubble. The larger this ratio is, the more instable the bubble is. With the knowledge of this ratio, both the size distribution of the daughter bubbles and the frequency of bubble breakages are calculated. Both an increase in stirrer speed and an increase of the primary bubble diameter yield more instable bubbles entering the shear field in the stirrer region. Increasing the ratio of instability yields smaller daughter bubbles and a higher

bubble breakage frequency. On the other hand larger bubbles have a smaller residence time in the shear field that in turn reduces the bubble breakage frequency and hence the number of daughter bubbles generated from one instable bubble. In addition, with increasing the size of the primary bubbles the size of the rest bubbles is increased resulting in both a larger Sauter mean diameter of the bubbles and a higher percentage of bubbles that cannot be kept in the bubble vortices. The result of applying the model to the determination of the size distribution of the daughter bubbles is also included in Fig. 11 (solid line).

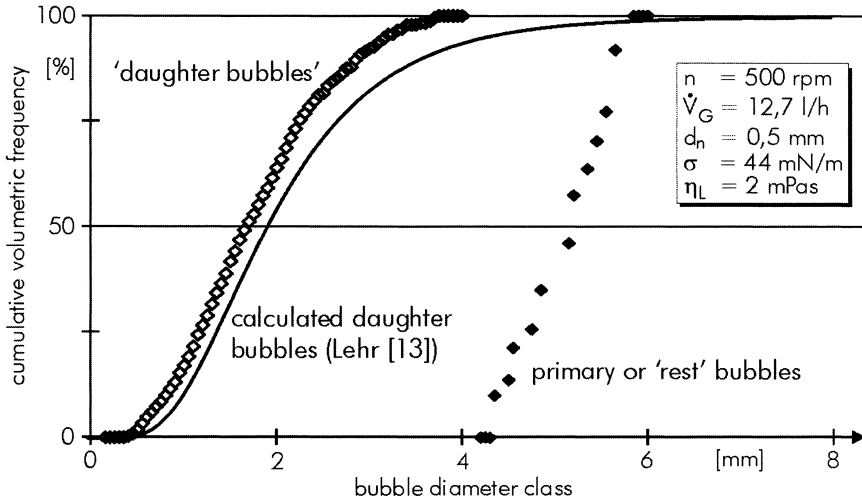


Fig. 11. Cumulative volumetric frequency of 'daughter' bubbles and 'rest' bubbles

The calculated size distribution slightly overestimates the sizes of the daughter bubbles (see Fig. 11). This is explained by the fact that the calculated distribution is the distribution of the generated bubbles, whereas the measured size distribution contains every daughter bubble in the vessel. As it was shown by means of the high speed recordings, the larger daughter bubbles can not be kept in the bubble vortices. Thus, by considering the residence time distribution of the daughter bubbles, the model can well describe the bubble dispersion. The obtained results deliver valuable input for numerical simulations of the two phase flow in the vessel.

Conclusion

The applied optical measurement technique, the short-time holography is a highly suitable measurement technique for analysis of aerated stirred vessels. The test section is recorded three dimensionally and unobtrusively, without disturbing the flow field. When a stereoscopic setup is applied, both the flow field and the size of the bubbles can be reconstructed very accurately in three dimensions.

Valuable data such as the bubble size distribution and the phase interface can be qualified, both of which have been impossible to determine directly using previous methods. The Sauter mean diameter of the bubbles is calculated based on the evaluation of the two holograms of each experiment. These can be determined highly accurately with high global and local resolution.

In combination with high speed recordings of the bubble dispersion process, short time holography provides the experimentally derived data needed to improve models to describe the two phase flow in aerated stirred vessels and to validate numerical simulations.

The Sauter mean diameter of the bubbles was found to decrease with rising impeller speeds and to increase with gas flow rate and the nozzle diameter through which the air is introduced.

When regarding the bubble size distribution, it can be stated that the Rushton turbine disintegrates relatively small bubbles from the primary bubbles and hence generates a large phase interface. However, a significant percentage of the air introduced directly leaves the vessels, since the liquid flow is too weak to keep larger bubbles in the bubble vortices. Therefore, it has to be distinguished between the mean diameter and the residence time of the 'daughter' bubbles and the mean diameter and the residence time of the 'rest' bubbles in the vessel, both of which vary. This is inherent to both the dispersion characteristics and the flow field of a Rushton turbine and not a function of the operating point.

Therefore, it has to be questioned whether the calculation of mean values, such as the Sauter mean diameter is appropriate to describe the dispersion characteristics of an aerated stirred vessel, when a Rushton turbine is applied as it is common in the literature. In addition, the analysis yields that the Rushton turbine is not an efficient tool to disperse the gaseous phase.

Literature

- [1] Barigou, M., Greaves, M.: Bubble-size distributions in a mechanically agitated gas-liquid contactor; *Chemical Engineering Science*, Vol. 47, No. 8, pp. 2009-2025, 1992
- [2] Barigou, M., Greaves, M.: Gas hold-up and interfacial area distributions in a mechanically agitated gas-liquid contactor; *TransIChemE*, Vol. 74, Part A, pp. 397-405, 1996
- [3] Brodkey, R. S.: *Turbulence in Mixing Operations. Theory and Applications to Mixing Reaction*; Academic Press, New York 1975
- [4] Chávez, A.: *Holografische Untersuchungen an Einspritzstählen, Fluidodynamik und Wärmeübergang durch Kondensation*, Dissertation TU München, 1991
- [5] Feldmann, O.; Mayinger, F.: Laser Pulsed Holography Applied to the three-dimensional Two-Phase-Flow in Aerated Stirred Vessels. In: *CD-ROM Proc. of the 8th Intl. Symp. on Flow Visualization, Sorrento, Italy, 1.-4. September 1998*. Eds.: C. M. Carlomagno et al. Edinburgh: 1998.

- [6] Feldmann, O.: Dispergieren in begasten Rührkesseln, Dissertation TU München, 2003
- [7] Feldmann, O.: Short Time Holography; In: Optical Measurements - Techniques and Applications 2nd Edition; Eds.: Mayinger, F. and Feldmann, O.; Springer Verlag, 2001
- [8] Feldmann, O.; Tauscher, R.: Digital image processing; In: Optical Measurements - Techniques and Applications 2nd Edition; Eds.: Mayinger, F. and Feldmann, O.; Springer Verlag, 2001
- [9] Gebhard, P.: Zerfall und Verdampfung von Einspritzstrahlen aus lamellenbildenden Düsen, Dissertation TU München, 1996
- [10] Hinze, J. O.: Fundamentals of the hydrodynamic mechanism of splitting in dispersion processes; AIChE J. Vol. 1, No. 3, 289-295, 1955
- [11] Kresta, S.: Turbulence in Stirred Tanks: Anisotropic, Approximate and Applied; The Canadian Journal of Chemical Engineering, Vol. 76, pp. 563-575, June 1998
- [12] Lee, K.C.; Yianneskis, M.: Turbulence Properties of the Impeller Stream of a Rushton Turbine; AIChE Journal, Vol. 44, No. 1, pp. 13-23; 1998
- [13] Lee, J.C.; Meyrick, B.: Gas-liquid interfacial areas in salt solutions in an agitated tank; TransIChemE, 48, T37-T45, 1970
- [14] Lehr, F.: Berechnen von Blasengrößenverteilungen und Strömungsfeldern in Blasen-säulen; Dissertation TU Hannover, 2001
- [15] Lu, W.-M.; Hsu, R.C.; Chien, W.C.; Lin, L.C.: Measurement of local bubble diameters and analysis of gas dispersion in an aerated stirred vessel with disc turbine impeller; Journal of chemical Engineering of Japan, Vol. 26, No. 5, pp. 551-557, 1993
- [16] Machon, V; Patek, A.W. Nienow, A.W.: Bubble Sizes in Electrolyte and Alcohol Solutions in a turbulent stirred Vessel; TransIChemE, Vol. 75, Part A, 1997
- [17] Mayinger, F., Chávez, A.: Measurement of direct-contact condensation of pure saturated vapor on an injection spray by applying pulsed laser holography, Int. J. Heat Mass Transfer, Vol 35, No. 3, pp. 691-702, 1992
- [18] Mayinger, F, Gebhard, P.: Evaluation of pulsed laser holograms of flashing sprays by digital image processing, ASME FED-VOL. 209, 13-22, Flow visualization and image processing of multiphase, 1995
- [19] Parthasarathy, R., Ahmed, N.: Bubble size distribution in a gas sparged vessel agitated by a Rushton turbine, Ind. Eng. Chem. Res., Vol. 33, No. 3, 1994
- [20] Parthasarathy, R., Ahmed, N.: Sauter mean and maximum bubble diameters in aerated vessels, TransIChemE, Vol. 72, Part A, July 1994

- [21] Werner, F., Mersmann, A.: An Engineering Approach to Turbulence; ICHIME Symposium Series No.: 136
- [22] Werner, F.: Über die Turbulenz in gerührten newtonschen und nicht-newtonschen Fluiden, Dissertation TU München, 1997
- [23] Zlokarnik, M.: Rührtechnik - Theorie und Praxis, Springer, Berlin, 1999
- [24] Zhou, G., Kresta, S. M.: Impact of Tank Geometry on the Maximum Turbulence Energy Dissipation Rate for Impellers, AIChE Journal, Vol. 42, No. 9, 2476 - 2490, 1996
- [25] Zhou, G., Kresta, S. M.: Correlation of mean drop size and minimum drop size with the turbulence energy dissipation and the flow in an agitated tank, Chemical Engineering Science, Vol. 53, No. 11, 2063 - 2079, 1998

PDA measurements and numerical simulation of turbulent two-phase flow in stirred vessels

A. F. Nassar, G. Zivkovic, B. Genenger and F. Durst

Institute of Fluid Mechanics (LSTM), Friedrich- Alexander- University Erlangen-Nürnberg, Cauerstrasse 4, D-91058 Erlangen, Germany

The local bubble size distribution in gassed stirred tanks was investigated experimentally by using phase Doppler anemometry (PDA) and simulated numerically. From the measurements, the mean bubble velocity and the mean diameter d_{32} according to Sauter were calculated. The flow fields produced by impellers have a considerable impact on the distribution of the mean diameter. Large bubble sizes were detected in the ring vortices present in the large-scale flow fields, with a significant increase occurring in the lower ring vortex produced by the Rushton turbine.

For the realistic treatment of bubble motion, the numerical code was implemented with the introduction of bubble break-up model. The model used is stochastic, based on the assumption that shear in the flow induces the breaking of the bubble. As a dominant parameter the dissipation of the turbulent kinetic energy was used.

Results of the computed bubble velocity field agree very well with the measurements. The calculated and measured values of the mean bubble diameter are of the same order, there is a deviation of about 20 % in the local diameter distribution. The data obtained contribute to a better understanding of gas-liquid flows in stirred reactors.

1. Introduction

Many industrially relevant stirred vessel processes are based on a specific gas-liquid dispersion. The challenge for an engineer is to select the best stirrer/vessel configuration from a wide range of possibilities to meet the requirements of the process, for example to ensure a sufficient mass-transfer rate. It is common practice to investigate the integral quantities of gas-liquid stirred vessel flows, such as the gassed power input and the gas hold-up, and to present them in the form of diagrams of normalised quantities which permit the results of laboratory studies to be transferred to large-scale stirred vessel systems with linearly scaled-up geometries of the stirred vessel (Tattersson 1991). Although the design rules resulting from such investigations are very useful for many practical applications, they permit very little information to be deduced on process and equipment improve-

ments. Such improvements require local data on process-related variables; for example, to prevent microorganism starvation, local gas hold-up and mass-transfer rates become important.

In more recent times, the emphasis has been on the development of numerical computation techniques (CFD) for the purpose of establishing accurate and low-cost design and dimensioning methods to be applied to various processes in stirred vessels. Recently, CFD has also been applied to analyse gas-liquid flows in stirred vessels (Bakker et al. 1994; Lo 1999). Numerical methods can be implemented for stirred tank reactors, but only in conjunction with precise, detailed experimental methods, which are essential for validation of the calculations and the methods used in the numerical schemes. Especially for gas-liquid flows, an accurate validation requires local information on the mean velocities, mean diameters and the size distributions of the bubbles throughout the entire tank.

2. Experimental set-up

The phase-Doppler anemometry (PDA) system used, shown in Fig. 1, was developed at LSTM. The system consists mainly of three parts: the measuring section, the PDA system, and the traversing system.

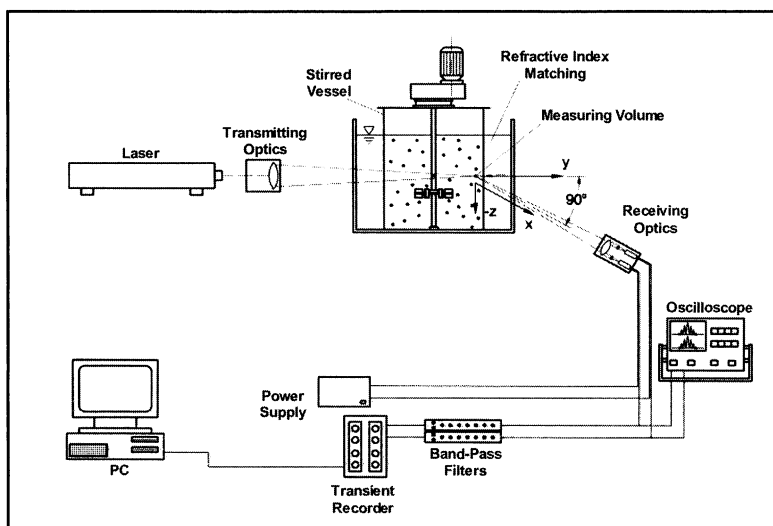


Fig. 1. Set-up of PDA test rig for measurements in stirred tank reactors

Table1. Dimensions of the mixing tank

Vessel Dimensions	
Tank diameter D (mm)	144
Liquid Height H (mm)	144
Baffle Width B (D/12)(mm)	11.5
Baffle Thickness (mm)	2.0
Baffle Clearance to Wall (mm)	2.9

The measuring section consists of a cylindrical baffled (four baffles) stirred tank equipped with an impeller. The geometries of the mixing tank are shown in Table 1. Two different impellers were used in the numerical simulation, namely the standard Rushton turbine (RT) and the pitched blade turbine (PBT), whereas only the standard Rushton turbine was used in the experimental measurements. Figs. 2, and 3, show the details of both impellers, which were mounted at a clearance of $h= D/3$. The blade thickness was 2 mm for the Rushton turbine and 0.9 mm for the pitched blade impeller.

The complete measuring section was refractive index matched. For this purpose, the cylindrical tank, the baffles and the stirrer blades were constructed from Duran glass that has the same refractive index as the model fluids. In addition, the stirred tank was located in a trough filled with the model fluid in order to eliminate distorting effects of the rounded surface of the vessel on the path of the laser beams and the scattered light. Two different liquids were used as a mixing fluid, a mixture of silicone oils and dimethyl sulfoxide (DMSO). The physical properties of the model fluids are listed in Table 2. The use of DMSO enabled us to measure in the turbulent regime, since its viscosity is relatively low with respect to the silicone oil mixture.

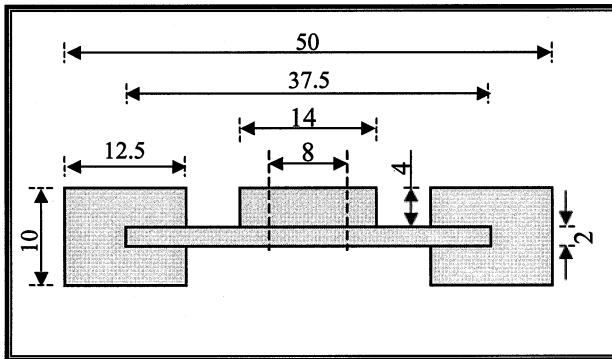


Fig 2. Geometry of the RT. (Dimensions in mm)

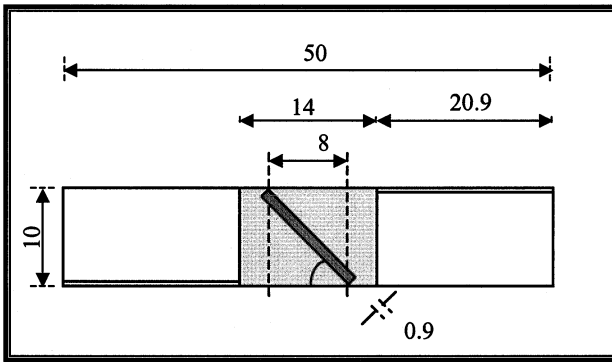


Fig 3. Geometry of the PBT. (Dimensions in mm)

Table 2. Properties of the model fluids

	Density (kg/m^3)	Viscosity ($\text{mPa}\cdot\text{s}$)	Refractive index	Surface tension N/m
Silicone Oil	1021	16.2	1.47	$23\cdot 10^{-3}$
DMSO	1100	2.14	1.478	$43\cdot 10^{-3}$

The PDA system consists of a laser, transmitting and receiving optics, PDA filters, and a PDA processor. Two lasers were used in the measurements, first an He-Ne laser (632.8 nm) and then an argon-ion laser (514 nm). All relevant parameters and characteristics of the measuring control volume are given in Table 3.

The traversing system is a 3-D traversing unit controlled by a PC via a controller. Since the receiving and sending optics are not aligned in one line, the refraction at the surface of the trough must be considered also for the sending optics. This means that for each movement in the sending optics for changing the position of the measuring volume, a different movement of the receiving optics is required. Therefore, the receiving optics were mounted on a fourth traversing unit, which was used for the re-adjustment of the APD detectors in both the x- and y-directions.

Air introduction to the tank was done at the beginning by one syringe needle fixed at the tank bottom at a distance of 26 mm from the tank center. Subsequently a new ring was designed and fabricated to introduce air in the tank through eight nozzles at the tank bottom at a radius of 13 mm; thus a homogeneous higher air distribution at the inlet was achieved. The needles used were able to produce spherical bubbles of a defined size, which is very important for PDA measurements, since the accuracy of the measurements depends significantly on the sphericity of the bubbles.

Table 3. Optical parameters and characteristics of the control volume

	Variable	He-Ne laser	Ar-ion laser
Sending optics			
Laser power (mW)	P_L	15	150
Wavelength (air) (nm)	λ	632.8	514
Focal length of sending lens (air) (mm)	f_T	400	400
Beam distance (mm)	D_B	50	50
Beam waist diameter (μm)	d_B	650	680
Beam crossing half-angle (air) ($^\circ$)	θ	3.58	3.58
Beam crossing half-angle (fluid) ($^\circ$)	θ_F	2.56	2.56
Shift frequency (MHz)		1.0	1.0
Receiving optics			
Focal length of receiving lens (air) (mm)	f_R	310	310
Focal length of collection lens (mm)	f_C	80	80
Diameter of collection lens (mm)	d_C	30	30
Diameter of pinhole (μm)	d_P	200	200
Off-axis angle ($^\circ$)	ϕ	90	90
Measuring volume			
Diameter (μm)	d_M	496	385
Length (mm)	l_M	11.09	6.16
Fringe spacing (μm)	d_F	7.08	4.12
Number of fringes (no shift frequency)	N_F	70	93
Intensity in measuring volume (W/m^2)	I	78,000	1,290,000

3. Computation

The main characteristic of the numerical code is the change of the geometry of the flow domain due to the change of the relative position of the blades of the stirrer with respect to the baffles. There exists a direct, unsteady approach, clicking grids, which was found to be extremely time consuming and not convenient for the case of two-phase flow computations. The problem was solved by introducing multiple-frame-of-reference method. According to this approach, the inner part of the flow field which comprehends the stirrer is rotating, which is simulated by introducing additional terms in the partial differential equations which describe the flow in that domain. These terms simulate centrifugal and coriolis forces. In the other part of the flow field everything stays the same. With this approach the relative motion of the blades with respect to the baffles was neglected, based on the assumption that, the relative position of the blades cannot influence significantly the field close to the baffles and that fluid close to the blades does not 'feel' the existence of blades. The border between the rotating and non-rotating parts was of course chosen to be far enough from both the baffles and blades. Wechsler et al. (Wechsler et al. 1999) have shown that there is no significant difference in the results obtained by the two approaches mentioned, which vindicates the use of the multiple-frame-of-reference method.

The emphasis in single flow computation was placed on flow regimes with $Re > 10000$. Therefore, a new type of the liquid in the stirred tank, DMSO, was used. Also, in addition to the computation of the flow in the stirred tank with the Rushton turbine, computations with the 45° pitch blade turbine were also performed. In Figs. 4 and 5 the geometries of these stirred tanks are presented.

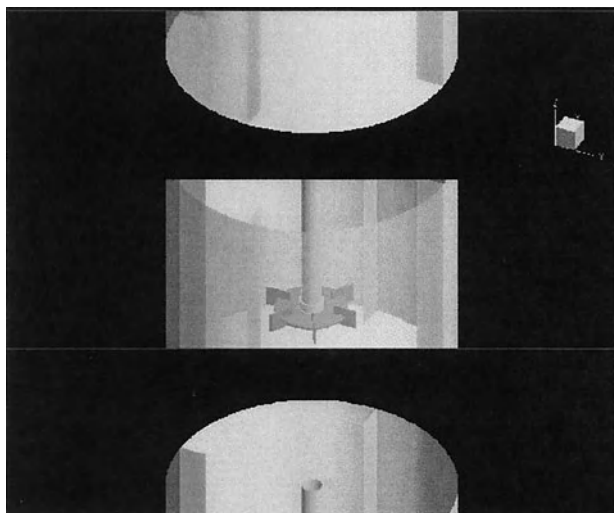


Fig 4. Rushton turbine

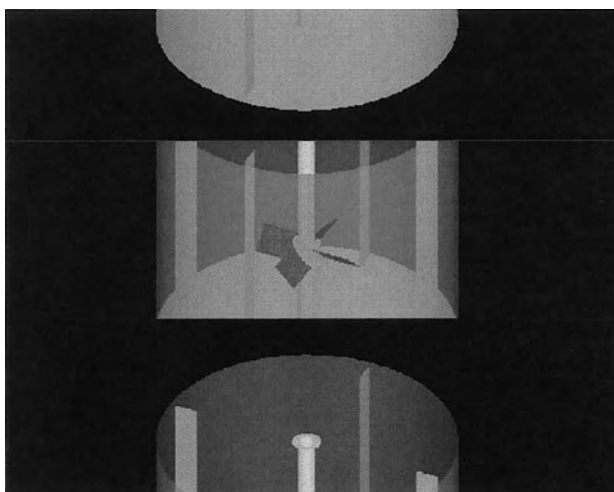


Fig.5. Pitch blade turbine

The computations with DMSO as a model liquid were performed for the tank with the Rushton turbine for a rotational speed of 600 rpm. This corresponds to a Reynolds number of 12850. In the computations with the pitch blade turbine, two different directions of turbine rotations were studied. Owing to the dependence of the flow pattern on the rotational direction, in one case an upstream and in the other a downstream recirculation zone were obtained. Both types of flow could be met in practice. The basic difference is that in the case of two-phase bubble-liquid flow the residence time of the bubbles in the open tank is much higher in the case of the downstream recirculation zone. The computations were performed for silicone oil, for a rotational speed of 850 rpm, corresponding to a Reynolds number of 2270.

Model of the bubble motion and break-up

As the basis for the modeling of the gas phase, the LAG3D code for the computation of two-phase gas-particle flow was used. This code was tested at LSTM on three typical cases of gas-particle flow, and showed good agreement with the experimental data (Bartels et al. 2002). The basic characteristics of the code were: (1) Lagrangian approach; (2) particles are treated as ideal spheres; (3) all relevant forces are included; (4) particle-wall interaction is included; (5) particle-particle interaction is included; (6) Langevin's model of particle-fluid turbulent eddy interaction. In order to extend the use of the code to gas-liquid problems also, it was necessary to add 'added mass' force in the equations of bubble motion. Also, in the process of stirring and mixing, bubble break-up is an inevitable and very important phenomenon. Therefore, it was necessary to create a model of the bubble break-up. Bubble coalescence can play an important role also, but only in cases of large gas hold-up, as in real industrial cases (10% and more). The sphericity of the particles (in this case bubbles) remained as the basic assumption of the model, which restricted the use of the model to air bubbles smaller than 2 mm. In the experiments the initial bubble diameter was about 1.7 mm in the case of silicone oil and 1.2 mm in the case of DMSO, and was therefore small enough.

As the basis for the developed model, the Martinez-Bazan approach (Martinez-Bazan et al. 1999, 1999), developed at San Diego University, was adopted. This is a statistical model in which the break-up of the bubble and the diameters of daughter bubbles are stochastic events. According to this model:

1. For a bubble to break, its surface has to deform. This deformation is provided by the turbulent stresses generated in the surrounding water. This assumption is in accordance with the already mentioned fact of the importance of the role of turbulent and shear stresses in stirring and mixing processes.
2. The probability of the splitting should be weighted with the difference between turbulent stresses and surface restoring pressure.

As the result of the break-up modeling, one obtains: (1) bubble splitting frequency; (2) number of daughter bubbles; (3) p.d.f. function of daughter bubble diameters.

The minimum energy E_s to deform the bubble could be connected with the bubble surface tension σ :

$$E_s = \pi\sigma D^2 \quad (3.1)$$

From this, the surface restoring tension is obtained:

$$\tau_s = \frac{6E_s}{\pi D^3} = \frac{6\sigma}{D} \quad (3.2)$$

On the other hand, turbulent stress can be connected with the mean squared velocity difference on two opposite points on the bubble sides:

$$\tau_t = \frac{1}{2} \rho \overline{\Delta u^2} \quad (3.3)$$

$$\overline{\Delta u^2} = \overline{[u(x+D, t) - u(x, t)]^2} = \beta(\varepsilon D)^{2/3} \quad (3.4)$$

where $\beta = 8.2$ (the Batchelor constant) and ε represents the dissipation of turbulent kinetic energy.

In order for a bubble to break, it is necessary that $\tau_t > \tau_s$. From this criterion one can find the critical diameter; the diameter of the bubble should be larger than this in order for the bubble to break

$$D_c = \left(\frac{12\sigma}{\beta \rho} \right)^{3/5} \varepsilon^{-2/5} \quad (3.5)$$

The minimal distance between the positions of turbulent fluctuations is found to be

$$L_{\min} = \left(\frac{12\sigma}{\beta \rho D} \right)^{3/2} \varepsilon^{-1} \quad (3.6)$$

It was assumed that the rate at which the break-up process takes place is inversely proportional to the difference between the deformation and restoring forces. According to that assumption, the break-up time t_b is proportional to

$$t_b \propto \frac{D}{\sqrt{\Delta u^2 - \frac{12\sigma}{\rho D}}} \quad (3.7)$$

The break-up frequency is then given by

$$g \propto t_b^{-1} = K_g \frac{\sqrt{\Delta u^2 - \frac{12\sigma}{\rho D}}}{D} = K_g \frac{\sqrt{\beta(\varepsilon D)^{2/3} - \frac{12\sigma}{\rho D}}}{D}, \quad (3.8)$$

where K_g is a constant whose value was determined experimentally in order that the computation fitted the experimental results (Martinez-Bazan et al.).

A good characteristic of the model is that there exists a value of the bubble diameter for which the break-up frequency reaches its maximum value, which is in accordance with the experiments. In this way, the same model could be applied to a wide range of sizes of the bubble diameter. A weak aspect of the model is that the turbulent kinetic energy was introduced indirectly, over the value of the turbulent kinetic energy dissipation. It is known that ε is much harder to measure, and even in the computation of single-phase fluid flow the field of ε obtained is in many cases not quite accurate. Therefore, even when the break-up model in itself is correct, owing to the inaccuracy in the ε field, obtained from the computation of the single phase, the results obtained may not be completely reliable.

The following assumption of the model is that in the break-up process the mother bubble breaks into only two daughter bubbles. This assumption is acceptable, as any breaking process which gives more than two daughter bubbles could be resolved on a few different processes (which give as the result of breaking only two daughter bubbles) simply by reducing the time step Δt between the two calculated instants.

The following, crucial assumption of the model is that the probability that turbulent fluctuations would act at a certain distance should be weighted by the difference between the values of turbulent and restoring stress for that distance. That is:

$$L < L_{\min} \Rightarrow P(L) = 0, \quad (3.9)$$

$$L > L_{\min} \Rightarrow P(L) = \left[\frac{1}{2} \rho \beta(\varepsilon L)^{2/3} - \frac{6\sigma}{D_0} \right]. \quad (3.10)$$

According to the proposed model, L represents the diameter of the part of the mother bubble which splits into two halves of diameter D_1 . Therefore

$$D_1 < 0.794L_{\min} \Rightarrow P(D_1) = 0, \quad (3.11)$$

$$D_1 > 0.794L_{\min} \Rightarrow P(D_1) \propto \left[0.583 \rho \beta(\varepsilon D_1)^{2/3} - \frac{6\sigma}{D_0} \right]. \quad (3.12)$$

The difference in p.d.f in the proposed model and the model of Martinez- Bazan is shown in Fig. 6. There, $D^* = D/D_0$, where D represents the smaller of the two daughter bubbles. Both models give qualitatively the same results. Nevertheless, the proposed model does not suffer from inner inconsistencies, hence in the process of splitting one can obtain bubbles of deliberately small sizes, which is in accordance with the experiments.

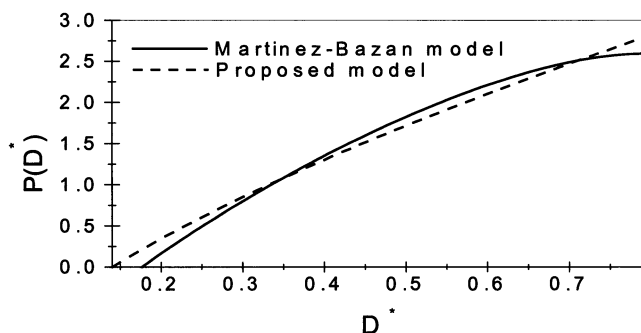


Fig 6. Adjustment of the model

4. Results

The PDA system was used to gain local information on gas-liquid characteristics in the stirred vessel. Measurements were made using RT in an r-z plane located exactly in the middle between two baffles ($\theta = 45^\circ$) with a radial and axial resolution of 10-24 mm throughout the whole tank. With silicone oil the flow rate of the air was 0.41 ml/s, and two different speeds were used, 750 rpm ($Re = 1970$) and 850 rpm ($Re = 2232$). For DMSO, two different cases were tested. In the first the air flow rate was 0.53 ml/s (gas hold-up 0.58%) with a stirrer speed of 600 rpm ($Re = 12850$). In the second test case a ring sparger was used, and therefore an increased air flow rate of 3.08 ml/s was possible, which corresponds to a 3.1% gas hold-up, and the speed of the stirrer was 550 rpm ($Re = 11780$). The local bubble size distribution and the corresponding velocities were recorded.

In the computations, the local gas concentration, bubble diameter and velocity were calculated. Both RT and PBT were computed. For silicone oil speeds of both 750 and 850 rpm were tested using RT, and 850 rpm for both pumping up and pumping down PBT. For DMSO the computations were done only with the RT with a speed of 650 rpm.

In Figs. 7 and 8, the computational and experimental results of the bubble axial velocity in the tank with the Rushton turbine are presented. The results are for the same geometry; Fig 7 shows the velocity field in silicone oil, and Fig. 8 presents the velocity field in DMSO. The velocity field is as expected, where the two large

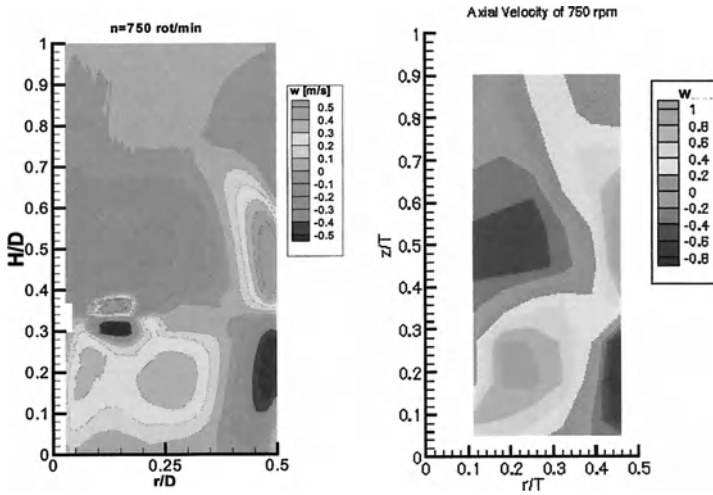


Fig 7 Bubble axial velocity profiles in silicone oil (left computed; right measured)

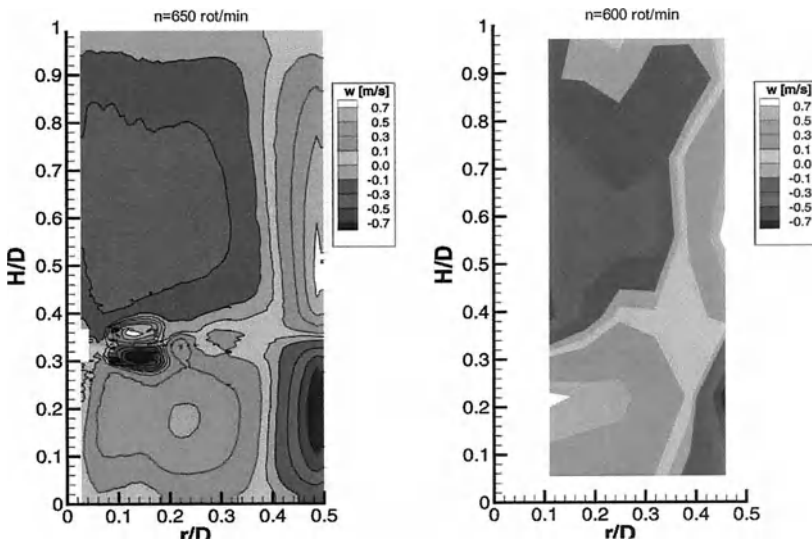


Fig 8 Bubble axial velocity profiles in DMSO (left computed; right measured)

recirculation zones below and above the impeller should be noted. It can be seen that qualitatively the results agree. The agreement in Fig. 8 is quantitatively much better where measurements were made with the argon-ion laser and the number of

measuring points per grid was larger. Therefore, it is to be expected that with increase in the number of measured points the agreement will be even better.

The Sauter mean bubble diameter distribution is presented in Figs. 9 and 10. Here, the agreement between measurements and calculations is not so good. As expected, regions of larger bubble sizes were detected in the measurements especially in the core of the low vortex, where larger bubbles are captured. This is because the radial jet from the RT hinders the larger bubbles from escaping from the lower to the upper vortex. In contrast, the upper ring vortex is of less intensity so that larger bubbles can escape easily to outside the tank (Schäfer et al. 2000). This phenomenon is very clear in Fig. 10. In addition, no circulation is present in the uppermost flow region of the tank so that the bubbles leaving the upper vortex are not circulated back to the liquid and pass through the measuring volume of the PDA system at a maximum of once in their lifetime. Therefore, smaller mean diameters were obtained in the uppermost flow regions. The mentioned phenomenon is not observed in the calculations.

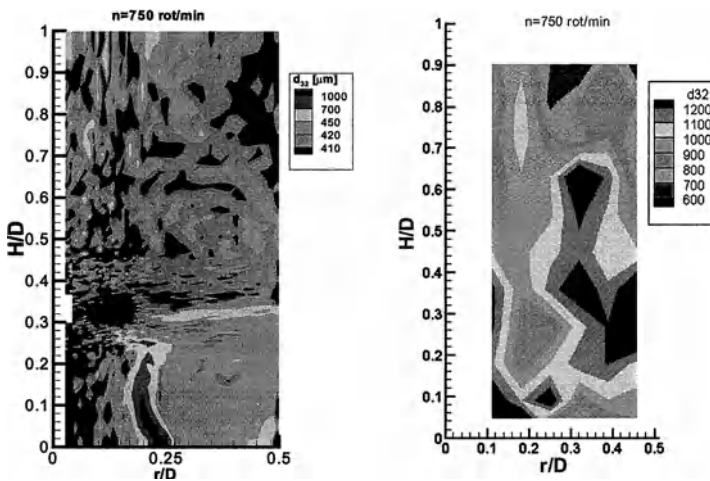


Fig 9 Sauter mean diameter profiles in silicone oil (left computed; right measured)

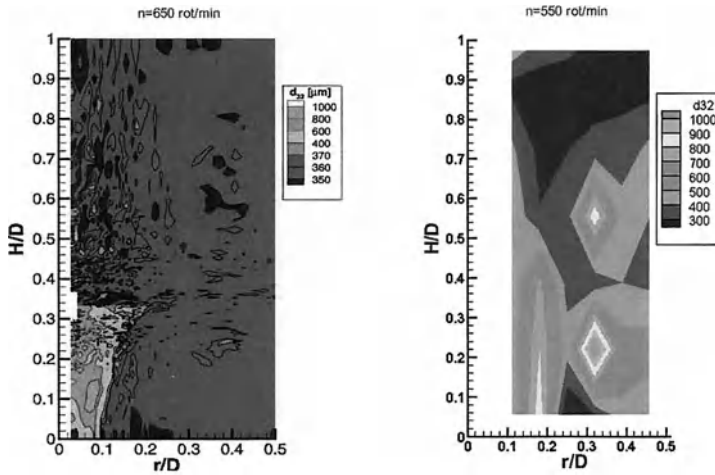


Fig 10 Sauter mean diameter profiles in DMSO (left computed; right measured)

The results of the computation of the gas phase in the tank with the pitch blade stirrer are presented in Figs. 11 and 12. The axial velocity profiles of the gas phase are, in both up-flow and down-flow, similar to the liquid velocity profiles, which shows the strong dependence of the bubble trajectories on the liquid velocity profile.

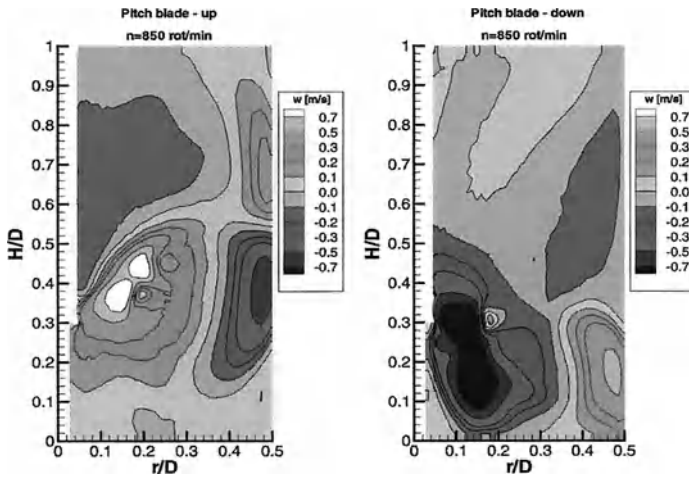


Fig 11 Bubble axial velocity profiles in silicone oil (left pumping up; right pumping down)

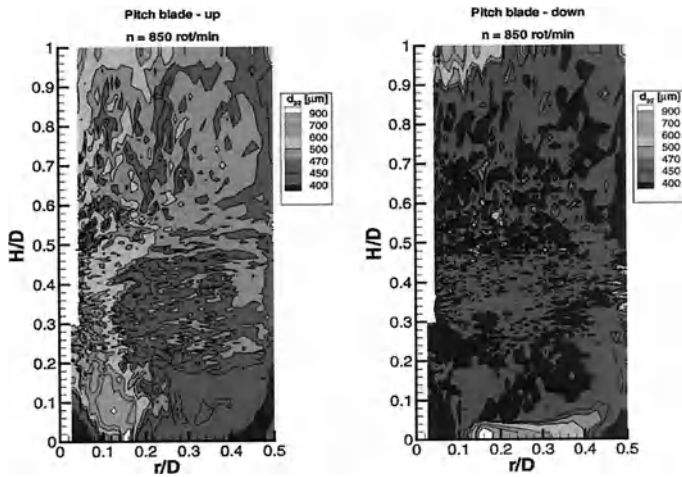


Fig 12 Sauter mean bubble diameter profiles in silicone oil (left pumping up; right pumping down)

It is observed that the Sauter mean diameter is much smaller in the down-flow case. This could be explained only by the fact that down-flow rotation keeps bubbles much longer in the stirrer than up-flow, with the consequence that the probability that bubbles pass through the regions of high turbulent kinetic energy becomes greater, and consequently more bubbles break, giving a smaller average diameter. For smaller bubbles it now becomes even more difficult to escape; they move randomly through the stirrer, carried by the liquid, giving a more or less average diameter size distribution. In up-flow, large bubbles find their way to the surface much easier, do not break so frequently, and since they carry most of the mass of the gas phase they cause a high concentration of gas phase in the regions through which they pass.

Conclusions

PDA has been successfully applied to investigate turbulent gas-liquid flows in stirred vessels with a higher gas hold-up (3.1%). A mathematical technique including a bubble break-up model was used to simulate the flow field inside aerated stirred vessels. Results of the computed bubble velocity field agree very well with the measurements. The calculated and measured values of the mean bubble diameter are of the same order, there is a deviation of about 20 % in the local diameter distribution. The flow regimes inside the vessel have a high impact on the local mean diameter of the bubbles and on their velocity profiles.

The data set produced should be extended by further measurements by changing some parameters such as the impeller type, gas flow rate, and impeller speed. Also, the adjustment of the break-up model is necessary in addition to the introduction of the coalescence model.

Acknowledgements

The authors acknowledge the Deutsche Forschungsgemeinschaft (DFG) for its support and Prof. Dr. M. Sommerfeld (Institute of Process Engineering, Mechanical Process Engineering, Martin-Luther-University of Halle-Wittenberg), who developed the code LAG3D used for the implementation of the bubble break-up model.

References

- Tatterson GB (1991) *Fluid Mixing and Gas Dispersion in Agitated Tanks*. McGraw-Hill, New York
- Bakker A, Smith JM and Myers KJ (1994) How to Disperse Gases in Liquids. In: *Chem. Eng.*, vol. 101, No. 12, pp. 98-104
- Lo S (1999) Application of population balance to CFD modeling of bubbly flows via the MUSIG model. In: *4th International Conference on Gas-Liquid and Gas-Liquid-Solid Reactor Engineering*, Delft, August 23-25, 1999
- Wechsler K, Breuer M and Durst F (1999) Steady and Unsteady Computations of Turbulent Flows Induced by a 4/45° Pitched Blade Impeller. In: *J. Fluids Eng.*, vol. 12, pp. 318-329
- Bartels C, Breuer M, Wechsler K and Durst F (2002) Computational fluid dynamics applications on parallel-vector computers: computations of stirred vessel flows. In: *Computers & Fluids*, vol. 31, pp. 69-97
- Martinez-Bazan C, Montanes JL and Lasheras JC (1999) On the break-up of an air bubble injected into a fully developed turbulent flow. Part I: Break-up frequency. In: *J. Fluid Mech.*, vol. 401, pp. 157-182
- Martinez-Bazan C, Montanes JL and Lasheras JC (1999) On the break-up of an air bubble injected into a fully developed turbulent flow. Part II: Size PDF of the resulting daughter bubbles. In: *J. Fluid Mech.*, vol. 401, pp. 183-207
- Schäfer M, Wächter P and Durst F (2000) Experimental investigation of local bubble size distributions in stirred vessels using Phase Doppler Anemometry. In: van den Acker HEA, Derksen JJ (Editors) *10th European Conference on Mixing* (Delft, July 2-5, 2000), ELSEVIER